School of Electrical Engineering & Computing
International Centre for Radio Astronomy Research
Curtin Institute of Radio Astronomy

Interstellar and Intergalactic Scattering as Astrophysical Probes

Jun Yi Koay

**This thesis is presented for the Degree of
Doctor of Philosophy
of
Curtin University**

August 2012

To the best of my knowledge and belief, this thesis contains no material previously published by any other person except where due acknowledgement has been made. This thesis contains no material which has been accepted for the award of any other degree or diploma in any university.

....
JUN YI KOAY
10 August 2012

to the AGN of my life, Agnes,
our spritely little jets Jacynth & Jaydon,
and
YHWH, who unsettles, uproots and surprises

Preface

A significant portion of the work presented in this thesis lies within a larger framework of the Micro-Arcsecond Scintillation Induced Variability (MASIV) Survey and its follow-up observations. I was not personally involved in the proposal, experiment design and data acquisition related to the MASIV follow-up observations, but have used the data extensively in this study. However, the reduction, calibration, error estimation, and characterization of the variability data (in Chapter 2), as well as all the scientific analysis presented in Chapters 3 to 5 of this thesis, are all my own work. Due to the possible ground-breaking nature of the results, there were extensive discussions with my supervisors and the rest of the MASIV team on the analysis techniques as well as the interpretation and conclusions drawn from the results. From these discussions, I took many valuable comments and suggestions on board. Chapter 6 is primarily my own work, with comments and suggestions from my supervisors.

Publications directly resulting from work done for this thesis are as follows:

- H. E. Bignall, D. L. Jauncey, L. Kedziora-Chudczer, **J. Y. Koay**, J. E. J. Lovell, J.-P. Macquart, R. Ojha, T. Pursimo, C. Reynolds, and B. J. Rickett, 'Combining VLBI and MASIV – How Intrinsic Properties Influence Interstellar Scintillation of AGN,' *Proceedings of Resolving The Sky - Radio Interferometry: Past, Present and Future*, Manchester, UK, in press.

- **J. Y. Koay**, J.-P. Macquart, B. J. Rickett, H. E. Bignall, D. L. Jauncey, T. Pursimo, C. Reynolds, J. E. J. Lovell, L. Kedziora-Chudczer, & R. Ojha, 'Why Do Compact Active Galactic Nuclei At High Redshift Scintillate Less?,' *The Astrophysical Journal*, 756, 29, 2012.

- **J. Y. Koay**, J.-P. Macquart, B. J. Rickett, H. E. Bignall, D. Jauncey, J. E. J. Lovell, C. Reynolds, T. Pursimo, L. Kedziora-Chudczer, and R. Ojha, 'Interstellar Scintillation as a Cosmological Probe: Prospects and Challenges,' *Proceedings of the International Astronomical Union*, Symposium 285: New Horizons in Time Domain Astronomy, Oxford, UK, 2011.

- **J. Y. Koay**, J.-P. Macquart, B. J. Rickett, H. E. Bignall, J. E. J. Lovell, C. Reynolds, D. Jauncey, T. Pursimo, L. Kedziora-Chudczer, and R. Ojha, 'Interstellar Scattering as a Cosmological Probe,' *Proceedings of the International Union of Radio Science (URSI) General Assembly and Scientific Symposium*, Istanbul, Turkey, 2011.

- **J. Y. Koay**, H. E. Bignall, J.-P. Macquart, D. L. Jauncey, B. J. Rickett, & J. E. J. Lovell, 'Detection of Six Rapidly Scintillating Active Galactic Nuclei and the Diminished Variability of J1819+3845,' *Astronomy & Astrophysics*, 534, L1, 2011.
- **J. Y. Koay**, J.-P. Macquart, B. J. Rickett, H. E. Bignall, J. E. J. Lovell, C. Reynolds, D. L. Jauncey, T. Pursimo, L. Kedziora-Chudczer, & R. Ojha, 'Dual-frequency Observations of 140 Compact, Flat-spectrum Active Galactic Nuclei for Scintillation-induced Variability,' *The Astronomical Journal*, 142, 108, 2011.
- H. Bignall, **J. Y. Koay**, J.-P. Macquart, J. Lovell, R. Ojha, M. Dutka, T. Pursimo, B. Rickett, D. Jauncey, and L. Kedziora-Chudczer, 'On the Redshift Dependence of Scintillating AGN: Results of the MASIV Survey and Follow-Up Observations,' *Proceedings of the International Square Kilometre Array Forum (ISKAF) Science Meeting*, Assen, Netherlands, 2010.

Other publications during the course of my PhD candidacy are:

- D. L. Jauncey, H. E. Bignall, L. Kedziora-Chudczer, **J. Y. Koay**, J. E. J. Lovell, J.-P. Macquart, R. Ojha, T. Pursimo, C. Reynolds, and B. J. Rickett, 'Microarcsecond Resolution with Interstellar Scintillation,' *Proceedings of Resolving The Sky - Radio Interferometry: Past, Present and Future*, Manchester, UK, in press.
- T. Pursimo, R. Ojha, D. L. Jauncey, B. J. Rickett, M. S. Dutka, **J. Y. Koay**, J. E. J. Lovell, H. E. Bignall, L. Kedziora-Chudczer, & J.-P. Macquart, 'Redshifts and Optical Properties of Scintillating and Non-Scintillating Extragalactic Radio Sources in the MASIV Survey,' *The Astrophysical Journal*, submitted.
- J.-P. Macquart, M. Bailes, R. Bhat, G. Bower, J. Bunton, S. Chatterjee, T. Colegate, J. M. Cordes, L. DAddario, A. Deller, R. Dodson, R. Fender, K. Haines, P. Hall, C. Harris, A. Hotan, S. Johnston, D. L. Jones, M. Keith, **J. Y. Koay**, T. J. W. Lazio, W. Majid, T. Murphy, R. Navarro, C. Phillips, P. Quinn, R. A. Preston, B. Stansby, I. Stairs, B. Stappers, L. Staveley-Smith, S. Tingay, D. Thompson, W. van Straten, K. Wagstaff, M. Warren, R. Wayth, & L. Wen, 'The Commensal Real-Time ASKAP Fast Transients (CRAFT) Survey,' *Publications of the Astronomical Society of Australia*, 27, 272, 2010.

Acknowledgements

This journey of three years and three months has been, on one hand, exhilarating and fulfilling, while on the other, challenging and demanding. I would not have made it this far without the many people who, in the midst of their own journeys, have travelled alongside me, even if only for a little while.

I will forever be indebted to my supervisor, Professor Peter Hall, for trusting my abilities despite my 'obscure' background and fully supporting my scholarship application, thesis candidacy, travel arrangements and research. It is through this unwavering support that I now have the opportunity to pursue and live a dream. Words will not suffice in describing the extensive role that Dr. Jean-Pierre Macquart, my co-supervisor, has played in nurturing my fledgling career as a researcher. My heartfelt thanks go to him for always availing himself, for setting high standards and goals, and for occasionally driving me forward with a stick. His weird tales, anecdotes and sarcasm never fail to both challenge and inspire. The greatest lesson that both my supervisors have taught me is that the best presentations and papers are the ones that are the simplest and most succint.

This thesis would not have been possible without the work and effort of the entire MASIV team — Dr. Jim Lovell, whose expert scheduling of the MASIV Survey and follow-up observations continue to amaze me, and who provided the core AIPS script for reducing the data; Dr. Cormac Reynolds and Dr. Hayley Bignall, for the countless discussions and helpful tips on the data reduction; Professor Barney Rickett, who has been an unofficial external supervisor to me, and whose vast experience, attention to detail, and thoughtful advice have greatly improved the quality of my work; Dr. Dave Jauncey, for being always enthusiastic and encouraging, for always having great ideas, and for critically evaluating every result; Dr. Tapio Pursimo, for the painstaking work of reducing the optical data to obtain source redshifts critical for my work; as well as Drs. Roopesh Ojha and Lucyna Kedziora-Chudczer for their invaluable comments and support.

I am also thankful to many others from ICRAR and other institutions, with whom I have had the pleasure of discussing my work through random chats in the corridor, or in official discussions and meetings. In particular, I thank Dr. Leith Godfrey, the resident expert on AGN jet physics; Dr. Cathryn Trott, the statistics guru; Dr. Roberto Soria, the X-ray guy who gives excellent talks and whose wicked sense of humour is legendary; Professor Ron Ekers, the man some hold responsible for Pluto's fall from grace; Dr. Greg Taylor, the one behind the Long Wavelength Array (LWA); Dr. James Miller-Jones, the one we refer to as the 'paper machine'; Dr. Sarah Burke-Spolaor, who found the suspicious 'perytons'; Professor Bryan Gaensler, who introduced me to the 'impostor syndrome', Dr. Adam Deller, creator of the DiFX correlator; and Dr. John O'Sullivan, inventor of Wi-Fi. I must not forget Dame Jocelyn Bell Burnell whom I have been fortunate enough to have met, and whose life story continues to inspire me. Additionally, I thank Dr. Nathan Clarke, Dr. Stephen Ord, and Professor Steven Tingay, who have been excellent project leaders and managers, for providing financial support for my publications and travel. I am extremely grateful to Barney and Holly Rickett for their hospitality during our visit to San Diego. I also have Drs. Geoff Bower and Casey Law to thank for accommodating me at UC Berkeley for 2 weeks, and especially to Geoff Bower for driving us to the Hat Creek Observatory to pay the Allen Telescope Array a visit.

To my fellow ICRAR ~~slaves~~ postgraduate students past and present, including Florian Beutler, Chittawan Choeysakul, Tim Colegate, Jacinta Delhaize, Owen Giersch, John Goldsmith, Laura Hoppmann, Aziz Jiwani, Aquib Moin, Toby Potter, Hayden Rampadarath, Tom Russell, Morag Scrimgeour, Bruce Stansby, Divya Palaniswamy, Mick Todd, and Stefan Westerlund; thanks for keeping me sane. It is good to know that I am not alone on this crazy ride. Special thanks go to Claire Trenham for sharing her thesis template in LaTeX, which I have used to prepare this document.

I cannot thank Jennifer Talbot, Tanya Jones, Rachel Kennedy, and Tina Sallis enough for their excellent administrative support which allowed me to focus on my research, not forgetting their constant mothering of us kids at CIRA. I greatly appreciate Dr. Megan Argo, Kirsten Gottschalk, and Pete Wheeler for giving me countless opportunities to be involved in the wonderful world of education and outreach. I must also say a big 'thank you' to all the inquisitive kids out there who are not afraid to ask 'why'; they endlessly remind me of why I am doing what I do.

Moving to a new country and starting from scratch is never easy, and I have Denny Thevarakam and Sheela Sudhakaran to thank for making this transition so much smoother. Our 'extended family' from South Perth Uniting Church have also provided tremendous support to my family through this period of our lives. I am extremely grateful to Judy Siddins, Perry Swanborough and Mike Dombrose for volunteering to read through the thesis and providing different perspectives on it.

I would not have been able to do this without the patience, support and prayers of my family, who remind me each day that there is more to life than my thesis. Last but not least, I thank God, who first set me on this journey of discovering the Universe and

my place in it.

I would like to acknowledge Curtin University for providing financial support through the Curtin Strategic International Research Scholarship (CSIRS). I have made full use of various resources during the course of my PhD work, including data from the NASA/IPAC Extragalactic Database (NED), operated by the Jet Propulsion Laboratory, California Institute of Technology, under contract with NASA, as well as the SIMBAD database, operated at CDS, Strasbourg, France. I made extensive use of the NASA Astrophysics Data System as well. The observational data used in this study were mainly acquired using the Very Large Array (VLA), which is part of the National Radio Astronomy Observatory (NRAO), a facility of the US National Science Foundation (NSF) operated under cooperative agreement by Associated Universities, Inc. This study also made use of data from the Wisconsin H-Alpha Mapper (WHAM) Northern Sky Survey, which is funded by the NSF.

Abstract

The scattering of radio waves and multipath propagation in the interstellar medium (ISM) of our Galaxy produces various observable phenomena such as the interstellar scintillation (ISS) and angular broadening of compact radio sources, as well as the temporal smearing of impulsive radio bursts. These effects have been harnessed as probes of the ISM and of the background sources themselves. On the other hand, scattering in the intergalactic medium (IGM) has yet to be incontrovertibly detected, and is a main target of future surveys and instruments, since the IGM constitutes the main reservoir of baryons in the Universe. The first part of this thesis makes use of observational data from a survey of interstellar scintillation (ISS) of compact Active Galactic Nuclei (AGNs) to further investigate the nature of these sources, the ISM, ISS, and methods of handling variability data in the presence of stochastic and systematic errors. This study therefore acts as a technical and scientific demonstrator for future large-scale surveys of ISS and the variable radio sky. The results of this study further strengthen the link between AGN variability at radio wavelengths with ISS, and show how the spectral indices and mean flux densities of the sources, as well as observing frequencies, all influence the observed ISS characteristics. Six new rapid scintillators with characteristic time-scales of $\lesssim 2$ hours were identified in the sample, providing new insight into the origin of rapid and extreme scintillation. This thesis also presents the first detailed investigation into the origin of the suppresion of ISS for AGNs at $z \gtrsim 2$ as discovered by the Micro-Arcsecond Scintillation Induced Variability (MASIV) Survey, a precursor to the present work. I determined that the redshift dependence of ISS is partially linked to the steepening of source spectral indices ($\alpha_{4.9}^{8.4}$) with redshift, caused either by selection biases or AGN evolution, coupled with weaker ISS in the $\alpha_{4.9}^{8.4} < -0.4$ sources. Selecting only the $-0.4 < \alpha_{4.9}^{8.4} < 0.4$ sources, the redshift dependence of ISS is still significant, but is not significantly steeper than the expected $(1+z)^{0.5}$ scaling of source angular sizes due to cosmological expansion for a brightness temperature and flux-limited sample of sources. No significant evidence of scatter broadening in the IGM was found, placing the strongest upper limit to date of $\lesssim 8\mu$as at 4.9 GHz for sight-lines to the most compact, $\sim 10\mu$as sources. The second part of the thesis makes use of this observational limit on IGM scattering, together with extensions of

ISM scattering models to cosmological scales, to investigate the detectability of the IGM with next generation radio arrays. While angular broadening in the IGM is insignificant for most sight-lines and appears difficult to resolve even with space VLBI, significant temporal smearing of extragalactic radio transients cannot be ruled out, and provides the best chance of detecting IGM scattering. However, the corresponding reduction in the signal-to-noise ratio of these bursts potentially places crippling limits on the detectability of such transient pulses in the first place, particularly at frequencies below ~ 1 GHz. This has important ramifications for the optimization of observational strategies for detecting extragalactic radio transients with low-frequency instruments such as the Murchison Widefield Array (MWA), the Low Frequency Array (LOFAR) and the low frequency component of the Square Kilometre Array (SKA).

Abbreviations

AGN	Active Galactic Nucleus
AIPS	Astronomical Image Processing System
ASKAP	Australian SKA Pathfinder
AT20G	Australia Telescope 20 Gigahertz
ATA	Allen Telescope Array
BLRG	Broad-Line Radio Galaxy
CDQ	Core-Dominated Quasar
CLASS	Cosmic Lens All-Sky Survey
CMB	Cosmic Microwave Background
CRAFT	Commensal Real-Time ASKAP Fast Transients
CSS	Compact Steep-Spectrum
DM	Dispersion Measure
EM	Emission Measure
ESE	Extreme Scattering Event
EVLA	Expanded Very Large Array
EVN	European VLBI Network
FIRST	Faint Images of the Radio Sky at Twenty Centimeters
FITS	Flexible Image Transport System
FR-I	Fanaroff-Riley Type I
FR-II	Fanaroff-Riley Type II
FSRQ	Flat-Spectrum Radio-Loud Quasar
GPS	Gigahertz Peaked-Spectrum
GRB	Gamma-Ray Burst
HPQ	Highly Polarized Quasar
ICM	Intracluster Medium
ICRAR	International Centre for Radio Astronomy Research
IDV	Intraday Variable/Variability
IF	Intermediate Frequency
IGM	Intergalactic Medium
IHV	Intrahour Variable/Variability

IPM	Interplanetary Medium
IPS	Interplanetary Scintillation
ISM	Interstellar Medium
ISS	Interstellar Scintillation
JVAS	Jodrell-Bank/VLA Astrometric Survey
K-S	Kolmogorov-Smirnov
LISM	Local Interstellar Medium
LOFAR	Low Frequency Array
LST	Local Sidereal Time
LWA	Long Wavelength Array
MASIV	Micro-Arcsecond Scintillation Induced Variability
MERLIN	Multi-Element Radio-Linked Interferometer Network
MOST	Molonglo Observatory Synthesis Telescope
NASA	National Aeronautics and Space Administration
NLRG	Narrow-Line Radio Galaxy
NRAO	National Radio Astronomy Observatory
NVSS	NRAO VLA Sky Survey
MWA	Murchison Widefield Array
OVV	Optically Violently Variable
QSO	Quasi-Stellar Object
RFI	Radio Frequency Interference
RM	Rotation Measure
SF	Structure Function
SKA	Square Kilometre Array
SM	Scattering Measure
SSRQ	Steep-Spectrum Radio-Loud Quasar
SUMSS	Sydney University Molonglo Sky Survey
Syf1	Seyfert 1 Galaxy
Syf2	Seyfert 2 Galaxy
UV	Ultraviolet
VAST	Variables and Slow Transients
V-FASTR	VLBA Fast Radio Transients Experiment
VLA	Very Large Array
VLBA	Very Long Baseline Array
VLBI	Very Long Baseline Interferometry
WHAM	Wisconsin H-Alpha Mapper
WHIM	Warm-Hot Intergalactic Medium
WIDAR	Wideband Interferometric Digital Architecture

Contents

List of Tables

List of Figures

Chapter 1

Introduction

To the natural philosopher there is no natural object unimportant or trifling... a soap bubble... an apple... a pebble... A mind that has once imbibed a taste for scientific enquiry has within itself an inexhaustible source of pure and exciting contemplations. Where the uninformed and unenquiring eye perceived neither novelty nor beauty, he walks in the midst of wonders.

— ***Sir John Herschel, A Preliminary Discourse in the Study of Natural Philosophy***

1.1 Preamble

This thesis deals with the scattering of radio waves in interstellar and intergalactic media, and its application as a probe of the physics of the scattering material and the background sources. A significant portion of the thesis pertains to the radio scintillation, or twinkling, of highly luminous and compact sources known as Active Galactic Nuclei (AGNs), caused by scattering in the turbulent and ionized interstellar medium of our own Galaxy. I therefore begin by introducing the physical concepts behind radiowave scattering and scintillation, as well as their potential as astrophysical probes, in Section 1.2. This is followed by an introduction to the structure and emission mechanisms of AGNs, and how their variability observed on time-scales of hours to days at radio wavelengths have in the last decade been linked to interstellar scintillation (ISS) (Section 1.3). While scattering in the interstellar medium (ISM) of our Galaxy is relatively well studied, there are no confirmed detections of scattering in the intergalactic medium (IGM). I discuss why the detection and study of IGM scattering is important in Section 1.4, as well as why it is one of the main targets of future instruments and surveys. In Section 1.5, I describe recent, ongoing and future surveys on current and next generation radio telescopes to study the variable and transient radio sky; I also elaborate on their relevance to studies of ISS, as well as scattering in the ISM and IGM in general. I then identify areas where there are unanswered questions, or where more work needs to be (and can be) done at present, leading up to next generation instruments and surveys (Section 1.6); these provide the motivation and justification for the work presented in this thesis. In Section 1.7, I narrow down my research objectives and present the scope of this thesis against this wider backdrop.

1.2 Radiowave Scattering and Its Observable Effects

I introduce here the observational history and the physics behind three main observable manifestations of scattering — scintillation (Section 1.2.1), angular broadening (Section 1.2.2) and temporal smearing (Section 1.2.3). I then discuss how these scattering effects have been harnessed as astrophysical probes in the past (Section 1.2.4), and how more recent observations have revealed complex scattering structures in the ISM. More extensive reviews of these topics have been written by Rickett (1990) and Lazio et al. (2004).

1.2.1 Scintillation

Radio waves from astronomical sources are scattered as they propagate through the various ionized media before arriving at the Earth. Variations in the refractive indices due to the density inhomogeneities of the media distort the wavefronts, generating regions of focussing and defocussing (or interference patterns) on the plane of the Earth's surface. Any relative motion between the source or scattering medium and the Earth causes the scattered wavefronts to drift across the telescope, observed as intensity fluctuations of the source. This phenomenon, called scintillation, is responsible for the twinkling of stars when observed through the turbulent atmosphere at optical wavelengths.

At radio wavelengths, scintillation by the Earth's ionosphere was first studied in the 1950's by Smith (1950), Hewish (1952) and Ratcliffe (1956). Studies of the interplanetary scintillation (IPS) of radio sources caused by the solar wind came soon after (Hewish, 1964; Readhead et al., 1978; Hewish, 1988).

Scheuer (1968) was the first to propose that long-term variability of pulsar amplitudes were caused by scintillation in the ISM of our Galaxy, opening up an entire subfield of radio astronomy dedicated to the study of ISS. Following the work of Sieber (1982), who found a correlation between the time-scales of pulsar amplitude variations and line-of-sight electron column densities (inferred from the radio dispersion of the pulses), it was confirmed that the slow variations in pulsar pulse amplitudes were due to propagation effects, namely ISS. It soon became apparent that there were two different ISS regimes associated with diffractive effects (Spangler, 1988) and refractive effects (Rickett et al., 1984; Cordes et al., 1986; Romani et al., 1986).

1.2.1.1 Scintillation Regimes

Consider a plane wave of unit amplitude originating from a point source at infinite distance, arriving at a thin 'scattering screen' located at a distance D_L from the observer (Figure 1.1). This scattering screen introduces phase changes, $\phi(\mathbf{r})$, to the plane wave at vector position $\mathbf{r}$ at the screen. The amplitude of the wave received at vector position $\mathbf{R}$ at the plane of the observer, is then given by the Fresnel-Kirchhoff integral (Born & Wolf, 1980):

$$\psi(\mathbf{R}) = \frac{e^{-i\pi/2}}{2\pi r_F^2} \int \exp\left[i\phi(\mathbf{r}) + \frac{i(\mathbf{r}-\mathbf{R})^2}{2r_F^2}\right] d^2\mathbf{r}. \tag{1.1}$$

The term $r_F = \sqrt{cD_L/2\pi\nu}$ is the Fresnel scale, where c is the speed of light and ν is the frequency of the wave. While the first term in the square brackets represents phase changes introduced by scattering, the second term represents phase changes caused by differences in geometric pathlengths as the waves travel from points $\mathbf{r}$ at various locations of the scattering screen to point $\mathbf{R}$.

If $\phi(\mathbf{r}) = 0$, indicating no occurrence of scattering, $\psi(\mathbf{R})$ is then dominated by the $i(\mathbf{r}-\mathbf{R})^2/2r_F^2$ term, which causes the exponential term in the integral to vary quickly as $|\mathbf{r}-\mathbf{R}|$ becomes comparable to r_F. Therefore, only elements of the wavefront within a region on the scale of r_F at the scattering screen, known as the Fresnel zone, contribute coherently to $\psi(\mathbf{R})$. Outside the Fresnel zone, the phases wrap around quickly and do not contribute coherently to the wave amplitude at point $\mathbf{R}$.

If there is scattering due to density inhomogeneities at the screen, $\phi(\mathbf{r})$ is non-zero. Assuming that the density fluctuations at the screen are wide-sense stationary and Gaussian, the statistics of the phases of the scattered wavefront can be fully described by the phase structure function:

$$D_\phi(\mathbf{r}) = \left\langle \left[\phi(\mathbf{r}+\mathbf{r}') - \phi(\mathbf{r}')\right]^2 \right\rangle, \tag{1.2}$$

where the ensemble average is over all possible realizations of the scattering screen. These phase fluctuations are often assumed to arise from a power law spectrum of density inhomogeneities in the scattering screen cut off at an inner and outer scale, giving:

$$D_\phi(\mathbf{r}) = \left(\frac{r}{r_{\text{diff}}}\right)^{\beta-2}. \tag{1.3}$$

The value of β is found to be $\sim 11/3$ in the ISM, similar to that of Kolmogorov turbulence (Armstrong et al., 1995). The diffractive scale, r_{diff}, which represents the strength of the turbulence at the scattering screen, is defined as the length-scale over which the rms phase difference is equivalent to one radian. The value of r_{diff} relative to r_F determines whether phase changes caused by the variations in geometric pathlengths or density fluctuations at the screen dominate.

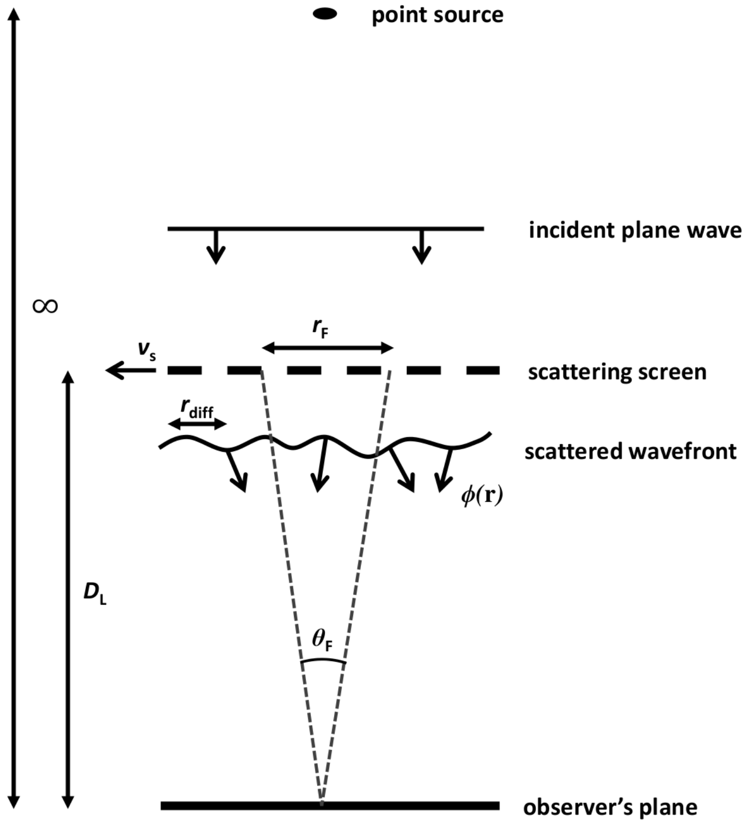

Figure 1.1 — *A thin scattering screen imprints phase changes, $\phi(\boldsymbol{r})$, onto a plane wave originating from a point source at infinite distance. Relative motion between the scattering screen and the observer results in scintillation as the regions of focussing and defocussing drift across the observer.*

If $r_{\text{diff}} \gg r_F$, meaning that the phase changes resulting from the density fluctuations at the screen are less than a radian within the Fresnel zone, the perturbations of the wavefront at the plane of the observer are caused only by the weak focussing and defocussing of coherent patches of size r_F at the screen. This is known as the weak regime of scattering. If the source angular size, θ_S, is smaller than the angular size of the Fresnel zone, $\theta_F = r_F/D_L$, the source appears scattered over a region of size r_F. Relative motion between the screen and the observer causes these phase fluctuations on the scale of r_F to drift across the telescope and produce intensity fluctuations on timescales of $\tau_F \sim r_F/v_s$, where v_s is the relative velocity between the scattering screen and the observer.

The regime of strong scattering corresponds to the case where $r_{\text{diff}} \ll r_F$, so that the phase fluctuations caused by density inhomogeneities at the scattering screen vary by many radians within the Fresnel zone. r_F therefore becomes irrelevant, and the size

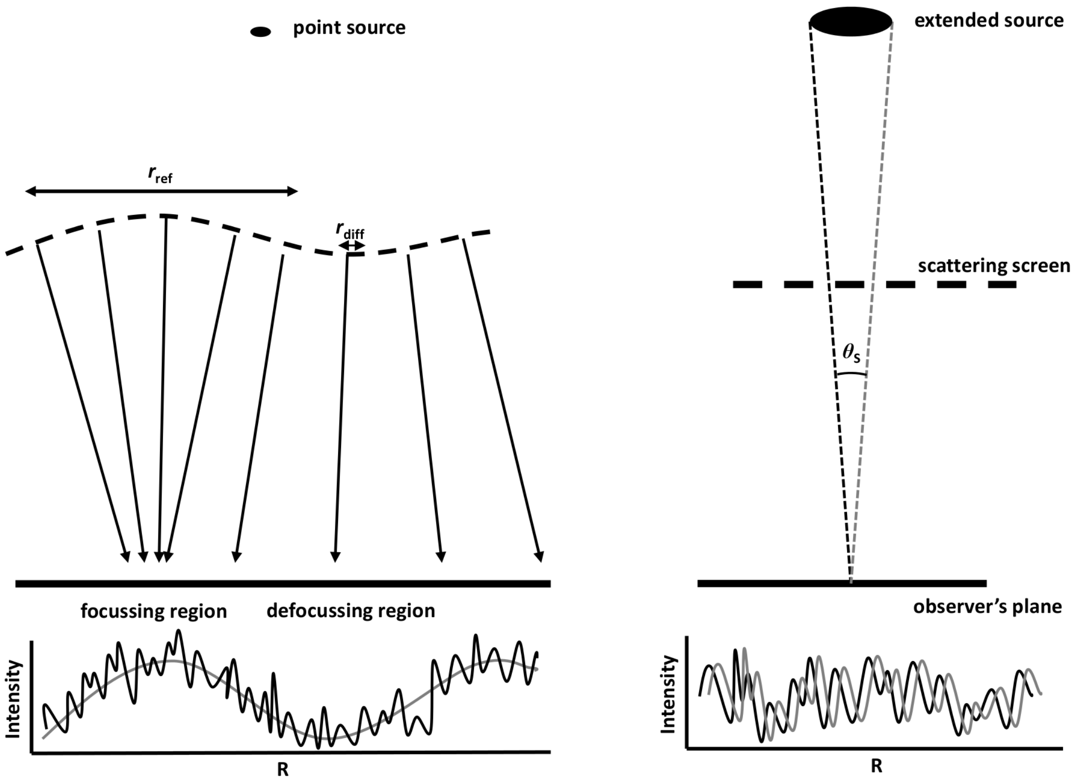

Figure 1.2 — *In strong scattering, large-scale density fluctuations on scales of* r_{ref} *focus and defocus the coherent patches of size* r_{diff}*, resulting in the superposition of small scale intensity fluctuations on larger scale fluctuations at the plane of the observer (left panel). The phase fluctuations of waves arriving from different elements of an extended source are shifted in space, and smear out when summed over all the elements of the source (right panel).*

of the coherent patch is now given by r_{diff}. Each of these coherent patches acts like a diffractive slit scattering the waves into a cone with an opening angle of $\theta = c/(2\pi\nu r_{\mathrm{diff}})$. Multipath propagation becomes important, resulting in the observation of multiple coherent patches of size r_{diff} within a region of size $D_L\theta = r_F^2/r_{\mathrm{diff}}$. As these coherent patches drift across the observing telescope, diffractive scintillation is observed.

Another form of scintillation in the regime of strong scattering is refractive scintillation, caused by large-scale density fluctuations on the order of $r_{\mathrm{ref}} = r_F^2/r_{\mathrm{diff}} \gg r_{\mathrm{diff}}$. These phase fluctuations of size r_{ref} focus and defocus the multiple coherent patches of size r_{diff} (see left panel of Figure 1.2). When a region of focussing drifts across the observing telescope, radiation from a larger number of coherent patches are received, including that outside the Fresnel zone, thus increasing the observed flux. The converse is true when a defocussing region drifts across the telescope.

Table 1.1. Summary of scintillation characteristics of point sources for various scattering regimes as given by Narayan (1992).

Scattering Regime	Source Size	$r_{\rm scint}$	$\tau_{\rm scint}$	m_p
weak	$\theta_S < \theta_F$	r_F	$\tau_F = r_F/v_s$	$(r_F/r_{\rm diff})^{5/6} < 1$
strong diffractive	$\theta_S < \theta_{\rm diff}$	$r_{\rm diff}$	$\tau_{\rm diff} = r_{\rm diff}/v_s$	1
strong refractive	$\theta_S < \theta_{\rm ref}$	$r_{\rm ref} \gg r_{\rm diff}$	$\tau_{\rm ref} \gg \tau_{\rm diff}$	$(r_{\rm diff}/r_F)^{1/3} < 1$

Note. — $r_{\rm scint}$ is the typical length-scale of the phase fluctuations at the wavefront, $\tau_{\rm scint}$ is the typical scintillation time-scale, and m_p is the point source modulation index, defined as the rms variations as a fraction of the source mean flux density. The other symbols are defined in Section 1.2.1.1 of the text.

The characteristics of scintillation at these various scattering regimes are summarised in Table 1.1 for point sources. Further details can be obtained in the excellent review by Narayan (1992).

1.2.1.2 Frequency Dependence of ISS

The strength of ISS, as characterised by the modulation index (defined as the ratio of rms variations to the source mean flux density), is frequency-dependent. At the transition frequency between weak and strong ISS (ν_t, when $r_F \approx r_{\rm diff}$), the point source modulation index is given by $m_p \sim 1$. In weak ISS, m_p scales with $(\nu_t/\nu)^{17/12}$, while in strong refractive ISS, m_p scales with $(\nu/\nu_t)^{17/30}$ (see Walker (1998)). At mid-Galactic latitudes, the transition frequencies are typically at a few GHz.

1.2.1.3 Effect of Extended Source Size

The observed amplitude of scintillation is highly sensitive to the angular sizes of the background sources. In an extended source, its amplitude is suppressed relative to that of a point source. A well-known example at optical wavelengths is the quenching of atmospheric scintillation in planets, whose angular sizes are larger than that of stars.

The suppresion of scintillation amplitudes by extended sources is caused by the smearing of the phase fluctuations when integrated over the emission originating from each element of the extended source. Consider two elements at the opposite ends of an extended source, separated by an angle θ_S (see Figure 1.2, right panel). The waves originating from these elements intersect the scattering screen at different angles on the way to the observer, so the intensity fluctuations of the scattered wavefronts are partially decorrelated. The variance of the sum of the intensity fluctuations of these

Table 1.2. Summary of scintillation characteristics of extended sources for various scattering regimes as given by Narayan (1992).

Scattering Regime	Source Size	$r_{\rm scint}$	$\tau_{\rm scint}$	m_e
weak	$\theta_S > \theta_F$	$r_F(\theta_S/\theta_F)$	$\tau_F(\theta_S/\theta_F)$	$(r_F/r_{\rm diff})^{5/6}(\theta_F/\theta_S)^{7/6}$
strong diffractive	$\theta_S > \theta_{\rm diff}$	$r_{\rm diff}(\theta_S/\theta_{\rm diff})$	$\tau_{\rm diff}(\theta_S/\theta_{\rm diff})$	$(\theta_{\rm diff}/\theta_S)$
strong refractive	$\theta_S > \theta_{\rm ref}$	$r_{\rm ref}(\theta_S/\theta_{\rm ref})$	$\tau_{\rm ref}(\theta_S/\theta_{\rm ref})$	$(r_{\rm diff}/r_F)^{1/3}(\theta_{\rm ref}/\theta_S)^{7/6}$

Note. — $r_{\rm scint}$ is the typical length-scale of the phase fluctuations at the wavefront, $\tau_{\rm scint}$ is the typical scintillation time-scale, and m_e is the modulation index of the extended source, defined as the rms variations as a fraction of the source mean flux density. The other symbols are defined in Section 1.2.1.1 of the text.

wavefronts are less than the variance of the intensity fluctuations of a point source. The timescale of the scintillation also increases, due to the smearing out of the finer structures of the intensity fluctuations.

The definition of an extended source differs for each of the scattering regimes, since significant decorrelation of the wavefronts occur when θ_S becomes comparable to the angular scales of the intensity fluctuations. A source is therefore considered to be extended if its angular size, θ_S, exceeds that of $\theta_F = r_F/D_L$, $\theta_{\rm diff} = r_{\rm diff}/D_L$ and $\theta_{\rm ref} = r_{\rm ref}/D_L$ for weak, diffractive and refractive scintillation respectively. The scintillation characteristics of extended sources are summarised in Table 1.2 for the various scattering regimes.

1.2.2 Angular Broadening

The multipath propagation of radio waves as a result of scattering also distorts the observed image of the source. As described in Section 1.2.1.1, a source undergoing strong scattering is observed as multiple images or 'speckles' of size $r_{\rm diff}$, within a region of $r_{\rm ref}$. If the integration time of the instrument, $t_{\rm int}$, is shorter than the diffractive scintillation time-scale, $\tau_{\rm diff}$, these speckles can be seen in the resultant image with sizes equivalent to the angular resolution of the telescope. If the integration time of the instrument is sufficiently large, so that $t_{\rm int} > \tau_{\rm diff}$, the random phase fluctuations degrade the resolution of the image to an angular size of $\sim \theta_{\rm ref}$. The angular size of the source is hence considered to have been scatter broadened. This effect is well-known in optical astronomy, where 'seeing' in the atmosphere places limits on the resolution of ground based optical telescopes.

In radio astronomy, angular broadening is well-discussed in the context of interferometer imaging (Cohen & Cronyn, 1974; Rickett & Coles, 1988). A comprehensive theoretical treatment of scatter broadened images in various regimes of imaging (dependent on t_{int} relative to τ_{diff} and τ_{ref}) is given in Goodman & Narayan (1989) and Narayan & Goodman (1989). Angular broadening by the ISM has been observed in many compact radio sources such as masers (Reid & Moran, 1981), pulsars (Gwinn et al., 1988), Sgr A* (Backer, 1988) at the Galactic centre and its nearby stars (van Langevelde & Diamond, 1991), as well as quasars (Dennison et al., 1984; Spangler et al., 1986; Moran et al., 1990).

1.2.3 Temporal Smearing

Multi-path propagation also causes delays in the arrival times of radio waves travelling through longer paths, so that signals from an impulsive source are also broadened in time. This temporal smearing caused by scattering in the ISM has been observed in pulsar pulses (Rankin et al., 1971; Counselman & Rankin, 1971; Bhat et al., 2004), while theoretical treatments of this phenomenon are given by Sutton (1971), Williamson (1972), and Lee & Jokipii (1975).

1.2.4 Interstellar Scattering as an Indispensable Tool

Once they were better understood, these scattering phenomena were soon developed into powerful probes of the scattering media as well as the background sources themselves. Little & Hewish (1966) and Cohen et al. (1967) used IPS to determine the angular sizes of radio sources at sub-arcsecond scales, prior to the development of Very Long Baseline Interferometry (VLBI).

The interference of coherent waves arriving from regions separated by distances on the scales of r_{ref} (up to $\sim 10^6$ km in the ISM) allows the ISM to function as an interstellar interferometer to probe the background sources down to μas scales. This angular resolution is orders of magnitude better than can be achieved by any ground based telescope. Cordes et al. (1983) and Gwinn et al. (1997) have attempted to use the ISS of pulsars to constrain the sizes of pulsar emission regions. ISS has also been used to probe the angular sizes and structures of the most compact μas components of scintillating AGNs such as PKS 1519-273 (Macquart et al., 2000), PKS 1257-326 (Bignall et al., 2003, 2006), PKS 0405-385 (Kedziora-Chudczer, 2006) and J1819+3845 (Macquart & de Bruyn, 2007), using both polarised and total intensity data. Observations of time delays between scintillation patterns at two observing frequencies have been attributed to μas-scale angular shifts in the optically thick cores of the source PKS 1257-326 (Bignall et al., 2003; Bignall & Hodgson, 2012).

Propagation effects have also proven to be excellent probes of the scattering material in the ISM. Lee & Jokipii (1976) proposed that the observed ISS of 3 pulsars are consistent with scattering in a turbulent ISM with power law density inhomogeneities with a Kolmogorov spectrum. Armstrong et al. (1995) also used the ISS of 17 pulsars to study the power spectrum of the density inhomogeneities of the ISM, and also found it to follow a power law. Spangler & Gwinn (1990) found evidence for an inner-scale cutoff of the Kolmogorov spectrum at 50 to 200 km by observing the angular broadening of galactic and extragalactic radio sources. This cutoff could be associated with the length-scales at which the turbulent energies are dissipated. Empirical data from a number of interstellar scattering observations have been used together with radio dispersion data to model the distribution of scattering material in the ISM; these include Galactic models by Taylor & Cordes (1993) and more recently by Cordes & Lazio (2003).

Studies in the last few decades have further revealed a myriad of interesting yet mysterious interstellar scattering phenomena, hinting at the presence of complex scattering structures in the ISM. One such example is the discovery of a class of discrete structures known as extreme scattering events (ESEs). Fiedler et al. (1987) observed a $\sim 50\%$ dip in the flux density of the quasar 0945+698 at 2.7 GHz, in between a $\sim 30\%$ increase in flux density. Fiedler et al. (1994a) reported a further 9 similar ESEs in AGN lightcurves, linking these highly frequency-dependent phenomena to scattering at regions of enhanced turbulence (Fiedler et al., 1994b) i.e. supernovae remnants. Romani et al. (1987) proposed that these events are caused by discrete refractive sheets or filaments in the ISM. Walker & Wardle (1998), on the other hand, suggested that the scattering occurs at photoionized outer layers of self-gravitating neutral clouds, to solve the problem of why these discrete structures have not dissipated. Further evidence for discrete structures in the ISM came from the intermittency of scintillation in AGNs such as PKS 0405-385 (Kedziora-Chudczer, 2006), which can be explained if the scattering region responsible for the scintillation drifts off the line of sight. However, the relation between ESEs and the intermittency of ISS in such sources, and to the ionized ISM as a whole, remains unknown.

Another example is the observation of anisotropic scattering structures in the ISM. Rickett et al. (2002), Dennett-Thorpe & de Bruyn (2003), and Bignall et al. (2006), in observing the scintillation of the extragalactic radio sources PKS 0405-385, J1819+3845 and PKS 1257-326 respectively, inferred anisotropic scattering by elongated density structures possibly aligned along magnetic fields. Brisken et al. (2010) also found highly anisotropic scattering structures toward the line-of-sight to the pulsar B0834+06, which may even be linked to ESEs.

1.3 Active Galactic Nuclei: Structure, Physics and Variability

The term Active Galactic Nucleus (AGN) encompasses a wide-ranging, observationally disparate group of extragalactic objects with continuum emissions detected over a large range of frequencies, from radio up to gamma-rays. These objects were initially given various names, such as Seyfert galaxies, quasars, BL Lac objects, and radio galaxies, until evidence accumulated to show that underlying these different observable phenomena were similar physical objects. These objects radiate anisotropically, thereby appearing as distinct objects when observed at different angles to the line of sight. As the name suggests, AGNs are now known to be the compact cores of a special class of galaxies known as active galaxies, so-called because their emissions are dominated by activity at the core, unlike in normal galaxies where thermal emission from the stars and gas dominates.

1.3.1 AGN Components

The current paradigm posits that at the heart of all AGNs is a supermassive black hole, with a mass 10^6 to 10^9 times that of the Sun, concentrated in a region $\lesssim 0.01$ pc in diameter. The gravitational potential energy around the black hole is the ultimate source of power for AGNs, as clouds of gas, dust and perhaps even stars accrete onto the black hole. This accretion disk radiates brightly at UV and soft X-ray frequencies. Around this accretion disk is a region containing clouds of high-velocity gas (shown as black dots in Figure 1.3) of order $10^5\,\mathrm{kms}^{-1}$, often referred to as the broad-line region due the Doppler broadening of emission lines observed in their optical/UV spectra as a result of the extreme cloud velocities. This broad-line region is obscured when viewed from certain angles (see Figure 1.3) by a donut-shaped, dusty torus. In fact, the existence of this torus was proposed to account for the fact that broad emission lines are observed in some AGNs but not in others. Further out from the broad-line region is the narrow-line region (shown as grey blobs in Figure 1.3), where the gas velocities are lower than that of the broad-line region; this region is not obscured by the torus. Along the poles of the accretion disk are energetic outflows that form highly collimated jets of particles, with speeds comparable to the speed of light. Observed mainly at radio frequencies, these jets are known to extend up to kpc scales, believed to be collimated by twisted magnetic field lines. They plough through the surrounding intergalactic medium, sometimes terminating in bright hotspots with large radio lobes (see right panel of Figure 1.4).

1.3.2 Classification and Unification Schemes

AGNs are often separated into two main groups depending on their relative radio luminosities. AGNs with ratios of 5 GHz radio flux to B-band optical flux $\gtrsim 10$ are classified as radio-loud (Kellermann et al., 1989), while those with lower ratios are classified as radio-quiet. About 15 to 20% of AGNs are radio-loud, with the main difference believed to be due to host galaxy type (Smith et al., 1986) or black hole spin

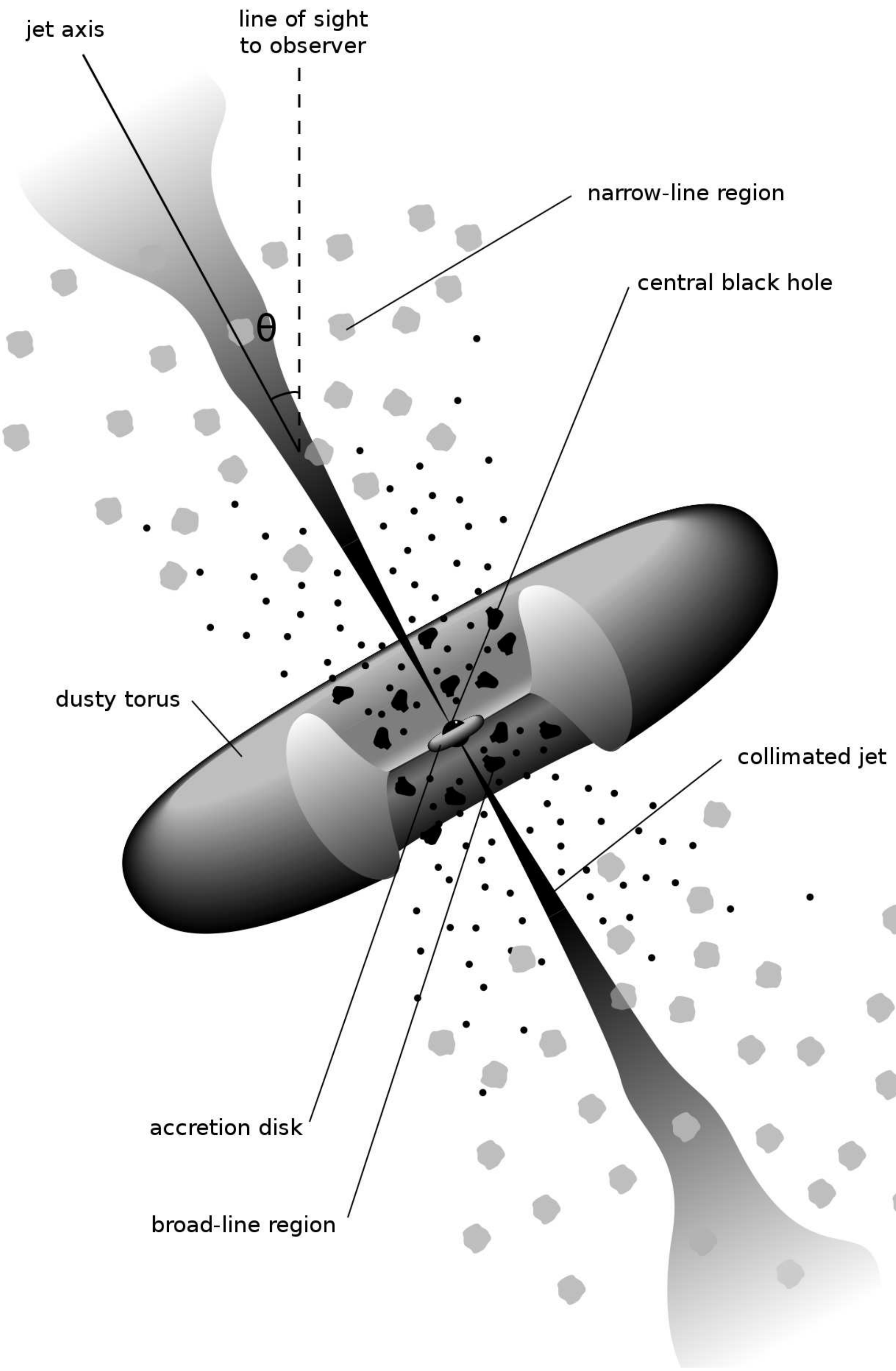

Figure 1.3 — *Components of an active galactic nucleus, based on the figure by Urry & Padovani (1995).*

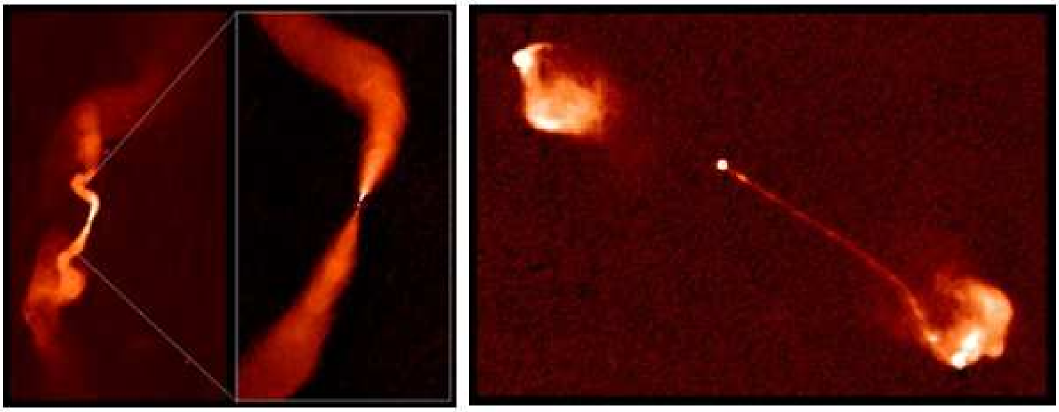

Figure 1.4 — *An example of a Fanaroff-Riley type I AGN, 3C31 (left panel) and a Fanaroff-Riley type II AGN, 3C175 (right panel). Both images were obtained from the NRAO website:* http://www.cv.nrao.edu/∼abridle/bgctalk/node4.html.

(Blandford, 1990).

On top of that, AGNs are also broadly classified into 3 types based on the observed properties of their emission lines. These variations in emission line properties are believed to result from differences in their orientations with respect to the line of sight. I briefly summarise the properties of these 3 types of AGNs, based on the review by Urry & Padovani (1995) and the references therein.

Type 2 AGNs have weak continuum emission and only narrow emission lines, indicating that their accretion disks and broad-line regions are obscured. These sources are therefore observed at large angles of θ (defined in Figure 1.3). The radio-quiet population of Type 2 AGNs include Seyfert 2 galaxies (Syf2), while the radio-loud population is composed of narrow-line radio galaxies (NLRGs) with symmetric radio jets. NLRGs are further divided into Fanaroff-Riley type I (FR-I) radio galaxies whose jets are brightest near the nucleus (left panel of Figure 1.4), and Fanaroff-Riley type II (FR-II) radio galaxies that are brightest at the hostspots where the jets terminate, often displaying large radio lobes (right panel of Figure 1.4).

Type 1 AGNs are characterised by the presence of broad emission lines. Radio-quiet populations include lower luminosity Seyfert 1 galaxies, as well as the higher luminosity radio-quiet quasars, historically known as quasi-stellar objects (QSOs) due to their being point-like sources resembling stars but whose emissions are non-thermal. The radio-loud sources include the broad-line radio galaxies (BLRGs), steep-spectrum radio-loud quasars (SSRQs) and flat-spectrum radio-loud quasars (FSRQs). These sources are all aligned close to the line of sight with small values of θ, so that the accretion disks and broad-line regions are not obscured by the torus. FSRQs are believed to be associated with FR-II radio galaxies, observed at different angles. Other quasars having a variety of names due to their observed properties, such as the optically violently variable (OVV) quasars, highly polarised quasars (HPQs), and core dominated quasars (CDQs), are thought to be similar objects to FSRQs, and so are lumped together as FSRQs here. Additionally, the classification of these Type 1 AGNs based on differences in radio and optical luminosities is purely historical; there may be no physical differences between these sources.

Type 0 AGNs have unusual/weak absorption or emission lines. This category includes radio-loud BL Lac objects, believed to be associated with FR-I radio galaxies. They are aligned very close to the line of sight and are observed directly down the jet. The relativistic Doppler-boosted jet radiation overwhelms any emission from the accretion disk or broad-line region. FSRQs are also thought to be aligned very close to the line of sight, so often in the literature, they are classified together with BL Lacs as a single category known as blazars.

There is also another group of very compact extragalactic objects with symmetric radio structures known as gigahertz peaked-spectrum (GPS) sources, and compact steep-spectrum (CSS) sources. GPS sources have well defined peaks in their radio spectra between 500 MHz to 10 GHz in the observer's frame, while the peaks in CSS spectra occur at lower frequencies $\lesssim$ 500 MHz (O'Dea, 1998), thought to be caused by a turnover in the emission spectrum due to synchrotron self-absorption (Hodges et al., 1984; Mutel et al., 1985). These sources are thought to be either younger versions of Type 2 radio galaxies (Phillips & Mutel, 1982), or old sources with jets confined and frustrated by their dense environments (O'Dea et al., 1991). A review of these objects is available in the paper by O'Dea (1998).

1.3.3 Emission Mechanisms and Spectra

It was proposed as early as the 1950's that continuum radio emission of cosmic sources detected by radio receivers were non-thermal in nature, and were mainly due to incoherent synchrotron emission (Alfvèn & Herlofsen, 1950; Shklovsky, 1953). Synchrotron emission is produced when relativistic electrons spiral around magnetic field lines, their acceleration producing highly beamed and polarised emission in the direction of their velocity vectors. The frequency of the radiation is dependent upon the frequency of the gyration of the electrons, which in turn is dependent upon the strength of the magnetic fields and the energy of the electrons. In a synchrotron emitting source, the electron energies are typically modelled by a power law distribution, with the energy spectrum given by $N(\epsilon) \propto \epsilon^a$, where a is the spectral index of the particle energies. The spectrum of emission of such a synchrotron source, therefore, also obeys a power law given by $I(\nu) \propto \nu^\alpha$, where the spectral index of the emission, α, and the spectral index of the particle energies are related by $\alpha = (a + 1)/2$. The exponents a and α

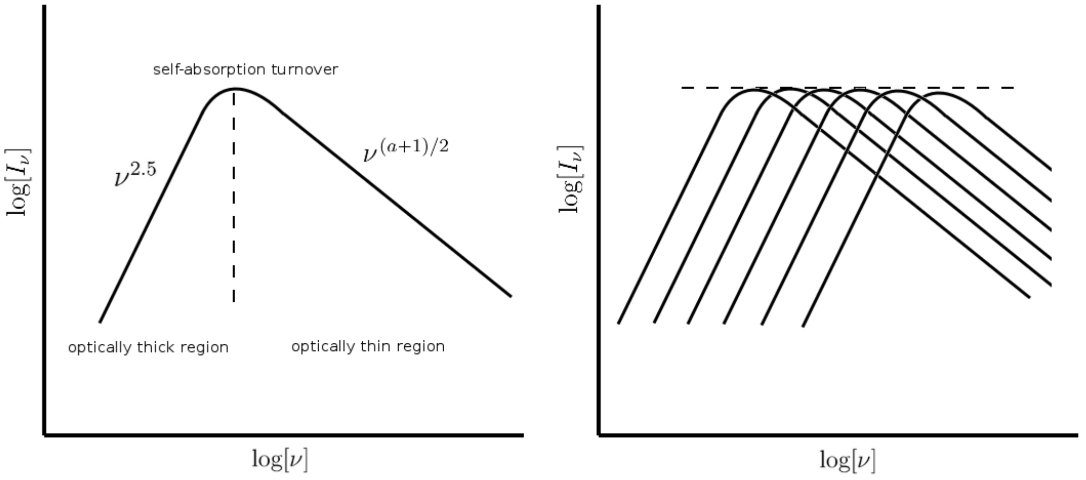

Figure 1.5 — *The emission spectrum of a synchrotron source with a power law distribution of electron energies* $N(\epsilon) \propto \epsilon^a$ *(left panel), and the superposition of many synchrotron components to produce a flat spectrum (right panel).*

typically have negative values; there are smaller numbers of high-energy electrons, and larger numbers of low-energy electrons; the intensity of emission is higher at lower frequencies, decreasing as the frequency increases. This is why some authors prefer to use $N(\epsilon) \propto \epsilon^{-a}$ to define the spectral index. In this thesis, however, I use $N(\epsilon) \propto \epsilon^a$ and $I(\nu) \propto \nu^\alpha$.

For a continuous stream of electrons, the electrons producing the synchrotron radiation will also absorb the radiation in a process known as synchrotron self-absorption. The absorption increases with decreasing frequencies, which causes the synchrotron emission spectrum to turn over at lower frequencies so that α has a positive value of 2.5, having what is called an inverted spectrum (Figure 1.5). This region where absorption is important is also known as the optically thick region. At the steep-spectrum or the optically thin region where α is negative, absorption is unimportant. Many AGNs have been observed to have a flat spectrum, believed to result from a superposition of many synchrotron components turning over at different frequencies (Scheuer & Williams, 1968), as shown in the right panel of Figure 1.5. These flat-spectrum sources are believed to be AGN jets viewed at very small angles with respect to their axes (Blandford & Königl, 1979).

Even though synchrotron emission is non-thermal, an equivalent brightness temperature, T_b, is often used to characterise the intensity of the emission, defined as the temperature that would be required of a black body to produce the intensity observed if the emission is thermal. It is calculated as:

$$T_b = \frac{c^2 S_\nu}{2k\nu^2\Omega}, \tag{1.4}$$

where S_ν is the flux density of the source, k is the Boltzmann constant, c is the speed of light, and Ω is the solid angle subtended by the source. The brightness temperature of a source can be estimated from VLBI observations.

The brightness temperature can also be inferred from the variability of a source, which gives upper limits to Ω based on light travel-time arguments; the linear size of the emitting region must be $\leq 2c\tau$ if the variability is intrinsic, where τ is the timescale of the variations. The variability brightness temperature can then be calculated as (Lähteenmäki et al., 1999):

$$T_b^{var} = 5.87 \times 10^{21} h^{-2} \frac{\lambda^2 S_{max}}{\tau_{obs}} \left(\sqrt{1+z} - 1\right)^2, \tag{1.5}$$

where λ is the wavelength of observations in m, S_{max} is the maximum observed flux density in Jy, τ_{obs} is the observed variability timescale in days, and z is the source redshift. The source is assumed to be a homogenous sphere, and the cosmological parameters $H_0 = 100h\,\mathrm{kms}^{-1}\,\mathrm{Mpc}^{-1}$, $q_0 = 0.5$ are used.

The brightness temperature of a synchrotron source is limited by inverse Compton scattering, a process whereby photons are scattered to higher frequencies by relativistic electrons (thereby gaining energy). As the photons can be inverse Compton scattered multiple times, this leads to catastrophic losses in the electron energy densities when the source brightness temperature exceeds 10^{12} K (Kellermann & Pauliny-Toth, 1969), resulting in huge radiation losses until the brightness temperature drops below the limit again. There is, however, evidence that the brightness temperature limits may be at a lower value of $\sim 10^{11}$ K, set by the equipartition of energies between the radiating electrons and the magnetic fields (Readhead, 1994; Singal, 2009).

A thorough treatment of the emission, absorption and scattering mechanisms described here can be found in the classic textbook by Rybicki & Lightman (1979).

1.3.4 Relativistic Beaming and Doppler Boosting

Due to the relativistic bulk flow of particles, AGN jets are highly beamed in a forward cone with half-angles of order $\sim \Gamma^{-1}$ at the observer's frame even though the radiation may be isotropic at the rest-frame of the source. Γ is the Lorentz factor of the relativistic jets, given by:

$$\Gamma = \frac{1}{\sqrt{1-\beta^2}} \tag{1.6}$$

where β is the ratio of the jet speed to the speed of light, v/c. This causes jets pointing away to become faint or unobservable, while jets pointing toward the observer are intensified. Other observable effects include apparent superluminal motion of AGN jets (Cohen et al., 1977; Blandford et al., 1977), and compression of jet intrinsic variability timescales. The relativistic Doppler factor, a measure of the strength of relativistic effects in AGN, is then a function of the bulk Lorentz factor of the jet (jet speed), and the angle at which the jet is aligned relative to the observer:

$$\delta = \frac{1}{\Gamma(1 - \beta\cos\theta)} \tag{1.7}$$

These relativistic effects cause the observed brightness temperature of an AGN jet inferred from VLBI observations to be a factor δ larger than the intrinsic brightness temperature, after accounting for cosmological effects, due to the apparent increase in flux density and blue-shifting of the emission wavelengths (see, e.g., Readhead (1994); Lähteenmäki et al. (1999)). On the other hand, the source brightness temperature inferred from variability considerations is a factor of δ^3 larger than the intrinsic brightness temperature. This is the commonly accepted explanation for observations of AGNs with brightness temperatures exceeding that imposed by the inverse Compton limit.

1.3.5 The Core-Jet Model and Source Compact Fraction

VLBI images of flat or inverted-spectrum AGNs often show a very compact, core component that appears as a point source, surrounded by fluffy blobs of weaker mas-scale components referred to as the jet components. The core component is usually optically thick, while the jet component is optically thin.

The scintillating components of AGNs lie within the unresolved VLBI cores. One can thus envision a simple model in which the flat-spectrum AGN consists of an ultra-compact, optically thick μas core component that scintillates, surrounded by more extended, optically thin jet components, partially resolved by VLBI at mas scales.

The compact fraction, defined as the ratio of flux density of the core component to that of the extended components, is a measure of how core-dominated the emission is. This is important because of the way the source variability amplitude is quantified in this thesis and other studies; they are normalised by the mean flux density of the source, which will include the flux densities of the non-scintillating extended components unresolved by the instrument. The amplitude of scintillation therefore depends not only on the angular size of the actual scintillating component, but also on the core dominance of the source, increasing as the compact fraction of the core increases.

1.3.6 Radio Variability of AGNs and Its Link to ISS

Compact AGNs have been observed to ‘flicker’ at cm wavelengths on timescales of days (Heeschen, 1984, 1987). Heeschen (1984) noticed that the flat-spectrum sources scintillate, while the steep-spectrum sources did not. It was unknown then if this flickering was caused by intrinsic variability or scintillation in the ISM. The latter explanation was proposed by Heeschen & Rickett (1987) in order to resolve the brightness temperature problem in such highly-variable sources, since intrinsic variability on the time-scales observed implied brightness temperatures well over the 10^{12} K inverse Compton limit for incoherent synchrotron emission. The problem was further compounded by the discovery of intra-hour variable (IHV) sources such as PKS 0405+385 (Kedziora-Chudczer et al., 1997) J1819+3845 (Dennett-Thorpe & de Bruyn, 2000) and PKS 1257-326 (Bignall et al., 2003). For example, the variability of PKS 0405+385, if intrinsic to the source, implied observed brightness temperatures of 10^{21} K, or Doppler boosting factors well over 10^3.

Arguments for intrinsic variations came mainly from observed correlations between radio variability and that at higher energies in some sources (Quirrenbach et al., 1991; Wagner & Witzel, 1995). Such arguments, of course, demand either that the brightness temperatures of AGN cores greatly exceed limits imposed by inverse Compton scattering (thus requiring a revision of our understanding of radiative processes in these objects), or that the Doppler boosting factors of the relativistic jets are significantly higher than the $\delta \sim 5$ to 30 estimated from VLBI observations (Lähteenmäki & Valtaoja, 1999; Jorstad et al., 2005; Hovatta et al., 2009).

In the last few decades, the body of evidence linking the intraday variability (IDV) and IHV observed in many compact, flat-spectrum AGNs at cm wavelengths to the physical process of ISS has grown considerably. Time delays of up to 8 minutes have been observed in the scintillation patterns of the most rapid scintillators at widely spaced telescopes (Jauncey et al., 2000; Dennett-Thorpe & de Bruyn, 2002; Bignall et al., 2006), as would be expected of interference patterns drifting across the surface of the Earth as a result of relative motion between the ISM and the Earth. Annual cycles have also been detected in AGN variability time-scales (Rickett et al., 2001; Jauncey & Macquart, 2001; Bignall et al., 2003; Dennett-Thorpe & de Bruyn, 2003; Jauncey et al., 2003), interpreted as being modulated by the orbital motion of the Earth around the Sun. When the Earth's motion is parallel to the motion of the scattering medium, the variability time-scales are longer, while shorter timescale variability occurs when the Earth's motion is anti-parallel to that of the scattering medium.

The strongest evidence that the cm wavelength IDV of AGNs is predominantly due to ISS was obtained through the Micro-Arcsecond Scintillation Induced Variability (MASIV) Survey, which will be described in Section 1.5.

1.4 Scattering in the Intergalactic Medium

While radiowave scattering in the ionosphere, interplanetary medium (IPM) and ISM are all relatively well studied, scattering in the ionised IGM has yet to be incontrovertibly detected and is not well studied even at a theoretical level. Hall & Sciama (1979) developed a model for scattering in the intracluster medium found in rich clusters of galaxies. Ferrara & Perna (2001) suggested that intergalactic scintillation can be detected based on an extension of ISS models to cosmological scales, but the very long time-scales involved, estimated to be up to a month or more at mm wavelengths (up to years and decades at longer wavelengths), raise concerns about the practicality of such experiments. Lazio et al. (2004) briefly discussed the potential of detecting angular broadening in the IGM, claiming that angular resolutions better than 4 mas at 1.4 GHz may be sufficient. Although within the capabilities of ground-based VLBI, these predictions were based on the assumption that the scattering mainly occurs in galaxies similar to the Milky Way, rather than in the diffuse filamentary structures where the bulk of the baryons reside. More recently, Lazio et al. (2008) found an upper limit of 500 μas for angular broadening in the IGM at 1 GHz, using multifrequency VLBA observations of compact AGN cores. While consistent with the overall picture of the ionized IGM, they concluded that it did not place significant constraints on its properties.

One of the most tantalizing possible detections of IGM scattering came from the discovery of a single, bright burst of ms duration in the archival data of the Parkes radio telescope (Lorimer et al., 2007). The highly dispersed nature of the signal (caused by frequency dependent time-delays), in excess of expected effects in the ISM, indicated that some of the propagation effects originated in the ionized IGM. A slight increase in pulse width was observed at the lower frequencies, suggesting that the pulse could have been smeared by scattering in the IGM. While recent studies have since cast doubts as to the extragalactic origin of this so called 'Lorimer burst' (Burke-Spolaor et al., 2011), a second possible extragalactic burst detected by Keane et al. (2011) has reignited the controversy. More such sources will need to be detected and identified before it can be claimed with certainty that scattering in the IGM has been observed.2

The study of IGM scattering, and the IGM in general, is of great importance to astrophysics and cosmology for two main reasons. Firstly, the bulk of all the baryons in the Universe reside in the IGM (Fukugita et al., 1998); less than one tenth of the total baryonic content is found in stars and galaxies. In standard cosmological models, only 4% of the Universe is made up of baryons, while dark energy and dark matter consitute the other 96% (Fukugita & Peebles, 2004). The IGM, being the main reservoir of the only component of the Universe which we know about and can detect directly, therefore plays a critical role in studies of galaxy and structure formation. The IGM is thought to be predominantly neutral soon after the Big Bang as the Universe cooled down sufficiently for atoms to form. As the first stars and quasars lit up, their UV radiation began to reionize the IGM, so that the IGM is significantly ionized from redshifts $z \sim 6$ onwards to the present epoch (Djorgovski et al., 2001). Scattering in the IGM, being sensitive to the free electrons, is ideal for studying the ionized IGM. Its structures, density inhomogeneities and turbulence, along with their evolution, can be probed in the same way as that for the ISM of our Galaxy.

Secondly, half the baryons residing in the IGM are apparently missing in the present Universe. A recent census of the baryons by Fukugita & Peebles (2004) found that, while they could be accounted for at redshift $z \sim 3$, half of them have yet to be detected in the local Universe (at redshift $z \sim 0$). Cosmological hydrodynamical simulations (Cen & Ostriker, 1999, 2006) predict that these missing baryons lie in diffuse, highly ionized, filaments at high temperatures that are difficult to detect in both emission and absorption. Many attempts have been made to detect the missing baryons, mostly by searching for emission and absorption lines of metal ions such as $\mathrm{O_{VII}}$ and $\mathrm{O_{VIII}}$ at X-ray frequencies. Most of the claimed detections are either ambiguous or unconfirmed (see the critical review by Bregman (2007)). The search for these missing baryons in the IGM therefore form one of the key science drivers of next generation X-ray instruments. Scattering in the IGM provides an alternative means for detecting and probing these missing baryons.

1.5 New Horizons in Time Domain Astronomy

A number of planned surveys with current and next generation telescopes will revolutionise the way in which interstellar and possibly intergalactic scattering can be harnessed to probe the ISM, IGM as well as the background sources. The recent discoveries of new impulsive objects such as rotating radio transients (McLaughlin et al., 2006) and the 'Lorimer burst' (Lorimer et al., 2007), coupled with advances in computing and telescope technology, have sparked a renewed interest in the variable radio sky; the International Astronomical Union's recently held symposium in Oxford on 'New Horizons in Time Domain Astronomy' attests to this (Griffin et al., 2012). Driven by these developments, these future surveys aim to explore all aspects of the variable and transient radio sky at time-scales ranging from nanoseconds up to years. These surveys will undoubtedly lead to further observations of IDV and ISS, temporal smearing in transient bursts from known and as yet undiscovered sources, and perhaps even angular broadening of continuum sources by harnessing the resolving power of ISS. Studies of radio variability and radio transients will therefore be ineffably linked to studies of interstellar and intergalactic scattering.

The recent MASIV Survey, along with other variability and transient surveys on current telescopes, act as trailblazers for some of these future surveys. I first introduce the MASIV Survey, which features heavily in this thesis, before moving on to other variability and transient surveys on existing telescopes. I then describe the next generation radio telescopes and how their salient features will revolutionize time-domain astronomy.

1.5.1 The MASIV Survey

The Micro-Arcsecond Scintillation Induced Variability (MASIV) Survey was undertaken in 2002-2003 with the aim of constructing a large catalog of IDV sources for statistical studies (Lovell et al., 2003). An initial sample of 710 compact, flat-spectrum ($\alpha_{1.4}^{8.4} > -0.3$) sources was observed at 5 GHz over four epochs spaced throughout a year, with each epoch having a duration of 3 to 4 days. The observations were conducted at the Very Large Array (VLA), with the instrument split into 5 subarrays, each observing a different set of sources. After excluding 267 sources which either showed evidence of structure or confusion resulting in systematic errors in the time domain, or were used as calibrators, the final sample of 443 sources was used to examine the statistics of IDV with respect to source and ISM properties.

The main findings as reported by Lovell et al. (2008) can be summarised as follows:

- 58% of the 443 flat-spectrum sources were found to exhibit 2 to 10% rms flux density variations in at least one epoch, demonstrating the ubiquity of IDV.
- The flux normalised variability amplitudes of the sources demonstrated a strong correlation with Galactic latitudes as well as line-of-sight Galactic electron column densities, providing the strongest evidence to date that the IDV of AGNs is predominantly driven by ISS.
- The ISS amplitudes also increase with decreasing source mean flux densities, consistent with sources whose brightness temperatures are limited by inverse Compton losses.
- No significant correlation was found between ISS amplitudes and source spectral indices.
- An unexpected result was the non-detection of new extreme, intra-hour scintillators similar to J1819+3845 in the entire sample of sources, indicating that such sources were rare. This was surprising considering that the three well-known extreme scintillators were detected serendipitously.
- By far the most significant result was the discovery of a decrease in the fraction of scintillating sources and their ISS amplitudes beyond $z \sim 2$, due either to an increase in source angular sizes or a decrease in source compact fractions with increasing redshift. These in turn can be attributed to the space-time metric of an expanding Universe, intrinsic source size effects indicative of AGN evolution, or even scatter broadening in the ionized IGM. In fact, this discovery has been touted as possibly the first direct detection of scattering in the ionized IGM (Ojha et al., 2008; Pursimo et al., 2008). However, further investigation of all possible selection effects are required before a definitive conclusion can be obtained. Selection effects

that may potentially contribute to this redshift dependence of ISS include unequal distributions of source mean flux densities, line-of-sight Hα intensities, intrinsic luminosities, and Doppler boosting factors between the high and low redshift source samples. The sources are also observed at increasing rest-frame frequency with increasing redshift, which can also lead to biases. In any case, solving this puzzle has potentially important cosmological ramifications.

1.5.2 Other Recent and Ongoing Surveys

New and archival data obtained from existing telescopes are being (or have been) scoured for candidate transients and variable sources. They all provide a better understanding of the event rates of radio transients and the radio variability (including ISS) of continuum sources. Bower et al. (2011) conducted a 5-month long search of the Boötes field using the Allen Telescope Array (ATA) at 3.1 GHz. Although no radio transients were found, 20% of the 425 detected continuum sources exhibited variability on timescales of days to months, some of which may have been caused by ISS. The 5 GHz VLA observations by Ofek et al. (2011) over 16 epochs spaced throughout a year revealed a single transient candidate, and that $\sim 30\%$ of the point sources displayed variability at greater than 4σ levels. They linked the ~ 10 day timescale variations observed in these sources to ISS. An ongoing project, the VLBA Fast Radio Transients Experiment (V-FASTR), is an attempt to search for radio transients using the VLBA in commensal mode by piggy-backing on other observations (Wayth et al., 2011). While it has succesfully demonstrated the viability of using VLBI for transient searches, no transient sources have been detected so far (Wayth et al., 2012). Ofek & Frail (2011) augmented archival data from the NRAO VLA Sky Survey (NVSS) and the Faint Images of the Radio Sky at Twenty centimeters (FIRST) Survey to examine source variability at 1.4 GHz, while Bannister et al. (2011), searched through 22 years of archival 843 MHz data from the Molonglo Observatory Synthesis Telescope (MOST) for transient and variable sources. While these archival studies are less than ideal when compared to the MASIV Survey, the former found 43 variable sources with greater than 4σ variability (roughly 1% of the sample), and the latter found 53 variable sources and 15 transient sources from among 30,000 sources. As in the other studies, these variations were attributed to scintillation in the ISM.

1.5.3 Future Surveys on the SKA and Its Precursors

The Square Kilometre Array (SKA) (Hall et al., 2008; Dewdney et al., 2009) is an ambitious, next-generation radio telescope comprising thousands of antennas sprawled over distances of at least ~ 3000 km. It is expected to have a collecting area equivalent to one square kilometre, with a specified sensitivity of $A_e/T_{sys} \sim 12000\,\mathrm{m^2K^{-1}}$

(Schillizi et al., 2007). The SKA will be designed to operate at frequencies ranging from 70 MHz to 10 GHz. The SKA will be constructed in two phases, where the first phase, SKA1, will be a subset ($\sim 10\%$) of the second phase, SKA2 (Garrett et al., 2010; Schillizi et al., 2011). Various precursor instruments such as the Murchison Widefield Array (MWA) (Lonsdale et al., 2009), the Low Frequency Array (LOFAR) (de Vos et al., 2009), the Australian SKA Pathfinder (ASKAP) (DeBoer et al., 2009) and the MeerKAT (Jonas, 2009), are either being built, commissioned or conducting early science programs as demonstrators for SKA technology and science, including the area of time-domain astronomy. It has recently been announced that the SKA will be constructed in both South Africa and Australia, with the instrument separated into various components: (1) the SKA-low component of SKA1 and SKA2, operating at 70 to 450 MHz, will be hosted by Australia, (2) the SKA-dish component of SKA1 and SKA2, a sparse aperture array operating at 450 MHz up to 10 GHz, will be constructed in South Africa as an extension of MeerKAT, (3) the SKA-survey component, as part of SKA1, will be constructed in Australia as an extension of the ASKAP to exploit its wide-field of view achieved by phased array feeds (PAFs), and (4) the SKA-mid component, perhaps based on dense array components, will be hosted by South Africa as part of SKA2.

The improved capabilities of these next generation radio telescopes will be optimal for conducting surveys of transients and variability in continuum sources to study scattering in the ISM and IGM. Firstly, the implementation of phased array feeds in ASKAP and aperture arrays in the MWA and LOFAR increases the instantaneous field of view, greatly improving the survey speeds of these telescopes. The aperture arrays even allow the received signals to be electronically combined to form multiple beams to target different regions of the sky simultaneously. Secondly, the large collecting areas provided by the huge numbers of antennas, with the SKA at the pinnacle of this effort, will lead to orders of magnitude improvements in instrument sensitivity. These increase the likelihood of detecting transient sources, and allow a much larger sample of variable sources to be constructed for more robust statistical studies. The improved sensitivity also allows much lower levels of variability to be probed at higher signal to noise ratios, and for variability to be probed in fainter and more distant sources. Thirdly, vast improvements in computing and communication technology have paved the way for the efficient and reliable handling of the huge datasets these telescopes are expected to generate, not least in the areas of data storage, processing and transport. This is particularly important in transient searches where the speed of real-time data processing will determine telescope response times to follow-up on candidate sources. Finally, there is a shift towards observing frequencies below 300 MHz, considered by many to be the final frontier of unexplored spectrum of electromagnetic radiation in astronomy, in instruments such as the MWA, LOFAR and SKA-low. While this will likely reveal many new and unexpected phenomena, scattering effects in the ISM and IGM will become increasingly dominant at these frequencies, and may turn out to be either a boon or a bane for the various science goals of these telescopes.

Various surveys have been planned or are underway to probe time-variable and transient phenomena on the SKA precursor telescopes. The Variables and Slow Transients (VAST) Survey (Murphy & Chatterjee, 2009) and the Commensal Real-Time ASKAP Fast Transients (CRAFT) Survey (Macquart et al., 2010) consitute two key survey science projects of the ASKAP. One of the major goals of both these surveys is to probe propagation effects in the ISM and IGM using impulsive astronomical events and source variability. The VAST Survey, for example, may be able to probe ISS on scales even larger than that of MASIV, and potentially detect many more extreme scattering events. The MWA and LOFAR also have transient detection programs incorporated into their science goals (Fender et al., 2006; Hessels et al., 2008). The review by Fender & Bell (2011) compares the capabilities of these current and upcoming telescopes for transients detection in terms of their sensitivities, field of views and transient detection rates. Similar comparisons can be found in the papers by Macquart et al. (2010) and Colegate & Clarke (2011).

Of course, all these will eventually lead to the SKA which will provide orders of magnitude improvements in sensitivity. Searching for transients with the SKA is incorporated under the key science project 'exploration of the unknown' (Wilkinson et al., 2004). Cordes (2007) discusses how the SKA can be used as a transient survey telescope. Lazio et al. (2004), gives a general overview of how the SKA can be exploited to further study scattering effects including scintillation, temporal smearing and angular broadening in the ISM and IGM.

1.6 The Current State of Affairs

Having set the scene by introducing all the disparate concepts important for this study (i.e. scattering, scintillation, AGNs, and the IGM), as well as reviewing the important work already carried out in these fields, I now move on to identify areas where further progress still needs to be made. This section therefore serves as a bridge connecting all the prior sections to the next where I introduce the scope of my own research. This section provides the motivation and justification for my own work in the context of all that has been discussed.

The MASIV Survey was the first targeted variability survey of its scale in the radio regime, so there is still much to learn in terms of observing, handling and analysing variability data at these scales. Discriminating real astrophysical variability from variability arising from instrumental and man-made effects remains one of the key issues that will need to be addressed, in addition to the characterisation of variability amplitudes and time-scales. The development of efficient and effective algorithms to automate such processes will be critical in preparation for data-intensive, large-scale surveys with instruments such as ASKAP and the SKA.

The ISS explanation for IDV at cm wavelengths, while generally accepted within the astronomical community (a few dissenting voices do exist, see for example Fuhrmann et al. (2008)), needs to be further tested. For example, it is important to determine if ISS still dominates AGN variability at timescales much longer than 2 to 3 days, as well as at radio frequencies higher than the 5 GHz probed by the MASIV Survey. Additionally, while ISS places lower limits on the intrinsic brightness temperatures in these sources, some scintillating sources still exhibit brightness temperatures in excess of the inverse Compton limit of 10^{12} K (Macquart et al., 2000), so that the problem is not fully resolved.

There remain unanswered questions as to why some compact extragalactic radio sources scintillate while others do not (or scintillate less). Although this could reflect direction-dependent inhomogeneities in the turbulent ISM, the intrinsic μas and mas structures of the sources play an important role as well. The foremost question, and potentially the most tantalising, is why AGNs at high redshift scintillate less. Determining the origin of this redshift dependence of ISS, regardless of whether the cause is intrinsic or extrinsic to the sources, will allow future ISS surveys to be used as cosmological probes of either AGN evolution, scattering in the IGM or space-time curvature at μas scales. A thorough investigation into the many possible selection effects that may cause this redshift dependence of ISS has never been carried out. Another burning question deals with the origin of extreme, intra-hour scintillation; it is unknown whether their scarcity arises from the uniqueness of the sources or of the scattering material, or both. The answer may shed light on the properties and possible anisotropies of the scattering material in the ISM, or on the physics of these sources at AU-scales where AGN jets are thought to be launched.

While the MASIV Survey achieved its main objective of producing a large sample of scintillating sources for statistical analyses, it remains to be seen whether the data from such surveys can indeed be succesfully used to probe the statistics of AGN structure and the ISM, given the random and complex nature of ISS. While the recent surveys and archival searches discussed in Section 1.5.2 found many variable sources, not much has been gleaned from these data other than the identification of these sources as variable and possible scintillators. It is therefore important to ask what types of scientific output can be produced by such surveys (and such data), and what their value is to the wider astronomical community. There is a need for similar ISS surveys with current telescopes as previews of what is to be to expected (or not) from future instruments and surveys. These surveys will function not only as technical demonstrators, but also as scientific demonstrators of the potential of ISS as astrophysical and cosmological probes.

As described in Section 1.4, scattering in the ionized IGM is not well understood due to the lack of observational data and theoretical studies. While many surveys have been proposed to search for fast transients with the hope of detecting extragalactic bursts to probe the IGM, there is currently no investigation into whether scattering effects in the IGM are even detectable in the first place. Scattering models, simulations, and stronger observational constraints are sorely needed to address this dismal state of affairs.

A better understanding of angular broadening and temporal smearing in the IGM will provide critical feedback into the design, optimization and strategic use of upcoming instruments such as the SKA for the detection of IGM scattering and extragalactic radio transients. Conservation of energy dictates that the area under a pulse be conserved, so that the peak signal to noise ratio (SNR) of a temporally smeared pulse will decrease by a similar factor. This effect will influence the selection of observing frequencies, temporal resolution (determined by the computing power, which enters into instrumental cost equations), as well as survey strategies to maximise transient detections. In particular, the trade-off between instrument sensitivity and field-of-view is often a point of contention (Cordes, 2007; D'Addario, 2010; Macquart, 2011), and IGM scattering will factor into these discussions for extragalactic transient searches.

In the meantime, a follow-up survey has been carried out by the MASIV team to observe the variability of a subsample of the MASIV sources with the VLA at multiple frequencies over a duration of 11 days. The main objective of these multi-frequency ISS observations is to examine how the redshift dependence of ISS scales with frequency. This allows the various possible explanations for this redshift dependence of ISS to be discriminated, since space-time curvature, intrinsic source size effects, and angular broadening in the IGM all scale differently with frequency. The multi-frequency data also provides a unique opportunity to compare the ISS of the sources at different frequencies, which will go a long way in demonstrating the science case for ISS surveys. The longer time-span observations enable ISS and AGN variability to be studied on longer time-scales, in addition to enabling better characterisation of variability amplitudes as well as the scintillation timescales. Furthermore, these observations provide a robust means of discriminating flux variations of astrophysical origin from variations due to instrumental and systematic errors, allowing lower limits to be placed on the detectability of ISS amongst these errors using the VLA. The increased sensitivity from the larger number of antennas per subarray enables the measurement of rms flux density variations down to a lower level than that of the original MASIV Survey. They also provide a platform for exploring various methods of estimating and correcting for these errors, functioning as a demonstrator for similar large-scale surveys of the variable radio sky in the future.

1.7 Research Objectives and Scope of Thesis

This study aims to make use of the data from the multi-frequency MASIV follow-up observations to further our understanding of the compact μas components of AGNs, the scattering material in the ISM, the phenomenon of ISS, as well as the handling of variability data in such surveys. In particular, this study seeks to determine the origin and cosmological significance of the redshift dependence of AGN ISS, which will provide either the first direct detection of scattering in the ionized IGM or place strong constraints on it. Either way, the results will have important ramifications for the detection and probing of the ionized IGM and extragalactic radio transients in future surveys with next generation radio telescopes.

Therefore, the objectives of this study are to:

1. Identify and understand errors in the variability data from the MASIV follow-up observations, as well as develop novel techniques of error estimation, error correction, and variability characterization of the time-series data — providing feedback into future variability surveys on current and next generation radio telescopes.

2. Improve current understanding of ISS, the ISM, and AGN morphology through the analysis and interpretation of the data from the MASIV follow-up observations.

3. Determine the origin of the redshift dependence of AGN ISS, providing either the first direct detection of scattering in the ionized IGM, or placing the strongest constraints on it. This includes a thorough investigation of all possible selection effects that may bias the source sample.

4. Develop a scattering model for the IGM by extending interstellar scattering theory to cosmological scales, in order to obtain a better understanding of IGM scattering.

5. Explore strategies for probing the ionized IGM using current and next generation radio telescopes, as well as limits imposed by IGM scattering on the detectability of extragalactic radio transients, based on the scattering model and observational constraints.

Chapter 2 describes the MASIV follow-up observations in detail, along with the methods used in reducing and preparing the data for analysis, including calibration, error estimation as well as characterisation of source variability. The main results of the MASIV follow-up observations are presented in Chapters 3 to 5. Chapter 3 provides strong evidence to support ISS as the dominant mechanism behind the observed variability in the time-series data, and discusses how the intrinsic properties of AGNs influence the strength of ISS. This is followed by a discussion on the origin of the most rapid and extreme scintillators in Chapter 4, based on a search for the most rapid scintillators in the MASIV follow-up data and an analysis of their properties. In Chapter 5, I investigate the origin of the redshift dependence of AGN ISS, taking into consideration subtle selection effects in the source sample, and making use of theoretical models and Monte Carlo simulations to interpret the data. The observational and theoretical constraints on IGM scattering are presented in Chapter 6, where ISM scattering models are extended to cosmological scales and applied to the IGM. Their implications for the detection and probing of the ionized IGM and extragalactic transients with next generation radio telescopes are also presented. Chapter 7 summarizes the main results and conclusions of this thesis and provides suggestions for future work.

Chapter 2

Observations and Data Preparation

> *A scientist must also be absolutely like a child. If he sees a thing, he must say that he sees it, whether it was what he thought he was going to see or not. See first, think later, then test. But always see first. Otherwise you will only see what you were expecting.*
>
> — ***Douglas Adams, So Long, and Thanks for All the Fish***

Together with the contents of Chapter 3, a significant portion of this chapter has been published in *The Astronomical Journal*, in a paper entitled 'Dual-frequency Observations of 140 Compact, Flat-spectrum Active Galactic Nuclei for Scintillation-Induced Variability' (Koay et al., 2011a).

2.1 Introduction

As alluded to in Chapter 1, the handling of time-domain data is of great interest to the radio astronomical community, especially with the advent of future variability surveys on data-intensive instruments such as the SKA and its precursor telescopes. Current observations will therefore play key roles in exploring various observational strategies for conducting such surveys. Additionally, they will demonstrate how time-domain data from these surveys can be handled efficiently and reliably in the presence of a myriad of stochastic and systematic errors introduced by the instrument and other non-astrophysical sources.

The MASIV follow-up observations provide a perfect platform for exploring these issues. This chapter describes the entire process of obtaining, processing and preparing the data from the MASIV follow-up observations prior to the actual scientific analysis. The data from the MASIV follow-up observations used in this study were obtained using the VLA radio telescope, which I briefly introduce in Section 2.2 before describing the technical details of the observations. Section 2.3 then describes the reduction and calibration of the raw data. In Section 2.4, I explain how the variability of the sources are quantified. This includes a subsection detailing the estimation and correction of errors caused by instrumental and other systematic effects. A summary of this chapter is provided in Section 2.5, where lessons learned through the entire process are discussed where they are relevant for future variability surveys.

The discussions presented in this chapter assume prior knowledge of the fundamental principles of interferometry and aperture synthesis, as well as standard data reduction techniques. So as not to detract from the main work presented in this chapter, the basic concepts and terminologies are introduced in Appendix A rather than here.

2.2 Observations

2.2.1 The Very Large Array[1]

The Very Large Array (VLA) located near Socorro, New Mexico, USA provides one of the highest sensitivities of any currently operational interferometer, which is ideal for the study of ISS. It consists of 27 antennas arranged in a Y configuration on railway tracks, allowing the antennas to be moved further apart or closer together depending on the applications. The largest configuration is the A configuration with baselines up to 36 km apart, while the D configuration is the smallest with maximum baselines of 1 km. Each of the antennas is 25 m in diameter.

Each antenna of the VLA is fitted with 7 receivers, each operating at a particular frequency band (nearby 0.3, 1.4, 5.0, 8.3, 15.0, 23.0, and 42.0 GHz). Only one of these receivers can be selected at any one time for each antenna, although the entire array can be divided into a maximum of 5 sub-arrays with each sub-array observing at different frequency bands. Additionally, each receiver can be tuned to two frequencies from the same frequency band, as long as the frequency difference is no larger than $\sim$ 450 MHz. The antennas receive signals in two orthogonal circular polarisations at each of these two frequencies. Each of these four separate streams of data is often referred to as an intermediate frequency (IF) channel.

The correlator, where the signals from all antennas are combined, operates in both spectral-line mode and continuum mode. The spectral-line mode is used for observations of source spectral lines where a high frequency-resolution is desired, requiring each IF channel to be split into larger numbers of frequency channels with smaller bandwidths. In continuum mode, the frequency channels are combined into a single, higher bandwidth channel to provide a higher signal-to-noise ratio and higher sensitivity.

---

[1] The specifications of the VLA presented here are sourced from the VLA website: http://www.vla.nrao.edu/, where more information can be obtained.

During the observations to obtain the data for this study, the VLA receivers were being upgraded to that of the Expanded Very Large Array (EVLA), which provide larger bandwidths and allow the IF channels in each band to be tuned further apart in frequency. However, the correlation was still being performed using the old correlator rather than the WIDAR correlator which was still in development.

2.2.2 The MASIV Follow-up Observations

A sample of 140 sources were selected from the original MASIV set of sources. Seventy of these sources have measured redshifts of $z > 2$, while the remaining 70 have redshifts of $z < 2$ as a control sample. Since the MASIV survey found that the variability of the sources are dependent on Galactic latitudes, line-of-sight Hα intensities and mean flux densities of the sources (Lovell et al., 2008), great care was taken to ensure that both sub-samples have similar distributions of these parameters to avoid source selection biases. The selected sources were expected to have flux densities above 100 mJy at 8.4 GHz, and to be unresolved when observed with the VLA in its largest configuration (maximum baseline of 36.4 km and a FWHM synthesized beamwidth of 0.24 arcsecond at 8.4 GHz). The full list of these sources can be found in Appendix B together with their variability characteristics.

Observations were carried out over 11 days from 2009 January 15 to 2009 January 25 using the VLA, the antennas of which were in the process of being upgraded to that of the EVLA. The instrument was divided into two subarrays. One subarray comprised of 14 EVLA antennas observing in continuum mode with two 50 MHz IF channels per polarisation, one centered at 4.9 GHz and another at 6.6 GHz. The second subarray was a mix of 13 VLA and EVLA antennas observing at a centre frequency of 8.4 GHz with two continuum mode IF channels (contiguous 50 MHz bandwidths) per polarisation. During the observations, each source was observed for 1 minute at $\sim$ 2 hour intervals simultaneously on both subarrays while above an elevation of 15°. The correlator integration time was set to 3.3 seconds. Observations of the target sources were interspersed with observations of the primary flux calibrator (3C286) and 23 secondary calibrators, selected from the list of sources in the VLA calibrator manual. The observations were scheduled in sidereal time, so that each source was observed at the same time each sidereal day.

Unfortunately, 12 of the antennas from the 4.9 and 6.6 GHz subarray, as well as 8 antennas from the 8.4 GHz subarray, encountered data losses on the 7th and 8th day of the observations due to failure in the optical fibre links. This left only a single baseline on the 4.9 GHz subarray, which had to be flagged, and 10 baselines on the 8.4 GHz subarray. Thus no data were obtained at 4.9 GHz and 6.6 GHz on those days, while the data at 8.4 GHz were retained, although with a significant reduction in the number of baselines.

It is also important to note that the observations were conducted during reconfiguration of the VLA between the BnA and B configurations, so recently moved antennas may have introduced pointing errors into the data.

2.3 Data Reduction

The data are loaded into the Astronomical Image Processing System (AIPS) software package (Greisen, 2003), the standard package used for the processing of VLA data. Upon examination of the raw data, it is found that the 6.6 GHz data were subjected to extensive contamination by radio frequency interference (RFI). Hence, they are excluded from this study.

2.3.1 Calibration and Editing

The time-series data for the primary flux calibrator and all secondary calibrators are inspected for outliers and strong spurious signals caused possibly by RFI, which are then flagged and removed. This is followed by an inspection of the visibilities of all target sources at both frequencies, both polarisations, all IF channels, and all antennas to look for suspicious data, i.e. a large jump or drop in amplitude that appear only in a single IF channel, polarisation, baseline or antenna.

The amplitudes of the source visibilities are calibrated based on the flux densities of the primary calibrator. Standard techniques are then used to calibrate for amplitude variations due to atmospheric effects, as well as antenna gain and pointing errors, using the secondary calibrators. Phase self-calibration is then applied to all the target sources. Since the sources are expected to be variable in amplitude, no amplitude self-calibration is applied. Polarisation calibration and parallactic angle corrections are also applied. See Appendix A.3 for a more detailed explanation of these calibration techniques and the motivation for applying them to the data.

After calibration, each of the target sources are examined for outlying points and spurious data as was done for the calibrators, which are then flagged.

2.3.2 Inspection of Calibrated Data

The data are then converted into Flexible Image Transport System (FITS) format, so that they can be loaded into the Miriad software package (Sault et al., 1995), another standard astronomical data processing package which provides a more convenient means of generating the desired output in plain text format. Using Miriad, the source visibilities are coherently averaged over 1 minute and over all baselines (as well as across both channels for the 8.4 GHz data) to produce the calibrated time-series plots (lightcurves) for each source.

It is essential to ensure that the secondary calibrators are not themselves variable down to the $\sim 1\%$ variability levels probed by the survey. The target source lightcurves are then inspected by eye for possible contamination by spurious variability in the secondary calibrators. This is done by looking for similar variability patterns in sources that have been calibrated using the same secondary calibrator. Such patterns will be particularly obvious for the stronger sources where calibration errors are expected to dominate over errors due to random noise. While no calibrators are found to be variable this way, it does not rule out the presence of calibrator variability undetectable by eye, as they will probably be superposed on top of real scintillation and other sources of errors.

An examination of the lightcurves of all sources reveals that slightly more than a third of the sources exhibit variability patterns that repeat daily on at least one frequency, some of them superposed on top of larger and slower variations. There are two possible causes of these daily repeating patterns. Firstly, these repeating patterns may be errors in measurements of the source flux density as a result of confusing sources nearby or resolution effects. For an isolated point source, the visibility amplitude is uniform everywhere on the uv-plane, and is constant as a function of uv-distance. Therefore, the uv-coverage is not important, and a short scan (snapshot) provides a sufficient measurement of the flux density of the source. However, there may be weak extended structures surrounding the sources, or non-related sources that lie within the primary beam of the antennas, perhaps even detected through the sidelobes of the antennas. Since the observations were scheduled in sidereal time and each source was observed at the same time each sidereal day, any confusion or resolution effects appear as repeating patterns with a one sidereal day period, with the amplitude of the variations being independent of the source flux density. Secondly, such repeating patterns can also result from residual gain and pointing errors from the calibration process, in which case the apparent variations will be a percentage of the source flux density.

In about 95% of these sources, the daily repeating patterns turn out to be residual gain errors and pointing errors after calibration. This conclusion is arrived at after it is found that these patterns which repeat daily are at a very low level, typically varying by no more than $\sim 1\%$ rms. These daily repeating patterns are almost always found on the higher flux density, low-variability sources, where calibration errors are expected to dominate. Furthermore, snapshot images and plots of the visibility amplitudes vs. uv-distances reveal no visible structures or contaminating sources nearby for most of these sources. All data from 2 antennas in the 8.4 GHz subarray in which the residual pointing errors were the worst are removed entirely. Only 3 of these sources which exhibit daily repeating patterns are found to be slightly resolved, particularly at 8.4 GHz, remedied by the removal of visibilities from the longer baselines.

These preliminary methods of detecting calibrator variability and residual calibration errors are thus supplemented, and their effects corrected for, with further, more quantitative techniques discussed in Section 2.4.2. No recalibration of the target sources is necessary as these errors are accounted for via subtraction of the estimated error values from the calculated variability amplitudes for each source.

There also appears to be a large increase in the amplitude variations of the uncalibrated time-series data from day 7 of the observations onwards (typically increasing from 1% to 4% rms variations), after the data losses were encountered on the VLA (see Section 2.2.2). These are attributed to an increase in system gain variations. Although the calibration process successfully removed most of these effects, some residuals remain. These residuals are larger than the residuals in the first 6 days of continuous observations when the system gains were more stable. Therefore, the data between days 7 and 11 are treated with extra caution. Discarding all the data after 6 days may reduce the errors due to possible false variability, but results in a dataset with a reduced timespan with higher statistical uncertainties in the estimation of the variability characteristics. As a compromise, all subsequent data analyses in Chapter 3 are carried out using both sets of data — one containing data only from the first 6 days, and another containing data from the entire duration of the observations from which comparisons can be made. This provides another means of cross-examining the results of my analyses.

2.4 Characterisation of Source Variability

Figures 2.1 to 2.4 show four sample lightcurves of sources with different variability time-scales. Fast scintillators such as J1159+2914 (Figure 2.1) have variability time-scales on the order of hours. On the other hand, J0510+1800 (Figure 2.2) is a slow variable with longer characteristic time-scales of half a day at both frequencies. Some sources exhibit variability at multiple time-scales, where shorter and smaller amplitude variations are superposed on top of longer time-scale variations of larger amplitude. J0958+6533 (Figure 2.3) and J1734+3857 (Figure 2.4) are examples of such sources. This can be a result of different components in the source scintillating at different time-scales; with larger, more extended components causing slower variations and more compact components causing the faster variations. It can also be caused by a combination of short time-scale scintillation and longer time-scale intrinsic variability, although our analysis shows that this is not a dominant effect in our sample of sources (see Section 3.2).

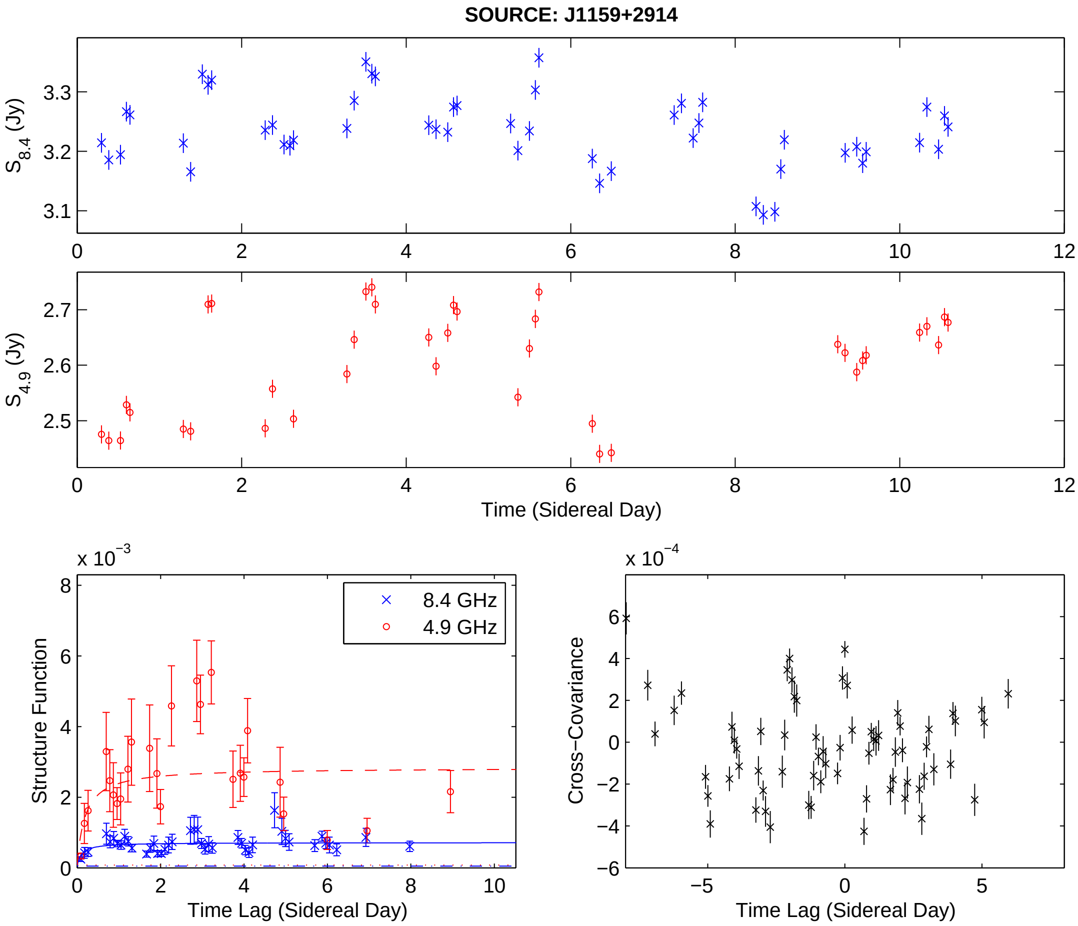

Figure 2.1 — *Lightcurves for the source J1159+2914 at 8.4 GHz (top) and 4.9 GHz (middle), with their corresponding structure functions calculated from Equation 2.2 (bottom left, where the solid curve and dashed curve represent the model fits at 8.4 GHz and 4.9 GHz respectively, the dash-dot line represents D_{noise} at 4.9 GHz and the dotted line represents D_{noise} at 8.4 GHz) and cross-covariance function calculated from Equation 3.1 (bottom right).*

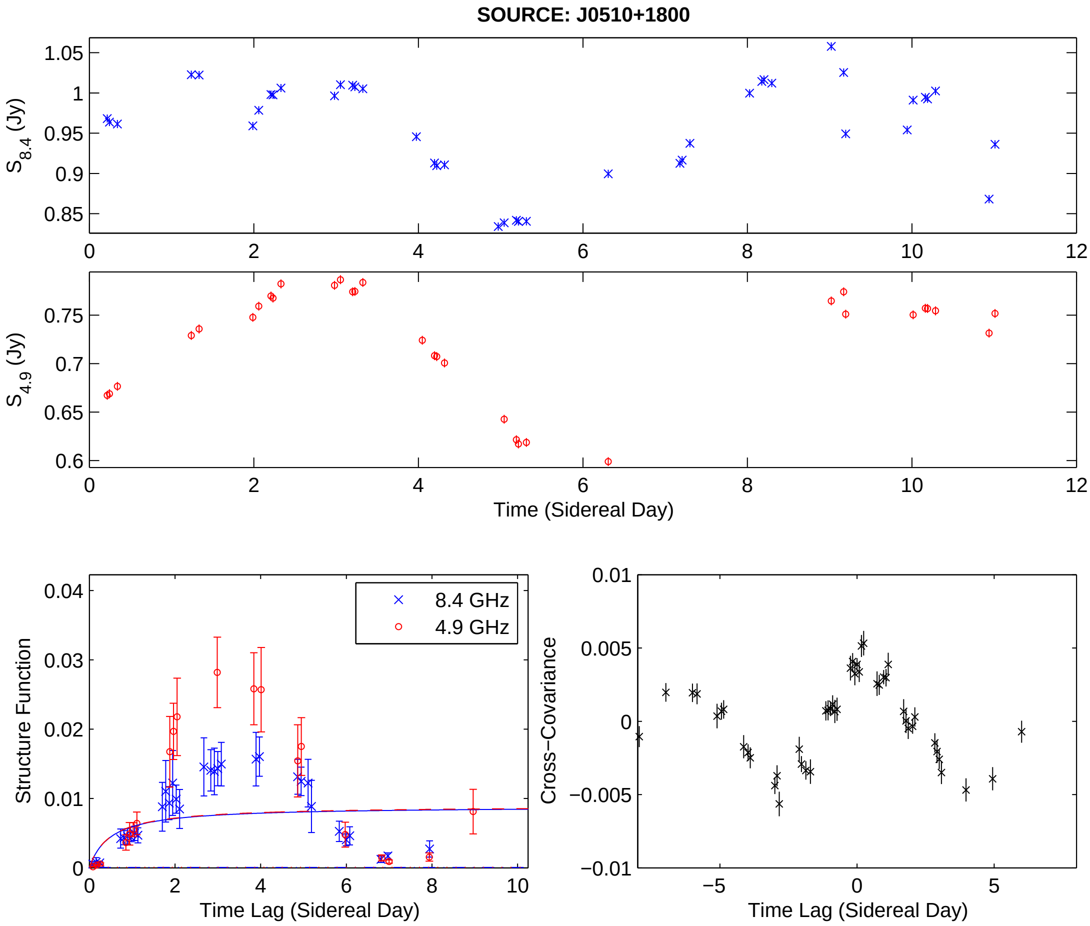

Figure 2.2 — *Lightcurves for the source J0510+1800 at 8.4 GHz (top) and 4.9 GHz (middle), with their corresponding structure functions calculated from Equation 2.2 (bottom left, where the solid curve and dashed curve represent the model fits at 8.4 GHz and 4.9 GHz respectively, the dash-dot line represents* D_{noise} *at 4.9 GHz and the dotted line represents* D_{noise} *at 8.4 GHz) and cross-covariance function calculated from Equation 3.1 (bottom right).*

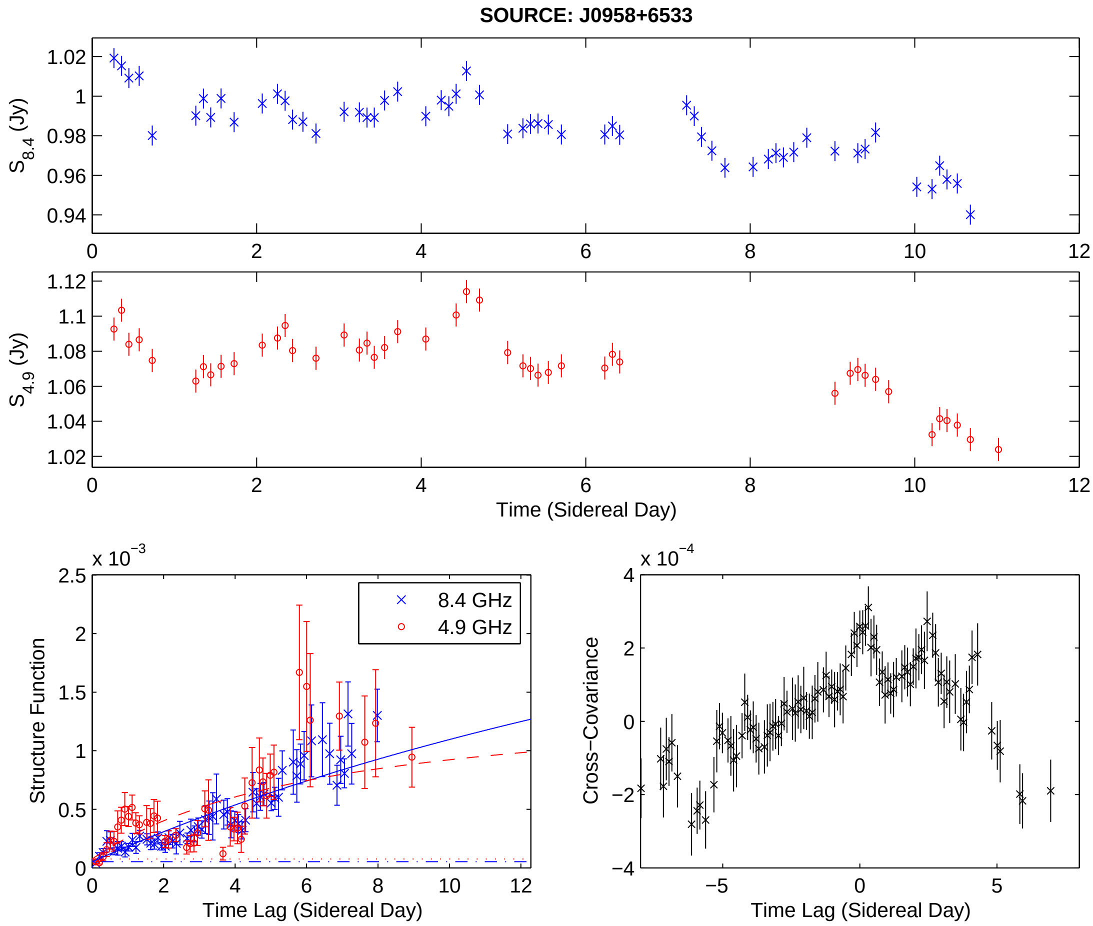

Figure 2.3 — *Lightcurves for the source J0958+6533 at 8.4 GHz (top) and 4.9 GHz (middle), with their corresponding structure functions calculated from Equation 2.2 (bottom left, where the solid curve and dashed curve represent the model fits at 8.4 GHz and 4.9 GHz respectively, the dash-dot line represents* D_{noise} *at 4.9 GHz and the dotted line represents* D_{noise} *at 8.4 GHz) and cross-covariance function calculated from Equation 3.1 (bottom right).*

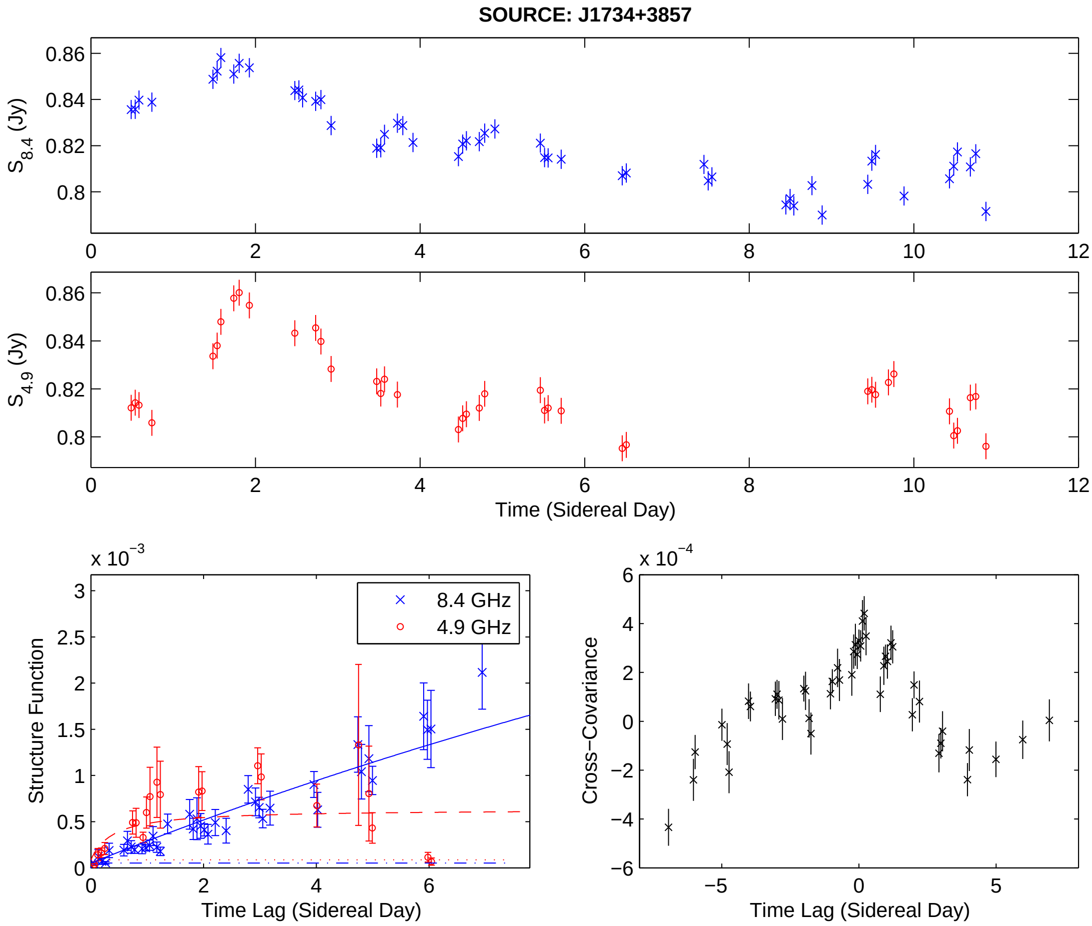

Figure 2.4 — *Lightcurves for the source J1734+3857 at 8.4 GHz (top) and 4.9 GHz (middle), with their corresponding structure functions calculated from Equation 2.2 (bottom left, where the solid curve and dashed curve represent the model fits at 8.4 GHz and 4.9 GHz respectively, the dash-dot line represents* D_{noise} *at 4.9 GHz and the dotted line represents* D_{noise} *at 8.4 GHz) and cross-covariance function calculated from Equation 3.1 (bottom right).*

2.4.1 Quantifying Source Variability

2.4.1.1 Structure Function

As in the analyses of the original MASIV data, the structure function (SF) is used to quantify the variability of each source, defined as:

$$D(\tau) = \left\langle [S(t+\tau) - S(t)]^2 \right\rangle , \tag{2.1}$$

where $S(t)$ is the flux density of the source at time t, normalized by its mean flux density calculated from the entire 11-day period. $D(\tau)$ is therefore a dimensionless quantity. The angular brackets indicate averaging over time, t. The observed SF at a given time-lag τ is calculated as:

$$D_{obs}(\tau) = \frac{1}{N_\tau} \sum_{j,k} [S(t_j) - S(t_k - \tau)]^2, \tag{2.2}$$

where N_τ is the number of pairs of flux densities with a time-lag τ, binned to the nearest integer multiple of the smallest time-lag between data samples (typically ~ 2 hours) for each source. Bins are selected for plotting the SF only if N_τ exceeded 20% of the total number of sample points in the lightcurve. This avoids the use of bins with large statistical errors due to small N_τ.

Errors in the SF amplitudes at each time-lag are calculated as a standard error in the mean, given by the standard deviation of the $[S(t_j) - S(t_k - \tau)]^2$ terms in that time-lag bin divided by $\sqrt{N_\tau - 1}$. Note that this method does not account for statistical errors resulting from the finite sampling of a random process, due to the limited timespan of the observations. Such statistical errors are dependent on the characteristic time-scale of the variations relative to the total observing span, increasing for sources with longer variability time-scales. A second method of calculating the SF errors is also tested, based on that used by You et al. (2007). In this case, the errors are given by $\sigma_D(\tau) = \langle D_{obs}(\tau) \rangle (\tau/\tau_{tot})^{1/3}$, where τ_{tot} is the total observation span, in this case 7 or 11 days, depending on which set of data is used. This estimation incorporates the fact that the number of possible pairs of flux densities that can be formed to calculate the SF generally decreases with increasing time-lag. However, it is found that errors can be underestimated for bins at small time-lags, yet have a low number of flux density pairs. Therefore, the first method is selected over the second method.

The SF has the advantage of being insensitive to gaps in the sampling of data in the MASIV survey and the follow-up observations, as opposed to a power spectrum analysis. Also, the SF is not as sensitive to biases resulting from errors in the estimation of the mean flux density of the source as the auto-correlation function.

Sources in which the SF amplitudes drop at integer multiples of time-lags of a sidereal day provide an additional means of detecting variability patterns that repeat daily. The SFs were in fact examined together with the lightcurves to weed out such sources as described earlier in Section 2.3.2.

2.4.1.2 Modulation Index

Another common parameter used in the literature to quantify the variability amplitudes of sources is the modulation index, m, defined as the ratio of the rms flux density to the mean flux density of the source. I therefore use both the modulation index and the SF amplitudes interchangably in the text. If the variability time-scales of the sources are much shorter than the span of the observations, the saturated SF amplitude can be approximated as $D(\tau \to \infty) \approx 2m^2$. The SF amplitude provides a measure of the variance, while the modulation index provides a measure of the standard deviation of the flux densities.

2.4.2 Error Estimation and Correction

As alluded to in Section 2.3, several instrumental and systematic effects can contribute to the perceived variability of a source. Variability caused by such errors contribute a constant additive noise floor, D_{noise}, to the SF of each source. Correcting for these errors thus requires D_{noise} to be subtracted from the SFs across all time-lags so that only genuine variability is retained. This is based on the assumption that the errors are independent of time-lag i.e. the errors are white. As noted in Lovell et al. (2008), there is a possibility that some systematic errors may result in non-white errors which are dependent on time-lag.

I compare 3 different techniques for estimating the errors quantitatively, of which the third method (Method C), is chosen for use in the final analysis.

2.4.2.1 Method A: 2-Hour Structure Function as an Error Estimate

A simple way of estimating D_{noise} is to assume that all variability at time-scales less than 2 hours (the typical minimum time-lag between data points on the lightcurve) is not true variability by directly using $D_{noise} = D_{obs}(\text{2hr})$ for each source, where $D_{obs}(\text{2hr})$ is the single sample estimate of the SF at 2-hour time-lags. However, using $D_{noise} = D_{obs}(\text{2hr})$ can lead to an overestimation of errors in some sources that do scintillate at time-scales of less than 2 hours, e.g. J1159+2914 (Figure 2.1). On the other hand, calibration errors such as the daily repeating patterns observed in some of the sources may be underestimated, since these sources do exhibit instrument-related variability up to time-scales of a day. This method is therefore tested but finally not used.

2.4.2.2 Method B: Model Fitting the Flux-Dependent and Flux-Independent Errors

In the original MASIV survey, the errors were calculated based on the quadratic sum of two error components, given by the following equation (Lovell et al., 2008):

$$\sigma_{err,s,p} = \sqrt{(s/\bar{S})^2 + p^2}, \tag{2.3}$$

where $\sigma_{err,s,p}$ is the rms error in each flux density estimate normalized by the mean flux density of the entire length of observations, $\bar{S}$. The two error components are denoted by s and p; s, which is in units of Jy, accounts for errors that are independent of the flux density of the source, including additive system noise and confusion effects, and affects mainly the weak sources; p, on the other hand, represents errors which are flux density dependent, such as errors in the calibration of the source as a result of residual pointing offsets, system gain variations and atmospheric absorption - these errors arise in part because there is a finite angular distance (as well as finite time interval between observations) between the target source and its calibrator. While a linear vector interpolation algorithm is used during the calibration process in AIPS to account for such effects, some residual errors will remain. Low-level variations in the calibrators themselves may also contribute to p. Since these errors are dependent on the source flux density, they are the dominant sources of error in the strong sources. The probability distribution of these additional variations can be assumed to be a convolution of the probability distribution of the flux density dependent errors with the distribution of the flux density independent errors, and thus can be estimated as a quadratic sum of the s and p error components.

The values of s and p can be estimated by again making use of the variability of sources at the shortest measured time-lag, 2 hours. The variability of each source at 2-hour time-lags is plotted against its mean flux density, as shown in Figure 2.5. In this case, the variability is quantified by the 2-hour modulation index, $m_{2\mathrm{hr}}$, calculated as $m_{2\mathrm{hr}} = \sqrt{D_{obs}(2\mathrm{hr})/2}$. Equation 2.3 is then used as a model fit for the resulting scatter plot (shown as a solid line), with s and p as free parameters. This allows p to be estimated based on the average 2-hour variability of the strong sources, and s to be estimated based on the average 2-hour variability of the weak sources. Based on the curve fits, the values obtained are $s = 0.0009$ Jy and $p = 0.0068$ at 8.4 GHz, and $s = 0.0012$ Jy and $p = 0.0065$ at 4.9 GHz. The value of s obtained this way for the 4.9 GHz data is close to the value of 0.0013 Jy used in the original MASIV data, but is lower for the 8.4 GHz data. The reduced system noise at 8.4 GHz is to be expected given that 11 antennas (originally 13, but data from 2 antennas were removed) were used in these observations as compared to the previous MASIV observations in which the VLA was sub-divided into 5 sub-arrays each with 5 or 6 antennas. However, while having a similar increase in the number of antennas, the system noise at 4.9 GHz is

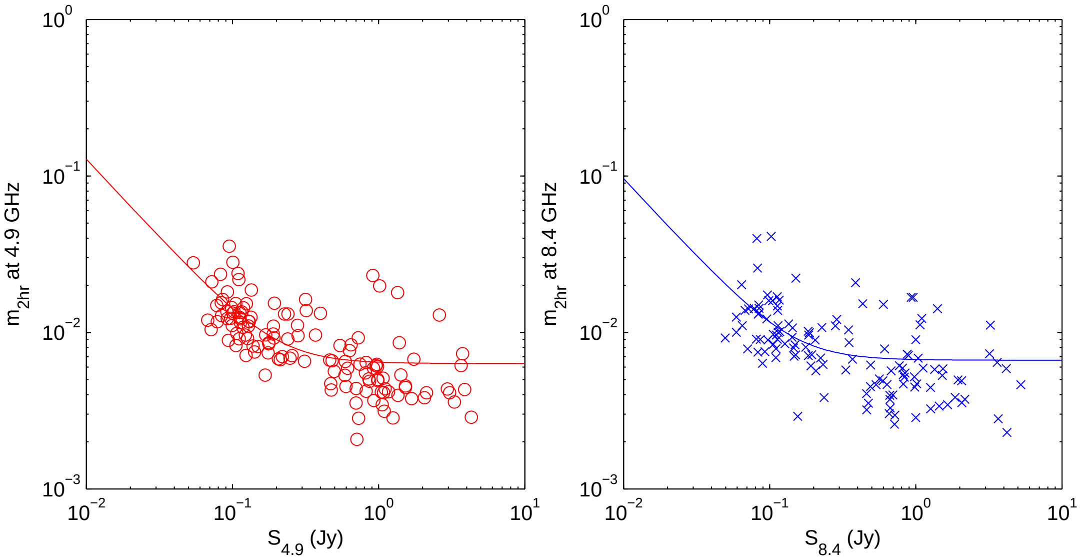

Figure 2.5 — *2-hour modulation index calculated for all sources at 4.9 GHz (left) and 8.4 GHz (right) plotted against their respective mean flux densities. The solid line represents a curve fit using Equation 2.3.*

comparable to that in the MASIV survey due to its use of only a single IF channel. The values of p used here are in the range of the values found in MASIV. These values of s and p are then used to calculate $\sigma_{err,s,p}$ for each source at both frequencies, from which $D_{noise} = 2{\sigma_{err,s,p}}^2$ can then be subtracted from the SFs of each source.

In Method A, D_{noise} is equivalent to $D_{obs}(2\text{hr})$ for each source, but in this second method using Equation 2.3, about half of the sources have $D_{obs}(2\text{hr}) > D_{noise}$, while the other half of the sources have $D_{obs}(2\text{hr}) < D_{noise}$. Therefore, this second method of estimating D_{noise} allows for about half of the sources to have real variability at time-scales less than 2 hours. While this is an improvement over the first method, it assumes that all sources have the same values of s and p, which is definitely not the case. It also does not correct for possible low-level variations of the calibrator in an explicit manner.

2.4.2.3 Method C: Source and Calibrator Dependent Error Estimates

This third method, which I developed, makes use of Equation 2.3 as well, but uses a different approach in the calculation of the values of s and p.

Since the amount of data flagged for each source varies and the additive errors increase as more data are flagged, it is decided that the value of s will be obtained separately for each source, calculated from the standard error in the mean from the 1 minute averaging of the 3.3 second visibilities over all baselines. Since each point on the lightcurve of each source has different errors, s for each source is then the average of the errors for all the points in its lightcurve. This gave values of s in the range of 0.0004 to 0.0041 Jy (with a mean of 0.0007 Jy) at 8.4 GHz and 0.0006 to 0.0031 Jy (with a mean of 0.0009 Jy) at 4.9 GHz. The range of values of s obtained here at both frequencies confirm that using a single s value for all sources will tend to overestimate additive system noise errors in some sources while underestimate it in others.

As alluded to in Section 2.3, the fact that the daily repeating patterns are found to appear mostly in the stronger sources with very low variability (with $D_{obs}(\tau) < 3\times10^{-4}$, or raw modulation indices of $m < 1\%$), provides a clue that these errors are linked to the calibration process. Upon further examination, it is found that for sources where the SF amplitudes are greater than 3×10^{-4} at one frequency and less than 3×10^{-4} at the other frequency, the daily repeating patterns are observable only at the frequency with $D_{obs}(\tau) < 3 \times 10^{-4}$. Where such daily repeating patterns are superposed on top of larger, longer time-scale variations, the SF amplitudes may be much greater at longer time-lags, but between 2 hours and 1 day, the SF amplitudes are generally $< 3 \times 10^{-4}$. The variability of these daily repeating patterns are therefore comparatively small. This leads to the conclusion that these repetitive patterns are calibration errors due to pointing errors and residual gain errors from the interpolation of gain solutions between target sources and their calibrators. Though these patterns can be detected by eye when they dominate the source variability, these effects should also add to the variability of the sources dominated by real scintillation and will thus need to be corrected for.

Recognizing that the values of p are calibrator dependent (due to the underlying low-level variations in the calibrator), and that the residual calibration errors need to be accounted for regardless of whether they are detectable as daily repeating patterns or not, it is decided that the value of p for each source will be calculated based on the calibrator that was applied to it. To achieve this, each one of the 23 calibrators is used as a calibrator for a subset containing N_c number of other calibrators with similar Local Sidereal Time (LST) coverage (with time interval between observations generally not exceeding 2 hours). N_c varies for each subset and there are 23 overlapping subsets paired with 23 calibrators. After calibration, the modulation indices of all N_c calibrators (I refer to them here as 'target calibrators') in each of the 23 subsets are then calculated and averaged to obtain 23 values of the mean modulation index, m_c. Each of the 23 values of m_c include both the variability of the chosen calibrator for that subset *and* the variability of the other 'target calibrators' in that subset. Since the distribution of m_c is a convolution of the probability distribution function of the flux density variations of the chosen calibrator (with a modulation index given by m_i) with the distribution function of the variations of the other N_c 'target calibrators' (with a mean modulation index given by $\langle m_{tc} \rangle$), m_c is thus given by:

$$m_c = \sqrt{{m_i}^2 + \langle m_{tc} \rangle^2}. \tag{2.4}$$

If one assumes that the variability amplitudes of all the calibrators are roughly similar, then $m_c \approx \sqrt{2m_i^2}$, so that the modulation index of the chosen calibrator for each subset can be obtained as $m_i = m_c/\sqrt{2}$. Therefore, the 23 values of m_c after being reduced by a factor of $\sqrt{2}$ are representative of the variability of the 23 chosen calibrators, which are then used as p for all the target sources that have been calibrated by the same calibrator. There are now 23 sets of p values distributed among the 140 target sources, depending on which calibrator was applied to them, with values ranging from 0.0048 to 0.0057 (with a mean of 0.0051) at 8.4 GHz and 0.0053 to 0.0069 (with a mean of 0.0062) at 4.9 GHz.

Another advantage of this method is that any apparent variability due to residual system gain and pointing errors are also incorporated into p, since these 'target calibrators' are calibrated in the same manner as the actual target sources. However, since there is a larger angular distance from the chosen calibrator to most of the N_c 'target calibrators' as compared to the angular distances to the target sources associated with it, such residual calibration errors arising from the interpolation of the gain solutions between calibrator and target source are slightly overestimated, increasing the apparent value of p. A more accurate calculation would involve reducing the mean modulation indices further by a factor that accounts for the overestimated residual calibration errors, but this factor is difficult to parameterize. Further analyses with Hα, spectral index and redshift data using the various estimates of D_{noise} also demonstrates that any further efforts to improve the accuracy of D_{noise} are unlikely to lead to further improvements in the final results for the purposes of this study.

2.4.2.4 The Case for Selecting Method C

Plotting the histograms of $D_{obs}(2\text{hr}) - D_{noise}$ (Figure 2.6) for both the weak ($S_{4.9} < 0.3\text{Jy}$) and strong ($S_{4.9} > 0.3\text{Jy}$) sources shows distributions with peaks located close to zero at both frequencies. For a sample of non-variable sources, one would expect a Gaussian distribution with a peak at zero. The histograms show tails towards larger values of $D_{obs}(2\text{hr}) - D_{noise}$, caused either by the presence of ISS-induced variability at 2-hour time-scales, or an underestimation of the errors, particularly for the weak sources. In fact, significant variability is found in 30% of the sources at 2-hour time-scales. These sources have $D(2\,\text{hr}) > 2 \times 10^{-4}$ on at least one frequency, so that $D_{obs}(2\,\text{hr}) > 3\sigma$ above D_{noise} ($\approx 1 \times 10^{-4}$ on average at both frequencies).

I argue here that it is more likely that the presence of significant variability at 2-hour time-scales after the subtraction of D_{noise} estimated via Method C is due to ISS rather than underestimated errors. The plot of $D_{obs}(2\text{hr}) - D_{noise}$ at 4.9 GHz against $D_{obs}(2\text{hr}) - D_{noise}$ at 8.4 GHz (Figure 2.7) demonstrates a clear correlation between the variability amplitudes at both frequencies. I obtain a statistically significant Pearson's linear correlation coefficient of 0.63, with a probability of 5.5×10^{-8} that this occurred

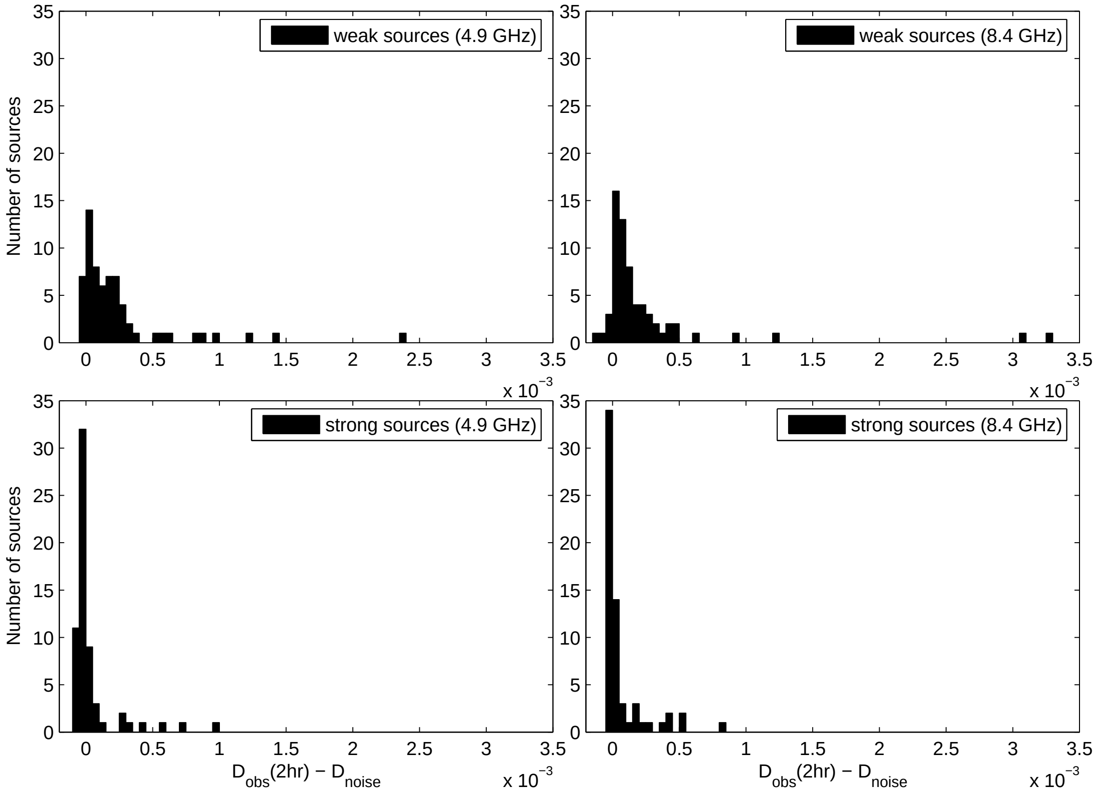

Figure 2.6 — *Histograms of* $D_{obs}(2\mathrm{hr}) - D_{noise}$ *for both weak* ($S_{4.9} < 0.3\mathrm{Jy}$) *and strong* ($S_{4.9} > 0.3\mathrm{Jy}$) *sources and at both frequencies.* D_{noise} *is estimated via Method C in Section 2.4.2.3.*

by chance (here and in all subsequent statistical tests, probabilities below 0.05 are considered statistically significant). Additionally, these sources also display strongly correlated variability patterns at both frequencies, based on an examination of the cross-correlation function at 0 time-lag (Figure 2.8), and a visual inspection of the lightcurves. Such correlations are unlikely to result from antenna-based or array-based errors as they were observed on two separate subarrays. While residual antenna gain errors can lead to correlated variability amplitudes and patterns, since the elevations of all antennas are roughly similar at any point in time, an underestimation of these errors would result in more significant variability in the stronger sources rather than in the weaker sources at 2 hour time-scales. Neither are these variations likely to be confusion, since the subarrays each have a different uv-coverage arising from dissimilar primary beams and synthesized beams at the two observing frequencies. On the other hand, flux variations due to weak ISS are expected to be correlated across a wide bandwidth (Narayan, 1992). The larger fractions of sources displaying significant 2-hour variability at 4.9 GHz and in the weak sample of sources is consistent with a population of brightness temperature-limited sources whose variability is dominated by weak ISS (Lovell et al., 2008). No similar variations are observed in sources close to each other, ruling out atmospheric effects. None of the sources were located at low solar elongations during the observations, so interplanetary scintillation is also negligible. The errors would therefore have been overestimated for these sources with $D_{obs}(2\mathrm{hr}) - D_{noise} > 0$ had Method A been used.

As a further comparison between Method C with Method B, Figure 2.9 shows the scatter plot of s vs p estimated through Method C, with the dashed lines showing the values of s and p estimated via Method B. As expected, with the exception of a few outliers, s is lower at 8.4 GHz than at 4.9 GHz. It appears that s is generally overestimated when Method B is used. This is most likely due to the fact that s in Method B is determined by the 2-hour modulation indices of the weak sources, which are known to scintillate more than the strong sources (Lovell et al., 2008). On the other hand, p is clearly underestimated in Method B as it does not account for low-level calibrator variability and residual calibration errors that have variability time-scales longer than 2 hours. The value of p appears to be larger at 4.9 GHz than at 8.4 GHz, whereas one would expect residual pointing errors and antenna-based gain related errors to be generally smaller at longer wavelengths. This can be explained by the removal of data from 2 antennas in the 8.4 GHz subarray in which the pointing errors appeared the worst, as mentioned briefly in Section 2.3. The removal of these antennas resulted in a negligible increase in s. I also attempted to remove data from 2 antennas in the 4.9 GHz subarray in an attempt to reduce p, but resulted in a similar magnitude increase in s (recall that the 4.9 GHz observations were conducted at half the bandwidth of the 8.4 GHz observations). Data from all antennas in the 4.9 GHz

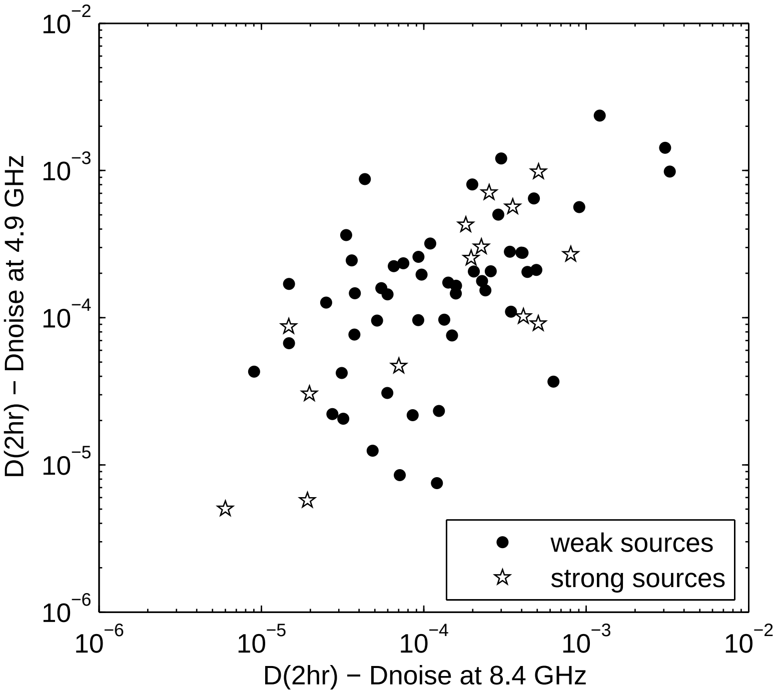

Figure 2.7 — *Scatter plot showing the correlation between* $D_{obs}(2\mathrm{hr}) - D_{noise}$ *at 4.9 GHz and* $D_{obs}(2\mathrm{hr}) - D_{noise}$ *at 8.4 GHz (for sources where the quantities are positive at both frequencies) based on the error estimation in Method C (Section 2.4.2.3).*

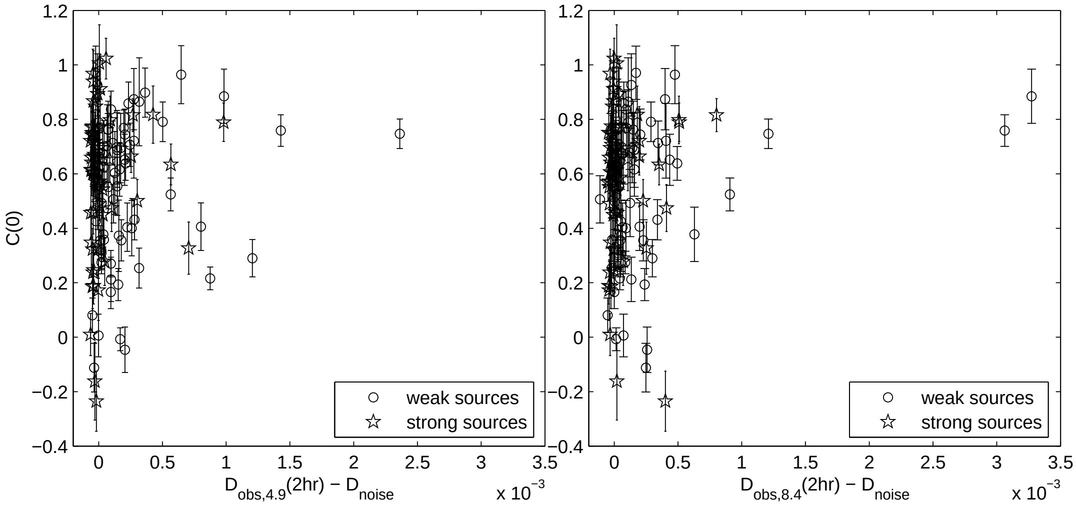

Figure 2.8 — *Cross-correlation of the lightcurves at 4.9 GHz (left panel) and 8.4 GHz (right panel) plotted against* $D_{obs}(2\mathrm{hr}) - D_{noise}$.

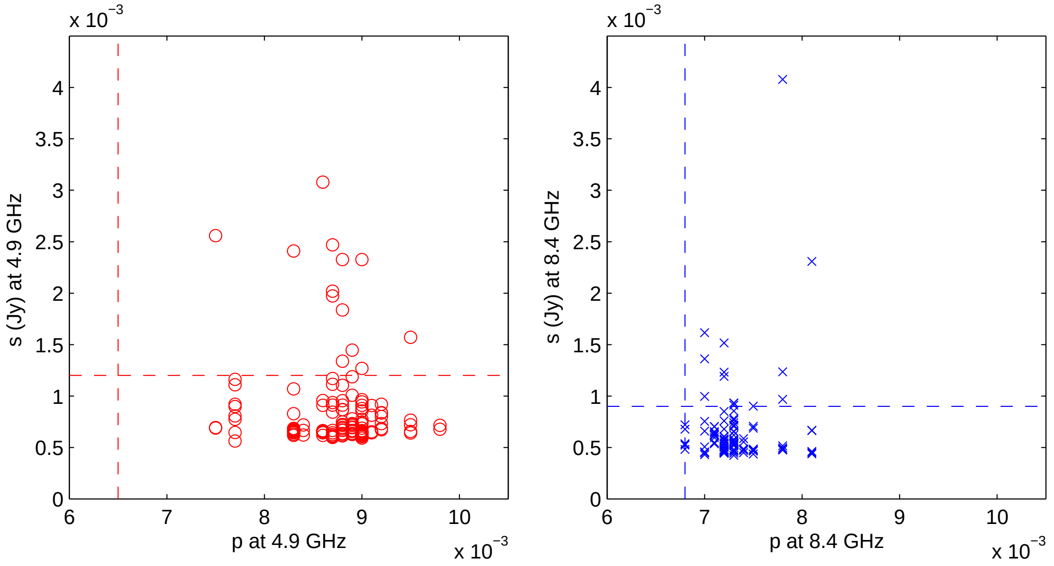

Figure 2.9 — *Scatter plot of s against p at 4.9 GHz (left) and 8.4 GHz (right) based on the error estimation in Method C (Section 2.4.2.3). The dashed lines represent estimated values of s and p from Method B (Section 2.4.2.2).*

subarray were therefore retained.

Figure 2.10 demonstrates the effectiveness of the error estimation and correction described in Method C; it shows a source with very low variability. Daily repeating patterns are observed at both frequencies, particularly between 2 to 6 sidereal days. Their effect on the SF is modelled successfully by D_{noise} as can be seen in the corresponding SF plots. At 8.4 GHz, $D_{obs}(\tau)$ is distributed around D_{noise} (shown as a dash-dot line), while for 4.9 GHz, $D_{obs}(\tau)$ is close to D_{noise} (shown as a dotted line) for time-lags up to about 3 days before rising to double the value of D_{noise}. Although the SF amplitudes at 4.9 GHz are not high, the daily repeating patterns are superposed on top of longer term variations, which are not visible in the 8.4 GHz lightcurves.

2.4.2.5 Sources with Uncharacterised Errors

Finally, a total of 12 sources are eventually removed from the present sample; J1535+6953 had a very low mean flux density ($\approx$ 30 mJy) in the current 2009 epoch, and upon further investigation, I find that its mean flux density had been steadily decreasing from 75 mJy in the first MASIV epoch to 60 mJy in the fourth MASIV epoch; the other 11 sources are found to have daily repeating patterns that vary with SF amplitudes exceeding 3×10^{-4}, possibly due to real confusion and resolution effects that are not detectable in the snapshot images and uv-data. In the latter group, their errors are not well-characterised by the method of error estimation described above,

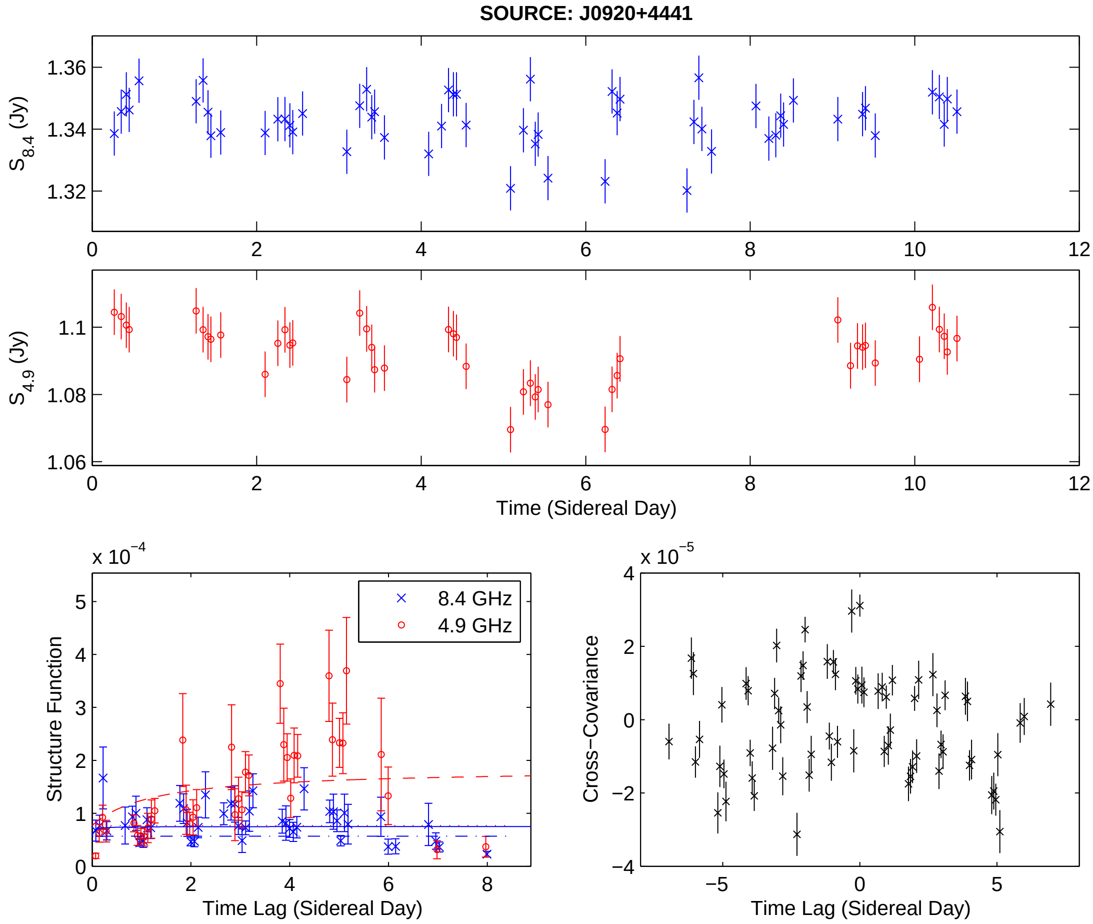

Figure 2.10 — *8.4 GHz (top) and 4.9 GHz (middle) lightcurves, structure functions calculated from Equation 2.2 (bottom left, where the solid curve and dashed curve represent the model fits at 8.4 GHz and 4.9 GHz respectively, the dash-dot line represents* D_{noise} *at 4.9 GHz and the dotted line represents* D_{noise} *at 8.4 GHz) and cross-covariance function calculated from Equation 3.1 (bottom right) for the source J0920+4441, as a demonstration of the error estimation and correction used.*

and cannot be removed by any other means.

2.4.3 Structure Function Fitting

Assuming that variability due to ISS approaches a stationary stochastic process when observed over a duration much longer than its characteristic time-scale, it is expected that the true SF, $D(\tau)$, will increase with time-lag and saturate at twice the true variance. Therefore, a simple model can be used to fit the observed SFs, given by:

$$D_{mod}(\tau) = D_{sat}\frac{\tau}{\tau + \tau_{char}} + D_{noise}, \tag{2.5}$$

where D_{sat} is the value at which the SF saturates, and is linked to the modulation index of the source through the relation $D_{sat} = 2m^2$. The characteristic time-scale, τ_{char}, is defined as the time-scale at which the SF reaches half of its value at saturation. D_{sat} and τ_{char} are both free parameters of the model. This is similar to the model used in the original MASIV data analyses, and assumes that the ISS is caused by a turbulent ISM distributed uniformly through a thick scattering region. Further details on the justification for its use can be found in Appendix A of Lovell et al. (2008). The model also assumes that variations due to systematic and instrumental errors contribute an additive term, D_{noise}, to the overall variability. D_{noise} is determined for each source using Method C explained in Section 2.4.2.3. The true SF, $D(\tau)$ can thus be obtained by subtracting D_{noise} from the model SF, $D_{mod}(\tau)$.

In fitting the model, each $D_{obs}(\tau)$ is weighted by $\sqrt{\langle D_{obs}(\tau)\rangle / \sigma_D(\tau)}$, where $\sigma_D(\tau)$ is the error of the SF estimate at that particular time-lag. The result is that these values of $D_{obs}(\tau)$ with smaller errors will have larger weights. If the estimation of the errors are accurate, the weights should be proportional to $1/\sigma_D(\tau)$. Due to uncertainties in the estimation of the SF errors, $1/\sqrt{\sigma_D(\tau)}$ is used instead. The weights are further normalized by $\langle D_{obs}(\tau)\rangle$, which is the ensemble average of all the SF estimates for the source at all timelag bins whose number of pairs of flux densities are above the threshold value (see Section 2.4). The fit is carried out using a non-linear least squares method.

Sample SFs are shown together with their corresponding model fits (represented by the solid curve and dashed curve for 8.4 GHz and 4.9 GHz respectively) in the bottom left corners of Figures 2.1 to 2.4. The dash-dot and dotted lines represent the D_{noise} values for 8.4 GHz and 4.9 GHz respectively. The SF for a fast scintillator such as J1159+2914 (Figure 2.1) reaches saturation on a time-scale of a couple of hours. Some sources such as J0958+6533 (Figure 2.3), however, have yet to saturate even at time-lags of 8 days. Some SFs have a periodic trend, caused by the lightcurves having periodic structures (as can be seen for J0510+1800 in Figure 2.2) within the limited timespan of the observations. If the timespan of the observations were to be increased, the fluctuations would become randomized and $D_{obs}(\tau)$ should approach that of $D_{mod}(\tau)$, demonstrating the deficiencies in the estimation of the error bars.

For the purpose of statistical analyses in the following subsections, unless otherwise stated, the SF amplitudes at 4 days are used, obtained from the model fit with D_{noise} subtracted, given by $D(4\text{d}) = D_{mod}(4\text{d}) - D_{noise}$. Instead of using Equation 2.5, I use an equivalent functional form:

$$D_{mod}(\tau) = D(4\text{d})\frac{1 + \tau_{char}/4}{1 + \tau_{char}/\tau} + D_{noise}, \tag{2.6}$$

so that $D(4\text{d})$ becomes a fitted parameter instead of $2m^2$. This way, the 95% confidence bounds of $D(4\text{d})$ from fitting the model can be obtained directly, which is used as an estimate of the errors in $D(4\text{d})$. As opposed to using the observed single time-lag estimates, $D_{obs}(4\text{d})$, the model fits provide better statistical representation, since they make use of the SF amplitudes at all available time-lags. The SF amplitudes at 4 days are chosen as standard characterization of source variability to ensure that a large majority of the SFs have reached saturation, and that there are still sufficient number of pairs at the nearby bins to provide reliable SF fits. While choosing $D(10\text{d})$ or $D(11\text{d})$ as standard characterisation of the variability will maximize the number of sources with saturated SFs, the fitted curve may not be as reliable at those time-lags.

$D(4\text{d})$ and τ_{char} at both frequencies are presented for each source in Appendix B. While the 11 day observations provide better constraints on τ_{char}, its errors are still very difficult to estimate. Therefore the values of τ_{char} for a source at a particular frequency are shown only if $D(4\text{d})$ exceeds $2 \times D_{noise}$ (equivalent to 3σ above D_{noise}), as sources with barely detectable variability tend to be dominated by sytematic errors and noise so that estimates of τ_{char} may be inaccurate. The values of τ_{char} also cannot be estimated for sources in which the SFs do not show signs of saturating, and I simply note in Appendix B that these sources have $\tau_{char} > 11$ days.

2.5 Chapter Summary: Lessons for Future Variability Surveys

In this chapter, I presented a detailed description of the dual-frequency MASIV follow-up observations, data reduction process, as well as variability and error characterisation methods used in preparation for the actual data analysis. A sub-sample of 140 flat-spectrum sources drawn from the original MASIV Survey were observed simultaneously at 4.9 GHz and 8.4 GHz over a duration of 11 days using the VLA. I used the structure function as a standard characterization of the source variability amplitudes at various time-lags. I then fitted a simple model, $D_{mod}(\tau)$, to the observed structure function, $D_{obs}(\tau)$, of each source, which assumes that ISS approaches a stationary stochastic process when observed over a duration much longer than its characteristic time-scale. The properties of any variability caused by instrumental and systematic errors were assumed to be white, contributing an additive noise, D_{noise} across all time-lags. I estimated D_{noise} as a quadratic sum of the flux independent errors i.e. system noise and confusion, and the flux dependent calibration errors, which are then subtracted from $D_{mod}(\tau)$ across all time-lags to obtain the 'true' variability, $D(\tau)$. Twelve sources were removed from the sample due to large errors that were not well quantified by my estimation of D_{noise}. I then used $D(\tau)$ at a time-lag of 4 days, $D(4\mathrm{d})$, for all subsequent analyses as a standard characterization of source variability amplitudes.

Many lessons have been learned through the entire process, some of which may be relevant for future large-scale surveys of the variable sky. They are summarised as follows:

1. Scheduling the observations in sidereal time is a good strategy for discriminating flux variations due to many forms of systematic errors from real astrophysical variability. Confusing sources in the background, resolved sources, as well as residual antenna gain and pointing errors produce patterns that repeat each sidereal day. Where variability surveys are conducted in commensal-mode, as a piggy-back on other long-term surveys, examining the variability of sources at time-lags of multiples of a sidereal day provide a quick way of negating all these systematic effects.

2. The flagging of RFI and spurious data were carried out manually for this study. Future surveys, with datasets orders of magnitude larger than that of the present survey, will require this time-consuming process to be automated.

3. The error bars for the structure functions calculated from the observed lightcurves did not include statistical errors, which increase as the source variability time-scales increase relative to the observing span. One way of achieving this is by bootstrapping the process, e.g. making an initial fit to the observed SFs to obtain an estimate of the variability timescales, then modifying the errors accordingly by increasing the errors in proportion to the ratio of the characteristic times-scales to the observing span, before fitting a model to the SFs again weighted by the new errors.

4. Separating the weak and strong sources and comparing their variability amplitudes at both frequencies at the shortest possible time-scales provided a very effective method of discriminating between the different types of instrumental and systematic errors.

5. The sensitivity of the VLA and careful calibration enabled noise and systematic errors to be reduced down to a level of $\lesssim 1\%$ of the mean flux density in this survey. For weak sources where gain-independent errors dominate, the level of astrophysical variability detectable by future telescopes will be limited by the

telescope sensitivity. Although a higher sensitivity instrument improves the signal to noise ratio, the likelihood of confusion by background sources will also increase. For the strong sources where gain-dependent errors dominate, the lower limit of detectable variability will be determined by the performance of the new calibration techniques being developed, the accuracy at which the calibrators can be modelled, as well as the selection of calibrators and scheduling of calibrator observations.

6. Method C successfully accounted for the stochastic and systematic errors in the variability amplitudes. However, Method B is sufficient for estimating errors in time-critical applications or when the variability levels studied are much larger than the $\lesssim 1 \times 10^{-3}$ level differences in the estimation of D_{noise} between Methods B and C.

7. Significant variability was detected in $\sim 30\%$ of the sources at 2-hour timescales, mostly from the weak sample of sources, with a strong case for these variations to be attributed to ISS. Future wide-field surveys with more sensitive telescopes will need to account for this background variability caused by confusing sources.

Chapter 3

Influence of Galactic and Source Intrinsic Properties on ISS

> *Twinkle, twinkle quasi-star*
> *Biggest puzzle from afar*
> *How unlike the other ones*
> *Brighter than a billion suns.*
> *Twinkle, twinkle quasi-star*
> *How I wonder what you are.*
> — ***George Gamow, Quasar***

Together with the contents of Chapter 2, a significant portion of this chapter has been published in *The Astronomical Journal*, as an article entitled 'Dual-frequency Observations of 140 Compact, Flat-spectrum Active Galactic Nuclei for Scintillation-Induced Variability' (Koay et al., 2011a).

3.1 Introduction

This chapter explores how source intrinsic and extrinsic factors both affect the variability, or more specifically the ISS, of AGNs. While the MASIV Survey was highly sucessful in answering some of these questions, and contains more sources in its sample, the multi-frequency data and longer span of the present follow-up observations provide further insight unachievable with the MASIV dataset.

In Section 3.2, I examine the Galactic dependence of IDV in the source sample, providing strong evidence that it is dominated by ISS. I then investigate in Section 3.3 the dependence of ISS on observing frequency, demonstrating how the cross-covariance of source lightcurves across two frequencies can be used to probe angular offsets of AGN cores arising from opacity effects. This is followed by an investigation of the dependence of ISS on source intrinsic properties including the spectral indices (Section 3.4) and mean flux densities (Section 3.5). The redshift dependence of ISS is briefly discussed in Section 3.6; the full analysis and interpretation of this effect merits its own chapter, so is deferred to Chapter 5. Section 3.7 comments on the variability of selected sources that were found to be interesting. Section 3.8 summarises the main findings of this chapter. The properties of the sources in the sample, including their mean flux densities, spectral indices, and redshifts, are listed in Appendix C.

3.2 Interpretation of Variability as Interstellar Scintillation

I begin the analysis of the MASIV follow-up observations by investigating whether the variations observed in the AGN sources are a result of ISS. Since the observations were carried out over a period of 11 days as compared to the 3 or 4 day observations in the original MASIV survey, it is important to determine if the source variability at longer time-scales can still be attributed to ISS rather than being intrinsic variations. To do so, I obtain the line-of-sight Hα intensities to each of the sources from the corresponding 1° grid in the Wisconsin Hα Mapper (WHAM) Northern Sky Survey database (Haffner et al., 2003). The Hα intensities, which I denote as I_α and is given in units of Rayleighs (R, where $1\text{R} = 10^6/4\pi$ photons $\text{cm}^{-2}\ \text{s}^{-1}\ \text{sr}^{-1}$ at Hα), provide estimates of the integral of the square of the line-of-sight Galactic electron column densities to all the sources. I_α is therefore a proxy for the amount of potential Galactic scattering material towards each source.

The scatter plots and binned plots in Figure 3.1 show a correlation between $D(4\text{d})$ and I_α at both frequencies. For the scatter plots, sources whose $D(4\text{d})$ are found to be less than D_{noise} have D_{noise} as an upper limit of their variability amplitudes (denoted as triangles in the scatter plots). The bottom panels of Figure 3.1 show the mean $D(4\text{d})$ in 4 separate bins. In obtaining the mean $D(4\text{d})$ values for each bin, the upper limits are used for sources whose $D(4\text{d})$ are found to be less than D_{noise}. While the plots shown here make use of the data from the entire 11 day duration of the observations, the correlation holds true even when only data from the first 6 days were used.

The non-parametric Kendall's tau test confirms statistically significant correlations between $D(4\text{d})$ and Hα intensities at both frequencies, with probabilities of 1.2×10^{-4} and 3.0×10^{-3} at 8.4 GHz and 4.9 GHz respectively, that they were obtained by chance. Here and in all subsequent analyses, I have chosen the standard significance level of 0.05. While statistically significant, the correlation is rather weak, with rank correlation coefficients of only 0.23 at 8.4 GHz and 0.18 at 4.9 GHz. This is not surprising, as ISS is dependent not only on the amount of scattering material in the sight-lines to the sources, but on their levels of turbulence and the angular sizes of the sources as well.

As a further test, the single sample estimates of the observed SF, $D_{obs}(\tau)$, with

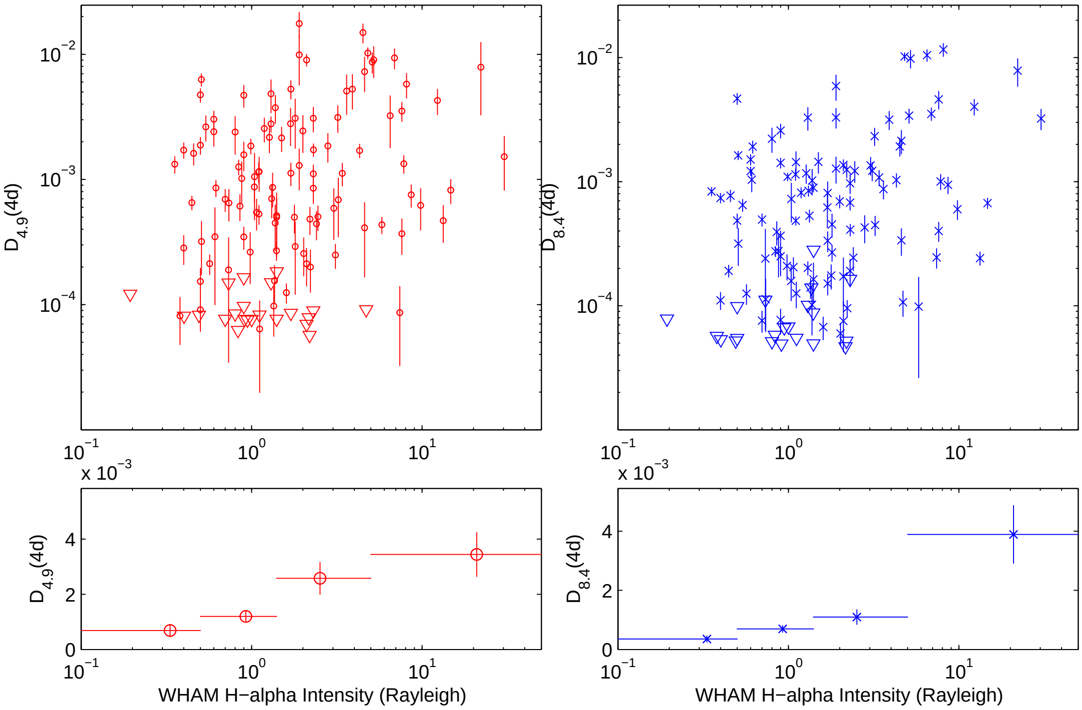

Figure 3.1 — *Scatter plot of* $D(\mathrm{4d})$ *at 4.9 GHz (top left) and 8.4 GHz (top right) plotted against WHAM* $H\alpha$ *intensities. The triangles represent upper limits of* $D(\mathrm{4d})$ *for sources where* $D(\mathrm{4d}) < D_{noise}$*. Corresponding binned averages of* $D(\mathrm{4d})$ *are also shown for 4.9 GHz (bottom left) and 8.4 GHz (bottom right).*

D_{noise} subtracted and $\tau = 1, 2, 3 \ldots 7$ days, are each used in succession to plot against the WHAM Hα intensities. The significant correlation of the SFs with Hα intensity is retained for all time-lags when data from all 11 days are used. Similar results are obtained for τ = 1,2,3 and 4 days when data from only the first 6 days of observations are used.

It can thus be reasonably concluded that the observed flux density variations in this study, including those at longer time-scales of up to 7 days, are predominantly caused by ISS. Intrinsic variability in the sources and instrumental errors simply cannot explain the observed Galactic dependence of the source variability amplitudes.

3.3 ISS Across Two Frequencies

According to the theory of ISS, weak scintillation should be correlated over a wide bandwidth, with a decorrelation bandwidth on the order of the observing frequency (Narayan, 1992). Although the 4.9 GHz observations are near the transition between weak and strong scintillation at mid-Galactic latitudes (Walker, 1998, 2001), some form of correlation is still expected to exist between the variability at 4.9 GHz and 8.4 GHz.

In Figure 3.2, $D_{4.9}$(4d) is plotted against $D_{8.4}$(4d) on a log scale for sources with $D(\text{4d}) > D_{noise}$ at both frequencies, showing that the source variability amplitudes are well-correlated between both frequencies. In $\sim$ 65% of the sources, $D_{4.9}$(4d) is larger than $D_{8.4}$(4d), consistent with weak ISS. In $\sim$ 35% of the sources, $D_{8.4}$(4d) is comparable to or larger than $D_{4.9}$(4d), which can be attributed to strong ISS or increased scatter broadening of the sources at 4.9 GHz relative to that at 8.4 GHz, thereby reducing $D_{4.9}$(4d) relative to $D_{8.4}$(4d). These effects are important in the discussion of the redshift dependence of ISS, and are discussed more thoroughly in Chapter 5.

While correlation of the variability patterns between the lightcurves at both frequencies can be clearly discerned by eye for some sources, the cross-covariance function provides a more quantitative means of detecting such a correlation, obtained as:

$$C(\tau) = \frac{1}{N_\tau} \sum_{j,k} [S_{4.9}(t_j) - \mu_{S_{4.9}}][S_{8.4}(t_k - \tau) - \mu_{S_{8.4}}], \tag{3.1}$$

where $S_{4.9}$ and $S_{8.4}$ are the normalized flux densities at 4.9 GHz and 8.4 GHz respectively, and N_τ is the number of pairs of flux densities with a time-lag of τ. $\mu_{S_{4.9}}$ and $\mu_{S_{8.4}}$ are the average values of $S_{4.9}$ and $S_{8.4}$ over the entire observation span. As in the calculation of the discrete SF in Equation 2.4.1.1 (see Section 2.4.1), time-lag bins at integer multiples of the smallest time-lag between data points are used, with time-lag bins selected for plotting only if the number of pairs in the bin exceeds 20% of the total number of points in the lightcurve.

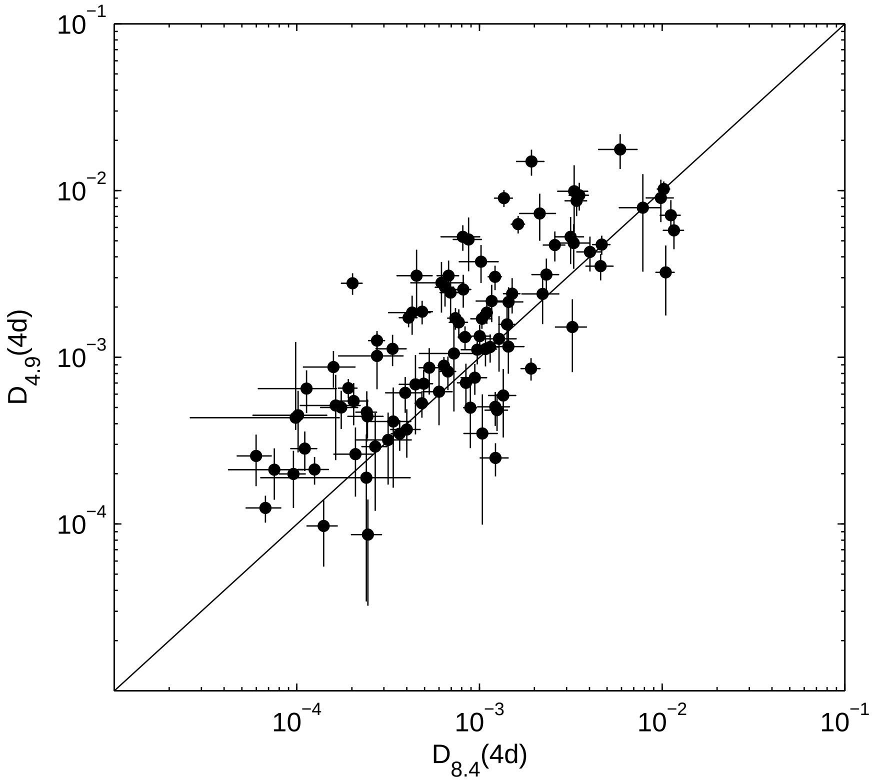

Figure 3.2 — $D_{4.9}$(4d) *vs* $D_{8.4}$(4d). *The solid line represents* $D_{4.9}(4\mathrm{d}) = D_{8.4}(4\mathrm{d})$ *as a demonstration of the correlation of the SFs at both frequencies and that* $D_{4.9}$(4d) *is generally larger than* $D_{8.4}$(4d).

The cross-covariance functions between the lightcurves at both frequencies are shown together with their associated lightcurves in the bottom right corners of Figures 2.1 to 2.4. For the majority of the variable sources, the cross-covariance peaks at time-lags of 0.00 ± 0.04 days. About 20% of the sources in the sample do not show any evidence of correlation in the lightcurves or have a very weak correlation (the cross-covariance function peaks at an amplitude $< 1 \times 10^{-4}$). In such cases, the variability also tends to be very weak, with very low SF values. It can be concluded that the variations seen in these lightcurves are most likely attributable to noise. Another possible explanation is that there is an offset in the positions of the source cores at the two frequencies, but these offsets are perpendicular to the direction of the relative motion between the interstellar scattering screen and the Earth, which weakens the correlation. The lightcurves may also be weakly correlated in cases where the variations are due to strong refractive scintillation where the variability timescales can be different at both frequencies.

The sources that show time delays in scintillation patterns at the two frequencies are of particular interest. This is discernible by a shift of the peak of the cross-covariance function towards a non-zero time-lag. Such a delay in the lightcurves between observing frequencies has been previously observed, and has been interpreted as being caused by a small shift in the position of the optically thick compact core when observed at different frequencies (Bignall et al., 2003). Such core shifts have been observed on mas scales in VLBI images of extragalactic radio sources at different frequencies (Kovalev et al., 2008; Tzioumis et al., 2010). A list of sources in which the cross-covariance function of the lightcurves at 4.9 and 8.4 GHz peaks at a non-zero time-lag is shown in Table 3.1. For this list, only sources with $D(4\mathrm{d}) > 2 \times 10^{-4}$ (equivalent to $> 3\sigma$ above D_{noise}) at both frequencies and whose cross-covariance peaks at time-lags greater than twice the size of the smallest time-lag bin were selected. A negative time-lag indicates that the 8.4 GHz scintillation pattern is lagging behind the 4.9 GHz scintillation pattern. While it is possible that intrinsic variability of the sources will also lead to lower frequency lightcurves lagging behind higher frequency lightcurves, due to the propagation of components along the optically thick jet, sources with negative time-lags are free from this concern.

Taking the source J0510+1800 (Figure 2.2) as an example, there appears to be a time delay, Δt of about 0.24 ± 0.04 days between the 4.9 GHz and 8.4 GHz variability patterns. Assuming typical scattering screen distances of $L = 500$ pc and screen velocities of $v = 50\ \mathrm{kms}^{-1}$, it is estimated that there is an angular separation of approximately $14 \pm 2\mu$as between the position of the cores at 4.8 and 8.4 GHz (the component parallel to the direction of screen velocity). The angular separation of the cores for the

Table 3.1. Sources whose lightcurves have non-zero timelags.

Source Name	Timelag (Days)
J0017+5312	-0.43 ± 0.05
J0154+4743	2.02 ± 0.06
J0308+1208	0.79 ± 0.04
J0342+3859	0.95 ± 0.04
J0409+1217	-1.08 ± 0.04
J0449+1121	2.89 ± 0.03
J0510+1800	0.24 ± 0.04
J0659+0813	0.24 ± 0.03
J0726+6125	-0.32 ± 0.04
J0741+2557	-0.16 ± 0.04
J0750+1231	0.80 ± 0.03
J0757+0956	1.05 ± 0.03
J0825+0309	0.21 ± 0.03
J1410+6141	-0.40 ± 0.04
J1417+3818	1.59 ± 0.04
J1535+6953	0.42 ± 0.05
J1701+0338	0.21 ± 0.03
J1734+3857	0.19 ± 0.03
J1800+3848	2.04 ± 0.04
J1905+1943	-0.26 ± 0.03
J1919+3159	-1.32 ± 0.02
J2012+6319	-0.37 ± 0.05
J2113+1121	1.20 ± 0.04
J2237+4216	0.31 ± 0.04
J2253+3236	1.91 ± 0.04

Note. — A negative time-lag indicates that the 8.4 GHz lightcurve lags behind the 4.9 GHz lightcurve, while a positive time-lag indicates that the 8.4 GHz lightcurve leads the 4.9 GHz lightcurve.

remaining sources in Table 3.1 can be calculated using the following:

$$\theta = 14 \left(\frac{\Delta t}{0.24\mathrm{days}}\right) \left(\frac{v}{50\mathrm{kms}^{-1}}\right) \left(\frac{L}{500\mathrm{pc}}\right)^{-1} \mu\mathrm{as}, \tag{3.2}$$

where the parameters of the scattering screen are normalized by their typical values, and Δt is obtained from the observations.

VLBI measurements of core shifts of extragalactic radio sources between frequencies of 2.3 and 8.6 GHz by Kovalev et al. (2008) have yielded angular separations ranging from 0.1 to 1.4 mas. In an ideal scenario, observations of source scintillation at 2-hour intervals (thus providing a minimum observable time-lag of 2 hours), enable core shifts to be probed down to about 5 μas, well beyond the capabilities of current VLBI. In practice, however, such observations are hampered by the dominance of systematic errors at these small time-lags. Using such small bin sizes for the time-lags in cross-covariance function analysis leads to large statistical errors. Conversely, using larger time-lag bins reduces the time-resolution that such a technique can probe. The fact that interstellar scattering in itself leads to shifts in apparent source positions adds to the complexity of the problem.

3.4 Dependence of ISS on Source Spectral Indices

In the MASIV survey, the SF amplitudes showed only a very weak trend with respect to the estimated source spectral indices (Lovell et al., 2008). A significant limiting factor in the MASIV analysis was that the flux density data used in the estimation of the spectral indices — the 1.4 GHz NVSS data (Condon et al., 1998), the 8.4 GHz Jodrell-Bank/VLA Astrometric Survey (JVAS) data (Patnaik et al., 1992; Browne et al., 1998; Wilkinson et al., 1998) and the Cosmic Lens All-Sky Survey (CLASS) data (Myers et al., 1995) — were non-simultaneous at different frequencies, and were thus affected by changes in source properties. Also, being highly compact and intrinsically variable, the sources could have undergone changes to their structure and other intrinsic properties in the time between the observations through which the spectral indices were derived and the four epochs of the MASIV survey.

The dual frequency observations in this present study enable the spectral index of each source to be estimated, bearing in mind the limitation of having the spectral indices determined by only two frequency measurements of the flux densities, which are also modulated by significant ISS. Figure 3.3 shows $D(4\mathrm{d})$ at both frequencies plotted against the source spectral indices calculated from the mean flux densities at both frequencies. The convention used here to define the spectral index, α, is $S \propto \nu^{\alpha}$. It is interesting to note that while only nominally ‘flat-spectrum’ sources with $\alpha_{1.4}^{8.4} > -0.3$ were selected for the MASIV Survey, based on the aforementioned less reliable estimations of the spectral indices, the scatter plots reveal that some of

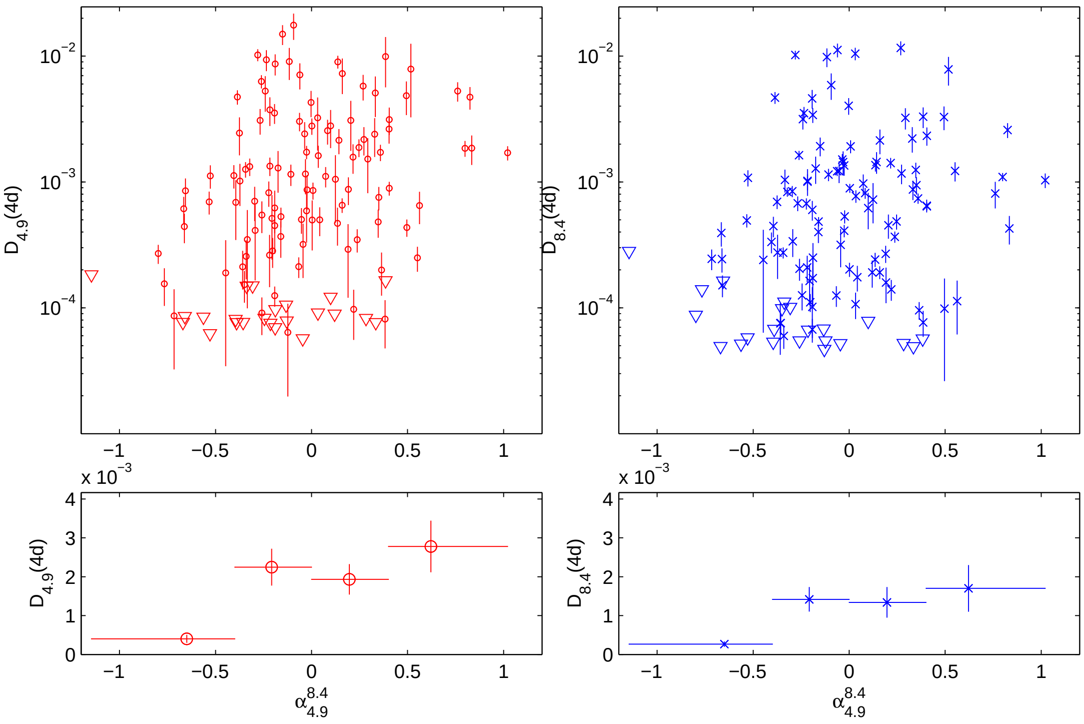

Figure 3.3 — $D_{4.9}$(4d) *(scatter plot at top left and binned plots at bottom left) and* $D_{8.4}$(4d) *(scatter plot at top right and binned plots at bottom right) plotted against source spectral index* ($\alpha_{4.9}^{8.4}$)*. The triangles represent upper limits of* D(4d) *for sources where* $D(4\text{d}) < D_{noise}$.

the sources have spectral indices of $\alpha_{4.9}^{8.4} < -0.4$, attesting to the variable nature of the sources. Furthermore, calculating the apparent spectral indices using each individual data point on the lightcurves of each source at both frequencies shows that the spectral indices vary even within the 11 day time-span of the observations, with a standard deviation of up to 0.13 from the mean spectral index (0.04 on average for all the sources).

While the binned plots show no clear trends for sources with $\alpha_{4.9}^{8.4} > -0.4$ at both frequencies, with only a marginal increase in the mean spectral index above $\alpha_{4.9}^{8.4} > 0.4$, there is a clear reduction of scintillation amplitudes for sources with $\alpha_{4.9}^{8.4} < -0.4$. The non-parametric Kendall's tau test gives correlation coefficients of 0.20 at 4.9 GHz and 0.19 at 8.4 GHz, with probabilities of 9.0×10^{-4} and 1.8×10^{-3} respectively that they were obtained by chance, showing that the correlations are statistically significant. However, when performing the same test using only sources with $\alpha_{4.9}^{8.4} > -0.4$, the correlation coefficient drops to 0.13 and only has a marginal statistical significance (with a probability of 0.05 that the correlation was obtained by chance). Again, these trends are also observed when data from only the first 6 days of observations are used.

It is well known that scintillating sources tend to have flat or inverted spectra, and that steep-spectrum sources do not scintillate (Heeschen, 1984). In standard AGN lore, the explanation is that flat-spectrum sources are dominated by very high-brightness temperature, optically thick, synchrotron self-absorbed components, thus most of their flux densities are confined to ultra-compact, μas scale cores. On the other hand, the steep-spectrum sources are dominated by optically thin, compact mas components that have lower brightness temperatures.

It has to be noted, however, that the $\alpha_{4.9}^{8.4} < -0.4$ sources in the present sample are compact, core-dominated sources, unlike the classical steep-spectrum sources reported by Heeschen (1984) which are dominated by their extended emission. The $\alpha_{4.9}^{8.4} < -0.4$ sources do scintillate, but their scintillation amplitudes are highly suppressed relative to that of the $\alpha_{4.9}^{8.4} > -0.4$ sources, due to the presence of very compact mas-scale components which reduces their compact fractions.

3.5 Dependence of ISS on Source Flux Densities

The observations confirm one of the main results from the MASIV Survey, that the ISS amplitudes of the sources decrease with the mean flux densities of the sources (see Figure 3.4). Kendall's tau tests find statistically significant inverse correlations between $D_{4.9}$(4d) and $S_{4.9}$ (with correlation coefficient of -0.28), as well as between $D_{8.4}$(4d) and $S_{4.9}$ (with correlation coefficient of -0.22), with probabilities of 2.2×10^{-6} and 3.0×10^{-4} respectively that they occurred by chance.

There are two possible explanations for this effect. The first is that the sources are brightness-temperature limited, so that the angular sizes of the sources increase with increasing mean flux densities (see Equation 1.4). The second is that the stronger, higher flux density sources have larger and brighter mas-scale components that reduce their compact fractions, thereby diminishing their variability. VLBI observations of a sub-sample of the MASIV sources provide evidence against the latter, finding no significant differences in the mas-scale morphologies of the weak flux density and strong flux density sources (Ojha et al., 2004b).

3.6 Dependence of ISS on Source Redshifts

Figure 3.5 shows a decrease in D(4d) with redshift at both frequencies, confirming the result of the MASIV survey. Kendall's tau rank correlation coefficients are calculated to be -0.34 at 8.4 GHz and -0.33 at 4.9 GHz with probabilities of 1.2×10^{-8} and 2.2×10^{-8} that they were obtained by chance.

There also appears to be a frequency dependence in the scaling of the mean D(4d)

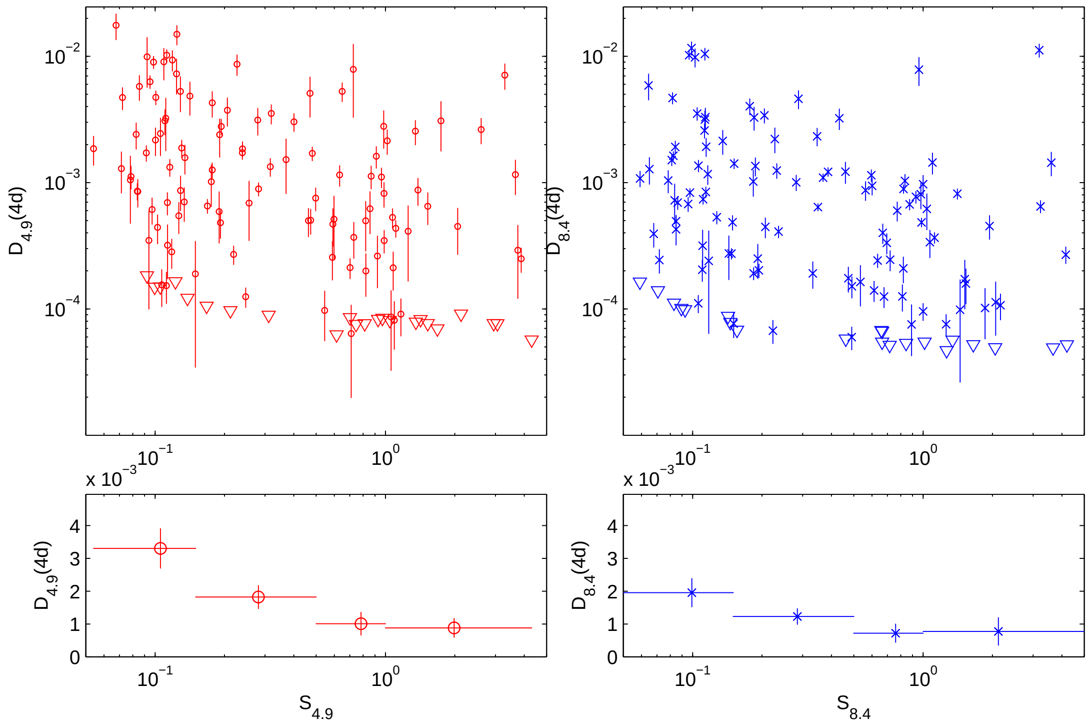

Figure 3.4 — $D_{4.9}$(4d) *(scatter plot at top left and binned plots at bottom left) and* $D_{8.4}$(4d) *(scatter plot at top right and binned plots at bottom right) plotted against corresponding mean flux density. The triangles represent upper limits of* D(4d) *for sources where* $D(4\mathrm{d}) < D_{noise}$.

with redshift. This can be seen in the binned plots in Figure 3.5, and in Figure 3.6 where the sources are grouped into just two redshift bins. The mean $D_{4.9}$(4d) at $z > 2$ is about a factor of 3 lower than its $z < 2$ counterpart. On the other hand, the mean value of $D_{8.4}$(4d) drops only by about a factor of 1.8 from low to high redshift. As the mean values of D(4d) at $z > 2$ for both frequencies are an order of magnitude larger than the lower limit of measureable variability, we know that this effect is not a result of the mean SFs at both frequencies hitting the noise floor. The two-sample Kolmogorov-Smirnov (K-S) test rejects the null hypothesis that the distributions of $D_{4.9}$(4d) and $D_{8.4}$(4d) at $z < 2$ are drawn from the same parent population, with a probability of 0.01 that this occured by chance. However, at $z > 2$, the K-S test no longer gives a statistically significant rejection of the same null hypothesis. While this in no way proves that the distributions of $D_{4.9}$(4d) and the $D_{8.4}$(4d) are similar at high redshift, it is still an interesting result.

This weaker redshift dependence of the mean $D_{8.4}$(4d) appears to support IGM scatter broadening as the cause of the drop in the mean $D_{4.9}$(4d) at high redshift.

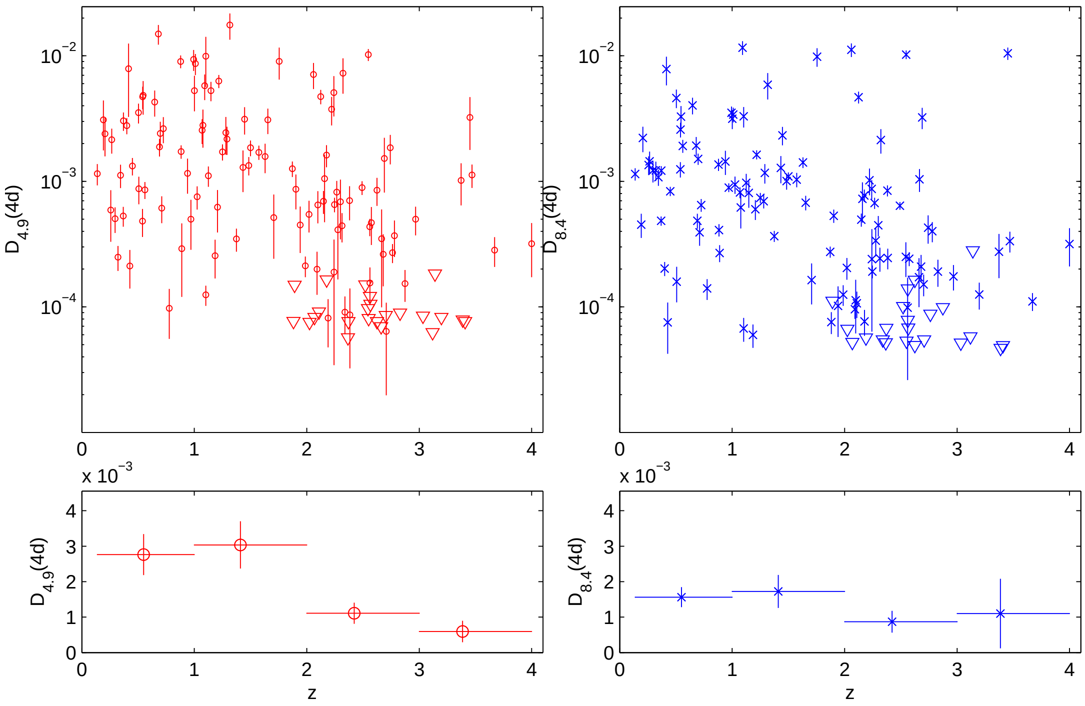

Figure 3.5 — $D_{4.9}$(4d) *(scatter plot at top left and binned plots at bottom left) and* $D_{8.4}$(4d) *(scatter plot at top right and binned plots at bottom right) plotted against source redshift. The triangles represent upper limits of* D(4d) *for sources where* $D\text{(4d)} < D_{noise}$.

Since the effects of scatter broadening decrease at higher frequencies, the high-redshift sources are less scatter broadened at 8.4 GHz, and therefore the drop in ISS amplitudes with redshift is less apparent.

Although the results appear tantalizing, it is important to note that a combination of various selection effects, including possible uneven distributions of source spectral indices (as demonstrated in Section 3.4) and luminosities (Bignall et al., 2010) in both samples, can lead to spurious interpretations. It is also crucial to understand why $D_{8.4}$(4d) is comparable to or larger than $D_{4.9}$(4d) in $\approx 35\%$ of the sources as seen in Figure 3.2. As mentioned in Section 3.3, this effect can be a result of stronger scatter broadening at 4.9 GHz than at 8.4 GHz in these sources, leading to an increase in apparent source sizes at 4.9 GHz relative to that at 8.4 GHz. It is also possible that these sources are exhibiting strong refractive scintillation, which can also result in $D_{8.4}$(4d) being larger than $D_{4.9}$(4d). Any bias towards strong ISS in the high redshift sample will affect the interpretation of Figure 3.6. I thus defer a full discussion of all these complicating effects and the origin of the redshift dependence of AGN ISS to a

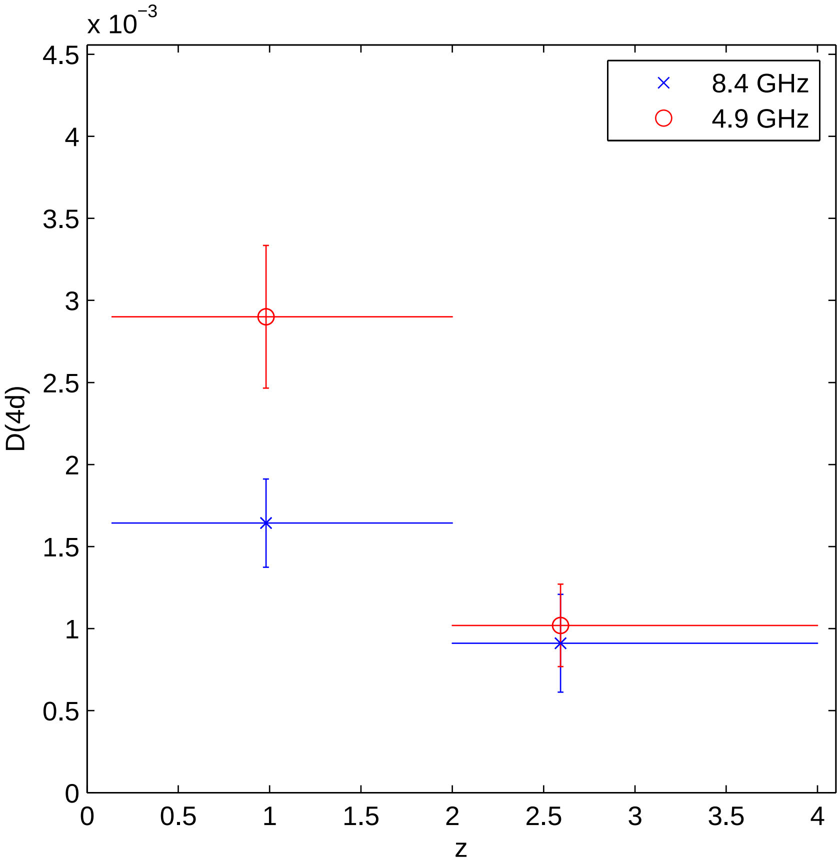

Figure 3.6 — *Mean* $D_{4.9}$(4d) *and* $D_{8.4}$(4d) *in two redshift bins, showing the frequency scaling of the redshift dependence of ISS.*

separate chapter (Chapter 5).

3.7 Comments on Individual Sources

I present here a brief discussion of the observed variability of selected sources that may be of particular interest. Some are well known sources often targeted for VLBI and ISS monitoring programs. They highlight the complexity of interpreting the underlying physics in AGN scintillation in the presence of various instrumental effects as well as the many factors that influence ISS.

3.7.1 J1159+2914

The optically violently variable quasar J1159+2914 (QSO 1156+295) (see Figure 2.1) was initially found to be scintillating at radio wavelengths (5 GHz) with 5.6% rms variations and with a time-scale of $\lesssim$ 12 hours by Lovell et al. (2003). 15 GHz

VLBI observations in 2007 (Savolainen & Kovalev, 2008) found the source to be scintillating with a modulation index of 13% and at a time-scale of 2.7 hours (calculated as the average of the peak-to-trough and trough-to-peak time). It was uncertain as to why the later epoch rms variations were larger at 15 GHz than earlier at 5 GHz. It was proposed that either the source was more compact during the VLBI observations than during the MASIV survey, or that the variability was due to strong scintillation rather than weak scintillation. The simultaneous dual-frequency observations indicate rms variations of 3.6% at 4.9 GHz and 1.9% at 8.4 GHz, so it is unlikely that the source is undergoing strong scintillation at the present epoch. The estimated timescales are $\sim$ 4 hours at 4.9 GHz and $\sim$ 2 hours at 8.4 GHz. However, it is difficult to make straightforward comparisons based on the modulation indices since VLBI measures the flux density at mas scales whereas the VLA flux includes larger scale components. The flux density of the actual scintillating component is in turn an unknown and variable fraction of the VLBI and VLA flux density. Examining the unnormalized variations give 0.6 Jy peak-to-trough variations at 5 GHz in Lovell et al. (2008), 0.7 Jy peak-to-trough variations at 15 GHz in Savolainen & Kovalev (2008), and 0.4 Jy peak-to-trough variations in our observations at both frequencies, which are all roughly similar. It is therefore likely that the descrepancy between the VLA and VLBI modulation indices arises from the higher resolution of VLBI observing a higher source compact fraction.

3.7.2 J1549+5038

The source J1549+5038 was visually classified as non-variable in the 2002 January and 2003 January epochs in the original MASIV Survey (Lovell et al., 2008). Its D(2d) was also found to be below that of the estimated noise level of 4×10^{-4}. In the present 2009 January follow-up observations, its D(4d) is found to be $> 3\sigma$ above the noise level at both frequencies, with $D_{4.9}(4\mathrm{d}) \sim 1.6 \times 10^{-3}$ and $D_{8.4}(4\mathrm{d}) \sim 7.7 \times 10^{-4}$. While it is possible that the variability amplitude of the source has increased, the improved sensitivity of the follow-up observations due to the larger number of antennas per subarray, coupled with the more accurate estimation of D_{noise}, has allowed lower level ISS to be detected at a $> 3\sigma$ level in this source. This demonstrates how improvements in the sensitivity of future instruments such as the SKA will lead to the detection of more sources exhibiting much lower levels of ISS.

3.7.3 J1819+3845

The well-known quasar J1819+3845 has been observed to consistently display 20 to 35% rms variations in its flux density since its extreme variability was discovered in 1999 (Dennett-Thorpe & de Bruyn, 2002, 2003), with scintillation timescales down to 15 minutes (Macquart & de Bruyn, 2007). This rapid scintillation is attributed to the presence of a nearby scattering region about 4 to 12 pc from the Earth. Surprisingly, the scintillations appeared to have stopped abruptly when no variability was detected in a VLBI observation in 2008 (Cimò, 2008). The present observations show significant rms variations of about 2% at both frequencies, and at 8.4 GHz is superposed on top of longer timescale variations > 11 days. Either the source has begun scintillating again (albeit at a lower level and at a slower timescale) after the abrupt halt, or these low-level scintillations were undetectable using the technique used by Cimò (2008). These are discussed in more detail in Section 4.3 of Chapter 4.

3.7.4 J1919+3159

J1919+3159 exhibits the strongest variability for a source amongst the $z > 3$ sample. The long timescale variations (> 11 days at both frequencies) suggest a relatively large angular size. The fact that $D_{8.4}(4\mathrm{d})$ is larger than $D_{4.9}(4\mathrm{d})$ appears consistent with a source undergoing weak ISS with its variability amplitude suppressed further at 4.9 GHz due to scatter broadening in the IGM. However, the line-of-sight Hα intensity of 6.5 Rayleighs and Galactic latitude of only 8.6° indicates that the source is observed through thicker regions of the Galaxy with higher transition frequencies between weak and strong ISS. Hence the more plausible explanation is that the source is undergoing strong refractive scintillation, which would also lead to long timescale variations and larger variability amplitudes at the higher frequency. The slow variations can also be attributed to intrinsic effects, although the observed ≈ 1 day lag in the 8.4 GHz lightcurve compared to that at 4.9 GHz renders this unlikely. Opacity effects in a synchrotron self-absorbed AGN jet would cause the 4.9 GHz lightcurve to lag behind the 8.4 GHz (which probes deeper down the jet) lightcurve instead. This example demonstrates the complex physics involved in the interpretation of the data, the understanding of which will be critical in any effort to investigate the redshift dependence of ISS.

3.7.5 J1931+4743

J1931+4743 is the source with the largest amplitude ISS in the sample, with rms variations $\sim 7\%$ at both frequencies. Its variability time-scales are estimated to be < 2 hours, and is therefore closest to being an ‘extreme scintillator’. It may even be an intermediary between the extreme and regular classes of scintillators. The source displayed consistent variability over all 4 epochs of the MASIV Survey, albeit at lower rms variations of ~ 2 to 4%. Further monitoring of J1931+4743 may reveal the physical relationship between extreme scintillators like J1819+3845 and other regular scintillators. The variability of this source in the 2009 January epoch is discussed again in Chapter 4 in the context of its link to extreme scintillation.

3.8 Chapter Summary

In this chapter, I analysed the statistical properties of the variability amplitudes of the sources at both frequencies to better understand ISS and the background AGN sources themselves. The main results and conclusions can be summarised as follows:

1. Statistically significant correlations with line-of-sight Hα intensities were obtained for the SF amplitudes up to 7-day time-lags at both frequencies, confirming that the variability of the sources is primarily due to ISS.

2. There is a strong correlation between the variability amplitudes of the sources at both frequencies, and, except in $\sim 20\%$ of the sources that are non-variable, in their variability patterns as well. This is consistent with the weak ISS of sources where the variations are expected to be broadband in nature.

3. In about $\sim 35\%$ of the sources, the $D_{8.4}(4\mathrm{d})$ was found to be comparable to or larger than $D_{4.9}(4\mathrm{d})$, due either to strong refractive ISS, or higher levels of scatter broadening at 4.9 GHz that increases the source angular size relative to that at 8.4 GHz.

4. For 25 sources, time delays of ~ 0.15 to 3 days were observed between the scintillation patterns at both frequencies, interpreted as being caused by a shift in core positions when probed at different optical depths. ISS provides an estimate of such core-shifts at a higher resolution than that of VLBI. Such observations will be important for astrometric applications in the selection of sources for an International Celestial Reference Frame. Combining multi-frequency scintillation observations with VLBI imaging (to obtain the true angular separation between the cores) raises the prospect of putting contraints on actual scattering screen distances and velocities, providing further insight into the physics of the ISM.

5. Although there is only a marginal increase in ISS amplitudes for sources with spectral indices of $\alpha_{4.9}^{8.4} > 0.4$, there is a significant reduction in ISS amplitudes for sources with $\alpha_{4.9}^{8.4} < -0.4$. These $\alpha_{4.9}^{8.4} < -0.4$ sources most likely have lower compact fractions than their $\alpha_{4.9}^{8.4} > -0.4$ counterparts.

6. A significant correlation between ISS amplitudes and mean flux densities were found at both frequencies, confirming the results of the MASIV Survey. This can be explained if the sources are brightness-temperature limited, so that the angular sizes of the sources increase with increasing mean flux density.

7. The observations confirmed that ISS amplitudes at 4.9 GHz drop significantly at $z \gtrsim 2$. Of even greater significance is the detection of a weakened redshift dependence of ISS at 8.4 GHz, with the mean variability of the $z > 2$ sources

dropping by about a factor of 1.8 when compared to the mean variability for sources at $z < 2$, as opposed to the factor of 3 decrease observed at 4.9 GHz.

Chapter 4

Rapid and Extreme Scintillation

> *Why, sometimes I've believed as many as six impossible things before breakfast.*
> — ***Lewis Carroll, Alice in Wonderland***

A large portion of this chapter has been published as a letter to the editor in *Astronomy & Astrophysics*, entitled 'Detection of six rapidly scintillating active galactic nuclei and the diminished variability of J1819+3845' (Koay et al., 2011b).

4.1 Introduction

Much of what has been learned about ISS came from the monitoring of a class of so called 'extreme scintillators' that display rms flux density variations $> 10\%$ on timescales $\lesssim 1$ hour, of which PKS 0405-385 (Kedziora-Chudczer et al., 1997), J1819+3845 (Dennett-Thorpe & de Bruyn, 2000) and PKS 1257-326 (Bignall et al., 2003) are the most well-known. Such rapid and large amplitude ISS has been attributed to the presence of nearby turbulent clouds, $< 30\,\mathrm{pc}$ from the Sun.

These extreme scintillators are surprisingly rare, considering that the three archetypal sources were detected serendipitously. In the MASIV survey, none of the sources, apart from J1819+3845, were found to display sustained modulation indices of more than 10%, although 16% of the sources were found to scintillate on timescales of < 12 hours (Lovell et al., 2008). This implied that the nearby, turbulent clouds responsible for extreme scintillation cover only a small fraction of the sky. It also begs the question as to whether the presence of these nearby clouds are the only necessary condition for rapid, large amplitude ISS, or if there are other factors that contribute to their scarcity (i.e. source compactness).

J1819+3845 was the most extreme of this class of sources. During a 4.8 GHz, 6-hour monitoring program on the European VLBI Network (EVN) in 2008 March, its extreme scintillation sustained over at least eight years was found to have ceased (Cimò, 2008), with an upper limit of 1% rms variations (Cimò, private communication).

Understanding the unexpected disappearance of the extreme variability of this source will shed some light on its origin at earlier epochs. It needs to be noted that episodic extreme scintillation has been observed in PKS 0405-385 (Kedziora-Chudczer, 2006), attributed either to the repeated appearance and expansion of new components in the source or spatially intermittent turbulent patches in the ISM drifting across its sightline.

In this chapter, I search the dual-frequency MASIV follow-up data for rapid scintillators, then make use of their properties to understand the origin of rapid and extreme radio scintillation. I present a novel method for identifying rapid scintillators and include a list of candidates in Section 4.2. In Section 4.3, I report on the variability of J1819+3845 subsequent to the period of extreme scintillation. I then discuss the implications of the results on the physics behind the most extreme scintillators in Section 4.4. The chapter summary is provided in Section 4.5.

4.2 Searching for the Rapid Scintillators

A method is devised to distinguish the rapid scintillators with characteristic timescales of $\tau_{char} < 2$ hours from the sources with much longer τ_{char} that display significant 2-hour variability (as seen in Figure 2.6 in Section 2.4.2.4). Recall that τ_{char} is defined as the time-scale at which $D(\tau)$ reaches half its value at saturation. $D(\tau)$ increases with τ^a and saturates at twice the true variance of the source, when the source is observed for a duration much longer than τ_{char}. Letting τ_{sat} be the time-scale at which $D(\tau)$ saturates, one obtains:

$$\frac{D(2\,\mathrm{d})}{D(2\,\mathrm{hr})} \begin{cases} = 1 & \text{if } \tau_{sat} \leq 2 \text{ hr} \\ = (\tau_{sat}/2 \text{ hr})^a & \text{if } 2 \text{ hr} < \tau_{sat} < 2 \text{ days} \\ \geq 24^a & \text{if } \tau_{sat} \geq 2 \text{ days.} \end{cases} \tag{4.1}$$

Figure 4.1 plots $D_{obs}(2\mathrm{d}) - D_{noise}$ against $D_{obs}(2\mathrm{hr}) - D_{noise}$ at both frequencies so that $D(2\mathrm{d})/D(2\mathrm{hr})$ is represented by a line of constant slope.

It is determined that a source must satisfy both of the following conditions on at least one frequency to be classified as a rapid scintillator, corresponding to shaded regions in Figure 4.1:

1. $D(2\mathrm{d})/D(2\mathrm{hr}) < 2$, since $\tau_{char} \geq 0.5(\tau_{sat})$ for $a \geq 1$. Sources that lie outside this region, but have 1σ error bars that extend into this region, are also included.

2. $D(2\mathrm{d})$ and $D(2\mathrm{hr})$ must be $> 4 \times 10^{-4}$, so that $D_{obs}(\tau) > 5\sigma$ above D_{noise}.

Six rapid scintillators are detected in the sample (listed in Table 4.1), out of an initial ten candidates that fulfill the conditions above. Four candidates are found to be slower scintillators after a visual inspection; they contain outliers in the lightcurves that

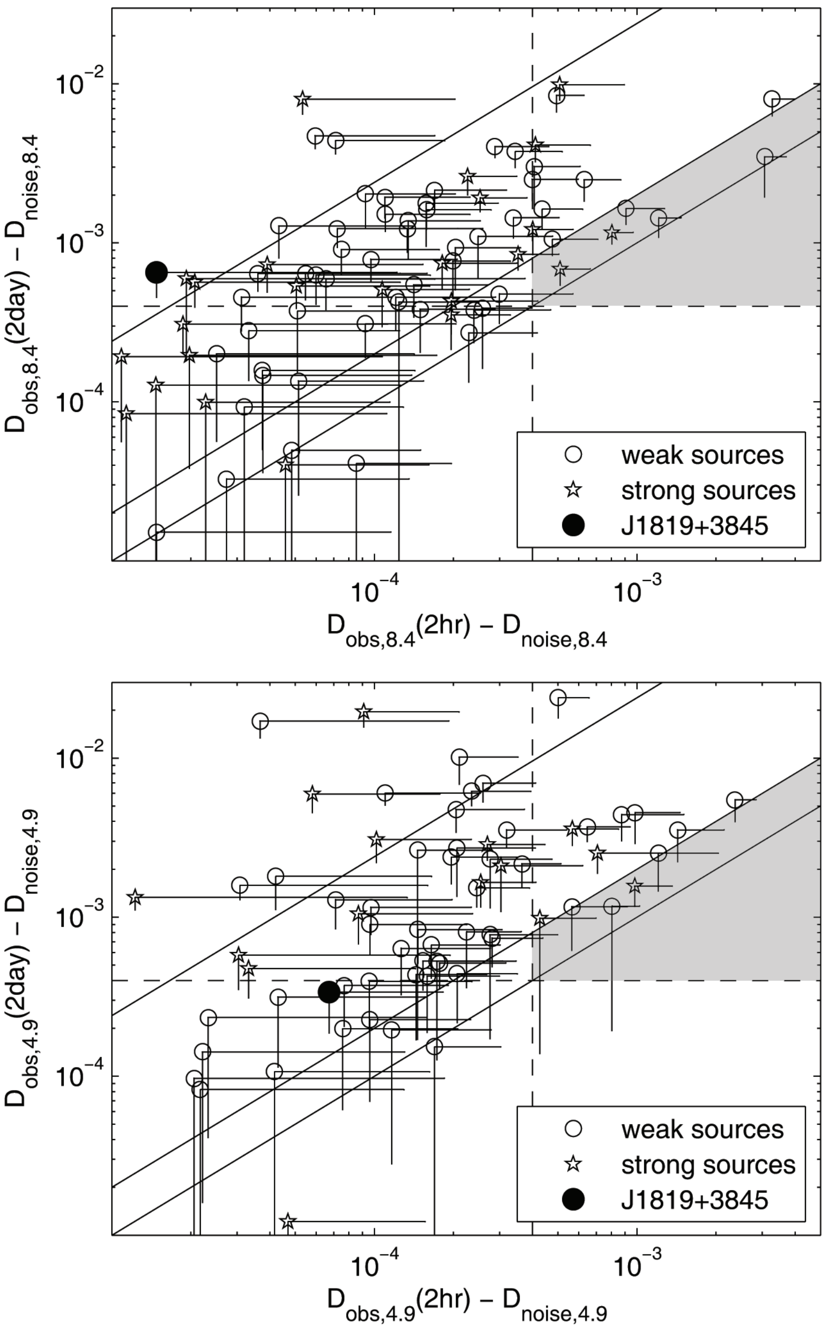

Figure 4.1 — *$D_{obs}(2\mathrm{d}) - D_{noise}$ plotted against $D_{obs}(2\mathrm{hr}) - D_{noise}$ at 8.4 GHz (top) and 4.9 GHz (bottom). For each source, only the lower limits of the 1σ errors in $D(2\mathrm{d})$ and the upper limits of the 1σ errors in $D(2\mathrm{hr})$ are shown. The solid lines have normalisation constants (equivalent to slopes on a linear plot) of 24, 2 and 1 (from top to bottom) respectively, corresponding to the different cases in Equation 4.1. The dashed lines represent the 5σ thresholds. Rapid scintillators with $\tau_{char} < 2$ hour are located within the shaded regions.*

Table 4.1. Rapid scintillators detected in the sample and their properties.

Source Name (J2000)	Galactic Coordinates l	b	I_α (R)	$S_{4.9}$ (Jy)	$S_{8.4}$ (Jy)	$m_{4.9}$ (%)	$m_{8.4}$ (%)	C(0)
J0800+4854	170.11	31.16	0.5	0.10	0.08	5.0	5.1	0.76
J0929+5013	167.66	45.42	0.6	0.40	0.39	4.1	2.6	0.82
J1049+1429	230.79	59.00	0.9	0.13	0.15	3.0	2.8	0.52
J1328+6221	115.56	54.23	0.5	0.10	0.08	5.9	3.0	0.75
J1549+5038	80.24	49.06	0.4	0.91	0.93	3.0	2.1	0.79
J1931+4743	79.98	13.53	5.2	0.11	0.10	7.2	7.4	0.88

Note. — Column 4 gives the line-of-sight Hα intensity in units of Rayleighs (R), from Haffner et al. (2003); columns 5 and 6 give the 2009 January VLA mean flux densities at 4.9 GHz and 8.4 GHz respectively; columns 7 and 8 give 2009 January raw modulation indices, without error subtraction; column 9 gives the cross-correlation between the lightcurves at both frequencies at timelag 0.

skew $D(2\text{hr})$ towards larger values, or display quasi-periodic structure in the lightcurves leading to quasi-periodicity in the SFs, thereby reducing $D(2\text{d})$ when 2 days is close to a multiple of the quasi-period. For the six confirmed rapid scintillators, a cross-check with their τ_{char} estimated by fitting a model to the SFs (Section 2.4.3) reveal that they were also estimated to be $\lesssim$ 2 hours on at least one frequency. The lightcurves of these six sources show strong correlation across both frequencies. An example, J1328+6221, is shown in Figure 4.2.

4.3 The Variability of J1819+3845

The present observations confirm that the character of the rapid and large amplitude scintillation in J1819+3845 has changed significantly (it is no longer exhibiting extreme scintillation, see Figures 4.1 and 4.3), as previously noted by Cimò (2008). I obtain rms variations of only 1.5% at 4.9 GHz and 2.5% at 8.4 GHz. Variations of $\tau_{char} \sim 6$ hours dominate at 4.9 GHz, while the variability at 8.4 GHz is dominated by the slow rise in flux density over the 11-day period, also discernible in the 4.9 GHz lightcurve. Such variations would not have been detected in the 6-hour observations by Cimò.

There are two possible explanations for the factor of $\sim$ 20 decrease in scintillation amplitude and the factor of $\sim$ 12 increase in timescale from the previously observed rms variations of 25-40% and time-scale of 30 minutes (Macquart & de Bruyn, 2007). Either the source has expanded, thereby quenching the scintillation, or the highly turbulent patch in the Local Interstellar Medium (LISM) responsible for the extreme scintillation

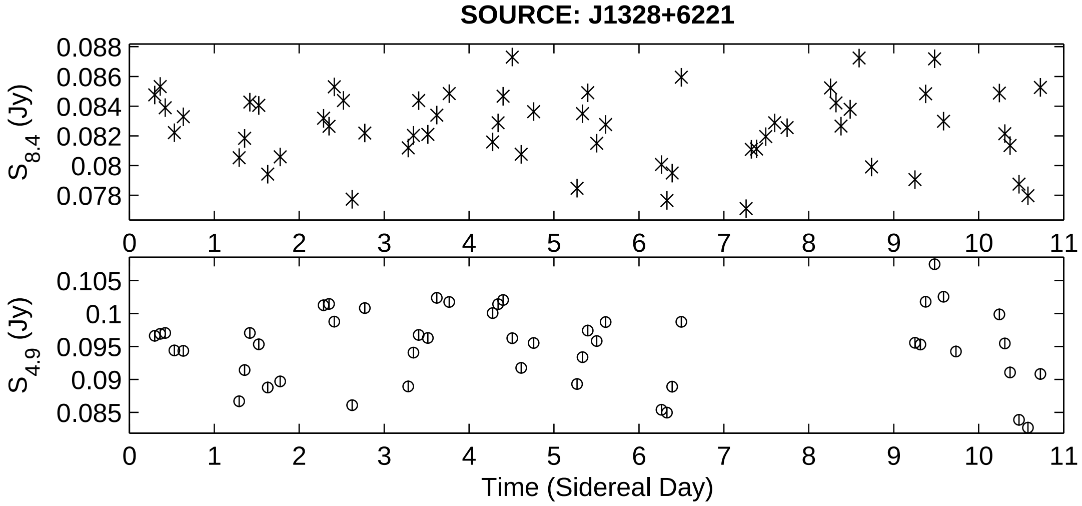

Figure 4.2 — *Lightcurves for the rapid scintillator J1328+6221 at 8.4 GHz (top panel) and 4.9 GHz (bottom panel).*

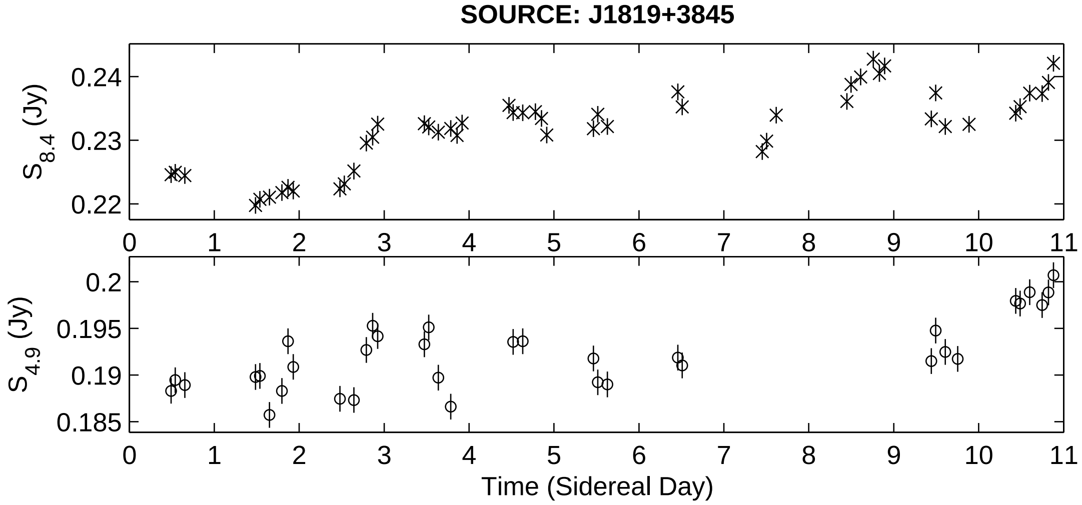

Figure 4.3 — *Lightcurves for the former extreme scintillator J1819+3845 at 8.4 GHz (top panel) and 4.9 GHz (bottom panel).*

has drifted off its sight-line. If the former is true, it would require the apparent angular size of the source to have expanded by a factor of 12 in < 2 years from 2006 to 2008. For a $> 100\,\mu$as source (65 pc at its measured redshift of 0.54, $H_0 = 70\,\mathrm{kms^{-1}Mpc^{-1}}$, $\Omega_M = 0.27$ and $\Omega_\Lambda = 0.73$), this requires an apparent expansion speed of $> 5.8c$. As there is no discernible change in its mean flux density, and the source remains unresolved at mas scales at all EVN baselines which includes the Urumqi telescope (Cimò, 2008), such an explanation is unlikely.

The latter explanation is therefore more likely. Assuming that the source size has not changed and assuming a scattering screen velocity of $50\,\mathrm{km\,s^{-1}}$, I estimate that the dominant scattering region is now located at a distance of 50 to 150 pc away, requiring also a factor ~ 9 decrease in the length-scale, $r_{\rm diff}$, of the phase fluctuations at the scattering screen to achieve the observed reduction in the modulation index (see Equation 4.2) in Section 4.4. The slower, $\tau_{sat} > 11$ day variations could be intrinsic to the source, or ISS at a second, more distant screen ~ 1.7 kpc away. In any case, these longer time-scale variations would have been masked by the previous rapid and large amplitude variations of J1819+3845.

4.4 The Origin of Rapid and Extreme Scintillation

The spatial distribution of the six rapid scintillators shows a dependence on Galactic latitude and line-of-sight free electron content, consistent with the view that the most rapid ISS in AGNs is caused by scattering at nearby regions. Of the six sources, five of them lie at Galactic latitudes of $> 30°$, and have Hα intensities obtained from the WHAM Northern Sky Survey (Haffner et al., 2003) of $I_\alpha \leq 1.0$ Rayleighs (see Figure 4.4 and Table 4.1). In fact, out of 20 sources in the sample that have $I_\alpha \leq 0.6$ Rayleighs, of which 14 have variability amplitudes 3σ above D_{noise}, four of them are rapid scintillators. On the other hand, in 108 sources with $I_\alpha > 0.6$ Rayleighs, there are only two rapid scintillators. Fisher's Exact Test for contingency tables confirms that the association between rapid ISS and low I_α is statistically significant. I calculate a probability of 0.0044 that the correlation was obtained purely by chance when considering the entire sample of 128 sources, and a probability of 0.0026 when considering only the $> 3\sigma$ variable sources. The significance holds even if J1819+3845 ($I_\alpha = 2.2$ Rayleighs) is considered as a rapid scintillator based on its history, and PKS 0405-385 and PKS 1257-326 are included in the sample, which have $I_\alpha < 0.5$ and $I_\alpha = 16$ Rayleighs respectively (obtained from the Southern H-Alpha Sky Survey Atlas, see Gaustad et al. (2001)). This is consistent with the MASIV results which show that the fraction of fast scintillators ($\tau_{char} < 0.5$ days) decreases with increasing Hα intensity (Lovell et al., 2008). These sight-lines with low Hα at higher Galactic latitudes correspond to regions of lower transition frequencies (ν_t) between weak and strong ISS (Walker, 1998), which imply lower effective scattering screen distances at a fixed observing frequency. Since the Galactic disk is thinner at these latitudes, it is more likely that the ISS is dominated by scattering at nearby regions. These nearby screens produce smaller scale interference patterns on the Earth's surface, leading to more rapid scintillation for a given screen velocity as they drift across the telescope.

The $\tau_{char} < 2$ hours can be attributed to scattering at an effective screen distance of $D_{\rm ISM} < 12$ pc for a $\sim 200\,\mu$as source component, or at $D_{\rm ISM} < 250$ pc for a $\sim 10\,\mu$as component, for typical transverse velocities of $50\,{\rm km\,s^{-1}}$. Assuming Kolmogorov turbulence and a transition frequency of $\nu_t = 3$ GHz, numerical computations using the fitting formula for ISS in Goodman & Narayan (2006) indicate that the former will produce the observed $\sim 5\%$ rms variations, giving brightness temperatures, T_b, of 4×10^{10} K if all the 100 mJy flux density is contained within the $\sim 200\,\mu$as component. The latter requires that the compact fraction, f_c, be $\sim 25\%$ to obtain $\sim 5\%$ rms variations, giving $T_b = 4 \times 10^{12}$ K for an observed 100 mJy source.

There are strong indications that both scenarios for rapid ISS occur in the present sample. Gaussian model fits to source core components in 8.4 GHz VLBI images (Ojha et al., 2004b) estimate core diameters of $\sim 200\,\mu$as ($D_{\rm ISM} < 12$ pc) in J1328+6221 and J1931+4743, as well as $\sim 40\,\mu$as ($D_{\rm ISM} < 60$ pc) in J1049+1429. The VLBI cores may contain an even more compact, unresolved component which could push the maximum screen distances further out. However, Linsky et al. (2008) have also shown that the extreme scintillation in J1819+3845, PKS 0405-385 and PKS 1257-326 may be associated with regions where multiple warm-ionized clouds < 15 pc from the Sun intersect, and possibly interact to form highly-turbulent screens. I find that J1328+6221 and J1931+4743 also have sight-lines through (or at the edge of) these multiple clouds (Figure 4.5), providing further evidence for screens < 15 pc. On the other hand, the sight-lines of J1049+1429 and the other three sources do not intersect these regions, suggesting larger screen distances.

That rapid ISS arises from a large range of source sizes and scattering screen distances explains why rapid scintillators are not as rare as initially thought; it is the sources that display *both* rapid *and* large rms variations $> 10\%$ that are rare. The six rapid scintillators constitute 5% of the 128 sources, yet none have rms variations $> 10\%$. No new extreme scintillators were found in the MASIV Survey (Lovell et al., 2008), although J0949+5819 and J0829+4018 did show $\sim 15\%$ rms variations at one epoch.

I argue that the scarcity of the extreme scintillators can be attributed to additional constraints required for rapid scintillators to also display rms variations $> 10\%$. In the regime of weak ISS where the observing frequency, $\nu > \nu_0$, the modulation index for an extended source whose angular size, θ_s, is larger than the Fresnel angular-scale at the scattering screen, θ_F, is given by Narayan (1992) and Walker (1998), which I rewrite

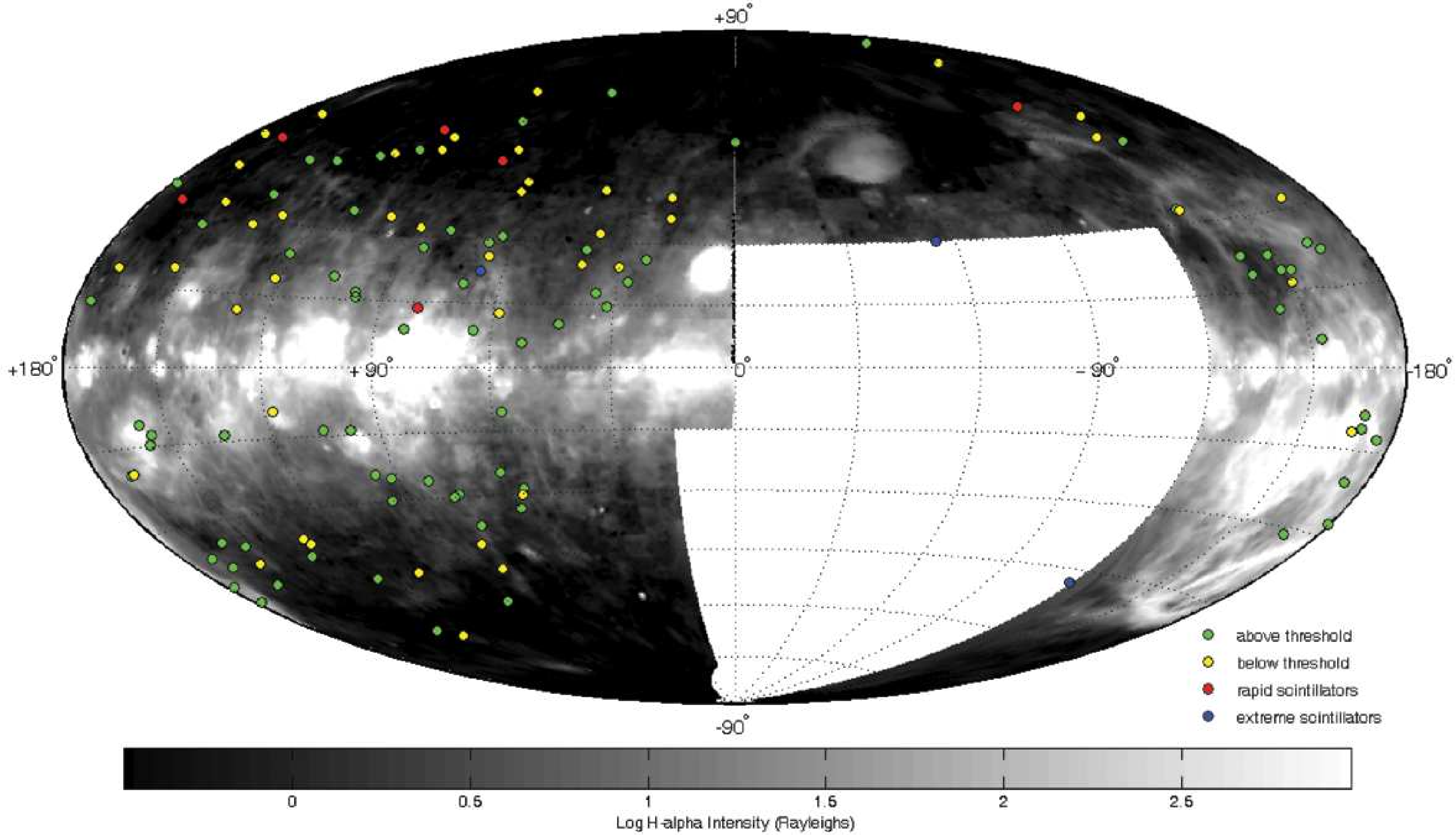

Figure 4.4 — *Spatial distribution of the sources in the sample in Galactic coordinates, overlayed on a* Hα *intensity map obtained from the WHAM Northern Sky Survey (Haffner et al., 2003). The sources are classified into one of the four following categories – sources that have* $D(4\,\mathrm{d})$ *above the* 3σ *of* D_{noise} *threshold, sources whose variability lies below the threshold, the rapid scintillators found in our sample, and the extreme scintillators (historically) J1819+3854, PKS 0405-385, and PKS 1257-326.*

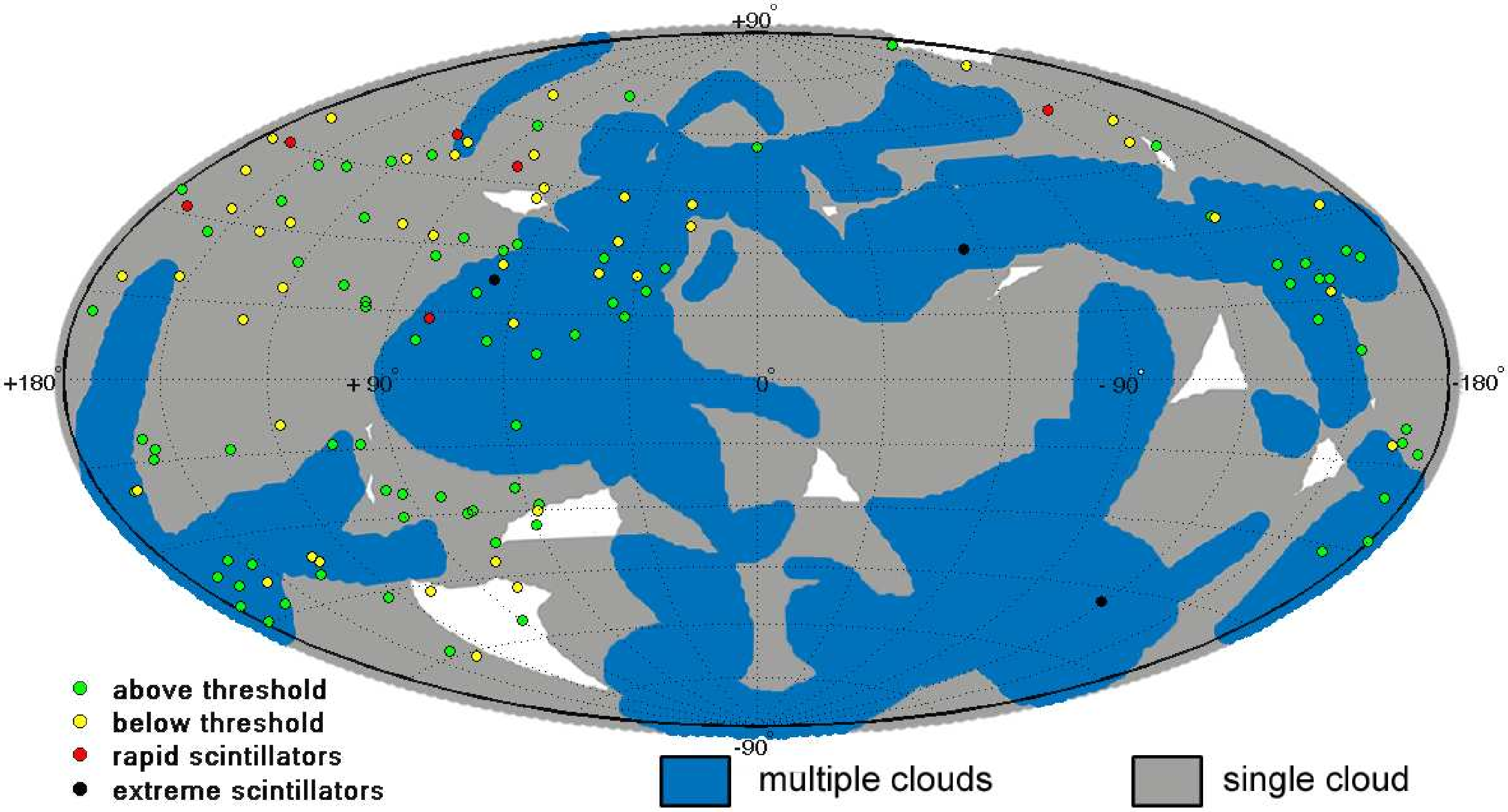

Figure 4.5 — *Spatial distribution of the sources in the sample in Galactic coordinates. The grey shaded regions indicate the presence of a single warm ionized cloud within 15 pc of the Sun, while the blue regions indicate where two or more clouds intersect and possibly interact to generate turbulence (obtained from Linsky et al. (2008)). The sources are classified into one of the four following categories – sources that have* $D(4\,\mathrm{d})$ *above the* 3σ *of* D_{noise} *threshold, sources whose variability lies below the threshold, the rapid scintillators found in our sample, and the extreme scintillators (historically) J1819+3854, PKS 0405-385, and PKS 1257-326.*

as follows:

$$m = f_c \Big(\frac{\nu_t}{\nu}\Big)^{\frac{17}{12}} \left(\frac{\theta_F}{\theta_s}\right)^{\frac{7}{6}} = \frac{c f_c}{2\pi\nu} \left(\frac{1}{r_{\rm diff}}\right)^{\frac{5}{6}} \left(\frac{1}{D_{\rm ISM}}\right)^{\frac{1}{6}} \left(\frac{1}{\theta_s}\right)^{\frac{7}{6}}, \tag{4.2}$$

where $\theta_F \approx r_{\rm F}/D_{\rm ISM} = \sqrt{c/(2\pi\nu D_{\rm ISM})}$, $r_{\rm F}$ is the Fresnel length-scale, $r_{\rm diff}$ is the diffractive length-scale determined by the strength of the turbulence at the scattering screen, and $r_{\rm F}/r_{\rm diff} = (\nu_t/\nu)^{17/10}$. Kolmogorov turbulence is assumed.

Firstly, the source must be observed at a frequency close to ν_t, where m for a point source ∼100%. This is also true in the regime of strong refractive ISS ($\nu < \nu_t$), as m decreases again with decreasing ν.

Secondly, the scattering screen must be highly turbulent (with small $r_{\rm diff}$). As discussed in Section 4.3, such a turbulent cloud has possibly moved away in the case of J1819+3845. These turbulent patches may be localized and intermittent, possibly causing the episodic extreme scintillation in PKS 0405-385 (Kedziora-Chudczer, 2006). Such AU-scale inhomogeneities deviate from standard models of the ISM with homogenous Kolmogorov turbulence. They are instead reminiscent of the clumpy, discrete clouds observed in extreme scattering events (Fiedler et al., 1987) and the scintillation of pulsar B0834+06 (Brisken et al., 2010). Scattering in such clouds would dominate the scintillation in PKS 1257-326 over any background ISS, despite its large line-of-sight I_α.

Thirdly, the source must have f_c close to unity. Comparing VLBI flux densities of the core components to that of the extended mas structures (Ojha et al., 2004b) gives upper limits to f_c at VLBI scales, albeit at a different epoch; $\lesssim 75\%$ for J0800+4854, J1328+6221 and J1931+4743, $\lesssim 100\%$ for J1049+1429. J1549+5038 also shows significant extended structure at mas scales (Fey & Charlot, 2000). At the resolution of the VLA, f_c will possibly be lower. This reduces the modulation indices in the six detected rapid scintillators in the present sample.

The source J1159+2914 (Section 3.7.1), which narrowly missed out on being selected as a rapid scintillator, provides the ideal example to support the third point. Savolainen & Kovalev (2008) reported $m \sim 13\%$ scintillation at a time-scale of 2.7 hours with a mean flux density ~ 1.5 Jy at 15 GHz, based on VLBI observations in 2007. The MASIV Survey and the follow-up observations give $m \sim 5\%$ at both frequencies, obtaining flux densities ~ 3.0 Jy. The unnormalized peak to trough variations in the three separate experiments are in fact comparable in amplitude, ≈ 0.5 Jy.

Therefore, while scattering screens at distances up to 250 pc can produce $\tau_{char} \lesssim 2$ hour ISS in AGN cores $\gtrsim 10$ μas, source compact fractions $\gtrsim 50\%$ are necessary for ~ 10 μas scintillating components ($\gtrsim 95\%$ for ~ 100 μas components) to display $\gtrsim 20\%$ rms variations at $\tau_{char} \sim 1$ hour when observed at $\nu = \nu_t \sim 4.9\,$GHz. I therefore predict that higher angular resolution observations will reveal more large amplitude rapid scintillators, providing more reliable constraints on the flux density of the scintillating components.

4.5 Chapter Summary

In this chapter, I searched for rapid scintillators with characteristic time-scales of $\tau_{char} < 2$ hours by examining the ratio of $D(2\text{d})$ to $D(2\text{hr})$ of each source. Based on the properties of the detected rapid scintillators, as well as the variability characteristics of J1819+3845 at the present epoch, I examined the origin of rapid and extreme scintillation observed in some sources. The main findings are summarised as follows:

1. The former extreme scintillator J1819+3845 was found to display $\sim 2\%$ rms variations at ~ 6 hour time-scales superposed on longer > 11 day variations, suggesting that the highly turbulent cloud responsible for its extreme scintillation has moved away, with its scintillation now dominated by a more distant scattering screen ≈ 50 to 150 pc away.
2. Six new rapid scintillators with characteristic time-scales of < 2 hours were detected in the sample, none of which have rms variations $> 10\%$.
3. Strong lines of evidence were found linking rapid scintillation to the presence of nearby scattering regions, estimated to be < 12 pc away for ~ 200 μas sources and < 250 pc away for ~ 10 μas sources.
4. Rapid scintillation is not as rare as initially thought, since it can arise if the source is very compact (~ 10 μas) or if the scattering screen is very nearby with distances of order ~ 10 pc or less; there is evidence to suggest that both scenarios are present in the six detected rapid scintillators.
5. The scarcity of rapid *and* large amplitude (extreme) scintillators can be attributed to the requirement of additional constraints; these include large source compact fractions, high levels of scattering screen turbulence, and observations close to the transition frequency between weak and strong ISS.

Chapter 5

The Redshift Dependence of AGN Scintillation

> *Because one astronomer's noise is another astronomer's data...*
> — ***Nicole Gugliucci, from her blog 'One Astronomer's Noise'***

This chapter has been published as an article, entitled 'Why Do Compact Active Galactic Nuclei at High Redshift Scintillate Less?', in *The Astrophysical Journal* (Koay et al., 2012).

5.1 Introduction: What Causes the Redshift Dependence of ISS?

One of the most far-reaching results of the MASIV survey was the discovery of a drop in ISS variability amplitudes and the fraction of scintillating sources at redshifts $z \gtrsim 2$ (Lovell et al., 2008). This was initially surprising, owing to the fact that sources with roughly similar linear sizes should appear to have smaller angular sizes at high redshift, and therefore scintillate more.

The MASIV follow-up observations has so far provided confirmation of this effect (see Section 3.6). Note that Ofek & Frail (2011) report no significant correlation between ISS amplitude at 1.4 GHz and source redshift, based only on 9 sources for which redshift data were available, in their investigation of the 1.4 GHz variability of sources in the NVSS and FIRST catalogs. Interestingly, Richards et al. (2011) found a 3σ significance drop in the variability amplitudes of sources at $z > 1$ in their 15 GHz observations of about 1500 Fermi-candidate blazars over a duration of 2 years. While these longer time-scale variations at 15 GHz are mainly intrinsic to the sources, it is conceivable that if these high-redshift sources are less compact (in angular and linear scales) than their low-redshift counterparts, they will exhibit lower levels of both ISS and intrinsic variability.

Determining the origin of this redshift dependence of AGN ISS has important cosmological consequences, potentially allowing the ISS of AGNs to be used as a cosmological probe with the highest angular resolution possible. The suppression of ISS at redshifts $z \gtrsim 2$ can be attributed either to an increase in the apparent angular diameters of the core components, or a decrease in the compact fraction of the sources, i.e. the emission from the ultra-compact scintillating component of the source becomes less dominant relative to that of the extended non-scintillating components. Possible interpretations include:

1. *Decrease in observed brightness temperature due to cosmological expansion* (Rickett et al., 2007) — In a sample of brightness temperature-limited sources in the emission frame, as is often assumed for radio-loud AGNs (Readhead, 1994), the mean observed brightness temperature decreases with redshift as a result of the expansion of the Universe. In a flux-limited sample, this results in an increase in the apparent angular diameters of sources with redshift. If this effect dominates, it provides an angular size-redshift relation for extragalactic radio sources that has long been sought after (Gurvits et al., 1999).

2. *Evolution of AGN morphologies* — The drop in ISS amplitudes could also be explained by a prevalence of sources with lower Doppler boosting factors at high redshift, which would result in either lower source compact fractions or larger angular diameters of the core components. However, little is currently known about the evolution of AGN core-jet morphologies with redshift, critical in studies of feedback processes in galaxy formation. It is therefore a target of very high resolution observations such as RadioAstron's early science programs.

3. *Source selection effects* — It is well known that a flux-limited sample of flat-spectrum AGNs is severely biased with redshift due to source orientation and relativistic beaming (Lister & Marscher, 1997). Variations in the distribution of intrinsic source luminosities and jet Doppler boosting factors with redshift can lead to a redshift dependence of the apparent mean angular sizes or source compact fractions. Furthermore, a survey at a fixed frequency observes the sources at increasing rest frame emission frequencies with increasing redshift, and thereby observes the optically thick sources at increasing optical depths with increasing redshift, as well as different portions of the spectrum of emission.

4. *Scatter broadening in the ionized intergalactic medium (IGM)* (Rickett et al., 2007) — Cosmological models demonstrate that supernovae-driven galactic outflows can inject turbulence into the IGM (Evoli & Ferrara, 2011). Such turbulence in the ionized IGM can cause angular broadening due to multipath propagation of

the scattered waves. If indeed the redshift dependence of ISS is a result of angular broadening in the IGM, it would present a first direct detection of scattering in the ionized IGM, and would open up a new method of probing the physics of the IGM where 90% of the baryons in the Universe reside (Fukugita & Peebles, 2004). As scattering is sensitive to the ionized components, it will complement Lyman-α studies of the neutral component. It may even provide an alternative means of detecting the warm-hot component of the IGM, widely believed to be the 'missing baryons' in the local Universe based on cosmological hydrodynamical simulations (Cen & Ostriker, 1999; Davé et al., 2001; Cen & Ostriker, 2006), but which has so far been difficult to detect (Bregman, 2007).

5. *Gravitational lensing by foreground sources* — The combined data from CLASS and JVAS revealed only 22 gravitational lens systems out of a sample of 16503 flat-spectrum sources (Browne et al., 2003; Myers et al., 2003). They were however, searching mainly for multiply imaged sources with arc-second resolution (with follow-up observations using VLBA and MERLIN for confirmation), thus would not have detected any low-level magnification in the sources caused by weak lensing. However, if weak lensing broadens the source images by 10 to 100 μas, it could supress the ISS of sources at high redshift. Such an explanation would have implications for the distribution of matter (both dark and baryonic) in the low redshift Universe.

Three lines of investigation are actively being pursued by the MASIV collaboration and others to better understand this ISS redshift dependence. The first involves a thorough examination of the optical properties of the MASIV sources to detect possible biases due to the presence of sources drawn from different AGN populations (Pursimo et al., submitted). This includes new observations to obtain more reliable redshift estimates and optical identifications (IDs) for the sources to complement archival data. New spectroscopic redshifts and IDs for many of the MASIV sources in which such data were not available, have also been obtained.

The second line of investigation makes use of VLBI data to examine the mas-scale structures of the sources to determine their effects on ISS (Ojha et al., 2004a). While it has been found that scintillating sources are more core-dominated than the non-scintillating sources at mas-scales (Ojha et al., 2004b), how their mas compact fractions scale with redshift is still being investigated. Multi-frequency VLBI observations to study possible angular broadening in a subsample containing 49 MASIV sources (Ojha et al., 2006) found no evidence of scatter broadening in the IGM at the resolution probed (Lazio et al., 2008), providing an upper limit of 500 μas at 1.0 GHz.

The third key to understanding the redshift dependence of ISS, which is the focus of this chapter, is to examine how this redshift dependence scales with observing frequency.

The motivation is that scatter broadening in the IGM scales roughly with ν^{-2} whereas intrinsic source size effects scale with ν^{-1} for a synchrotron self-absorbed source. On the other hand, the effects of cosmological expansion and gravitational lensing are achromatic. Therefore, while it is expected in general that the amplitude of weak ISS decreases at higher observing frequencies, one will observe either a similar or weaker redshift scaling of ISS amplitudes depending on which interpretation is correct. At the very least, the analysis of the data will either rule out some of the interpretations listed above, or place strong constraints on them.

The dual-frequency MASIV follow-up data are most suited for such an investigation, and were the main reason the observations were conducted in the first place. While the redshift dependence of the ISS amplitudes at 8.4 GHz appear marginally weaker than that at 4.9 GHz at first look (Figure 3.5), suggesting IGM scatter broadening, the presence of subtle selection effects such as those mentioned above, along with the complexity of the ionized ISM and the sources themselves, complicates the interpretation.

This chapter begins with a detailed discussion of the various selection effects in the source sample (Section 5.2). I then present a novel method of analysing the data which accounts for these selection effects by examining the structure function ratios (Section 5.3), making use of theoretical models and Monte-Carlo simulations to interpret the data (Section 5.4). One of the effects partially responsible for the redshift dependence of ISS is discussed further in Section 5.5, followed by the chapter summary in Section 5.6.

5.2 Source Selection Effects

The results of the MASIV Survey and the follow-up observations show that the presence of ISS is strongly correlated with source spectral indices, mean flux densities and line-of-sight Hα intensities (Lovell et al., 2008). I therefore examine here whether these parameters are similarly distributed across the low and high-redshift samples, as well as other selection effects that may bias the interpretation of the results.

The sources in the original MASIV sample were selected to be flat-spectrum, core-dominated AGNs, based on the spectral index criterion of $\alpha_{1.4}^{8.4} > -0.3$ (where $S \propto \nu^{\alpha}$). The cutoff was set at a higher than usual value of -0.3 (where -0.4 or -0.5 is normally used), to avoid the tail end of the distribution of the classical steep-spectrum sources peaked at $\alpha \sim -0.7$ (Scheuer & Williams, 1968), considering that the $\alpha_{1.4}^{8.4}$ values were estimated from non-coeval mean flux densities at different frequencies. However, there are 30 sources with spectral indices of $\alpha_{4.9}^{8.4} < -0.3$ in the present sample, of which 15 have $\alpha_{4.9}^{8.4} < -0.4$, calculated from the coeval mean flux densities in our 11 day observations.

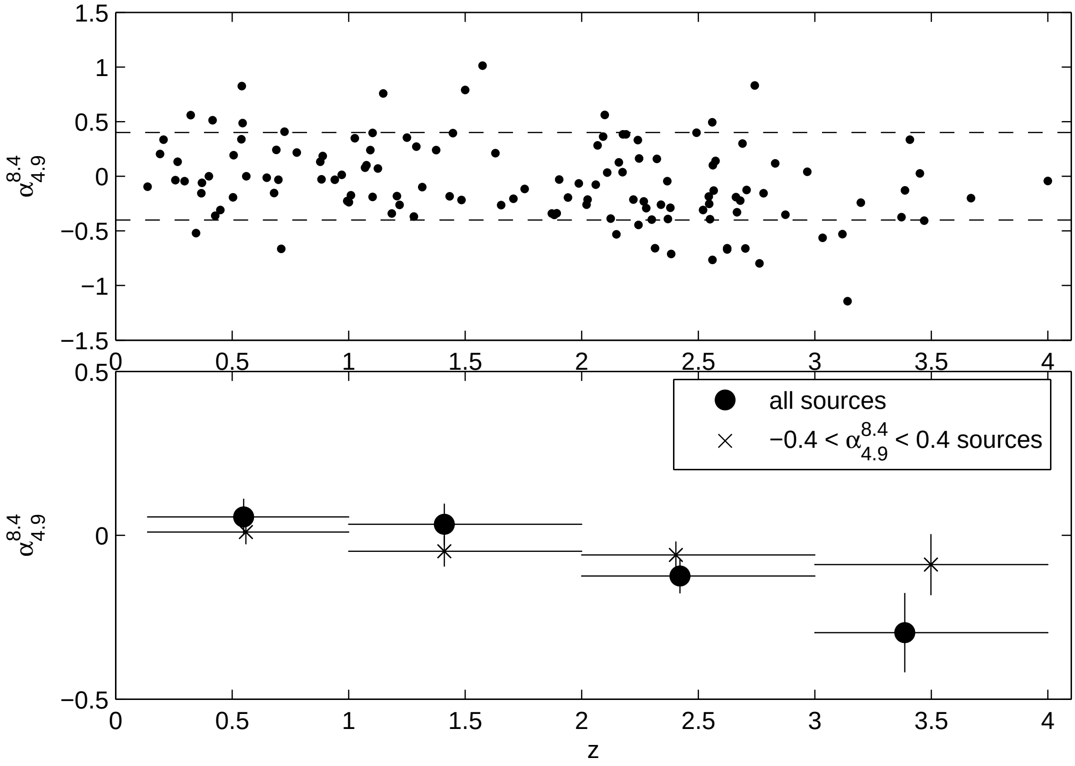

Figure 5.1 — *The top panel shows a scatter plot of source spectral indices against source redshift for all 128 sources. The horizontal dashed lines indicate* $\alpha_{4.9}^{8.4} < -0.4$ *and* $\alpha_{4.9}^{8.4} < -0.4$*, in between which the sources are considered as flat-spectrum sources. The bottom panel shows the mean spectral indices in four redshift bins before and after the removal of the inverted and steep-spectrum sources. The error bars in the binned plots indicate* 1σ *errors in the mean.*

I discover that the redshift dependence of ISS in the sample can be at least partially linked to the steepening of the mean values of $\alpha_{4.9}^{8.4}$ with redshift (see Figure 5.1). The Kolmogorov-Smirnov (K-S) test rejects the null hypothesis, that $\alpha_{4.9}^{8.4}$ of the low and high-redshift samples are drawn from the same parent population, with a 7.4×10^{-3} probability that this result was obtained by chance (here and in all subsequent analyses, probabilities below 0.05 are considered to be statistically significant). Of the 15 sources with $\alpha_{4.9}^{8.4} < -0.4$, which are known to scintillate less than the $\alpha_{4.9}^{8.4} > -0.4$ sources (see Section 3.4), 13 are found at $z > 2$. Furthermore, eight of the 11 sources with $\alpha_{4.9}^{8.4} > 0.4$ are found at $z < 2$, and there are indications that their scintillation amplitudes may be larger than that of the $-0.4 < \alpha_{4.9}^{8.4} < 0.4$ sources (Section 3.4). This z-$\alpha_{4.9}^{8.4}$ correlation in itself is of great interest and a full discussion of its significance is deferred to Section 5.5.

Since $\alpha_{4.9}^{8.4}$ is based on the coeval flux densities of the follow-up observations, -0.4 is used as a lower cutoff for the selection of sources. This allows a slightly higher number of sources to be retained for better statistical representation. Also, an examination of the 15 sources with $-0.4 < \alpha_{4.9}^{8.4} < -0.3$ finds that they are distributed roughly equally, with 8 at $z < 2$ and 7 at $z > 2$. I therefore remove only 11 sources with $\alpha_{8.4}^{4.9} > 0.4$ and 15 sources with $\alpha_{4.9}^{8.4} < -0.4$ (a total of 26 sources) from the sample, after which the K-S test shows that the distribution of $\alpha_{4.9}^{8.4}$ in the high and low-redshift samples no longer differ significantly. In any case, note that all subsequent analyses in this and the following Sections are performed on both the $-0.4 < \alpha_{4.9}^{8.4} < 0.4$ and $-0.3 < \alpha_{4.9}^{8.4} < 0.4$ samples, for which no differences are found in the conclusions. From here onwards, only the results for the $-0.4 < \alpha_{4.9}^{8.4} < 0.4$ sample of 102 sources are presented, comprising 46 sources at high redshift and 56 sources at low redshift.

Considering only the $-0.4 < \alpha_{4.9}^{8.4} < 0.4$ sources, it is found that the drop in ISS amplitudes at high redshift remains statistically significant. The K-S test confirms that the variability amplitudes of the high-redshift sources, characterized by $D_{4.9}(4\text{d})$ and $D_{8.4}(4\text{d})$, are significantly smaller than that of the low-redshift sources, with a probability of 5.1×10^{-5} that this occurred by chance. This is clearly seen in the histograms of Figure 5.2.

It needs to be noted also, that in the selection of sources for the MASIV follow-up observations, the $z < 2$ sample was biased towards the variable sources, while all sources with known redshifts were selected for the $z > 2$ sample. Although one could argue that the fraction of scintillating sources at low redshift is higher than that at high redshift anyway, as found in the MASIV survey (Lovell et al., 2008), this introduces another possible selection effect into the source sample. However, the significant decrease in ISS amplitudes at high redshift of the $-0.4 < \alpha_{4.9}^{8.4} < 0.4$ sources cannot be attributed solely to this selection effect, as the significance is retained even when only the most variable sources are selected. K-S tests show that $D_{4.9}(4\text{d})$ and $D_{8.4}(4\text{d})$ in the $z < 2$ sources are still significantly larger than their counterparts in the $z > 2$ sources when considering only the 72 sources where $D(4\text{d}) \geq 2 \times D_{noise}$ (equivalent to $\geq 3\sigma$ variability amplitudes) at both frequencies, with probabilities of 1.3×10^{-2} and 2.2×10^{-2} that they occured by chance. These 72 sources are drawn from only the $-0.4 < \alpha_{4.9}^{8.4} < 0.4$ sample.

The sources in the sample were also carefully selected so that their mean flux densities and line-of-sight Hα intensities would be evenly distributed in the high and low-redshift samples, but a large fraction of these sources are variable, so their mean flux densities may have changed. As a check, the K-S test is performed which finds no statistically significant differences in the distribution of mean flux densities and line-of-sight Hα intensities in the low and high-redshift samples. This is true before and after the removal of the 26 $\alpha_{4.9}^{8.4} > 0.4$ and $\alpha_{4.9}^{8.4} < -0.4$ sources, as well as for the 72 sources with $\geq 3\sigma$ variability.

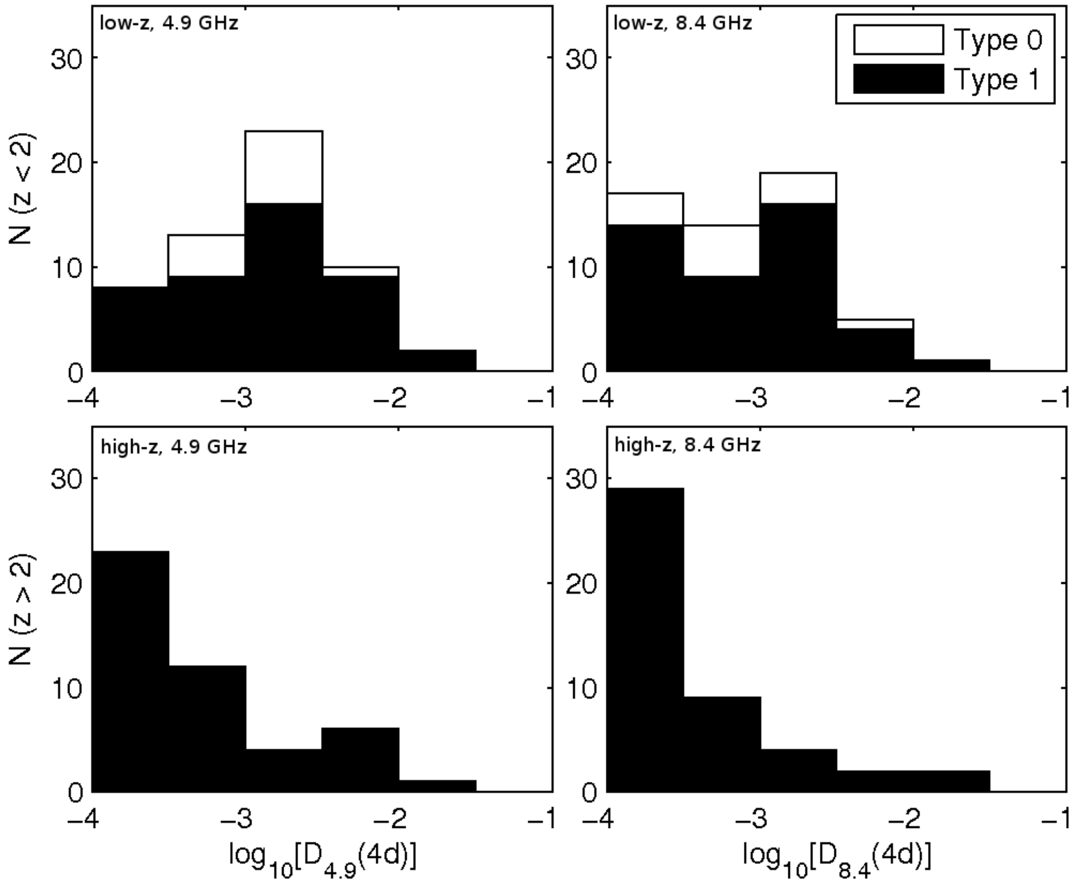

Figure 5.2 — *Distribution of* $D_{4.9}$(4d) *(left) and* $D_{8.4}$(4d) *(right) in the low (top) and high (bottom) redshift sample of sources. Only the 102 sources with* $-0.4 < \alpha_{4.9}^{8.4} < 0.4$ *are shown, classified into Type 0 or Type 1 AGNs based on their optical IDs. Since* $D_{noise} \approx 1 \times 10^{-4}$ *on average at both frequencies, we include all sources with* $D(\mathrm{4d}) < 1 \times 10^{-4}$ *in the* $-4 < \log[D(\mathrm{4d})] < -3.5$ *bin. The high redshift sources are significantly less variable than their low redshift counterparts.*

Another possible source of selection bias is the presence of sources with different optical IDs in the sample. Forty five out of the 46 high-redshift sources are identified as flat-spectrum radio-loud quasars (FSRQs), while the other source has yet to be identified, most likely an FSRQ. In the low-redshift sample however, 42 sources are identified as FSRQs, 12 are BL Lac objects, and 2 are Seyfert 1 galaxies. In standard AGN unification schemes (Urry & Padovani, 1995), FSRQs and Seyfert 1 galaxies are classified as Type 1 AGNs, with both having broad emission lines. They differ only in their radio and optical luminosities, the significance of which is historical rather than physical, so they are grouped together in the analysis. On the other hand, BL Lac objects are classified as Type 0 AGNs due to their weak or lack of emission lines. BL Lac objects have been observed to be more variable than FSRQs, intrinsically (Richards et al., 2011) as well as in terms of their ISS (Pursimo et al., submitted). I therefore carry out the analysis with and without the inclusion of the BL Lac objects to determine if they affect the interpretation of the data.

While biases caused by the aforementioned parameters can be mitigated through the careful selection of sources, there are other selection effects that are unavoidable in a survey such as this. These selection effects can increase or decrease ISS with redshift, biasing the result either way. For example, the sources are observed at increasing rest-frame emission frequency with increasing redshift. For an optically thick synchrotron self-absorbed source, the source size decreases with increasing rest-frame frequency.

Furthermore, a flux-limited survey will always be affected by the Malmquist bias arising from the scaling of source spectral luminosity, L_ν, with redshift. In fact, this perceived redshift dependence of ISS may even be interpreted as a luminosity dependence. It is possible that the higher-luminosity sources are intrinsically larger, and may therefore scintillate less. The plot of the 4.9 GHz spectral luminosities (calculated using $H_0 = 70\,\mathrm{kms^{-1}Mpc^{-1}}$, $\Omega_M = 0.27$, $\Omega_\Lambda = 0.73$ and assuming isotropic emission) against source redshifts (Figure 5.3) shows that at any particular redshift, there is a luminosity dependence of ISS because the stronger sources ($S_{4.9} \geq 0.3$ Jy) scintillate less than the weaker sources ($S_{4.9} < 0.3$ Jy). There is a visible redshift cutoff of $D_{4.9}(4\mathrm{d})$ at $z \gtrsim 2$ for both the weak and strong sources. There are also possible luminosity cutoffs at $L_{4.9} \sim 10^{28}\mathrm{WHz^{-1}}$ and $L_{4.9} \sim 10^{27}\mathrm{WHz^{-1}}$ for the strong and weak sources respectively. However, it is difficult in reality to determine if the ISS amplitudes of AGNs (in our present sample at least) have a redshift cutoff, luminosity cutoff or both, since S_ν, z and L_ν are inter-dependent. This problem is further compounded for relativistically beamed sources, where Doppler boosting complicates the definition of the intrinsic source luminosities. Intrinsically more luminous sources can be detected at larger angles of orientation to the line of sight, and may thus have lower Doppler boosting factors which decrease their compact fractions with redshift. On the other hand, if the high-redshift sources are dominated by highly Doppler-boosted sources with intrin-

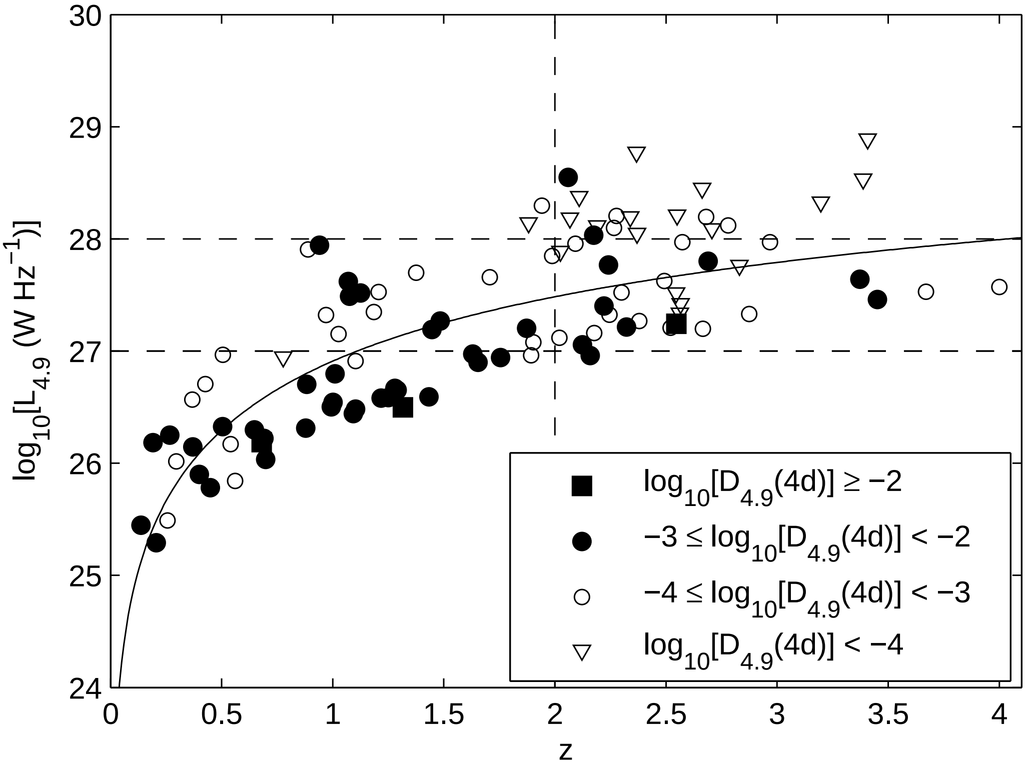

Figure 5.3 — *4.9 GHz spectral luminosity plotted against source redshifts, with sources separated into four* $D_{4.9}$(4d) *bins. Only the 102 sources with* $-0.4 < \alpha_{4.9}^{8.4} < 0.4$ *are included. The solid curve gives the* $L_{4.9}$-z *relation for a 0.3 Jy source, separating the strong* ($S_{4.9} \geq 0.3$ *Jy) sample of sources from the weak* ($S_{4.9} < 0.3$ *Jy) sample of sources. The vertical dashed line indicates the redshift cutoff of* $D_{4.9}$(4d) *at* $z \sim 2$*, while the dashed horizontal lines indicate possible luminosity cutoffs of* $D_{4.9}$(4d) *at log*[$L_{4.9} \sim 28\,\mathrm{WHz}^{-1}$] *and log*[$L_{4.9} \sim 27\,\mathrm{WHz}^{-1}$] *for the strong and weak sources respectively.*

sic luminosities comparable to their low-redshift counterparts, the compact fractions of the high-redshift sources may be larger.

5.3 Structure Function Ratios

I present a method to alleviate the effects of the selection biases discussed in Section 5.2, in particular the redshift dependence of source luminosities, Doppler boosting factors and rest-frame emission frequencies. Instead of examining the redshift dependences of the mean values of $D_{4.9}$(4d) and $D_{8.4}$(4d) separately, as was done in Section 3.6, it is more instructive to obtain the ratio of $D_{8.4}$(4d) to $D_{4.9}$(4d) for each individual source, then compare the mean and distribution of the ratios at high and low redshift. This normalizes each source by itself, thereby reducing the dependence of the results on these source parameters. The rest-frame emission frequencies also become irrelevant, since one is only interested in the ratio of the two observing frequencies. Parameters involving the properties of the ISM are also factored out. However, all these source parameters have to be assumed to be frequency independent. I provide a mathematical justification for these claims in Section 5.3.1 and present the results in Section 5.3.2.

5.3.1 Theoretical Basis

To obtain theoretical estimates of the structure function ratios for comparison with the observational data, I make use of standard ISS models in which the scattering region is approximated as a thin, phase-changing screen with an isotropic Kolmogorov spectrum. The quantity of interest is the spatial coherence, $\Gamma_4(r;\nu)$, of the flux measured at two locations separated by a distance r on the Earth at a frequency of ν (Goodman & Narayan (1989) provide the detailed formalisms). The model assumes that the phase structure function at the scattering screen is isotropic at the length-scales of interest and does not vary on the time-scales (τ) of interest, so that the spatial coherence can be simply related to the temporal coherence as measured by a single telescope by equating $r = v_s\tau$, where v_s is the transverse velocity of the scattering screen relative to the Earth. I then compute $D(4\mathrm{d}) = 2[\Gamma_4(0;\nu) - \Gamma_4(r = v_s \cdot 4\mathrm{d};\nu)]$.

Analytical solutions for $\Gamma_4(r;\nu)$ in the very weak and very strong scattering regimes are given in Coles et al. (1987) and Narayan (1992). They use the modulation index, m, as a measure of the source variability amplitude. Assuming that the structure functions saturate within 4 days, $D(4\mathrm{d}) \approx 2m^2$. In weak scintillation ($\nu \gg \nu_t$, where ν_t is the transition frequency between weak and strong ISS), the modulation index of a point source is given by Narayan (1992), and written in the following form by Walker (1998):

$$m_{p,w} = \left(\frac{\nu_t}{\nu}\right)^{17/12}, \tag{5.1}$$

For strong refractive scintillation ($\nu \ll \nu_t$), the point source modulation index is (Narayan, 1992; Walker, 1998):

$$m_{p,r} = \left(\frac{\nu}{\nu_t}\right)^{17/30}. \tag{5.2}$$

The modulation index of an extended source is then further suppressed relative to that of a point source by a factor that is dependent on the apparent angular size of the source, θ, as it appears to the scattering screen (Narayan, 1992; Walker, 1998):

$$m = m_p \left(\frac{\theta_{ext}}{\theta}\right)^{7/6}, \tag{5.3}$$

where m_p is equivalent to $m_{p,w}$ or $m_{p,r}$. θ_{ext} is the angular size above which the source can no longer be considered a point source. For weak ISS, θ_{ext} is equivalent to the angular size of the first Fresnel zone at the scattering screen, given by $\theta_F = \sqrt{c/(2\pi\nu D_{\rm ISM})} \propto \nu^{-0.5}$, where $D_{\rm ISM}$ is the distance from the Earth to the scattering screen and c is the speed of light. For strong refractive ISS, θ_{ext} is the refractive scale of the density inhomogeneities at the scattering screen, given by $\theta_r \propto \nu^{-2.2}$.

The ratio of $D_{8.4}$(4d) to $D_{4.9}$(4d), which I denote as R_D, can be calculated using the asymptotic limits of Equations 5.1 to 5.3 to obtain:

$$R_D \approx \frac{m_{8.4}^2}{m_{4.9}^2} = 0.217 \left(\frac{\theta_{F,8.4}}{\theta_{F,4.9}}\right)^{7/3} \left(\frac{\theta_{4.9}}{\theta_{8.4}}\right)^{7/3}, \tag{5.4}$$

for an extended source in the weak ISS regime, and:

$$R_D \approx 1.842 \left(\frac{\theta_{r,8.4}}{\theta_{r,4.9}}\right)^{7/3} \left(\frac{\theta_{4.9}}{\theta_{8.4}}\right)^{7/3}, \tag{5.5}$$

for an extended source in the strong refractive ISS regime. Any anisotropic properties of the ISM (i.e. the strength of turbulence and distance to the scattering screen), encapsulated in the terms ν_t, θ_F and θ_r, either cancel out or have known frequency dependences. R_D is therefore sensitive only to the ratio $\theta_{4.9}/\theta_{8.4}$.

The apparent source size, whose frequency scaling is dependent upon whether it is dominated by intrinsic effects or scatter broadening, can be modelled as:

$$\theta \sim \sqrt{\theta_{src}^2 + \theta_{scat}^2} \propto \nu^{-\beta}, \tag{5.6}$$

where θ_{src} is the intrinsic source angular size, and θ_{scat} represents additional contributions due to scatter broadening in the ISM or the IGM. If intrinsic source size effects dominate, $\theta \sim \theta_{src}$, and any source dependent parameters that θ_{src} is a function of, such as the luminosity, compact fraction and Doppler boosting factor, cancel out in Equations 5.4 and 5.5 assuming that they are frequency independent. R_D is therefore transparent to any redshift dependences of these parameters. The ratio of the emission-frame frequencies is a constant across all redshifts for a fixed pair of observing frequencies, so R_D is also insensitive to source properties that vary with increasing emission-frame frequencies. Typically, $\beta \sim 1$ for a synchrotron self-absorbed source, while $\beta \sim 0$ if the source size is frequency independent. On the other hand, $\beta \sim 2.2$ if the source size is dominated by scatter broadening so that $\theta \sim \theta_{scat}$.

I calculate R_D for different values of β in the asymptotically weak and strong refractive ISS regimes (see Figure 5.4). In the case of a point source ($\theta < \theta_{ext}$), $R_D \sim 0.2$ and $R_D \sim 1.8$ in the weak ISS and strong refractive ISS regimes respectively, and is independent of β. At the two observing frequencies and for sight-lines through mid-Galactic latitudes however, $\theta > \theta_{ext}$ for AGN in general. In this case, $R_D \lesssim 0.4$ when

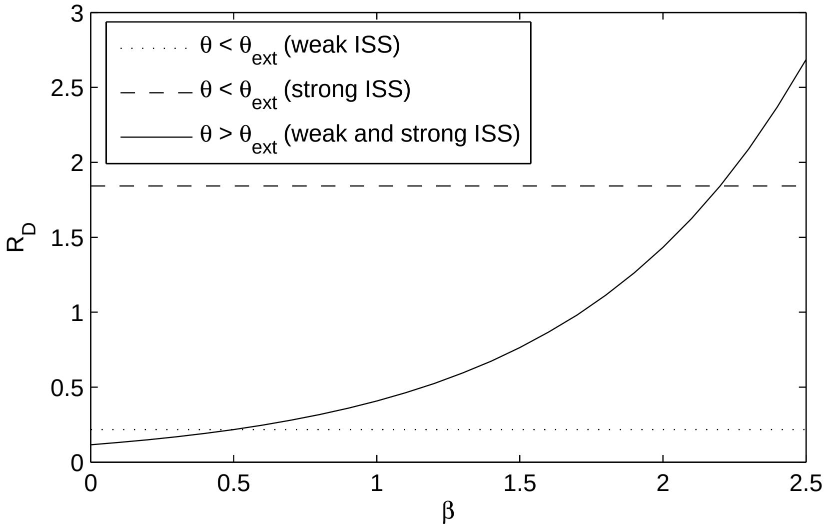

Figure 5.4 — *The relationship between R_D and β for the various ISS regimes and source sizes, based on analytical models applicable to the asymtotically weak and strong ISS regimes (Narayan, 1992; Walker, 1998).*

intrinsic source size effects dominate ($\beta \leq 1$) and $R_D \sim 1.8$ when scatter broadening dominates ($\beta = 2.2$).

In the intermediate scattering regimes typical of the observations, where there are no analytical solutions, I make use of the fitting functions for $\Gamma_4(r;\nu)$ provided by Goodman & Narayan (2006) based on numerical computations, which allow the calculation of R_D when $4.9\,\mathrm{GHz} \lesssim \nu_t \lesssim 8.4\,\mathrm{GHz}$. Figure 5.5 demonstrates how R_D varies with ν_t for $\beta = 0, 1$ and 2.2.

While the analytical approach provides a better understanding of the physics involved in the analysis of the SF ratios, it assumes asymptotically weak or strong refractive ISS of the sources. Furthermore, it assumes that the characteristic timescales of ISS are less than four days so that $D(4\mathrm{d})$ is well approximated by $2m^2$. The ISS timescales can vary with observing frequency, which affects R_D if the SFs have yet to saturate at one or both frequencies. From the Table in Appendix B, it can be seen that $\sim$ 20% of the sources have ISS timescales of more than four days on at least one frequency. On the other hand, the Goodman & Narayan (2006) fitting function makes no such assumption about the ISS timescales and simply calculates $\Gamma_4(v_s \cdot 4\mathrm{d};\nu)$. However, when the ISS timescales are longer than four days, note that R_D estimated from the fitting function becomes sensitive to the various scattering screen and source parameters, which will be true of the observations as well. In interpreting the data, I mainly use the fitting functions for comparisons with the observations.

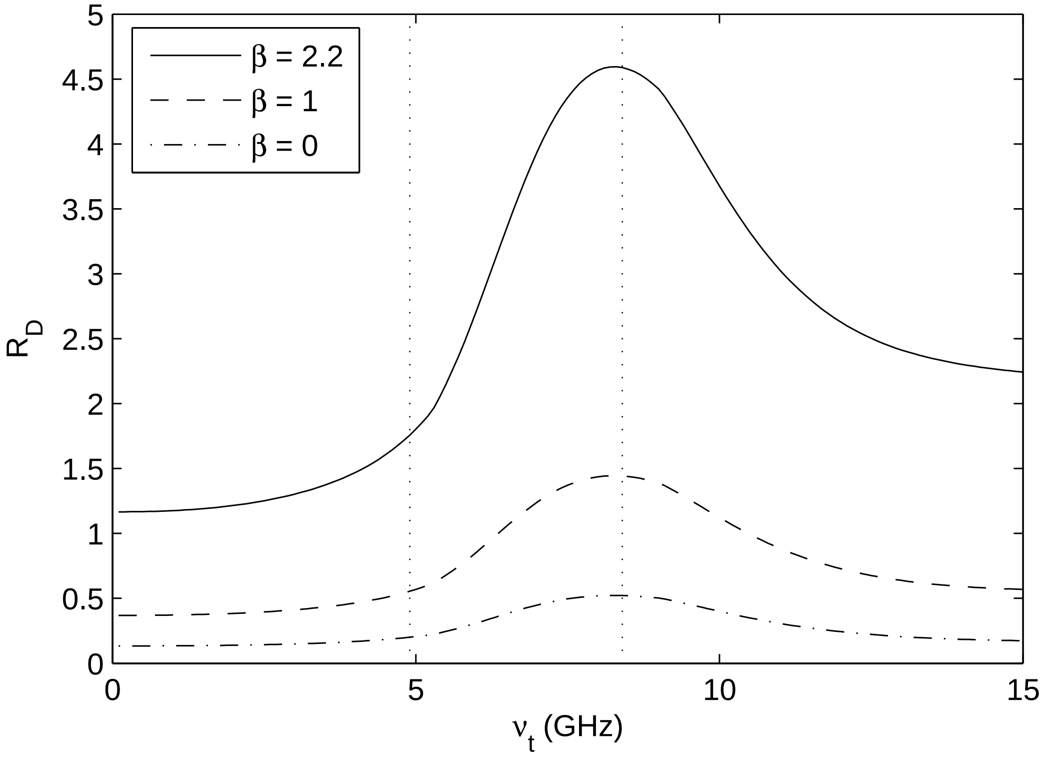

Figure 5.5 — *The structure function ratio, R_D, calculated for $\beta = 0, 1$ and 2.2 using the fitting function in Goodman & Narayan (2006) and plotted against the transition frequency between weak and strong scattering. We have adopted values of $v_s = 50\,\mathrm{kms}^{-1}$, $\theta = 100\,\mu as$ at 4.9 GHz, and a scattering screen distance of $d = 500\mathrm{pc}$. The vertical dashed lines represent $\nu = 4.9$ GHz and $\nu = 8.4$ GHz respectively.*

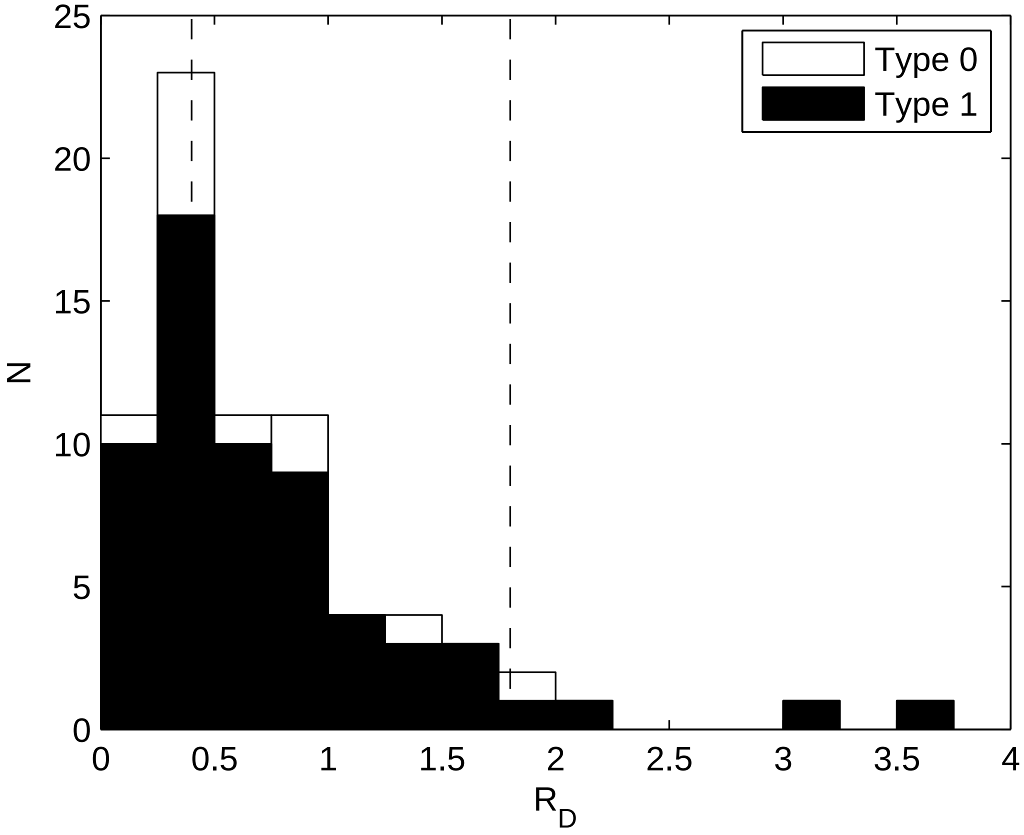

Figure 5.6 — *Histogram of* R_D *for 72 sources with* $D(4\mathrm{d}) \geq 3\sigma$ *at both frequencies, classified as Type 0 or Type 1 AGNs. The dashed vertical lines denote* $R_D = 0.4$ *and* $R_D = 1.8$.

5.3.2 Observational Results

The histogram of R_D as obtained from the observations exhibits a well defined peak in the $0.25 < R_D < 0.50$ bin (Figure 5.6), consistent with the weak ISS of sources dominated by intrinsic source size effects so that $\beta \leq 1$ (see Figure 5.5). As R_D is inaccurate for sources whose $D(4\mathrm{d})$ is close to or lower than the noise floor at one or both frequencies, the histogram includes only the 72 sources with $\geq 3\sigma$ variability amplitudes at both frequencies, selected from the $-0.4 < \alpha_{4.9}^{8.4} < 0.4$ sample, with 48 sources at low redshift and 24 at high redshift. Of the 48 low redshift sources, 11 are Type 0 AGNs (BL Lac objects) and 37 are Type 1 AGNs (FSRQs and Seyfert 1 galaxies).

However, the tail towards larger values of R_D indicates the presence of at least another important effect. Three effects potentially increase R_D so that it becomes comparable to or greater than unity. One is if $\nu_t \gtrsim 5$ GHz, so that the sources are scintillating in the strong ISS regime or at the transition between weak and strong ISS at one or both frequencies. The second possibility is that $\beta > 1$ due to scatter broadening at a second, more distant screen before the waves arrive at the scintillation-inducing screen. This second scattering screen can be Galactic or extragalactic. The third possibility is that the SFs have yet to saturate within 4 days, so that the assumption of $D(4\mathrm{d}) \approx 2m^2$ no longer holds. Since $\tau_{char} \propto \theta$, and assuming $\theta \propto \nu^{-1}$, the scintillation timescales are shorter at 8.4 GHz. This causes the 8.4 GHz SFs to rise faster and saturate earlier in comparison to that at 4.9 GHz, thereby increasing R_D.

It is determined that the sources with $R_D \gtrsim 1$ are not significantly scatter broadened, based on an examination of the R_D values in the weak ($S_{4.9} < 0.3$ Jy) and strong ($S_{4.9} \geq 0.3$ Jy) sample of sources. The weak and strong sources can be assumed to have similar mean intrinsic brightness temperatures, so that a ~ 0.1 Jy source tends to have a smaller angular diameter than a ~ 1.0 Jy source. This is not an unreasonable assumption, as it explains why the weak sources have been observed to scintillate more than the stronger sources (Lovell et al., 2008). Additionally, the lower ISS amplitudes in the strong sample of sources cannot be attributed to the presence of stronger mas-scale jet components, as confirmed by VLBI observations that found no significant difference in the mas-scale morphologies of the strong and weak flux density sources (Ojha et al., 2004b). From Equation 5.6, it can be seen that the effects of scatter broadening will be more dominant in sources with smaller intrinsic angular sizes. Therefore, if the sources in the sample are scatter broadened, one should observe higher values of R_D in the weaker sources than in the stronger sources. K-S tests do not show that the weak sources have R_D values significantly higher than that of the strong sources. This is true when all 72 sources are considered and when only the Type 1 AGNs are considered.

In fact, the converse is true. Figure 5.7 shows scatter plots of $D_{8.4}(4\mathrm{d})$ against $D_{4.9}(4\mathrm{d})$ for the 72 sources with $D(4\mathrm{d}) \geq 3\sigma$, classifying the sources into weak and strong samples. The dotted lines have slopes of 0.4 and 1.8, representing the possible values of R_D in the asymptotic weak and strong ISS regimes. The solid lines represent linear least-square fits for the two source categories. In obtaining the fits, each source is weighted by a factor:

$$w = \left(\sigma^2_{D,4.9} + \sigma^2_{D,8.4}\right)^{-0.5}, \tag{5.7}$$

where $\sigma_{D,4.9}$ and $\sigma_{D,8.4}$ are the normalized errors in $D_{4.9}(4\mathrm{d})$ and $D_{8.4}(4\mathrm{d})$ respectively. This means that sources that have smaller errors in $D(4\mathrm{d})$ have larger weights in the fitting process. The dashed lines are the 99% confidence bounds for those fits. It can be seen that the strong sources have a larger fitted R_D of 1.06 ± 0.34 as compared to a fitted R_D of 0.44 ± 0.17 for the weak sources at 99% confidence.

The values of R_D are found to be influenced by the strength of ISS as indicated by the line-of-sight Hα intensity to each source, obtained from the WHAM Northern Sky

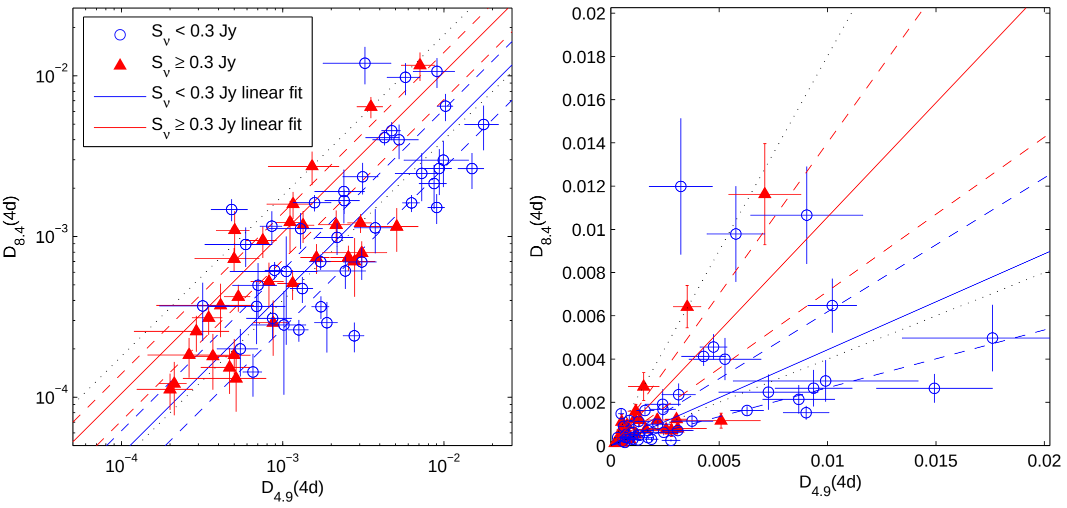

Figure 5.7 — *Plot of* $D_{8.4}$(4d) *against* $D_{4.9}$(4d) *in logarithmic (left) and linear (right) scales with sources classified as 'weak' or 'strong' based on their observed mean flux densities at 4.9 GHz,* $S_{4.9}$*. Only sources with* $D(4\mathrm{d}) \geq 3\sigma$ *at both frequencies are included. The dotted lines represent* $R_D = 0.4$ *and* $R_D = 1.8$*. The solid lines represent linear fits to the* $S_{4.9} < 0.3$ *Jy and* $S_{4.9} \geq 0.3$ *samples, while the dashed lines represent 99% confidence bounds for those fits.*

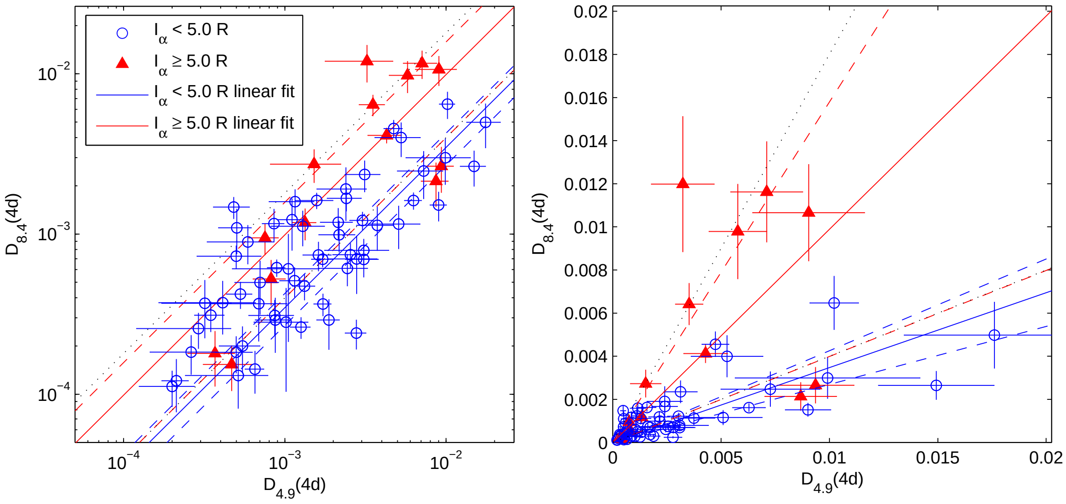

Figure 5.8 — *Plot of* $D_{8.4}$(4d) *against* $D_{4.9}$(4d) *in logarithmic (left) and linear (right) scales, where the sources are classified based on their line-of-sight Hα intensities,* I_α*, in units of Rayleighs. Only sources with* D(4d) $\geq 3\sigma$ *at both frequencies are included. The dotted lines represent* $R_D = 0.4$ *and* $R_D = 1.8$*. The solid lines represent linear fits to the* $I_\alpha < 0.5$ *R and* $I_\alpha \geq 0.5$ *R samples, while the dashed lines represent 99% confidence bounds for those fits.*

Survey (Haffner et al., 2003). The line-of-sight Hα intensity is in units of Rayleighs (R), denoted as I_α. The K-S test confirms that R_D in the $I_\alpha \geq 5$ R sample is significantly larger than that of the $I_\alpha < 5.0$ R sample, with a 1.3×10^{-2} probability that this occurred by chance when all sources are considered, and a probability of 4.0×10^{-2} when only the Type 1 AGNs are considered. The scatter plots and fits of R_D in Figure 5.8 also show that sources with $I_\alpha \geq 5$ R tend to have larger values of R_D. The fitted R_D is found to be 0.99 ± 0.59 for $I_\alpha \geq 5$ R as compared to 0.35 ± 0.08 for $I_\alpha < 5.0$ R at 99% confidence. The sight-lines with larger Hα intensities have higher electron column densities and are at lower Galactic latitudes where the sources are seen through thicker regions of the Galaxy. Therefore, one expects the transition frequencies to be higher through these sight-lines. This demonstrates that sources with $R_D \gtrsim 1$ are scintillating in the strong ISS regime or at the transition between weak and strong ISS. Additionally, the five most variable sources with $R_D > 1$ all have $I_\alpha \geq 5$ R, consistent with scintillation amplitudes being the highest at the transition frequency between weak and strong ISS.

In comparing the values of R_D in the $z < 2$ and $z > 2$ subsamples, I rule out scatter broadening in the IGM as the origin of the redshift dependence of ISS, in the present sample at least. Using the K-S test, it is found that R_D in the high-redshift sample is

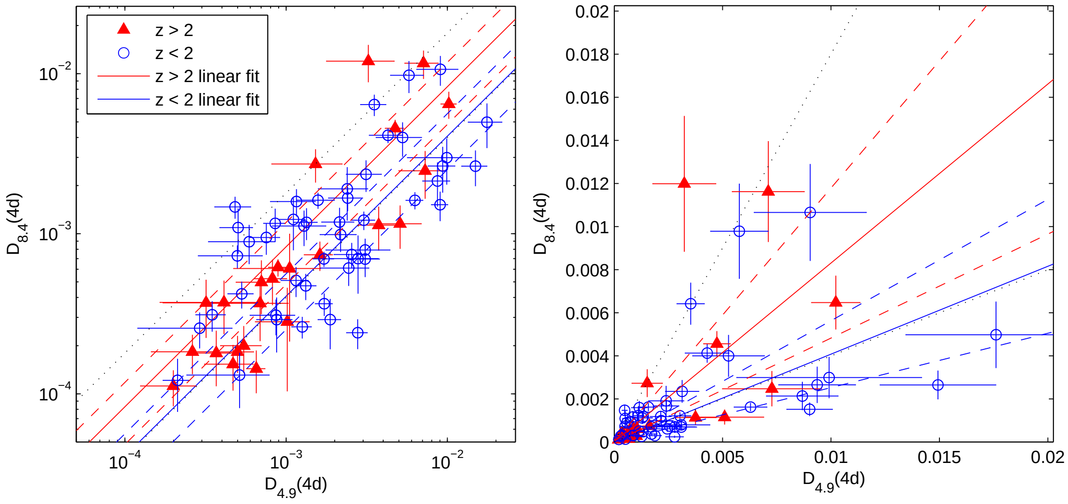

Figure 5.9 — *Plot of* $D_{8.4}(4\mathrm{d})$ *against* $D_{4.9}(4\mathrm{d})$ *in logarithmic (left) and linear (right) scales, where the sources are classified based on their redshifts. Only sources with* $D(4\mathrm{d}) \geq 3\sigma$ *at both frequencies are included. The dotted lines represent* $R_D = 0.4$ *and* $R_D = 1.4$*. The solid lines represent linear fits to the* $z < 2$ *and* $z > 2$ *samples, while the dashed lines represent 99% confidence bounds for those fits.*

not significantly higher than R_D in the low-redshift sample considering all sources and only the Type 1 AGNs. Figure 5.9 shows only a marginal increase in the fitted R_D of sources in the $z > 2$ sample as compared to the $z < 2$ sample, with 0.83 ± 0.35 for $z > 2$ and 0.41 ± 0.16 for $z < 2$ (99% confidence intervals). The fitted R_D values at low and high redshift are calculated separately for the weak and strong sample of sources, summarized in Table 5.1. The redshift dependence of R_D in the weak sources is not significantly steeper than that of the strong sources, providing more evidence against scatter broadening in the IGM or that it has any redshift dependence at the resolution of the observations.

In fact, the marginal increase in R_D with redshift is most plausibly attributed to intrinsic source size effects, since the stronger sources that have larger intrinsic angular sizes also have larger fitted R_D. This increase in R_D with redshift is explained in Section 5.4.

5.4 Decrease in Observed Brightness Temperature Due to Cosmological Expansion

I propose that the suppression of ISS at $z \gtrsim 2$, considering only the $-0.4 < \alpha_{4.9}^{8.4} < 0.4$ sources, can be sufficiently explained by the decrease in observed brightness temper-

Table 5.1. Comparison of fitted R_D values at low and high redshift.

AGN Class	Mean Flux Density	$z < 2$	$z > 2$
Type 1	$S_{4.9} < 0.3$ Jy	0.39 ± 0.20 (27)	0.70 ± 0.45 (13)
Type 1	$S_{4.9} \geq 0.3$ Jy	0.64 ± 0.51 (10)	1.25 ± 0.62 (11)
Type 0 & Type 1	$S_{4.9} < 0.3$ Jy	0.38 ± 0.19 (29)	0.70 ± 0.45 (13)
Type 0 & Type 1	$S_{4.9} \geq 0.3$ Jy	0.82 ± 0.45 (19)	1.25 ± 0.62 (11)

Note. — The numbers in brackets in the third and fourth columns indicate the number of sources in each category.

ature of a flux-limited sample of sources due to cosmological expansion. The angular size of a source, θ_{src} is related to its observed brightness temperature, $T_{b,obs}$ through the following well-known expression:

$$\theta_{src} = \sqrt{\frac{c^2 S_\nu}{2\pi\nu^2 k T_{b,obs}}}, \tag{5.8}$$

where ν is the observing frequency, S_ν is the observed flux density, c is the speed of light and k is the Boltzmann constant. On cosmological scales, the observed brightness temperature is a factor of $(1+z)$ lower than the brightness temperature in the frame of emission, $T_{b,em}$, due to the expansion of the Universe. $T_{b,em}$ is in turn a function of the intrinsic brightness temperature of the source, $T_{b,int}$, Doppler-boosted by a factor δ due to the effects of relativistic beaming in AGN jets. Since only the most compact components of the source core scintillate in the presence of turbulence in the ISM, and it is the sizes of these compact regions that is inferred from the source variability, S_ν is multiplied by the compact fraction, f_c of the source. Equation 5.8 then becomes:

$$\theta_{src} = \sqrt{\frac{(1+z)c^2 f_c S_\nu}{2\pi\nu^2 k\delta T_{b,int}}}, \tag{5.9}$$

This is the angular diameter of the source as it appears to the scattering screen in the ISM, assuming no additional increase in apparent size due to extrinsic propagation effects. Therefore, $\theta_{src} \propto (1+z)^{0.5}$ and one can expect the ISS amplitudes to decrease with redshift, contingent upon the following assumptions:

1. The mean flux densities of the sources do not vary with redshift, i.e. the sample is flux-limited.

2. The intrinsic brightness temperatures, $T_{b,int}$, have a cutoff, either at the inverse Compton limit at $\sim 10^{12}$ K (Kellermann & Pauliny-Toth, 1969), or at the energy equipartition limit at $\sim 10^{11}$ K (Readhead, 1994; Lähteenmäki et al., 1999).

Table 5.2. Input parameters for ISS model in Section 5.4.

Parameter	Symbol	Value
Scattering screen distance from Earth	$D_{\rm ISM}$	500 pc
Scattering screen velocity	v_s	50 $\rm kms^{-1}$
Transition frequency between weak and strong ISS	ν_t	4.0 GHz
Source intrinsic brightness temperature	$T_{b,int}$	10^{11} K
Source compact fraction	f_c	0.5
4.9 GHz and 8.4 GHz mean flux density (strong sources)	S_ν	1.00 Jy
4.9 GHz and 8.4 GHz mean flux density (weak sources)	S_ν	0.15 Jy

3. The mean Doppler boosting factors and compact fractions of the sources remain constant and do not evolve with redshift.

4. Any possible effect of decreasing angular sizes of the optically thick cores with increasing rest-frame emission frequencies is ignored.

Based on this model, I perform numerical computations using the fitting function in Goodman & Narayan (2006), plotting D(4d) of the weak and strong sources against redshift for various values of the Doppler boosting factor in Figure 5.10. The fiducial values shown in Table 5.2 are used as the model parameters. The phase fluctuations at the scattering screen are assumed to obey a power law with a Kolmogorov spectrum, and the sources are assumed to have a Gaussian intensity profile. The mean D(4d) obtained from the observations are shown for two redshift bins, separating the weak ($S_{4.9} < 0.3$ Jy) and strong ($S_{4.9} \geq 0.3$ Jy) sources.

The observed redshift dependence of the mean values of D(4d) in the 102 sources with $-0.4 < \alpha^{8.4}_{4.9} < 0.4$ appears to be consistent with the model and its assumptions. Even with the possible bias towards more variable sources at $z < 2$, the decrease in mean ISS amplitudes is no greater than that expected from this model. As further confirmation, this agreement holds, within the 1σ error bars, even when only the 72 sources with $\geq 3\sigma$ variability are used in obtaining the mean values of D(4d). From Figure 5.10, it can be seen that the model successfully explains the weaker redshift dependence of $D_{8.4}$(4d) as compared to that of $D_{4.9}$(4d), without having to invoke scatter broadening in the IGM. Furthermore, it explains why the ISS amplitudes of the strong sources have a weaker redshift dependence than that of the weak sources, as also reported by Pursimo et al. (submitted) for the larger MASIV sample.

The observations and assumptions of the model, particularly that of constant mean Doppler boosting factors with increasing redshift, are also consistent with other statistical studies of Doppler-boosted AGN sources. Monte Carlo simulations by Lister &

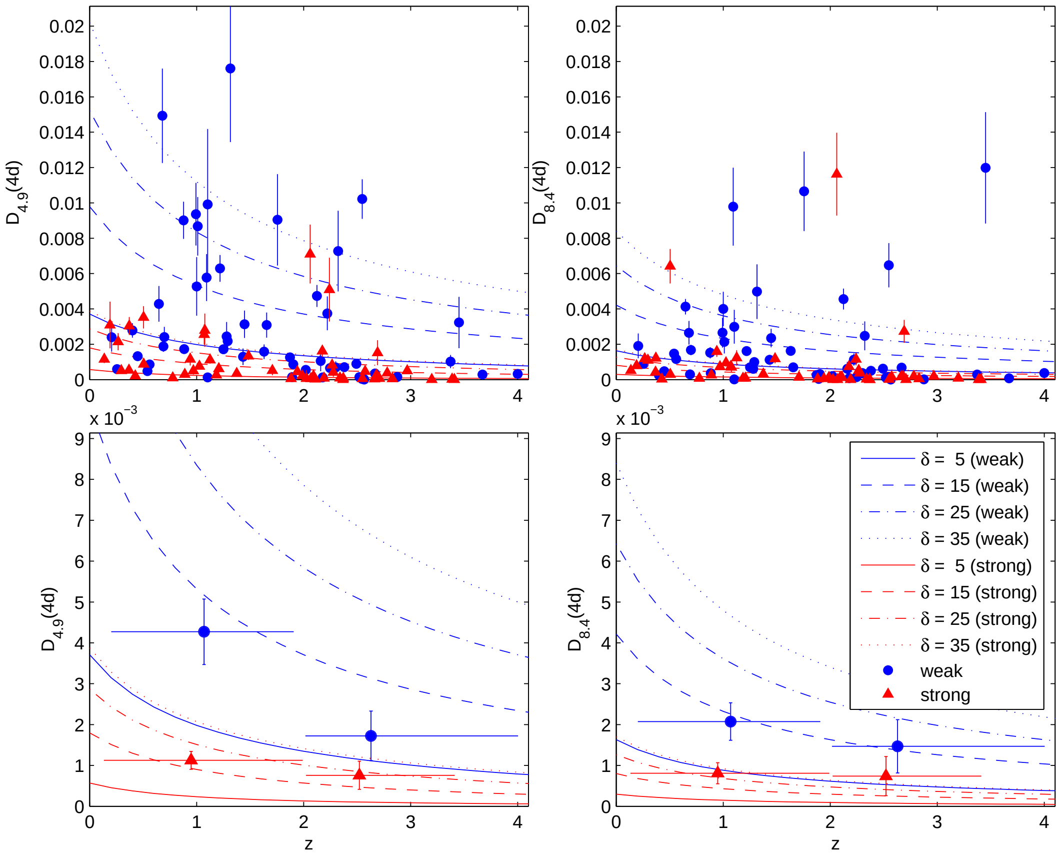

Figure 5.10 — *Observed* $D(4\mathrm{d})$ *at 8.4 GHz (left) and 4.9 GHz (right) plotted against redshift, shown as scatter plots (top) and in bin averages (bottom), for both the weak* ($S_{4.9} < 0.3$ *Jy) and strong* ($S_{4.9} \geq 0.3$ *Jy) sources. The vertical error bars in the binned plots represent one standard error in the mean. The lines in all panels show computed model values of* $D(4\mathrm{d})$ *for various values of the source Doppler boosting factor, assuming that cosmological expansion leads to a* $(1+z)^{0.5}$ *scaling of the intrinsic angular diameter in a flux and brightness temperature-limited sample of sources. The model parameters used are listed in Table 5.2.*

Marscher (1997) and recent observational data (Hovatta et al., 2009) suggest that the mean Doppler factors for a flux-limited sample of sources remains relatively constant at $z > 0.6$. The highly beamed sources with large Doppler factors are very rare, since their jets need to be aligned very close to the line of sight to be detectable. Considering that these large δ sources would also appear very luminous, one would expect to detect more of these sources with increasing redshift where the volume is also larger (thus increasing the likelihood of detecting these rare sources). However, this is offset by the large range in intrinsic luminosities of the sources, so that sources with large intrinsic luminosities and low Doppler factors (due to large angles of orientation) will also be included in the high-redshift sample. While the range of source Doppler factors increases with redshift in a flux-limited sample, the mean remains the same. According to Lister & Marscher (1997) and Arshakian et al. (2010), at redshifts $z < 0.6$, the mean Doppler boosting factor is lower due to the scarcity of sources with large Doppler factors ($\delta > 20$) within the small volume at such redshifts. This may explain why the most variable sources are not found below $z < 0.6$ at both frequencies, as can be seen in the scatter plots of Figure 5.10. This effect is seen in the original MASIV data as well (Figure 13 in Lovell et al. (2008)).

The marginal increase in R_D with redshift as seen in Figure 5.9 and Table 5.1 can also be sufficiently explained with the same model of decreasing $T_{b,obs}$ with redshift. Figure 5.11 shows model values of R_D (blue and red curves), calculated using the Goodman & Narayan (2006) fitting formula and the same input parameters in Table 5.2. The binned plots depict the fitted R_D at low and high redshifts, with the error bars given by the 68% confidence bounds (roughly equivalent to 1σ errors). The model calculations show that R_D can indeed increase with redshift without including any scatter broadening effects. This redshift dependence of R_D arises due to the increase in source angular size with redshift, which in turn increases the timescale of the scintillations for a fixed scattering screen velocity. As explained in Section 5.3, the timescales can increase sufficiently so that the SFs do not saturate within four days, leading to higher values of R_D. This also explains why the sources with high R_D also tend to be strong sources with larger angular sizes rather than weak sources, as seen for the fitted R_D from the observations. To further illustrate this point, Figure 5.11 includes the model values of R_D for the case where the scattering screen velocity is reduced to 20 $\mathrm{km\,s^{-1}}$ for the strong sources, shown as black curves. In this case, the SFs take a longer time to saturate, thereby increasing R_D even further. While the increase in fitted R_D from low to high redshift appears larger than that predicted by the model for the weak sources, this difference is $\lesssim 2\sigma$. In any case, this difference cannot be attributed to scatter broadening since the fitted R_D of the strong sources is clearly larger than that of the weak sources at both low and high redshift.

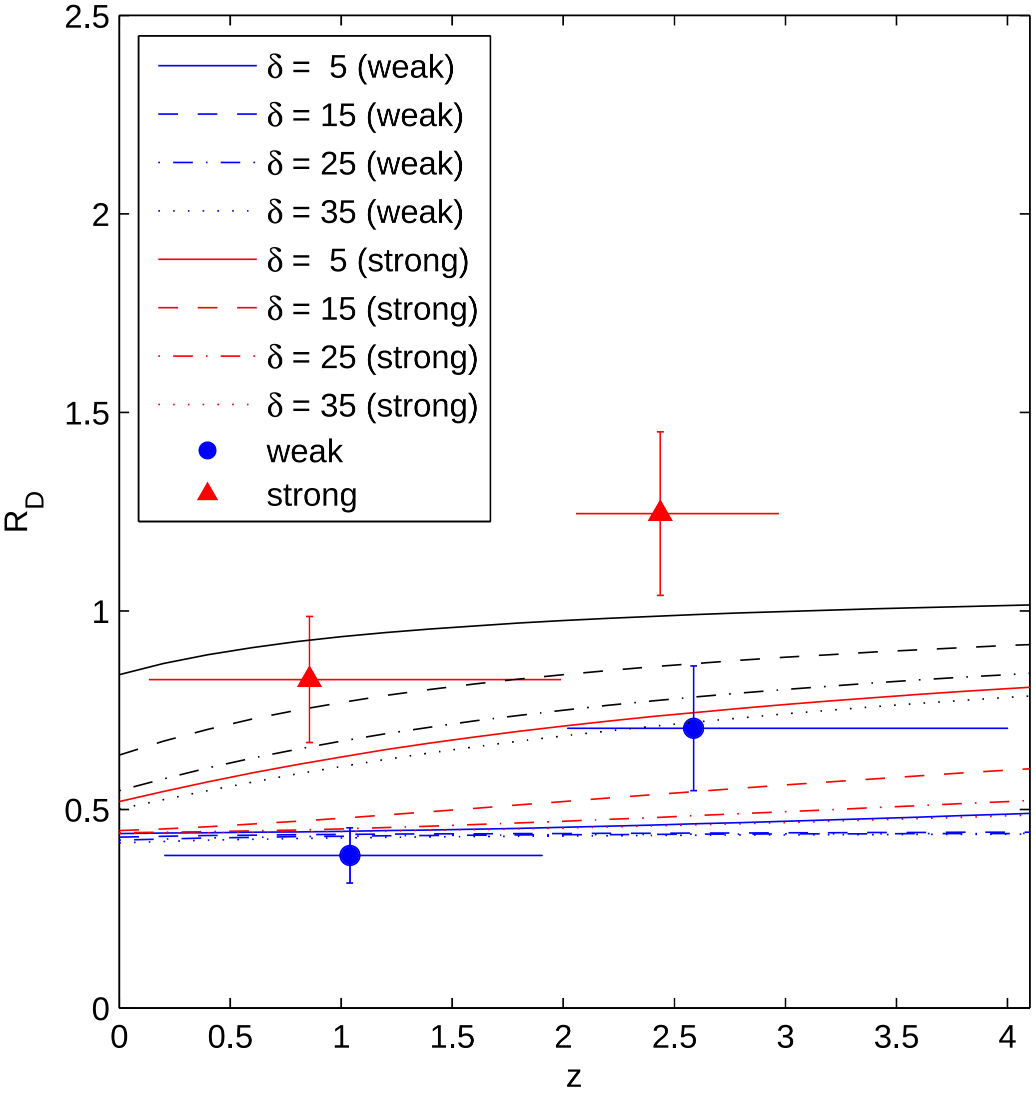

Figure 5.11 — *Observational values of the fitted* R_D *in two redshift bins with their corresponding 68% confidence bounds (roughly* 1σ *errors), separated into weak (*$S_{4.9} < 0.3$ *Jy) and strong (*$S_{4.9} \geq 0.3$ *Jy) sources. These are shown together with model values of* R_D *for various source Doppler boosting factors. For the blue and red curves, the model parameters are given in Table 5.2. The black curves show the corresponding model values for the strong sources at a screen velocity of 20* kms^{-1} *with the other parameters unchanged.*

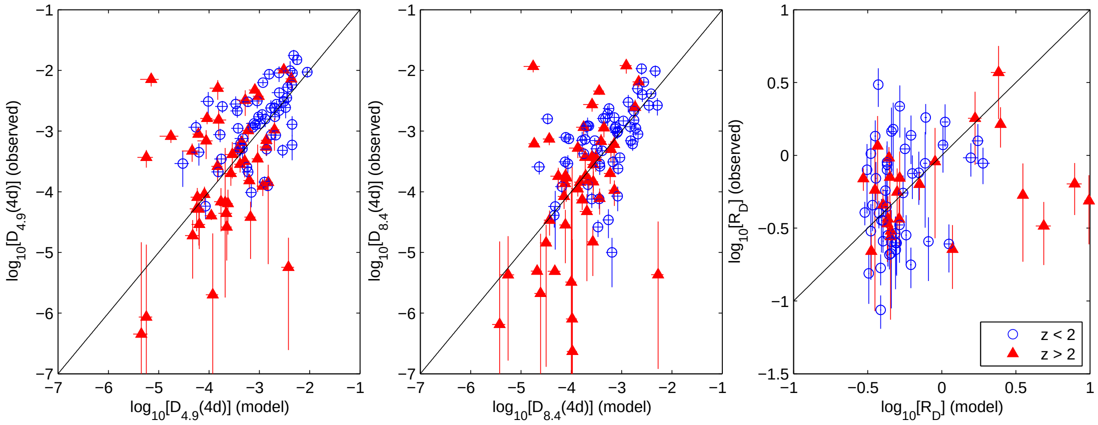

Figure 5.12 — *Observed values of $D_{4.9}$(4d) (left panel), $D_{4.9}$(4d) (middle panel) and R_D (right panel) plotted against their respective model values obtained by applying the Monte Carlo method to the Goodman & Narayan (2006) fitting functions (described in Section 5.4). For $D_{4.9}$(4d) and $D_{8.4}$(4d), all 102 flat spectrum sources are shown. For R_D, only the 72 sources with $\geq 3\sigma$ variability are shown.*

I apply the Monte Carlo method to the fitting functions to obtain simulated distributions of $D_{4.9}$(4d), $D_{8.4}$(4d) and R_D of each source for further comparisons. Figure 5.12 shows observed values of $D_{4.9}$(4d), $D_{8.4}$(4d) and R_D of the 102 sources with $-0.4 < \alpha_{4.9}^{8.4} < 0.4$ (72 sources with $\geq 3\sigma$ variability in the case of R_D) plotted against their corresponding median simulated values. The horizontal error bars are given by the median absolute deviation of the simulated values of $D_{4.9}$(4d), $D_{8.4}$(4d) and R_D for each source.

For each source, the 4.9 GHz and 8.4 GHz mean flux densities, as well as source redshift, are kept constant at their observed values, since these parameters are known. The transition frequency and scattering screen distance of each source are also kept constant, estimated from the line-of-sight Hα intensity and Galactic latitude of the source (see Appendix D for details). The intrinsic brightness temperatures and scattering screen velocities are fixed at the typical values of 10^{11} K and 50 kms^{-1} respectively for all sources. I then randomly generate 1000 values of the Doppler boosting factor and source compact fraction for each of the sources, with Gaussian distributions peaked at 15 and 0.5, and standard deviations of 4 and 0.1 respectively.

The observed values of $\log_{10}[D_{4.9}(4\text{d})]$, $\log_{10}[D_{8.4}(4\text{d})]$ and $\log_{10}[R_D]$ show statistically significant correlations with their simulated counterparts. Pearsons linear correlation coefficients of 0.54 are obtained for both $\log_{10}[D_{4.9}(4\text{d})]$ and $\log_{10}[D_{8.4}(4\text{d})]$ respectively, with probabilities of 4.0×10^{-9} and 3.9×10^{-9} that they were obtained by chance. I obtain a weaker correlation coefficient of 0.23 for $\log[R_D]$, with a probability of 0.05 that this was obtained by chance. The correlation is weaker for R_D due to the presence of sources with observed R_D values below 0.4, possibly due to errors in the estimation of R_D or intrinsic source sizes with frequency dependences flatter than the ν^{-1} used in the model.

The simulated dataset exhibits similar trends to that of the observations. K-S tests performed on the simulated SFs show that $D_{4.9}(4\mathrm{d})$ and $D_{8.4}(4\mathrm{d})$ of the $z < 2$ sources are larger than that of the $z > 2$ sources, with probabilities of 6.1×10^{-5} and 9.0×10^{-5} that these were obtained by chance. As in the observational data, the high-redshift R_D values are not significantly larger than the low-redshift R_D values, even though the six sources with the largest simulated R_D values are all at $z > 2$ (Figure 5.12). Additionally, the K-S tests show that R_D values for both the $S_{4.9} \gtrsim 0.3$ Jy and $I_\alpha \gtrsim 5.0$ R source samples are larger than R_D values in the $S_{4.9} < 0.3$ Jy (with a probability of 2.8×10^{-4} that this result was obtained by chance) and $I_\alpha < 5.0$ R (with a probability of 1.1×10^{-3} that this result was obtained by chance) source samples, broadly consistent with that of the observations.

This model of $\theta_{src} \propto (1+z)^{0.5}$ is consistent with that of the original 4.9 GHz MASIV dataset as well, for ~ 250 sources in which redshift data are available, except at $z > 3$ where the observed $D(2\mathrm{d})$ is $\sim 2\sigma$ below the predicted curves (Pursimo et al., submitted). However, this steeper than predicted drop in $D(2\mathrm{d})$ can be attributed to the additional effect of the z-α correlation, which cannot be further analyzed for the original MASIV sample due to observations at only a single frequency. The model and Monte Carlo simulations will hence need to be applied to the full MASIV dataset to further test this model of decreasing observed brightness temperatures, pending the acquisition of optical spectroscopic redshifts for the remaining sources for which they are not available. The larger sample may also allow the redshift-luminosity degeneracy to be broken, providing a stronger test of whether a redshift cutoff or luminosity cutoff is observed in $D(\tau)$.

5.5 The z-α Correlation: Selection Effect or Source Evolution?

I discuss here why the mean source spectral indices steepen with increasing redshift (Figure 5.1), and why 13 out of the 15 sources with $\alpha_{4.9}^{8.4} < -0.4$ in the sample lie at $z > 2$. This effect partially accounts for the redshift dependence of ISS in the present sample, as it has been established in Section 3.4 that the mean $D(4\mathrm{d})$ of the $\alpha_{4.9}^{8.4} < -0.4$ sources is a factor of ~ 6 lower than that of the $\alpha_{4.9}^{8.4} \geq -0.4$ sources. The $\alpha_{4.9}^{8.4} < -0.4$ sources therefore either have source sizes that are on average a factor of ~ 2 larger or compact fractions that are a factor of ~ 2.5 lower than their $\alpha_{4.9}^{8.4} \geq -0.4$ counterparts.

This z-$\alpha_{4.9}^{8.4}$ correlation in the present sample could simply be a selection effect. As mentioned in Section 5.2, the original MASIV Survey sources were selected to have $\alpha_{1.4}^{8.4} > -0.3$, but the sample could have been contaminated by sources whose spectral indices were inaccurately estimated due to the non-coeval, variable flux densities. The comoving spatial density of flat-spectrum radio sources has been found to decrease by a factor of ~ 5 between redshifts $2 < z < 4$ (Peacock, 1985; Dunlop & Peacock, 1990), perceived as evidence for a peak in quasar activity at $z \sim 2.5$. A similar but slower decline was found for steep-spectrum sources (Dunlop & Peacock, 1990), which may explain why there are more of these steeper $\alpha_{4.9}^{8.4}$ sources at high redshift. Two of the high-redshift, steep-spectrum sources have been optically identified as narrow-line radio galaxies (Type 2 AGNs with narrow emission lines), and so may be classical steep-spectrum sources. After removing these two sources from the original sample of 128 sources, the K-S Test still finds a statistically significant difference in the spectral indices in the low and high-redshift source samples. The fact that the $z < 2$ sample is biased towards variable sources, while all sources with known redshifts at $z > 2$ were selected regardless of variability, could also have biased the low-redshift sample towards flatter $\alpha_{4.9}^{8.4}$, and vice versa for the high-redshift sample.

It is also possible that some of these sources have convex spectra that steepen at higher frequencies, as found in gigahertz peaked-spectrum (GPS) sources; k-correction effects then lead to a steepening of spectral indices due to increasing rest-frame emission frequencies with increasing redshift. Jarvis & Rawlings (2000) have demonstrated that a significant portion of the most luminous radio-selected flat-spectrum sources are GPS sources. Since these GPS sources are not Doppler-boosted, they are less compact and therefore scintillate less. Furthermore, Chhetri et al. (2012) recently found a steepening of source spectral indices with redshift in compact radio sources from the Australia Telescope 20 GHz (AT20G) Survey. This z-α correlation was discovered to be more prominent when $\alpha_{4.8}^{8.6}$ is used as compared to $\alpha_{1.0}^{4.8}$, which they attribute to spectral curvature and k-correction effects.

A natural and physical explanation for this z-$\alpha_{4.9}^{8.4}$ correlation is also conceivable. The steepening of source spectral indices with redshift has long been observed in radio galaxies (classical steep-spectrum sources) (Laing & Peacock, 1980; Macklin, 1982), where spectral index cut-offs have been successfully used to search for radio galaxies at the highest redshifts. Traditional explanations for this correlation include (1) k-correction effects in sources with convex spectral energy densities (Gopal-Krishna, 1988) (2) inverse Compton losses associated with Cosmic Microwave Background (CMB) photons whose energy densities scale with $(1+z)^4$ (Krolik & Chen, 1991) and (3) a luminosity-spectral index relation coupled with the Malmquist bias (Laing & Peacock, 1980; Blundell et al., 1999). More recently, Klamer et al. (2006) argue that this z-α correlation could be due to higher ambient densities at high redshift, resulting in increased synchrotron and inverse Compton losses in pressure-confined radio lobes. The evidence comes from the observed properties of high-redshift radio galaxies, which include (1) similarities to low-redshift radio galaxies residing in dense clusters, (2) extreme rotation measures (RMs), and (3) knotty radio emission interpreted as frustrated jets in dense and clumpy environments. For radio galaxies, one would expect to observe increasingly compact sources at high redshift. All known radio-loud AGNs at $z > 4$ are steep spectrum sources, with VLBI images revealing compact double structures reminiscent of compact steep-spectrum (CSS) and GPS sources (Frey et al., 2008, 2010, 2011), thought to be young and 'frustrated' radio galaxies.

If the flat-spectrum, Doppler-boosted population of radio-loud AGNs reside in similar environments at high redshift, it is likely that pressure from the surrounding IGM, whose densities scale with $(1+z)^3$, will reduce their Doppler boosting factors. This in turn reduces the compact fractions of the sources and reduces their scintillation amplitudes. This will also result in a steepening of spectral indices, as the contribution of the optically thick core components to the mean observed flux densities is reduced relative to that of the optically thin jet components.

Multifrequency VLBI studies based on new observations and archival data will be needed to determine if this z-$\alpha_{4.9}^{8.4}$ correlation and its relationship to the redshift dependence of ISS, is mainly due to selection effects or interesting physical phenomena related to AGN evolution.

5.6 Chapter Summary

In this chapter, I analysed the dual-frequency MASIV follow-up observations to determine the origin of the redshift dependence of AGN ISS. I made use of two ISS models to interpret the data, one an analytical approximation (Narayan, 1992; Walker, 1998) for the asymptotically weak and strong ISS regimes, the other a fitting function (Goodman & Narayan, 2006) that is applicable at the transition between the weak and strong ISS regimes. I also took into consideration the various selection effects in the source sample. The main findings of the chapter can be summarised as follows:

1. The examination of the ratio of the SFs for each individual source is a good strategy for mitigating source selection effects in the sample, negating the redshift dependence of source luminosities, compact fractions, Doppler boosting factors and rest frame emission frequencies. Three effects can increase the ratio of $D_{8.4}$(4d) to $D_{4.9}$(4d) from $R_D \sim 0.4$ in the weak ISS regime to $R_D \gtrsim 1$: (1) scatter broadening, (2) scintillation at the strong ISS regime, or at the transition between weak and strong ISS, (3) and sufficiently large scintillation timescales so that the SFs do not saturate at one or both frequencies so that $D_{8.4}$(4d) rises faster than $D_{4.9}$(4d).

2. The examination of the correlation of the SF ratios, R_D, with source mean flux densities, line-of-sight Hα intensities and source redshifts allow these three competing causes of large R_D to be discriminated.

3. No significant evidence of scatter broadening was observed in the sources at the scales of tens and hundreds of μas probed by the MASIV follow-up observations, due either to the ISM or the IGM. I found no significant increase of IGM scatter broadening in the $z > 2$ sources compared to that of the $z < 2$ sources, ruling it out as the cause of the redshift dependence of ISS. In performing the analysis of R_D for the $\geq 3\sigma$ variable sources, note that only the most variable sources are included at any redshift, which could mean that they are the least scatter broadened sources. Similar observations with higher sensitivity instruments such as the planned SKA, will enable R_D to be accurately estimated for sources with even lower $D(\tau)$ at both frequencies, to determine if the sources with lower variability amplitudes are scatter broadened. Another weakness of the present analyses is that $\sim$ 85% of the $-0.4 < \alpha_{4.9}^{8.4} < 0.4$, high-redshift sources lie between $2 < z < 3$. There is a dearth of sources at $z > 3$. The inclusion of more $z > 3$ sources in similar future surveys will more robustly determine if there is significant scatter broadening of sources beyond $z \sim 3$.

4. A statistically significant steepening of source spectral indices ($\alpha_{4.9}^{8.4}$) with source redshift was found, which partially accounts for the redshift dependence of AGN ISS. This z-$\alpha_{4.9}^{8.4}$ correlation can be attributed to selection effects or frustrated AGN jets in high-redshift environments. Follow-up high-resolution imaging of these sources using VLBI or space VLBI may help to discriminate between these two effects.

5. Selecting sources in the spectral index range of $-0.4 < \alpha_{4.9}^{8.4} < 0.4$, the redshift dependence of AGN ISS is found to be still significant, and can be successfully modeled by a $(1+z)^{0.5}$ scaling of intrinsic angular sizes of a flux and brightness temperature-limited sample of sources due to the space-time metric of an expanding Universe.

Chapter 6

Detectability of the IGM and Extragalactic Radio Transients

I am putting myself to the fullest possible use, which is all I think that any conscious entity can ever hope to do.
— ***HAL 9000, in '2001: A Space Odyssey'***

A manuscript entitled 'Detectability of the Ionized Intergalactic Medium and Extragalactic Radio Transients', based on the work presented in this chapter, is in preparation and will be submitted to a refereed journal. Some of the contents of Section 6.3, including Figures 6.6 and 6.7, were included in a published paper together with the contents of Chapter 5 (Koay et al., 2012).

6.1 Introduction to the IGM

The theory of nucleosynthesis (Copi et al., 1995) and measurements of the abundances of light chemical elements (Burles & Tytler, 1998; Burles et al., 1999) indicate that the density of baryons in the Universe are only a fraction of the critical density, and in fact constitute only $\sim 4\%$ of the matter-energy budget of the Universe. Of these, only $\lesssim 10\%$ are found in galaxies between $z \sim 0$ to 3, while $\gtrsim 90\%$ reside in the IGM (Fukugita et al., 1998; Fukugita & Peebles, 2004). While the formation of large-scale structures in the Universe is dominated by the influence of dark matter, the baryons act as a tracer, and are therefore critical, for studying the evolution of these structures.

The baryonic components of the Universe are often classified into four phases based on their temperatures, T, and overdensities, δ, relative to the mean baryon density of the Universe (Cen & Ostriker, 1999; Davé et al., 2001; Cen & Ostriker, 2006), of which the latter three constitute the IGM:

1. *Condensed* – stars and cool galactic gas residing in galaxies, with $T < 10^5$ K and $\delta > 1000$.

2. *Warm* – diffuse, photoionized gas, giving rise to Lyα absorption lines in quasar spectra, with $T < 10^5$ K and the distribution of δ peaked at ~ 1.
3. *Warm-Hot* – gas shock-heated to temperatures of $10^5 < T < 10^7$ K as they fall into gravitational potential wells to form filamentary structures, 80% of which have $10 < \delta < 30$.
4. *Hot* – intracluster gas found in rich clusters of galaxies where large-scale filamentary structures intersect, shock-heated to temperatures of $T > 10^7$ K, and distribution of δ peaked at ~ 1000.

While both the warm and hot components of the IGM have respectively been detected through Lyα absorption systems (see the review by Rauch (1998) and the references therein) and in X-ray emission (see review by Sarazin (1986)), the warm-hot intergalactic medium (WHIM) has been extremely difficult to detect. The WHIM is highly ionized due to the high temperatures, so cannot be detected in absorption except in X-ray lines of heavy elements such as oxygen. It is also too diffuse for its thermal emission to be detected with current X-ray instruments. Cosmological hydrodynamical simulations (Cen & Ostriker, 1999; Davé et al., 2001; Cen & Ostriker, 2006) show that while warm gas consitutes $\sim 90\%$ of the mass fraction of baryons at $z \sim 3$, the WHIM becomes the dominant component at $z \sim 0$ with a mass fraction of $\sim 50\%$. Measurements of the mass densities of stars, galaxies and Lyα absorption systems at $z \sim 3$ find that the baryon densities can be accounted for, but summing over all observable contributions at $z \sim 0$ reveals only about 50% of the baryonic density (Fukugita et al., 1998; Fukugita & Peebles, 2004), further evidence that half the baryons reside in this mostly undetected warm-hot phase of the IGM at the present epoch.

There have been many attempts to search for these 'missing baryons' constituting the WHIM at $z \sim 0$ using current UV and X-ray instruments, with various claimed detections of O$_{\rm VI}$, O$_{\rm VII}$ and O$_{\rm VIII}$ emission and absorption lines associated with the WHIM (see Mathur et al. (2003); Nicastro et al. (2002); Danforth & Shull (2005); Nicastro et al. (2005) for examples). However, these detections are either ambiguous, unconfirmed or arise from the tail end of the distribution of WHIM overdensities or temperatures (a critical evaluation of these and other 'detections' can be found in the review by Bregman (2007)). The most significant detection so far comes from O$_{\rm VII}$ absorption lines associated with the Sculptor Wall in the spectra of quasar B2356-309 (Fang et al., 2010; Zappacosta et al., 2010). Detecting and studying the WHIM therefore forms one of the key science drivers of next generation X-ray intruments.

In the radio regime, various methods have been proposed as to how the WHIM and the ionized IGM as a whole can be detected and studied. Goddard & Ferland (2003) suggest searching for the hyperfine line of nitrogen N$_{\rm VII}$ in absorption, but the Earth's atmosphere is opaque at its resonant frequency at 53.2 GHz for absorbers at $z \sim 0$.

The potential of harnessing intergalactic scintillation (Ferrara & Perna, 2001) as well as radio dispersion of impulsive phenomena such as gamma-ray bursts and their afterglows (Ioka, 2003; Inoue, 2004) to probe the ionized IGM have also been explored. The possibility of detecting scattering effects such as angular broadening of compact sources and temporal smearing of impulsive signals due to the ionized IGM with the SKA are briefly discussed by Lazio et al. (2004).

As discussed in Chapter 1, one of the main goals of searching for fast radio transients of duration < 5s through current and future programs such as V-FASTR (Wayth et al., 2011) and the CRAFT Survey (Macquart et al., 2010) is to probe the ionized IGM through propagation effects such as dispersion and temporal smearing. Radio dispersion and scattering are sensitive not only to the WHIM but all ionized components of the IGM, including the hot intracluster gas and the ionized components of the warm photoionized gas, the latter of which Lyα absorbers trace only the neutral components. In addition to that, scattering also probes the turbulence and density inhomogeneities of these intervening media.

However, the detection of radio transients at cosmological distances is in itself limited by temporal smearing which reduces the amplitude of the pulses. This will have important implications for future transient surveys on the SKA and its precursor telescopes, providing critical feedback into the optimization of search strategies to maximise detection rates.

This chapter is mainly concerned with the potential of intergalactic scattering as a probe of the various components of the ionized IGM. In Section 6.2, the thin screen model for the ISM is extended to cosmological scales to model angular broadening and temporal smearing in the IGM. These models and observational data, including that of AGN ISS used in the previous chapters, are used to constrain the effects of scattering and the turbulence of the IGM in Section 6.3. Strategies for detecting angular broadening and temporal smearing with current and next generation radio arrays are explored in Section 6.4. Section 6.5 discusses the limits on the detectability of extragalactic radio transients as a result of temporal smearing in the IGM.

6.2 A Thin-Screen IGM Scattering Model

A common parameter used to quantify the level of turbulence in the ISM is the spectral coefficient, C_n^2, for a truncated power law distribution of the power spectrum of electron density fluctuations (δn_e) in the ISM:

$$P_{\delta n_e}(q) = C_n^2 q^{-\beta}, \; \frac{2\pi}{l_0} \lesssim q \lesssim \frac{2\pi}{l_1}, \tag{6.1}$$

where q is the wavenumber, l_0 and l_1 are the outer and inner scales of δn_e, and β is found to have a value of 11/3 for the ISM (Armstrong et al., 1995), similar to that of

Kolmogorov turbulence. For lack of better alternatives, the turbulence in the IGM is also assumed to follow a Kolmogorov spectrum in the present study. The scattering measure (SM), which can be derived from observables, is then the line-of-sight path integral of C_n^2 to the source at distance D_S:

$$\mathrm{SM} = \int_0^{D_S} ds C_n^2. \tag{6.2}$$

The SM can also be expressed as (Lazio et al., 2008):

$$\mathrm{SM} = C_{\mathrm{SM}} \overline{F n_e^2} D_S, \tag{6.3}$$

where the constant $C_{\mathrm{SM}} = 1.8\mathrm{m}^{-20/3}\,\mathrm{cm}^6$, n_e is the electron density and F is a fluctuation parameter, given by (Taylor & Cordes, 1993):

$$F = \frac{\zeta \epsilon^2}{\eta} \left(\frac{l_0}{1\mathrm{pc}} \right)^{-\frac{2}{3}}. \tag{6.4}$$

ζ is the normalized intercloud variance of the mean electron densities of each cloud, ϵ is the normalized variance of the electron densities within a single scattering cloud, η is the filling factor for ionized clouds in the path.

The SM is a function of the square of the electron densities, which for the IGM will need to be modelled as a function of redshift. The mean free-electron density in the Universe as a function of redshift is given by:

$$n_e(z) = x_e(z) n_{e,0} (1+z)^3, \tag{6.5}$$

where $x_e(z)$ is the ionization fraction, and $n_{e,0}$ is the mean free electron density at $z \sim 0$. The IGM is known to be significantly ionized out to $z \lesssim 6$, based on the lack of Gunn-Peterson troughs in quasars at $z < 6$ (Gunn & Peterson, 1965; Djorgovski et al., 2001). Therefore, it can be assumed that $x_e(z) \sim 1$ at the redshifts of interest in this study. $n_{e,0} = 2.1 \times 10^{-7}\mathrm{cm}^{-3}$ assuming hydrogen is fully ionized and helium is singly ionized (Yoshida et al., 2003; Inoue, 2004). At $z \lesssim 3$, helium may be fully ionized, giving $n_{e,0} = 2.2 \times 10^{-7}\mathrm{cm}^{-3}$ (Sokasian et al., 2002; Lazio et al., 2008), which is not significantly different. The latter is used in the present calculations.

The effects of scattering will be most significant in overdense regions of the IGM, so that Equation 6.5 is modified by an additional term, δ_0, representing the overdensity at $z \sim 0$, giving:

$$n_e(z) = \delta_0 x_e(z) n_{e,0} (1+z)^\gamma, \tag{6.6}$$

where $\delta_0 = p_0 / \langle p_0 \rangle$, which is the ratio of the baryon density of the IGM component to the mean baryon density of the Universe at the present epoch, and assumes that the electron overdensities have a one to one relationship with overall baryonic overdensities. The manner in which these overdensities scale with redshift will modify the exponent of the $(1+z)$ term, which is quantified here as γ. For an overdense region that is virialized and gravitationally bound at the redshifts of interest, as would be expected of the intracluster media (ICM) and galaxies, $\gamma \sim 0$. For components of the IGM that expand with the Hubble flow and have constant comoving densities, $\gamma \sim 3$. In IGM components with $0 < \gamma < 3$, the rate of gravitational infalling into potential wells is lower than the rate of the expansion of the Universe, so that from high to low redshift, the comoving densities are increasing but the proper densities are decreasing. For components with $\gamma < 0$, the rate of gravitational infall is higher than the rate of the expansion of the Universe, so that both the comoving densities and proper densities are increasing from high to low redshift.

Angular broadening and temporal smearing can be calculated as a function of the SM, which I will extend to cosmological scales here to model these effects in the IGM.

6.2.1 Angular broadening

The full width half maximum (FWHM) angular size of a scatter broadened image of an extragalactic source due to the ISM with homogenous Kolmogorov turbulence is given by Taylor & Cordes (1993) as:

$$\theta_{ism} = 128\ \mathrm{SM}^{\frac{3}{5}} \left(\frac{\nu}{1\,\mathrm{GHz}}\right)^{-2.2} \text{mas}. \tag{6.7}$$

To extend the equation to cosmological scales for the IGM, the frequency at the rest frame of the scattering screen needs to be written in terms of the observing frequency, so that $\nu = \nu_{screen} = \nu_{obs}(1+z_L)$ for a screen at redshift z_L. One must also account for the so called 'lever-arm effect' resulting from the geometry of the problem (see Figure 6.1), in converting actual scattering angles in the IGM, θ_{igm}, to the observed scatter broadening angle, given by:

$$\theta_{scat} = \frac{D_{LS}}{D_S}\theta_{igm} = 128\ \mathrm{SM}^{\frac{3}{5}} \left(\frac{D_{LS}}{D_S}\right) \left(\frac{\nu_{obs}}{1\,\mathrm{GHz}}\right)^{-2.2} (1+z_L)^{-1.2}\ \text{mas}, \tag{6.8}$$

where in the cosmological context, D_S is the angular diameter distance to the source and D_{LS} is the angular diameter distance from the source to the scattering screen in the IGM. This follows from the notations used in gravitational lensing literature (Narayan & Bartelmann, 1997; Macquart, 2004). This lever-arm effect is ignored for the scatter broadening of extragalactic sources in the ISM, since $D_{LS} \approx D_S$ so that $\theta_{scat} \approx \theta_{ism}$. The formulation of Equation 6.8 is shown in more detail in Appendix E.

The dependence of θ_{scat} on the scattering screen redshift is reliant upon two opposing effects. The redshift dependence of the rest-frame frequency at the scattering screen for a fixed observing frequency, together with the geometrical lever-arm effect, causes θ_{scat} to decrease with increasing z_L, for a fixed source redshift z_S. On the other hand, the mean electron density of the Universe scales with $(1+z_L)^3$, so that the SM scales

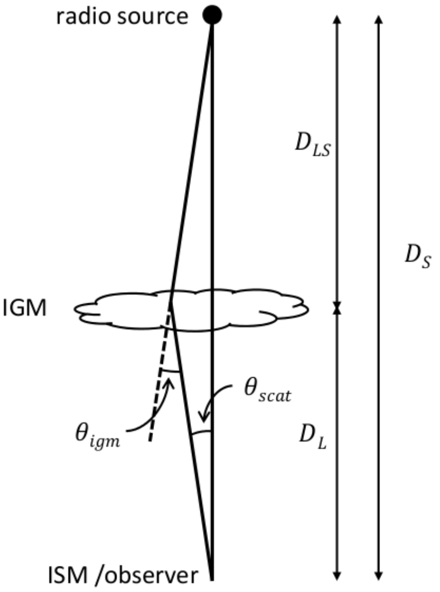

Figure 6.1 — *The geometry of angular broadening in the intergalactic medium, demonstrating the lever-arm effect. See text in Section 6.2.1 for a description of the various symbols used.*

with $(1+z_L)^6$ following Equation 6.3. Figure 6.2 shows θ_{scat} for various values of z_L, z_S and l_0, for electron densities equivalent to the mean electron densities of the Universe ($\delta_0 = 1$) at all epochs (Equation 6.6). For simplicity, $\zeta \sim \epsilon \sim \eta \sim 1$ is assumed for all redshifts, implying that the turbulence is fully developed at all redshifts of interest. l_0 is also assumed to be independent of z_L, so that turbulence is continually injected into the IGM at the same scales at all redshifts. At $z_L \lesssim 0.5z_S$, θ_{scat} is dominated by the increasing mean electron densities with redshift, causing θ_{scat} to increase with z_L. At $z_L \gtrsim 0.5z_S$, the lever-arm effect combined with the increasing rest-frame frequencies of the screen begin to dominate, so that θ_{scat} decreases with z_L.

The values of θ_{scat} range from sub-μas to hundreds of μas (for outer scales of turbulence between 1 Mpc and 0.001 pc) for $\delta_0 \sim 1$, but increase for overdense regions in the IGM. This is shown in similar plots in Figure 6.3, for a source at $z_S \sim 4$ and scattering screens of overdensity $\delta_0 \sim 30$ (left panel) and $\delta_0 \sim 1000$ (right panel). Screen densities that expand with the Hubble flow are shown as blue curves, whereas gravitationally bound screens with constant proper densities are shown as black curves. Scatter broadening in gravitationally bound scattering screens is therefore dominated by objects at $z_L \sim 0$, since there is no $(1 + z_L)^3$ dependence of electron densities to counter the lever-arm effect and the increasing frequencies at the rest-frame of the scattering screen.

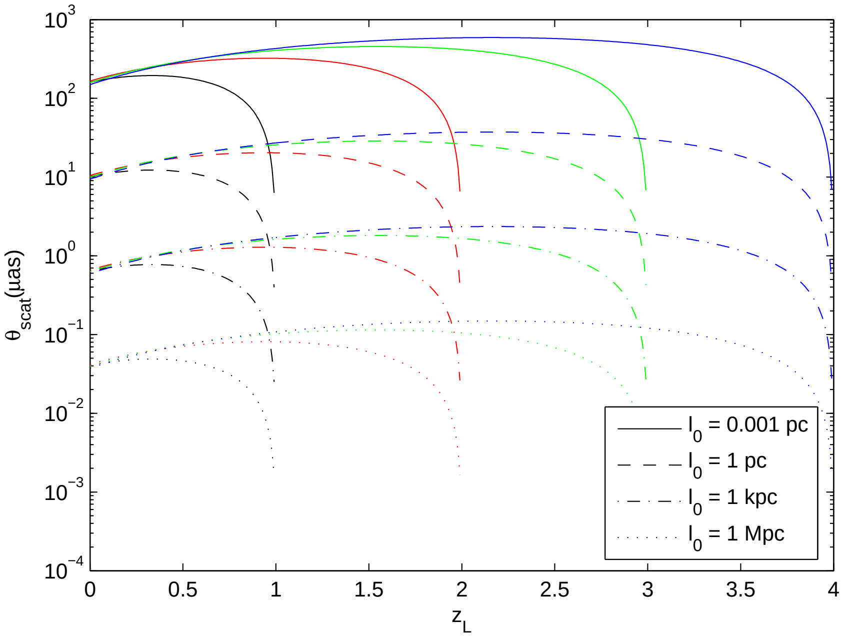

Figure 6.2 — *Theoretical estimates of angular broadening, θ_{scat}, at 1 GHz due to scattering at a single thin screen at redshift z_L, with Kolmogorov turbulence cut off at various outer scales, l_0. The electron densities at the scattering screen are assumed to be equivalent to the mean electron densities of the universe at the screen redshift, and therefore have constant comoving densities. The black, red, green and blue curves represent source redshifts of 1, 2, 3 and 4 respectively.*

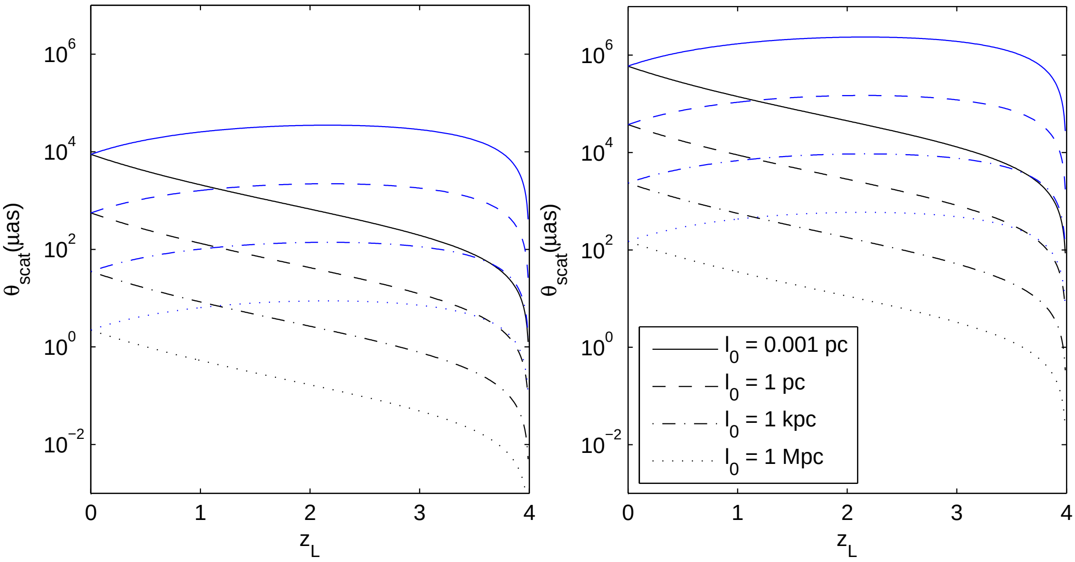

Figure 6.3 — *Theoretical estimates of angular broadening, θ_{scat}, at 1 GHz for a source at redshift 4, due to scattering at a thin screen at various redshifts z_L, various outer scales of turbulence, l_0, and with overdensities of $\delta_0 = 30$ (left panel) and $\delta_0 = 1000$ (right panel). The blue curves denote screens with constant comoving densities, while the black curves denote screens with constant densities.*

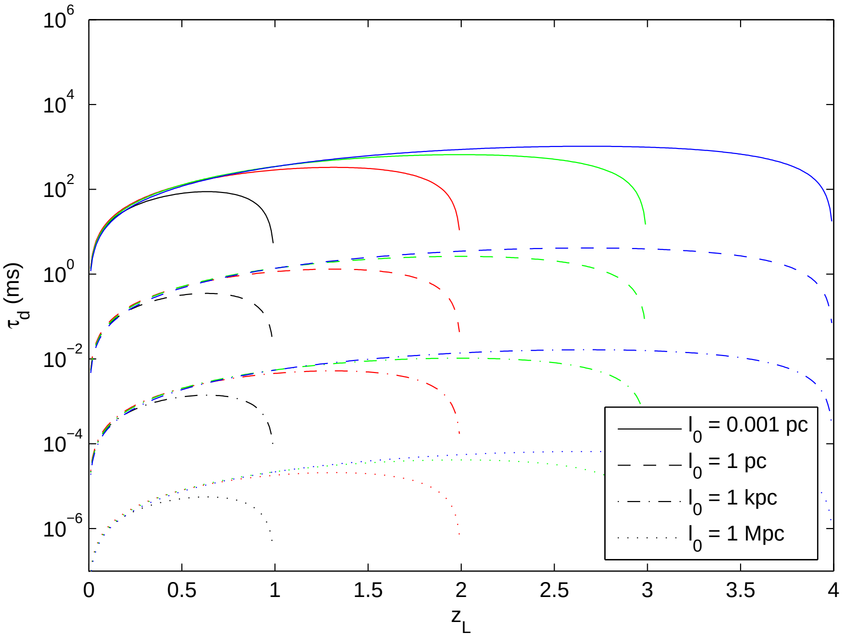

Figure 6.4 — *Theoretical estimates of temporal smearing, τ_d, at 1 GHz due to scattering at a single thin screen at redshift z_L, with Kolmogorov turbulence cut off at various outer scales, l_0. The electron densities at the scattering screen are assumed to be equivalent to the mean electron densities of the universe at the screen redshift, and therefore have constant comoving densities. The black, red, green and blue curves represent source redshifts of 1, 2, 3 and 4 respectively.*

6.2.2 Temporal Smearing

The amount of temporal smearing of impulsive signals is determined by the longest paths traversed by the radio waves from the source to the observer. It is therefore dependent upon the amount of angular broadening caused by the intervening screen. Temporal smearing in the IGM can be estimated as (see Appendix E):

$$\tau_d = \frac{D_L D_S \theta_{scat}^2}{2cD_{LS}(1+z_L)} = 19.83\ \mathrm{SM}^{\frac{6}{5}} \left(\frac{D_L}{D_S}\right) \left(\frac{D_{LS}}{1\,\mathrm{Mpc}}\right) \left(\frac{\nu_{obs}}{1\,\mathrm{GHz}}\right)^{-4.4} (1+z_L)^{-3.4}\ \mathrm{s}. \quad (6.9)$$

Since τ_d is a function of θ_{scat}, its trends as a function of z_L broadly resembles that of θ_{scat} (see Figures 6.4 and 6.5). One slight difference is that τ_d peaks at $z_L \approx (2/3)z_S$ for the case where the comoving electron densities are constant with redshift (Figure 6.4), even when θ_{scat} begins to decrease at $z_L \approx 0.5z_S$. This is because the pathlengths (and therefore τ_d) will increase as z_L increases for fixed values of θ_{scat} and source redshift, so the decrease in θ_{scat} with increasing z_L begins to dominate the trend of τ_d only at higher values of z_L.

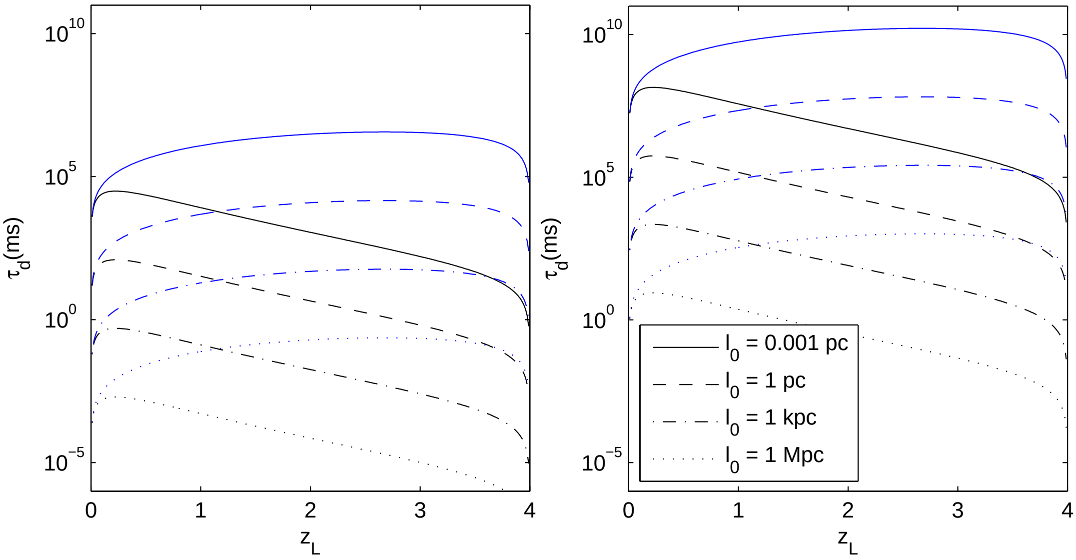

Figure 6.5 — *Theoretical estimates of angular broadening, τ_d, at 1 GHz for a source at redshift 4, due to scattering at a thin screen at various redshifts z_L, various outer scales of turbulence, l_0, and with overdensities of $\delta_0 = 30$ (left panel) and $\delta_0 = 1000$ (right panel). The blue curves denote screens with constant comoving densities, while the black curves denote screens with constant densities.*

The major difference between the trends of τ_d and θ_{scat} is that the value of τ_d drops quickly for $z_L \lesssim 0.1$ for a source at $z_S \gtrsim 1$, irrespective of whether the screen proper densities increase or remain constant with redshift (see Figure 6.5). This is because the increase in pathlengths caused by scattering at nearby screens is not significantly higher than that caused by more distant screens, even though θ_{scat} is largest for the nearest screens for a fixed screen density. This is entirely a geometrical effect. Therefore, as opposed to angular broadening where the ISM will dominate, the contribution of the IGM to temporal smearing of extragalactic sources may still be significant and even dominate over that of the ISM due to the longer pathlengths, despite the ISM having higher electron densities.

Another point to note is that temporal smearing scales more strongly with frequency than angular broadening, so can become very important in low frequency observations.

6.3 Observational Constraints on IGM Scattering and Turbulence

6.3.1 Constraints on Angular Broadening

The strongest constraints for angular broadening in the IGM can be obtained from the most compact extragalactic radio sources known to date — scintillating Gamma-Ray Burst (GRB) afterglows and AGN cores, the latter of which includes the sources analysed in the previous chapters.

Therefore, while the MASIV follow-up observations provide no clear detection of scatter broadening in the IGM or that it has any significant redshift dependence between the $z < 2$ and $z > 2$ subsamples, the data can be used to place strong constraints on it. The top panel of Figure 6.6 shows estimated apparent angular sizes of all sources, $\theta_{4.9}$, calculated from their $D_{4.9}(4\text{d})$ values using the Goodman & Narayan (2006) fitting functions. For all sources in which $D_{4.9}(4\text{d}) \geq D_{noise}$, the upper limits of $\theta_{4.9}$ are calculated using compact fractions of $f_c \sim 1$, while the lower limits are calculated using $f_c \sim 0.1$. For sources in which $D_{4.9}(4\text{d}) < D_{noise}$, upper limits to $\theta_{4.9}$ cannot be obtained, while the lower limits are calculated using $f_c \sim 0.1$ and setting D_{noise} as the upper limit to the source variability. For each source, ν_t and D_{ISM} are similar to that used in Section 5.4 for the Monte Carlo simulations. The estimation of $\theta_{4.9}$ makes no assumptions about the brightness temperatures and Doppler boosting factors of the sources. The upper limits of $\theta_{4.9}$ are also effectively upper limits of the 4.9 GHz θ_{scat} and θ_{src} for the sight-lines to these sources (Equation 5.6); they are shown proportional to the sizes of the circles in the lower panel of Figure 6.6 in Galactic coordinates.

The angular broadening can be further constrained by making use of the quantity $R_D = D_{8.4}(4\text{d})/D_{4.9}(4\text{d})$ obtained for the $\gtrsim 3\sigma$ variable sources. At 4.9 GHz, the upper limit to scatter broadening can be formulated from Equations 5.4 and 5.6 in the weak ISS regime as:

$$\theta_{scat} \leq \theta_{src(max)} \left[\frac{2.16\big(R_{D(max)}\big)^{\frac{6}{7}} - 1}{1 - 0.59\big(R_{D(max)}\big)^{\frac{6}{7}}} \right]^{0.5}, \tag{6.10}$$

for $0.4 < R_{D(max)} < 1.8$, where $R_{D(max)}$ is the upper limit of R_D and $\theta_{src(max)}$ is the upper limit to the intrinsic source angular size at 4.9 GHz. Again, the relations $\theta_{src} \propto \nu^{-1.0}$ and $\theta_{scat} \propto \nu^{-2.2}$ are used. This inequality posits that sources scintillating in the weak ISS regime will have $R_D \sim 0.4$ when completely dominated by intrinsic source size effects. As an increase in IGM scatter broadening increases R_D, the upper limit to θ_{scat} is determined by the level of increase in R_D above this nominal value. The dominance of θ_{scat} is also dependent on θ_{src}; sources with smaller intrinsic angular sizes are more likely to be dominated by θ_{scat} than sources with larger angular sizes.

The weak ISS approximation (Narayan, 1992; Walker, 1998) is used here because

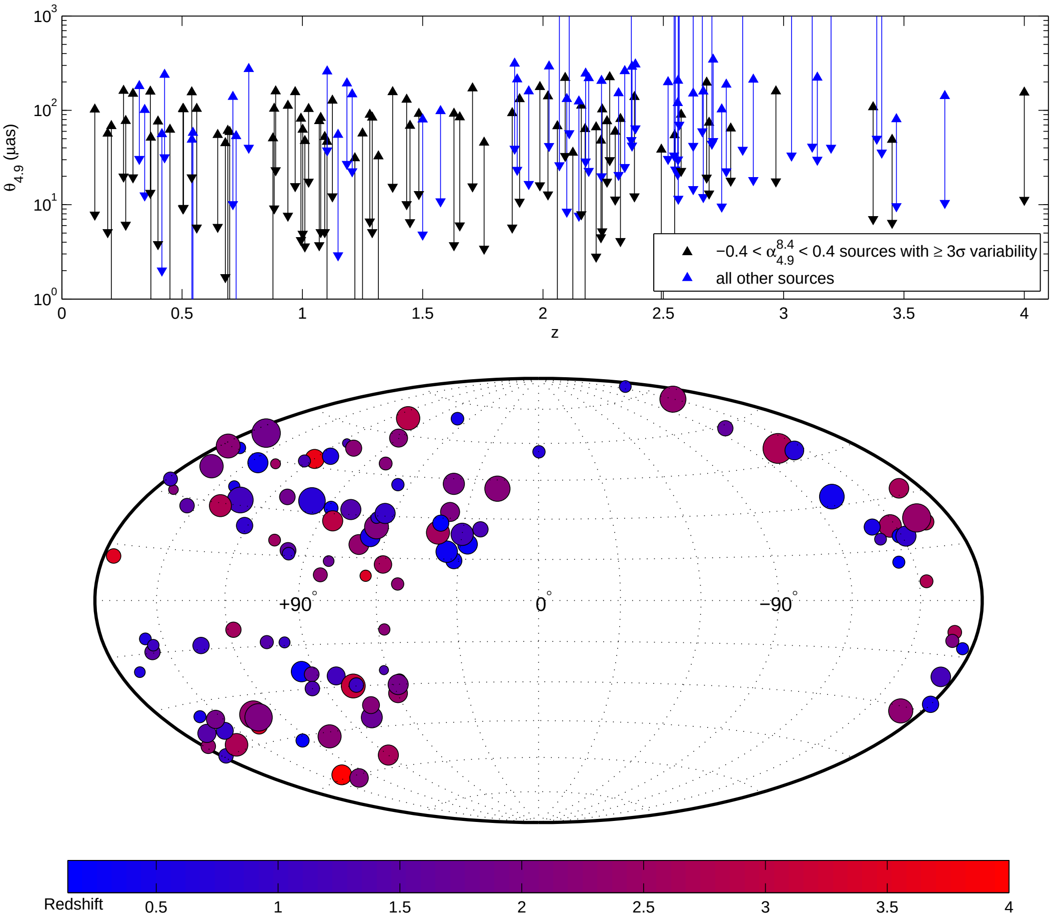

Figure 6.6 — *Top panel: Constraints on the 4.9 GHz apparent angular sizes,* $\theta_{4.9}$*, for all 128 sources (including those with inverted and steep-spectra), calculated based on* $D_{4.9}(4\mathrm{d})$ *using the Goodman & Narayan (2006) fitting function. Bottom panel: Upper limits of* $\theta_{4.9}$ *for all sources in which they can be obtained, shown proportional to the sizes of the circles and plotted in Galactic coordinates. They are also effectively upper limits of* θ_{scat} *for all lines of sight to our sources. The circles are also color-coded based on the redshifts of the sources.*

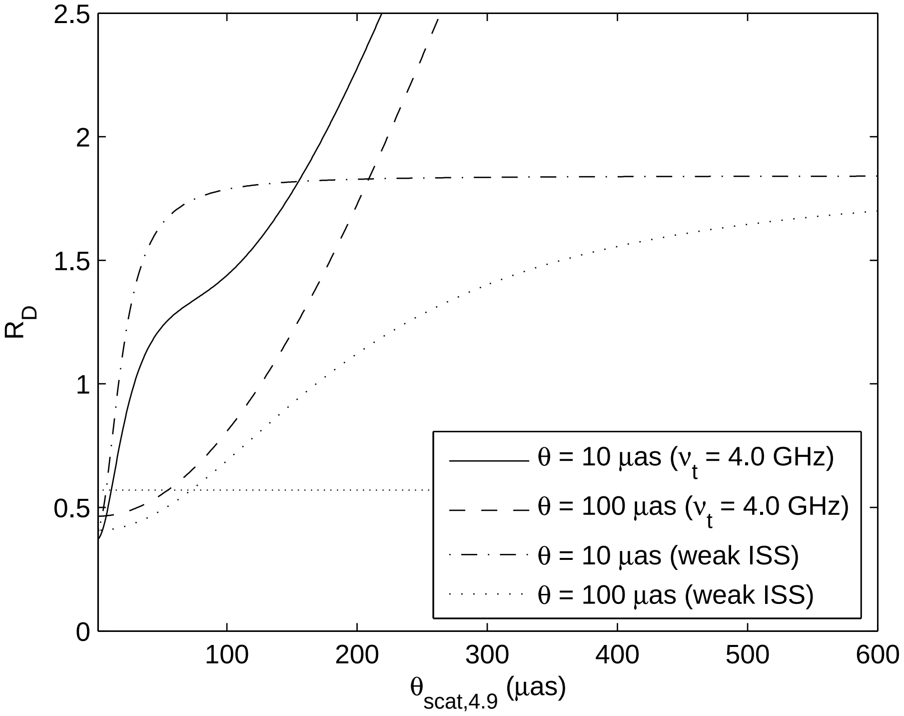

Figure 6.7 — *R_D at increasing values of θ_{igm} for sources with intrinsic angular sizes of 10 μas and 100 μas. The plots are based either on model calculations in the weak ISS regime assuming that the SFs have all saturated, or the fitting formula of Goodman & Narayan (2006) with $v_s = 50\,\mathrm{kms}^{-1}$, $d = 500\mathrm{pc}$ and $\nu_t = 4.0$ GHz. The dotted horizontal line represents $R_D = 0.57$, which is the upper limit to R_D fitted to all sources in the low redshift sample, at a confidence level of 99%.*

it gives the most conservative upper limit to scatter broadening in the IGM and is not dependent on any other model parameters. Comparing the Goodman & Narayan (2006) fitting function with the weak ISS model in calculating R_D, it is found that both provide similar constraints when $\theta = \sqrt{\theta_{src}^2 + \theta_{scat}^2}$ is $\lesssim 50\mu$as (see Figure 6.7). As opposed to the weak ISS model where $D(4\mathrm{d}) \approx 2m^2$ is assumed, R_D rises faster in the Goodman & Narayan (2006) fitting function with increasing θ when θ is of an order $\sim 100\mu$as, as the scintillation timescales exceed 4 days and the SFs do not saturate (the same reason why R_D increases marginally with redshift in Figure 5.11). Although the Goodman & Narayan (2006) fitting functions give stronger constraints, they are very dependent on the parameters of the model when θ is large.

Since the upper limit of the fitted R_D for the low-redshift sources is 0.57 at 99% confidence, $\theta_{scat} \lesssim 110\mu$as on average at 4.9 GHz, assuming that the intrinsic angular sizes of the scintillating components in all our sources are no larger than 150 μas (as seen for the $\gtrsim 3\sigma$ variable sources at low redshift in the upper panel of Figure 6.6).

The strongest constraints can be derived from the fitted R_D of the weak sources, which is also no more than 0.57 at 99% confidence for the weak, low redshift sources. With flux densities of $\sim$ 0.1 Jy, θ_{src} can be as low as $\sim 10\mu$as. For example, the source PKS 1519-273 (not in the MASIV follow-up sample) has an estimated core size as low as 15 to 30 μas (Macquart et al., 2000), while the most compact component of the extreme scintillator J1819+3845 has been estimated to be as small as $\sim 7\mu$as (Macquart & de Bruyn, 2007). In the present data, the rapid scintillator J1328+6221 has the lowest upper limit of $\theta_{4.9}$, estimated to be $\lesssim 15\mu$as. Although Figure 6.6 shows that the estimated lower limits of $\theta_{4.9}$ in some sources drop well below 1μas if their compact fractions are sufficiently small, it is unknown if the compact fractions of these sources do indeed have values as low as 0.1.

The very compact, $\sim 10\mu$as sources give $\theta_{scat} \lesssim 8\mu$as for most lines of sight at 4.9 GHz. This can be extrapolated to give $\theta_{scat} \lesssim 264\mu$as at 1.0 GHz, which is about a factor of 2 lower than the upper limit of 500μas obtained by Lazio et al. (2008) at the same frequency. This limit is comparable to that for the sight-line to the Gamma-ray Burst GRB 970508 inferred from its angular size of $\lesssim 3\mu$as at 8.4 GHz ($\lesssim 9\mu$as at 4.9 GHz), determined from observations of diffractive scintillation in its radio afterglow (Frail et al., 1997). The extrapolations of these constraints to frequencies ranging from 50 MHz to 10 GHz are shown in Figure 6.8.

Maximum values of the SM for the IGM can be computed from the upper limits of θ_{scat}, by inverting Equation 6.8 to obtain:

$$\mathrm{SM} \lesssim \left[\frac{\theta_{scat(max)}}{128\,\mathrm{mas}}\left(\frac{D_S}{D_{LS}}\right)\left(\frac{\nu}{1\,\mathrm{GHz}}\right)^{2.2}(1+z_L)^{1.2}\right]^{\frac{5}{3}}\mathrm{kpc\,m}^{-\frac{20}{3}}. \tag{6.11}$$

This is similar in form to the equation provided in Lazio et al. (2008) for calculating the SM of the IGM; the main difference is that their equation is applicable only to scattering screens at $z \sim 0$, since they do not account for the lever-arm effect and the increasing rest-frame frequencies at the scattering screen with increasing redshift. Upper limits to the SM for different values of z_L and z_S are shown in Figure 6.9, revealing that the nearest scattering screens provide the strongest constraints on the SM. As discussed in Section 6.2, it is most likely that angular broadening will be dominated by nearby screens of overdensities $\gg 1$, assuming that these regions are gravitationally bound. At $z_L \sim 0$, we obtain SM $\lesssim 3.3 \times 10^{-5}\,\mathrm{kpc\,m}^{-20/3}$ for $\theta_{scat(max)} \sim 8\mu$as, regardless of source redshift.

6.3.2 Constraints on Temporal Smearing

An equivalent constraint on temporal smearing can be inferred from the upper limits to angular broadening obtained above, based on Equation 6.9. While angular

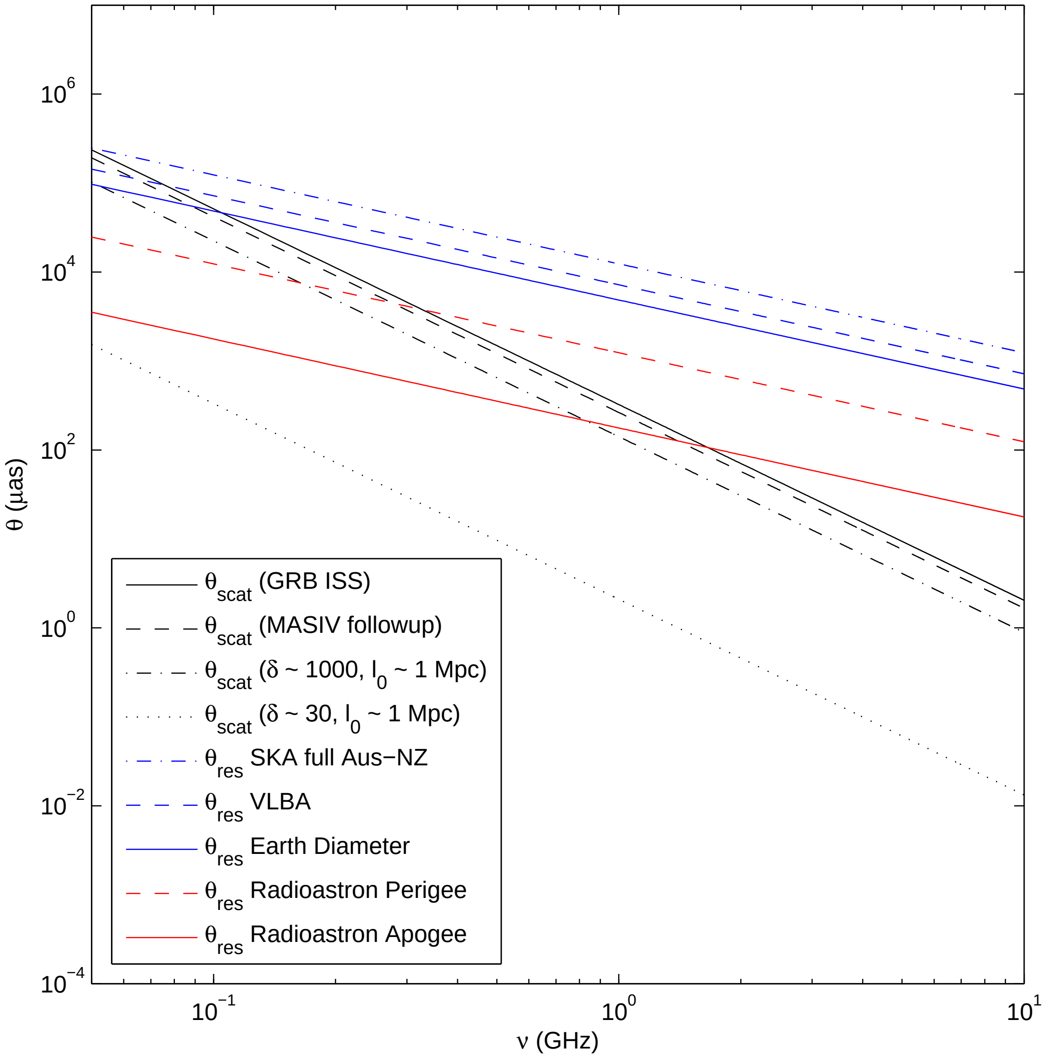

Figure 6.8 — *Observational constraints and model values of angular broadening in the IGM, θ_{scat}, shown together with the angular resolutions at various array baselines, θ_{res}, extrapolated to various observing frequencies. The model θ_{scat} is based on a screen at $z_L \sim 0$ where scatter broadening is expected to be highest for gravitationally bound components.*

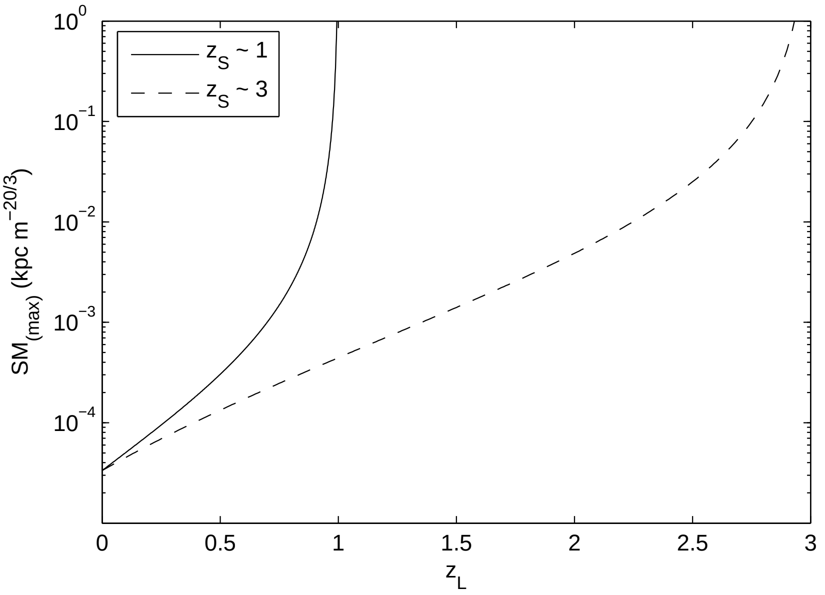

Figure 6.9 — *Upper limits to the scattering measure (SM) for various IGM scattering screen redshifts,* z_L*, for sources at redshifts* $z_S \sim 1$ *and* $z_S \sim 3$

broadening is largest for the nearest gravitationally bound objects of high overdensities, temporal smearing is largest, for such regions, at $z_L \sim 0.2$ for a source at $z_S \sim 4$ (Figure 6.5). Figure 6.10 shows an extrapolation of this constraint to frequencies between 50 MHz and 10 GHz, for $z_L \sim 0.2$. Upper limits of $\tau_d \lesssim 50\mu$s, $\tau_d \lesssim 50$ ms and $\tau_d \lesssim 1400$ s are obtained at 5 GHz, 1 GHz and 0.1 GHz respectively.

Other constraints on temporal smearing in the IGM come from the most impulsive extragalactic radio sources. The 'Lorimer burst' is reported to have a pulse width of ~ 5.0 ms (Lorimer et al., 2007) at ~ 1.4 GHz, with hints of the pulse width increasing with decreasing frequency across the observing band that are consistent with scatter broadening. It is entirely possible that the intrinsic pulse width is much smaller than 5.0 ms and the pulse has been temporally smeared. A second similar burst (referred to as J1852-08) was detected with a pulse width of ~ 7.3 ms (Keane et al., 2011), also at 1.4 GHz. Although the timescales of these bursts are consistent with the IGM temporal smearing limits implied from the constraints on angular broadening, the extragalactic origins of these bursts are suspect. Further studies indicate that the 'Lorimer burst' may be terrestrial in nature (Burke-Spolaor et al., 2011), while the burst detected by Keane et al. (2011) was determined to be extragalactic based on a 40% excess of dispersion measure (DM) in comparison to the NE2001 model for Galactic electron densities (Cordes & Lazio, 2003), which may be inaccurate.

If these bursts are indeed extragalactic in nature, they provide marginally stronger

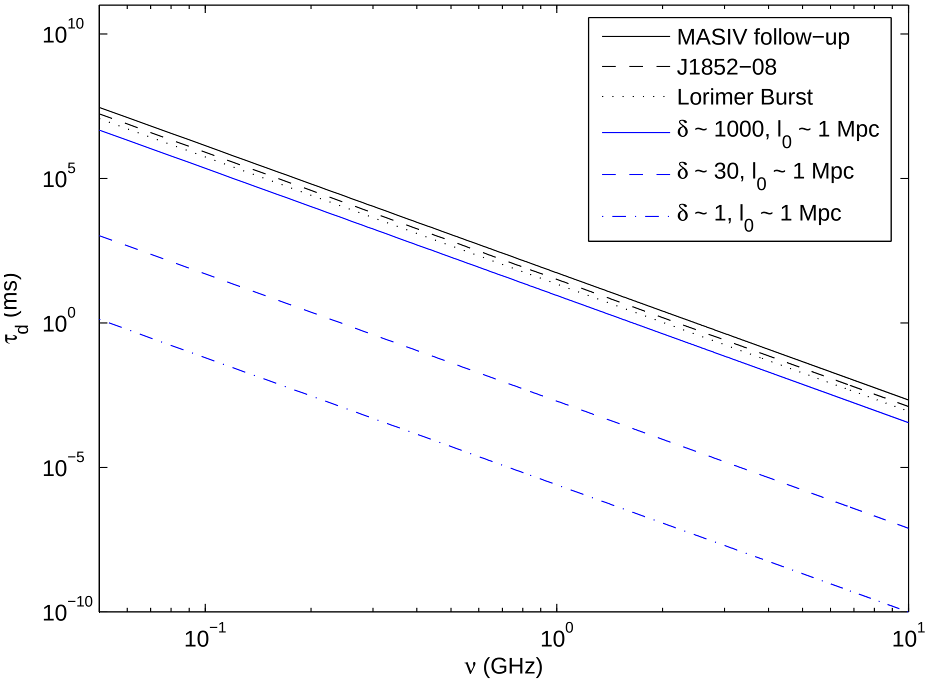

Figure 6.10 — *Observational constraints and model values of temporal smearing in the IGM,* τ_d*, extrapolated to various observing frequencies.*

constraints on temporal smearing (see Figure 6.10) in the IGM. Using source redshifts estimated from the excess DMs, $z_S \sim 0.3$ for the 'Lorimer burst' (Lorimer et al., 2007) and $z_S \sim 0.1$ for J1852-08 (Keane et al., 2011), upper limits of SM $\lesssim 4.6 \times 10^{-5}$ and SM $\lesssim 1.2 \times 10^{-4}$ are obtained for the sight-lines to these sources for screen redshifts of $z_L \sim 0.1$ and $z_L \sim 0.04$ respectively. These are consistent with that obtained from the MASIV follow-up observations. The screen redshifts are chosen where the temporal smearing would have the largest values (and therefore the SM the lowest) at the estimated source redshifts, assuming gravitationally bound IGM components.

6.3.3 Constraints on IGM Turbulence

Quantitative limits can also be placed on the level of turbulence in the IGM. Following Lazio et al. (2008), $\overline{n_{e,0}} < 2.2 \times 10^{-7}\mathrm{cm}^{-3}$ at $z \sim 0$ is adopted based on the assumption that helium is fully ionized, and $\zeta \sim \epsilon \sim \eta \sim 1$. This gives a fluctuation parameter (see Section 6.2) of $F \lesssim 230$ and outer scales of turbulence of $l_0 \gtrsim 3 \times 10^{-4}$ pc for a source at $z \sim 1$ ($D_S \sim 1.7$ Gpc), using SM $\lesssim 3.3 \times 10^{-5}\,\mathrm{kpc\,m}^{-20/3}$ as obtained from the angular broadening constraints from the MASIV follow-up observations. For comparisons, Cordes & Lazio (2003) give $F \sim 0.2$ and $F \sim 10$ respectively in the thick disk and spiral arm components of our Galaxy. For higher overdensities where scatter

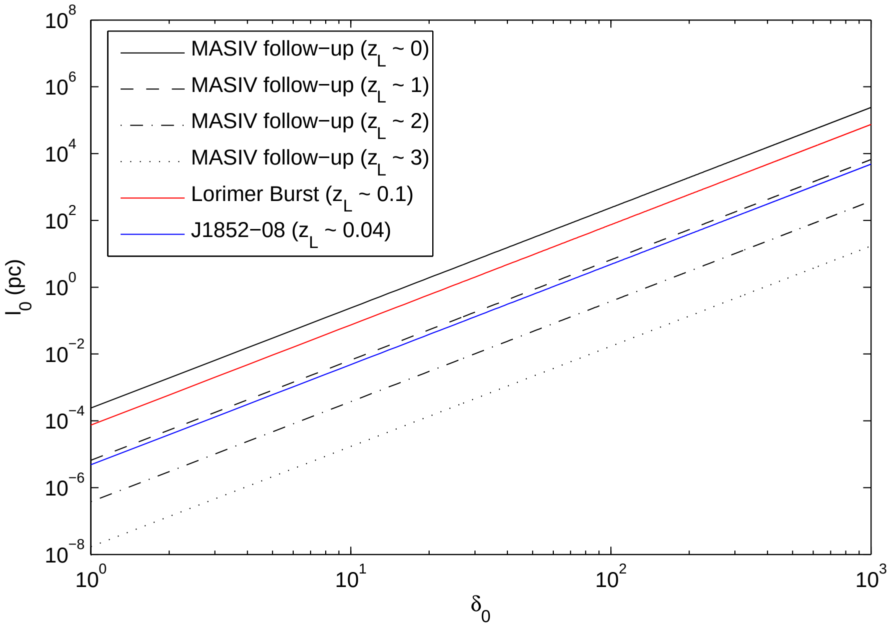

Figure 6.11 — *Lower limits to the outer scale of turbulence, l_0, for various values of IGM overdensities δ_0 and scattering screen redshifts, assuming a Kolmogorov spectrum. The black lines are based on the limit $\theta_{scat} \lesssim 8\mu as$, while the red and blue lines are based on the limit $\tau_d \lesssim 5$ ms and $\tau_d \lesssim 7$ ms respectively.*

broadening is more likely to occur, the lower limits on the outer scales of Kolmogorov turbulence increase further, with $l_0 \gtrsim 8$ pc for $\delta_0 \sim 30$ and $l_0 \gtrsim 0.3$ Mpc for $\delta_0 \sim 1000$, as seen in Figure 6.11. The limits on l_0 are also shown for various values of δ_0 for SM limits obtained from the Lorimer burst and J1852-08, again assuming that they are extragalactic.

Figure 6.11 implies either that the IGM is not stirred at length-scales below the lines for the various component overdensities, or that such regions, if they exist, do not dominate the lines-of-sight to the sources in the MASIV follow-up observations.

For a diffuse warm IGM where $\delta_0 \lesssim 1$ and the volume fractions are $\gtrsim 90\%$ between $0 \leq z \leq 3$ (Cen & Ostriker, 2006), it is safe to conclude that $l_0 \gtrsim 3 \times 10^{-4}$ pc for such components of the IGM since they will dominate the sight-lines to all sources. This is consistent with current knowledge, where l_0 can range from ~ 1 pc (similar to our own Galaxy) up to the ~ 0.1 Mpc scales of the largest jet sources that can inject turbulence into the IGM.

Outer scales of turbulence at pc-scales may be found in galaxies similar to our own, where $\delta_0 \gg 1000$, but it is unlikely that such intervening galaxies dominate the sight-lines to a random sample of sources (although the sources in the MASIV follow observations are far from being a random sample). The optical depth for the intersection of objects up to a redshift z is given by Padmanabhan (2002) as:

$$\tau(z) = \int_0^z \frac{\pi c r_G^2 n(z') d_H(z')}{(1+z')} dz', \tag{6.12}$$

where r_G and $n(z)$ are the typical proper radius and proper number density of the object, and $d_H(z) = H_0^{-1}(\Omega_M(1+z)^3 + \Omega_\Lambda)^{-1/2}$ for a Friedmann Universe where $\Omega_M + \Omega_\Lambda = \Omega = 1$. Assuming that the number densities of galaxies are conserved over the redshifts of interest, $n(z) = n_0(1+z)^3$, where n_0 is the number density at the present epoch. For $r_G \approx 10h^{-1}$ kpc and $n_0 \approx 0.02h^3\mathrm{Mpc}^{-3}$ (Peebles, 1996; Padmanabhan, 2002), the fraction of the sky intersected by galaxies is only $\sim 3\%$ out to $z \sim 1$, and $\sim 16\%$ out to $z \sim 3$. For the sample of 72 sources with $\geq 3\sigma$ variability, with 48 sources at $z < 2$ and 24 sources at $z > 2$, one would roughly expect about 1 of the $z < 2$ sources and 4 of the $z < 2$ sources to be intersected by a galaxy. Therefore, for these objects, the MASIV follow-up observations do not place strong contraints on their outer scales of turbulence.

As found for individual galaxies, the MASIV follow-up observations do not place strong constraints on the outer scales of turbulence in the hot intracluster medium (ICM) in rich clusters of galaxies with overdensities of $\delta_0 \sim 1000$. For $r_G \sim 1h^{-1}$ Mpc and $n_0 \approx 10^{-5}h^3\mathrm{Mpc}^{-3}$ (Bahcall, 1996), the probability that a $z \sim 1$ and $z \sim 3$ source will intersect such a cluster is $\sim 16\%$ and $\sim 75\%$ respectively, assuming that their number densities are conserved out to those redshifts and their sizes do not evolve. While their number densities are much lower than that of galaxies, their sizes are much larger, significantly increasing the probability of intersection. For the sample of 72 sources, one expects about 8 of the 48 $z < 2$ and 18 of the 24 $z > 2$ sources to intersect such clusters. While it is indeed possible that $l_0 \gtrsim 0.3$ Mpc and $l_0 \gtrsim 16$ pc for the ICM at $z \sim 0$ and $z \sim 3$, the lack of a significant redshift dependence of scatter broadening despite the large intersection probabilities can be attributed to other factors. As demonstrated in Section 6.2, angular broadening is always dominated by the nearest screens where θ_{scat} is largest for gravitationally bound and virialized objects. Even though the optical depth for intersecting the ICM approaches 1 as z approaches 4, only the $z_L < 1$ scattering screens with intersection probabilities of $\lesssim 16\%$ contribute significantly to the scatter broadening. It is difficult to constrain the values of l_0 for these components of the IGM unless it is known with certainty that the line-of-sight to a particular source intersects such a cluster at low redshift. This is discussed further in the next section.

6.4 Future Prospects for Probing the IGM

While the MASIV follow-up observations provide constraints on scattering and turbulence in the IGM that are broadly consistent with current knowledge, the ultimate goal is to retrieve parameters such as l_0, F, C_n and their redshift dependences for various components of the IGM based on actual detections of scattering. This will nicely complement studies of the radio dispersion of extragalactic transients at radio frequencies which will provide information on the line-of-sight column densities, in addition to absorption and emission line studies at optical and X-ray frequencies that will provide information on gas velocities, densities and redshifts. Furthermore, unlike dispersion, scatter broadening and temporal smearing are both much less sensitive to the electron content of the host galaxy (as can be inferred from Figures 6.2 to 6.5), allowing its effects to be discriminated from that of the actual intervening IGM.

I therefore investigate in this section possible strategies for detecting and probing (or at the very least place even stronger constraints on) IGM scattering, using current and next generation radio telescopes.

6.4.1 Detecting Angular Broadening

6.4.1.1 Direct Imaging

One strategy of detecting angular broadening is to image compact background sources such as blazars with VLBI at multiple frequencies to determine if their angular sizes scale with $\nu^{-2.2}$, as was attempted by Lazio et al. (2008). In discussing the feasibility of using the Square Kilometre Array (SKA) to detect intergalactic scatter broadening, Lazio et al. (2004) and Godfrey et al. (2011) propose that angular resolutions better than 4 mas at 1.4 GHz and 80 mas at 0.33 GHz are required. Our most conservative constraints on IGM scatter broadening push these limits lower. A simple extrapolation using $\theta_{scat} \lesssim 110\mu$as at 4.9 GHz gives $\theta_{scat} \lesssim 1.7$ mas at 1.4 GHz and $\theta_{scat} \lesssim 42$ mas at 0.33 GHz. Based on the tighter constraint of $\theta_{scat} \lesssim 8\mu$as, this can be extrapolated to $\theta_{scat} \lesssim 126\mu$as at 1.4 GHz and $\theta_{scat} \lesssim 3$ mas at 0.33 GHz.

In fact, Figure 6.8 demonstrates that even with baselines comparable to that of the longest baselines of the SKA (~ 5500 km for Australia-New Zealand, where SKA-lo and the survey component will be constructed), the VLBA (8611 km) and the diameter of the Earth (12,700 km), scatter broadening will be barely resolved down to frequencies as low as 50 MHz (calculated using $c/\nu b$, where b is the maximum baseline length). This is true for the majority of sight-lines at least. If the imaged sources intersect regions of overdensities comparable to ~ 1000 at $z \sim 0$, which are more rare, ground-based telescopes may be able to resolve the scatter broadening at frequencies below ~ 100 MHz, provided that the outer scales of turbulence in these regions are much smaller than the 1 Mpc for which the theoretical curves are shown in Figure 6.8.

Space VLBI has the best potential for directly imaging scatter broadening in the IGM. Figure 6.8 shows that for an overdense region of $\delta_0 \gtrsim 1000$ at $z \sim 0$ with $l_0 \sim 1$ Mpc, IGM scatter broadening can be resolved below frequencies of $\sim$ 150 MHz and $\sim$ 800 MHz for baselines equivalent to that of RadioAstron at perigee ($\sim$ 50,000 km) and apogee ($\sim$ 350,000 km). However, the contribution of the WHIM with $\delta_0 \lesssim 30$ to angular broadening appears undetectable even with the baselines of RadioAstron, unless the outer scales of turbulence are on the order of 1 kpc or lower, and even that, only at apogee below frequencies of $\sim$ 200 MHz.

By far the greatest impediment is that angular broadening will be dominated by contributions from the ISM, the effects of which will be difficult to disentangle from that of the IGM. Even for IGM screens at $z \sim 0$ where the rest-frame frequency is equal to the observing frequency, the higher density and most likely smaller l_0 of the ISM, together with the lever arm effect will favour the ISM. Such observations will therefore need to be carried out off the Galactic plane. Another option is to subtract the Galactic contribution to angular broadening through observations of the angular broadening of pulsars close to the line-of-sight of the target AGN, as has been proposed by Lazio et al. (2004), or through empirical models of the Galactic electron distribution i.e. NE2001 (Cordes & Lazio, 2003).

6.4.1.2 Resolving With ISS

Another strategy for detecting IGM scatter broadening is to observe AGN ISS at multiple frequencies and analyse the ratios of the variability amplitudes, as was done in Chapter 5, but for even more compact sources with $\theta_{src} \sim 1\mu$as or lower. The crux of the previous chapters is that ISS allows source angular sizes to be resolved down to μas scales - with the sample of sources from the MASIV follow-up observations providing constraints on scatter broadening down to the 8μas level for sight-lines to the weak $\sim$ 100 mJy sources with $\sim 10\mu$as angular sizes.

ISS observations of $\sim$ 1 mJy or even μJy sources with a highly sensitive instrument such as the SKA may have the potential of probing angular sizes at much higher resolution, allowing lower level scatter broadening to be detected in the ISS variability ratios. This follows from the observed correlation of ISS amplitudes with mean flux densities in the MASIV Survey (Lovell et al., 2008) and in this study (Section 3.5), implying that these scintillating AGN cores may be brightness temperature-limited. Therefore, lower flux density sources have smaller intrinsic source sizes and are more likely to be dominated by scatter broadening. For a full SKA sensitivity of $A_e/T_{sys} \sim 12000\,\mathrm{m}^2\mathrm{K}^{-1}$ as specified by Schillizi et al. (2007), the array will be able to probe $> 5\%$ variations in a 100 μJy source at $> 5\sigma$ levels with a bandwidth of 350 MHz and an integration time of 1 minute per pointing (refer to Equation 6.15 in Section 6.5).

A model based on the fitting functions of Goodman & Narayan (2006) is used to

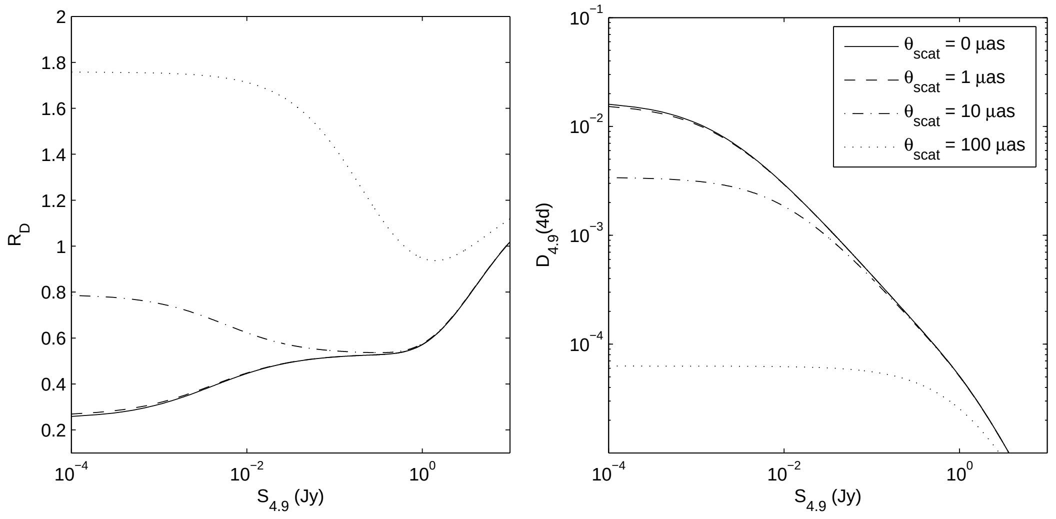

Figure 6.12 — *The left panel shows the ratio of the 4-day structure function at 8.4 GHz to that at 4.9 GHz, R_D, calculated using the Goodman & Narayan (2006) fitting formula, plotted against source mean flux density for various values of θ_{scat}. The right panel shows the amplitude of the 4-day structure function at 4.9 GHz plotted against source mean flux density. The model assumes that the sources are brightness temperature limited so that the source angular sizes scale with mean flux densities (see text in Section 6.4.1.2 for more details).*

further explore the potential of such observations to detect IGM angular broadening. The left panel of Figure 6.12 shows how the ratio of the structure function of ISS at 8.4 GHz to that at 4.9 GHz varies with different source flux densities, modelled as a function of source angular size for a constant brightness temperature of 10^{11} K, compact fraction of 1, and Doppler boosting factor of 15. The ISS model also assumes screen distances of $D_{\rm ISM} \sim 500$ pc, transition frequencies between weak and strong ISS of $\sim$ 4.9 GHz, and screen velocities of $\sim 50{\rm kms}^{-1}$. Corresponding changes in $D_{4.9}(4{\rm d})$ with $S_{4.9}$ are also shown in the right panel of Figure 6.12.

As expected, above $S_{4.9} \sim 1$ Jy, R_D increases as the source mean flux density (and intrinsic angular size) increases. This results from an increase in the ISS time-scales so that $D(4{\rm d})$ at both frequencies do not saturate, with $D_{8.4}(4{\rm d})$ rising faster than $D_{4.9}(4{\rm d})$. At these flux densities, the source is dominated by its intrinsic source size so that scatter broadening at $\sim$ 1 to 10μas scales produces no discernible effect. This effect can be discriminated from large R_D values caused by scatter broadening by increasing the observational period and using $D(\tau > 4{\rm d})$ to obtain R_D.

As the intrinsic source size decreases, the effects of scatter broadening begin to dominate. For $\theta_{scat} \sim 100\mu$as, scatter broadening quickly dominates and R_D saturates at the value of ~ 1.8. Since there is still a factor of > 2 increase in the value of R_D from $\theta_{scat} \sim 1$ to $\theta_{scat} \sim 10\mu$as, θ_{scat} can still be probed between these values for the $\lesssim 1$ mJy sources. This of course depends on how well the errors in the ISS amplitudes, mainly from confusing background sources, can be minimised or characterised for such low flux density sources when observed with the SKA. For $\theta_{scat} \lesssim 1\mu$as, R_D no longer differs significantly from that where the source is not scatter broadened at all, even if θ_{src} decreases further and θ_{scat} dominates. The reason is that the apparent angular size of the source as it appears to the ISM scattering screen (estimated by Equation 5.6) has dropped below the Fresnel scale, where the source effectively becomes a point source in the weak ISS regime and the ISS amplitudes are no longer dependent on the angular size.

The model therefore demonstrates that such an experiment with the SKA only slightly improves the resolution at which scatter broadening may be probed by weak ISS. The Fresnel scale of the ISM scattering screen places a physical limit below which apparent source angular sizes can no longer be probed by weak ISS. Another difficulty arises from the fact that at the lower end of the flux density scale, below mJy levels, starburst galaxies begin to dominate the population of radio sources, rather than radio-loud AGNs (Seymour et al., 2008; De Zotti et al., 2010).

However, there are advantages in using the SKA to conduct similar observations to that of the MASIV follow-up observations. Its higher sensitivity increases the redshifts to which these compact scintillating sources can be detected, as well as the number of detectable sources at high redshift, greatly improving the statistics. The SKA will also be able to detect variations at a much lower level in the sources, allowing R_D to be estimated more accurately, even for the sources with very low $D(4\text{d})$. As pointed out in Section 5.3.2, R_D is reliable only when $D(4\text{d}) \gg D_{noise}$.

The disadvantage of the SKA, however, is that many of these compact, flat-spectrum sources will contain components that will be resolved by the longest baselines of the array. This results in additional variability as these complex structures rotate relative to the array, increasing the systematic errors. Removing the longest baselines from the SKA when conducting such observations effectively also reduces its sensitivity. Other challenges in resolving IGM angular broadening using ISS arises from:

1. the difficulty of discriminating ISS from intrinsic source variability. This can be done for large samples at a statistical level through correlation with line-of-sight Hα intensities. For individual sources however, annual cycles or time-delays between widely separated telescopes will need to be observed.

2. the limitation of having to carry out these observations at GHz frequencies where ISS is strongest and most rapid at mid-Galactic latitudes (as compared to time-scales of months and years below 1 GHz), but where θ_{scat} is smaller than that at

lower frequencies.

3. the introduction of more parameters into the model, including the ISS screen distance and velocity, all of which will need to be determined.

6.4.1.3 Targeted Searches

The discussions in Section 6.3 and above lead to the conclusion that the best way to detect scatter broadening is to carry out targeted searches. Compact extragalactic radio sources known to be intersected by intervening rich clusters, galaxies, or even Damped Lyman-Alpha Systems where $\delta_0 \gtrsim 1000$ can be observed to determine if their angular sizes scale with $\nu^{-2.2}$, preferably if these intervening objects are at $z \sim 0$. This will allow the turbulence of the ionized medium within these objects (i.e. the ISM and the ICM) to be probed or more strongly constrained, particularly since their redshifts and overdensities can be determined from observations at optical and higher frequencies.

The same is true for the WHIM, where in the last few years, X-ray detections of $\mathrm{O}_{\mathrm{VII}}$ absorption lines showing characteristics consistent with WHIM gas have been reported. The most significant detection to date comes from an absorption line at a redshift of $z \sim 0.03$ with estimated overdensities of ~ 30 in the X-ray spectrum of the BL Lac object B2356-309 (Fang et al., 2010), with a source redshift $z_s \sim 0.1651$. Substituting these parameters into Equations 6.3 and 6.8, the outer scale of turbulence in the candidate WHIM cloud can be constrained as:

$$l_0 \gtrsim 0.28 \left[\frac{\theta_{scat(max)}}{1\,\mathrm{mas}} \left(\frac{\nu}{1\,\mathrm{GHz}} \right)^{2.2} \right]^{-\frac{5}{2}} \mathrm{pc}, \tag{6.13}$$

assuming Kolmogorov turbulence and $\zeta \sim \epsilon \sim \eta \sim 1$. Of course, if scatter broadening is detected, the equation becomes an equality rather than an inequality. Only an upper limit to the source size at a particular frequency is needed to constrain l_0. If a component of angular size 1 mas is found for B2356-309 at 0.33 GHz for example, feasible with space VLBI, it would imply that the outer scales of Kolmorov turbulence is $\gtrsim 14$ pc for this particular WHIM cloud intersecting it. While there is an unresolved radio counterpart to B2356-309 listed in the Sydney University Molonglo Sky Survey (SUMSS) catalogue (Mauch et al., 2003), no VLBI images of this source have been published or are available in known archives.

High angular resolution radio observations thus provide a good follow-up of possible future detections of more WHIM absorption lines at X-ray frequencies to constrain turbulence in the WHIM. Since the search for these X-ray absorption lines tend to focus on BL Lac objects due their featureless spectra, it is likely that these sources will have very compact cores at radio frequencies and will tend to scintillate.

6.4.2 Detecting Temporal Smearing

As shown in Section 6.3.2, while angular broadening may be insignificant and difficult to detect ($\lesssim 8\mu$as at 4.9 GHz), temporal smearing can still be large, up to $\tau_d \sim 50$ ms and $\tau_d \sim 1400$ s at 1 GHz and 0.1 GHz respectively (Figure 6.10). Even for outer scales of turbulence as low as ~ 1 Mpc, τ_d can be as large as ~ 1 ms at 1.4 GHz for screen overdensities of $\delta_0 \sim 1000$, well within the capabilities of current instruments. For WHIM clouds of $\delta_0 \sim 30$ and with $l_0 \sim 1$ Mpc, the temporal smearing is at $\sim 0.1\mu$s scales at 1.4 GHz. τ_d increases further at lower frequencies and if these components have lower values of l_0.

The main advantage of probing the IGM with impulsive phenomena is that while temporal smearing scales with $\nu^{-4.4}$, the temporal-resolution of the instrument has no frequency dependence, unlike the angular resolution. We are therefore limited only by the capabilities of the computing hardware and software. Many algorithms have been and are being developed (see e.g. Bannister & Cornwell (2011), Trott et al. (2011)), to efficiently utilize the computing power available to search for such pulses in future interferometric surveys in real time.

Another advantage of using temporal smearing of extragalactic sources as a probe of the IGM is that the effects in the IGM may dominate over that in the ISM due to the longer pathlengths, as opposed to angular broadening where the effects of the ISM will dominate, as discussed in Section 6.2.2.

Of course, probing the IGM through the dispersion and temporal smearing of transient radio pulses is completely dependent on first being able to detect such transient bursts at extragalactic distances, as well as confirming their astrophysical and extragalactic origins. The detectability of extragalactic bursts will in itself be limited by temporal smearing in the IGM, which will be the focus of the next section.

6.5 Limits on Extragalactic Transient Detection

The distance out to which a transient burst of luminosity L_ν can be detected, assuming isotropic radiation, is given by:

$$D_S < \sqrt{\frac{L_\nu}{4\pi f(\tau_d) S_{\nu,0}}}, \tag{6.14}$$

following Macquart (2011), where at cosmological scales, D_S is the luminosity distance. $S_{\nu,0} = \sigma_n \mathrm{SNR}$ is the minimum flux density detectable by the telescope, determined by the rms noise level, σ_n, and the minimum signal-to-noise ratio, SNR, for which a spike in flux density is considered to be statistically significant in the time-domain. The rms noise level of a telescope for two polarisations is given by:

$$\sigma_n = \frac{2k_B T_{sys}}{A_e\sqrt{2\Delta\nu\Delta T}}, \tag{6.15}$$

where k_B is the Boltzmann constant, T_{sys} and A_e are the system temperature and effective area of the telescope, $\Delta\nu$ is the bandwidth, and ΔT is the integration time. For this study, the integration time is assumed to be optimally matched to the total transient pulse width, T, so that $\Delta T = T \approx \sqrt{\Delta t^2 + \tau_d^2}$, where Δt is the intrinsic pulse width of the source. The pulse is also assumed to be fully dedispersed.

The function $f(\tau_d)$ in Equation 6.14 is a modifying factor that accounts for the decrease in amplitude of the pulse due to temporal smearing, estimated as (Macquart, 2011):

$$f(\tau_d) \approx \frac{T}{\Delta t} = \frac{\sqrt{\Delta t^2 + \tau_d^2}}{\Delta t}. \tag{6.16}$$

Note that there is a corresponding factor of $\approx \sqrt{T/\Delta t}$ increase in $S_{\nu,0}$ if the integration time is optimally matched to a temporally smeared pulse. Therefore, temporal smearing in effect decreases the measured flux density of a pulse by a factor of $\sqrt{f(\tau_d)} = \sqrt{T/\Delta t}$. The maximum luminosity distance out to which a transient burst of luminosity L_ν can be detected, D_S, is also reduced by a factor of $(T/\Delta t)^{1/4}$. If the width of the pulse is dominated by τ_d, this means that the reduction in pulse amplitude as encapsulated by $f(\tau_d)$ scales with $\nu^{-4.4}$, but the actual decrease in flux density of the pulse scales with $\nu^{-2.2}$.

The strongest constraints available to date indicate that temporal smearing in the IGM has the potential to severely limit the detectability of extragalactic radio bursts with current or future radio telescopes at low frequencies. The upper limits of $\sqrt{f(\tau_d)} = \sqrt{T/\Delta t}$ as a function of frequency is shown in the left panel of Figure 6.13 for an intrinsic pulse width of 1 ms, based on the constraints on τ_d estimated from the MASIV follow-up observations. The flux density of an extragalactic pulse of duration 1 ms intrinsically can be reduced by up to an order of magnitude at $\sim$ 1 GHz, and up to $\sim$ 3 orders of magnitude at $\sim$ 50 MHz. Similar curves are shown using values of τ_d obtained from the thin screen IGM model for a source at $z \sim 0.1$ and various δ_0 and $l_0 \sim 1$ Mpc. Based on these model estimates, τ_d does not significantly reduce the flux densities of a pulse of width $\gtrsim 1$ ms down to 50 MHz for sightlines where $\delta_0 \sim 1$ if $l_0 \sim 1$ Mpc. The effects will be important, however, for sight-lines intersecting rich clusters of galaxies with $\delta_0 \sim 1000$.

The maximum distance out to which a burst of 1 ms intrinsic pulse width can be detected can be reduced by up to a factor $\sim$ 2 at 1 GHz, and up to $\sim$ 2 orders of magnitude at 50 MHz (Figure 6.13, right panel). Even without the effects of temporal smearing, a 1 ms pulse of luminosity 10^{20} WHz^{-1} can be detected at an SNR of 5 only up to $\sim$ 20 Mpc, assuming full SKA sensitivity and a bandwidth of 350 MHz. This is not much further than the distance to the Virgo Supercluster, a possible target for future transient surveys. Temporal smearing may reduce this distance down to 10 Mpc at 1 GHz, and 0.2 Mpc at 50 MHz. This ignores any spectral index of the source

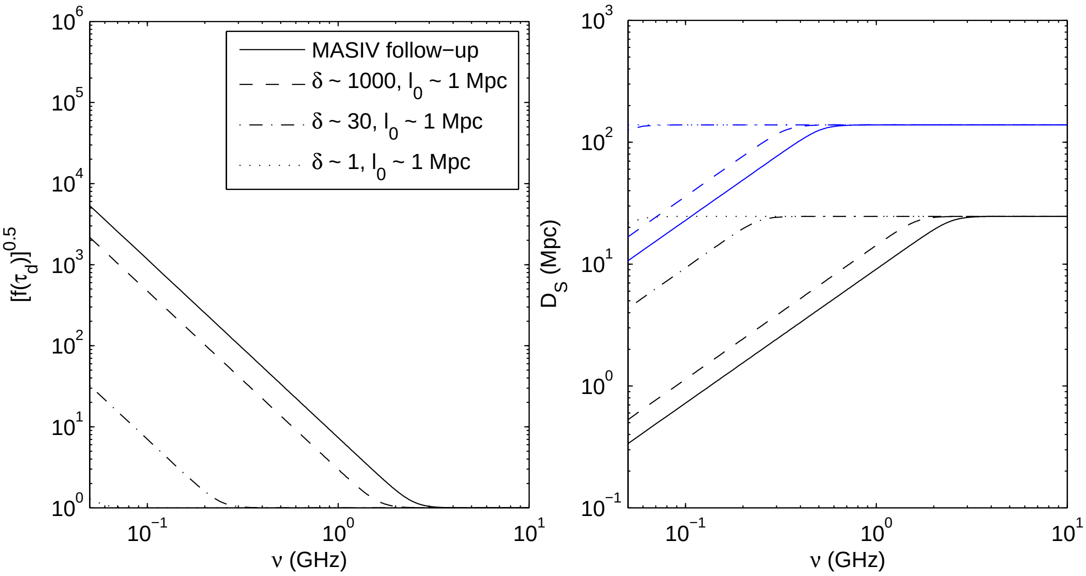

Figure 6.13 — *The reduction in flux density of a burst with an intrinsic pulse width of 1 ms due to temporal smearing at various observing frequencies (left panel), estimated using constraints from the MASIV follow-up observations and the thin screen IGM model at various overdensities and* $l_0 \sim 1$ *Mpc. Also shown are the maximum distances out to which a source of luminosity* $10^{20}\,\mathrm{WHz}^{-1}$ *can be detected at SNR* ~ 5 *with the full SKA sensitivity with a 350 MHz bandwidth (right panel). The blue curves are for a 1 s burst.*

luminosity, where objects such as pulsars are known to be more luminous at lower frequencies (Lorimer et al., 1995; Maron et al., 2000).

The situation is improved for longer duration transients. If the intrinsic pulse width is on the order of ~ 1 s, D_{max} increases to slightly greater than 100 Mpc if the integration time is optimally matched to the pulse width. The frequency at which τ_d begins to significantly affect $\sqrt{f(\tau_d)} = \sqrt{T/\Delta t}$ also decreases. It can thus be argued that longer duration pulses are more likely to be detected at Mpc distances, for a fixed luminosity, placing less stringent constraints on computational speeds for real time detections of extragalactic radio transients.

A 1 ms pulse of luminosity $4\,\mathrm{kJy\,kpc}^2$, similar to that of the giant pulses of the Crab pulsar (Cordes et al., 2004), can be detected only up to ~ 500 kpc at an SNR of 5, assuming full SKA sensitivity and a bandwidth of 350 MHz. This is well short of the distance to the Andromeda Galaxy. Temporal smearing may reduce this distance down to ~ 200 kpc at 1 GHz. These distances may be even lower if the intrinsic pulse widths are of order 1μas as observed in actual giant pulses.

For 'Lorimer burst' type transients, with luminosities of order $30\,\mathrm{Jy\,Gpc}^2$ (Lorimer et al., 2007), they can be detected up to luminosity distances of ~ 100 Gpc with full SKA sensitivity, equivalent to $z \sim 9.5$. This could be further reduced down to ~ 40 Gpc ($z \sim 4.5$) at 1 GHz and ~ 1.5 Gpc ($z \sim 0.3$) at 50 MHz. These values are based on the constraints from the MASIV follow-up observations, which contain sources up to $z \sim 4$, so temporal smearing in the IGM could be much more significant at higher redshifts.

Since known phenomena such as pulsar giant pulses are unlikely to be detectable beyond 1 Mpc even with the full sensitivity of the SKA, probing the cosmological evolution of the IGM and its turbulence with extragalactic radio bursts is dependent upon the detection and confirmation of new classes of impulsive objects with luminosities $\gg 10^{20}\,\mathrm{WHz}^{-1}$. The fundamental limit to the detection of these objects is the sensitivity of the telescope, as opposed to the angular broadening of continuum sources where the integration time can be increased for higher sensitivity observations.

The detection rate, R_ν, has been developed as a metric for quantifying and comparing the capabilities of telescopes with different array configurations, observing modes, and bandwidths for a given density distribution of transient sources, to investigate optimal strategies for transient detection. The detection rate is given by Macquart (2011) as:

$$R_\nu = \rho_0 \frac{\Omega}{4\pi} V_{max} = \frac{1}{3} \rho_0 \Omega D_S^3, \tag{6.17}$$

where ρ_0 is the volume density of these transient objects per unit time, Ω is the field of view of the instrument in units of solid angle, and $V_{max} = 4\pi D_S/3$ is the spherical volume that can be surveyed by the limited sensitivity of the instrument. Using this and another related metric, the event rate per unit cost, Colegate & Clarke (2011) found the SKA1 and SKA2 to be excellent and cost-effective transient detection machines at low frequencies (see also Hall et al. (2012)). While temporal smearing in the ISM was considered in these studies, similar effects in the IGM were not considered. Additional contributions from the IGM will reduce the detection rates predicted in these studies by a factor of $f(\tau_d)^{3/4}$ for extragalactic sources, since $R_\nu \propto D_S^3$ and $D_S \propto f(\tau_d)^{-1/4}$.

6.6 Chapter Summary

In this chapter, a model was used to estimate angular broadening and temporal smearing due to the IGM, based on an extension of the thin screen scattering model of the ISM to cosmological scales. The model was used together with the MASIV follow-up observations of AGN ISS and candidate extragalactic radio bursts to place constraints on IGM scattering and turbulence. The possibility of detecting and probing the IGM with new and next generation radio telescopes was presented, followed by a discussion on how temporal smearing in the IGM limits the detectability of extragalactic radio transients. The conclusions of the chapter can be summarised as follows:

1. At 4.9 GHz, angular broadening in the IGM is $\lesssim 110\mu$as for all lines of sight to the sources in the MASIV follow-up observations, and down to $\lesssim 8\mu$as for sight-lines to the $\sim 10\mu$as sources. An upper limit is also obtained for the SM of the IGM at $3.3 \times 10^{-5}\,\mathrm{kpc\,m^{-20/3}}$ for these latter lines of sight.

2. Temporal smearing in the IGM is estimated to be $\lesssim$ 100ms at 1 GHz, consistent with that obtained from candidate extragalactic radio bursts detected by Lorimer et al. (2007) and Keane et al. (2011).

3. The outer scales of turbulence in the diffuse IGM is $\gtrsim 3 \times 10^{-4}$ pc assuming a Kolmogorov spectrum, implying that mechanical energy is not injected into the IGM at scales smaller than this. The outer scales of turbulence in intervening galaxies and the hot cluster gas could not be constrained since these objects do not dominate the sight-lines to the MASIV follow-up sample.

4. Angular broadening in the IGM can barely be resolved with ground-based interferometers, and can only be detected below 800 MHz at space VLBI baselines of $\sim 350,000$ km for sight-lines through regions of overdensity $\delta_0 \sim 1000$, for fully developed Kolmogorov turbulence with outer scales $\sim$ 1 Mpc. For the WHIM with $\delta_0 \sim 30$, angular broadening can only be detected if the outer scales of turbulence are $<$ 1 kpc.

5. Examining the ratios of ISS variability amplitudes of $<$ 100 mJy sources with the SKA does not significantly improve the resolution at which angular broadening

can be probed with weak ISS. However, conducting surveys similar to that of the MASIV follow-up observations using the SKA will probe fainter sources at much higher redshifts and lower levels of ISS at greater SNR, providing more robust and complete statistical samples. This will provide better representations of the distribution of ISS amplitudes in the $z > 3$ sources.

6. Temporal smearing of impulsive extragalactic radio sources due to the IGM can still be significant, providing the best chance of detecting IGM scattering. For Kolmogorov turbulence with outer scales of order ~ 1 Mpc, regions with $\delta_0 \sim 30$ and 1 give temporal smearing timescales of ~ 100 and 0.1 ms respectively at 0.1 GHz.

7. Potentially crippling limits on the detectability of extragalactic radio transients at low frequencies cannot be ruled out even by the strongest available observational constraints on temporal smearing as obtained from the upper limits of angular broadening of scintillating AGNs. This has possible detrimental implications for transient surveys on the MWA, LOFAR and SKA-low. The flux density of an extragalactic burst with intrinsic pulse width of 1 ms can be reduced by up to an order of magnitude at ~ 1 GHz, and up to ~ 3 orders of magnitude at ~ 50 MHz. Thin-screen scattering models developed for the IGM indicate, however, that these values may be much lower for most sight-lines. These models and observational upper limits will need to be revised, should there be successful detections of IGM scattering on precursor instruments such as the MWA and LOFAR, which will then guide the system design of the SKA for transient experiments.

Chapter 7

Conclusions and Scope for Future Work

> *Nothing is so fatal to the progress of the human mind as to suppose our views of science are ultimate; that there are no mysteries in nature; that our triumphs are complete; and that there are no new worlds to conquer.*
>
> — ***Sir Humphry Davy***

While the potential of using ISS as a probe of the ISM and the background sources has long been recognised, the MASIV survey was the first ever large-scale survey designed specifically to observe AGN ISS, thereby enabling statistical studies of the phenomenon. The MASIV follow-up observations have added to the original MASIV dataset by providing more sensitive, simultaneous multi-frequency observations for a longer duration of 11 days, offering their own unique insights not only into the dependence of ISS on the structure of AGN cores and the ISM, but also into variability caused by systematic and instrumental effects. I now summarize in Section 7.1 the main contributions and findings presented in this thesis, based mainly on the processing and analysis of the MASIV follow-up observations, and situate them within their wider contexts. I then highlight the implications of this study on transient and variability surveys with the SKA and its precursor telescopes in Section 7.2. Section 7.3 then explores possible directions this research can be steered towards in the near future to improve on current techniques and observations, as well as to resolve some of the outstanding questions in the field, some of which were raised in this study.

7.1 Summary of Main Contributions and Findings

A thorough analysis of the source visibilities, lightcurves and structure functions has provided a much better understanding of the stochastic and systematic errors affecting time-domain astrophysical data, allowing these errors to be estimated and discriminated from real astrophysical variability. This was achieved by recognising that weak and strong sources are dominated by different types of errors, and through comparisons of source lightcurves and variability amplitudes at the shortest timescales possible at both frequencies. The daily repeating patterns observed in about a third of the sources, in particular, were originally a mystery to my colleagues from the MASIV collaboration and me; it was attributed to confusion in the MASIV paper by Lovell et al. (2008), but the analysis described in Chapter 2 of this thesis has revealed that they originate from residual post-calibration gain errors in $\sim 95\%$ of the cases. A method to estimate these residual gain errors was developed successfully, based on the 'cross-calibration' of secondary calibrator sources. These analyses have provided valuable lessons for similar observations and variability surveys in the future, such as the VAST Survey planned for the ASKAP, where efficient pipelined algorithms are required to reduce and process the large data streams.

Significant correlation of ISS amplitudes with Galactic Hα emission was found for observing spans triple that of each MASIV epoch and for longer timescales of up to 7 days. These provided further confirmation that ISS is the dominant mechanism behind IDV at GHz frequencies, over and against arguments that IDV mainly arises from intrinsic variability in the sources, as espoused by some members of the astronomical community. This is important for the understanding of the physics of AGNs, indicating that the brightness temperatures and Doppler boosting factors of these objects are less extreme than would be implied by intrinsic variability. The emerging picture, as first revealed by the MASIV results and further confirmed by this study, is that the μas components of scintillating AGNs are brightness temperature limited, as inferred from the correlation of ISS amplitudes with source mean flux densities.

This study has also highlighted the potential of probing AGN core shifts down to μas scales by observing time-delays in scintillation patterns across multiple frequencies. However, due to the sparse sampling of flux densities (~ 2 hours between observations) and the use of lightcurves at only two frequencies, the candidate sources with core-shifts reported in Chapter 3 will need to be confirmed with further observations at more frequencies and smaller gaps in sampling. Studying these core shifts at different frequencies will be important for astrometric applications in the selection of sources for the International Celestial Reference Frame.

Although it is well known that steep-spectrum sources do not scintillate while flat-spectrum sources do, this study provided the first significant detection of correlation between ISS amplitudes and the spectral indices of classical 'flat-spectrum', core-dominated sources. These $\alpha_{4.9}^{8.4} < -0.4$ sources do scintillate but at significantly lower levels, which can be explained by a decreased dominance of the μas cores relative to their compact mas components, perhaps due to weaker Doppler boosting. Why the fraction of these $\alpha_{4.9}^{8.4} < -0.4$ sources with weaker ISS increases at $z > 2$ in the MASIV follow-up sample of sources remains unknown; it can be attributed either to selection biases or AGN evolution.

A method was developed to search for rapid scintillators in the MASIV follow-up sample of sources, allowing rapid and extreme ISS to be analysed statistically. Observational evidence was found to support theoretical calculations that rapid scintillation can arise from both very nearby screens or very compact sources. To explain the scarcity of 'extreme scintillators', I argued that 3 additional constraints are required for a source exhibiting rapid scintillation of timescales $\lesssim 2\,$hours to also exhibit $> 10\%$ rms variations: (1) high levels of turbulence at the scattering cloud, (2) large source compact fractions at the resolution of the telescope, and (3) observations of the source close to the transition frequencies between weak and strong ISS. The second constraint predicts that VLBI will reveal more extreme scintillators than the VLA. The link between the highly turbulent clouds responsible for extreme scintillation and that of ESEs remains a mystery. The MASIV survey and the follow-up observations have painted a picture consistent with models in which ISS arises from an ISM with homogenous turbulence for most lines-of-sight, but is interspersed with sight-lines dominated by discrete, highly turbulent clouds giving rise to ESEs and extreme scintillation. The origin of these discrete clouds is also unknown.

Chapter 5 presented the first thorough investigation into the origin of the redshift dependence of AGN scintillation and the selection effects associated with it, revealing a complexity far greater than initially expected when the MASIV follow-up observations were proposed. A novel technique of analysing the ISS amplitude ratios was developed to account for the many selection biases. As far as can be determined from the dual-frequency ISS observations, the redshift dependence of AGN ISS can be sufficiently explained as a combination of two effects: (1) the $(1+z)^{0.5}$ scaling of source angular sizes of a flux-limited and brightness temperature-limited sample of sources due to the space-time metric of an expanding Universe, and (2) the weaker ISS amplitudes in the $\alpha_{4.9}^{8.4} < -0.4$ sources coupled with the z-$\alpha_{4.9}^{8.4}$ correlation. However, the results presented in Chapter 5 do not have the last word on this puzzling effect, mainly due to the dearth of sources above $z > 3$ and the sensitivity down to which the ratios of the ISS amplitudes can be estimated accurately, limiting the analysis of the variability ratios to the most variable sources. Solving this puzzle carries important cosmological ramifications for future ISS surveys, providing a potential μas-scale probe of the Universe.

The lack of any significant detection of angular broadening in the MASIV follow-up observations has placed the strongest constraints on IGM scatter broadening to date, down to $\lesssim 8\mu$as for sight-lines to the most compact $\sim 10\mu$as sources. The SM of the IGM was then found to be $\lesssim 3.3 \times 10^{-5}\mathrm{kpc\,m^{-20/3}}$. These constraints are consistent with that obtained from the temporal smearing of possible extragalactic bursts such as the 'Lorimer burst' and J1852-08 as well as that estimated from the thin-screen IGM scattering model. They are also broadly consistent with our current understanding of the ionized IGM, but place no significant limits on its properties.

Detections of scattering in the WHIM and the ionized IGM as a whole remain elusive, or ambiguous at best. The possibility of detecting angular broadening and temporal smearing in the IGM using current and next generation radio telescopes was explored. The simple, thin-screen scattering model posits that angular broadening will most likely be undetectable for an IGM with homogenous Kolmogorov turbulence except through the most dense regions such as intervening galaxies or the ICM of rich clusters of galaxies, or unless the outer scales of turbulence in the IGM are of order kpc or lower. There are at present no known mechanisms for injecting turbulence at these scales into the diffuse or WHIM gas in the IGM. However, the temporal smearing of impulsive extragalactic signals by the IGM can be of order ms or higher at MHz frequencies, well within the capabilities of current instruments. The good news, is that temporal smearing in the IGM presents the best bet for probing the turbulence in the ionized IGM, provided that these impulsive sources exist, are detected at cosmological scales, and their extragalactic origins are confirmed.

The bad news, however, is that temporal smearing in the IGM can potentially place severe limits on the detectability of extragalactic radio transients below frequencies of 1 GHz. This study has shown that even with the strongest available constraints on IGM scattering to date, the reduction in pulse amplitudes can be sufficiently high that the pulse amplitudes of such sources may be attenuated beyond the detectability of instruments even as sensitive as the SKA.

Overall, the work presented in this thesis has reinforced the fact that the various manifestations of scattering phenomena at radio wavelengths, including scintillation, angular broadening and temporal smearing of pulses, whether in the ISM or the IGM, can be successfully harnessed to probe the physics of the most compact background objects and that of the scattering medium. While the analyses in this study have revealed a high level of complexity in the interpretation of the data, these challenges were not insurmountable. With the advent of wide-field, survey telescopes such as the ASKAP and the SKA, the MASIV survey and this study act as trailblazers in demonstrating the scientific potential of statistical studies of these phenomena - not just showing how it can be done, but also why it should be done.

7.2 Implications for the SKA and Its Precursors

This study has shown that the aims of VAST, CRAFT and other variable and transient surveys on the SKA and its precursors to directly detect the IGM may be more difficult to achieve than expected. The strong limits on angular broadening obtained from the MASIV follow-up observations, as well as the theoretical models, imply that angular broadening in the IGM is beyond the resolution of the SKA. This study also cannot rule out that temporal smearing in the IGM may significantly reduce the SNR of transient pulses below the detectability thresholds of the SKA and its precursors, thus reducing the likelihood of detecting these sources at cosmological distances to probe the IGM. The detection rates of extragalactic transients as estimated by Colegate & Clarke (2011) may be reduced by a factor of $f(\tau_d)^{3/4}$, where $f(\tau_d)$ can be as high as 10^8 for an intrinsic pulse width of 1 ms at 50 MHz based on the strongest observational limits available to date. This may modify the optimum frequency, as well as the trade-off between sensitivity and field of view for maximizing the detection of extragalactic transients.

However, the SKA still remains the best instrument for extragalactic transient searches due to its orders of magnitude improvements in sensitivity over other telescopes. The exquisite sensitivity of the SKA also makes it an ideal instrument for studying ISS and other forms of variability. It will be able to observe ISS in weak sources with flux densities orders of magnitude below the 100 mJy level, as well as ISS at levels below the 1% lower limit probed by the MASIV Survey and this study. This allows the SKA to potentially detect angular broadening in the IGM, or place much stronger constraints on it, using the resolving power of ISS, down to the $\sim 1\,\mu$as level. The survey speeds achievable with the wide fields of view means that more scintillating sources can be observed to form more statistically robust source samples. The SKA will thus reveal even more exciting physics associated with the ISM and the background scintillating sources.

This is, of course, provided that errors in the time-domain due to confusion and calibration residuals can be reduced to a level comparable to that of the system noise. This is where the precursor instruments will play an important role in enabling further examination and understanding of these errors. While this study has provided a much better understanding of errors in variability data, the lower frequencies probed by instruments such as ASKAP, LOFAR and MWA, as well as their wider fields of view with many confusing background sources, will uncover many other potential sources of systematic errors. In fact, preliminary analysis of the early MWA data have revealed that the low flux density sources exhibit up to 30% variability levels that are not yet understood (Kudryavtseva, private communication). Understanding these sources of errors will go a long way in ensuring that the SKA and its precursors achieve their full potential in time-domain astronomy.

7.3 Scope for Future Work

Several improvements can be made in the reduction and preparation of time-domain data for variability studies. Algorithms for automating RFI detection and excision, for example, will need to be developed. Another area that requires further investigation is the estimation of statistical errors in the structure functions and how this can be included as part of the pipelined process. Estimating characteristic timescales in itself is a major challenge, requiring further exploration, especially when the observation spans are limited. In any case, these techniques and algorithms will be suitably trialled on the MASIV and follow-up data.

In preparation for the new telescopes, the effects of confusion and other sources of errors can be simulated to determine their impact on time-domain data obtained with instruments of such sensitivity and wide fields of view. These will also determine if the methods of error estimation used here will be necessary, suitable or sufficient for future surveys on these telescopes, or if new algorithms are required.

The rich dataset of MASIV and the MASIV follow-up observations can be mined further to maximise their scientific output. The variability of the polarized components of these compact radio sources is not well understood, the study of which will provide insight into the magnetic fields in the ISM as well as that of the background sources. With the multi-frequency data, estimates of rotation measures can be obtained to determine if they correlate with ISS amplitudes or Galactic Hα emission. There is also data from the third frequency of the MASIV follow-up observations, which were severely contaminated with RFI and as yet undetermined instrumental effects. Very careful calibration, RFI excision and comparisons with lightcurves at the other two frequencies will be required before the data can be used. This additional frequency will be critical for confirming and providing more accurate estimates of core shifts, spectral indices, rotation measures and the ratios of the variability amplitudes. There is also the prospect of searching for more rapid and extreme scintillators in the original MASIV data, although it will be difficult to confirm with only one frequency of observation.

There is a strong case for conducting similar follow-up observations to further study ISS and its relation to the morphologies of compact AGNs. Having demonstrated the power of multi-frequency observations of ISS, an ideal experiment would be to conduct surveys similar to MASIV and its follow-up on the EVLA. The tuneable wide-band receivers and correlator enable a full 4 GHz of bandwidth to be observed between 4 and 8 GHz, at the transition frequencies between weak and strong ISS. Observations of such ‘dynamic spectra’ of AGN ISS will more accurately determine the transition frequencies for each source, an important parameter in modelling the observations. It will also provide better estimates of the source spectral index. Instead of examining the redshift dependence of ISS at just two frequencies, one can analyse it at the entire range of frequencies. Furthermore, such an experiment will enable the probing of the frequency dependent core-shifts by cross-correlating the ISS lightcurves across the large number of contiguous channels.

As already mentioned above, the identification of the rapid scintillators as well as core shifts in the sources presented will need to be confirmed. In fact, I am working with colleagues from ICRAR in preparing a proposal to conduct multi-frequency observations of the most rapid scintillators in our sample using the EVLA to search for core-shifts in these sources. Combining these observations with images and lightcurves from VLBI will place stronger constraints on the compact fractions and modulation indices of the scintillating components, in addition to providing core shift measurements at mas scales for comparisons.

One important question that needs to be answered is the origin of ISS intermittency, requiring multi-year surveys on the scales of MASIV. Such surveys will determine if the intermittency of ISS is dominated by annual cycles arising from relative motions between the scattering screens and the Earth (more evidence that the variability is ISS rather than intrinsic), or if it is dominated by intrinsic changes in the source morphology, or perhaps even due to discrete structures in the ISM reminiscent of ESEs and extreme scintillators. The link between extreme scintillators and ESEs needs to be further explored, and is one of the goals of future variability surveys such as the VAST Survey on ASKAP, which aims to detect a large number of ESEs for statistical studies.

ISS studies at radio wavelengths will need to be expanded to incorporate multi-wavelength data, either from archives if available or from new observations. Questions that can be asked include: (1) What is the degree of correlation between ISS/IDV at radio wavelengths with variability at higher energies? (2) Is there a correlation between ISS and Gamma-ray luminosities? (3) Do quasars with known DLA absorption systems scintillate less due to possible scatter broadening, and is there a correlation between ISS and the column density of line-of-sight absorbing material, which act as tracers for IGM clouds?

Another line of investigation involves searching for unpublished data or carrying out new observations to detect the most compact radio components in sources such as B2356-309, with claimed X-ray WHIM absorbers in its sight-line, to place lower limits on the outer scales of turbulence in the candidate WHIM clouds. One can also search for scatter broadening in compact sources with known galaxy clusters in the foreground.

To provide stronger conclusions on the redshift dependence of ISS and the z-α correlation, the results of this study will need to be complemented with further VLBI analysis and observations. Although Ojha et al. (2004b) found differences in core dominance at mas scales between scintillating and non-scintillating sources, further analysis is required to determine if the mas structures of these sources vary with spectral index and redshift. New observations with RadioAstron, for example, will probe the structures of these objects at even higher angular resolution. It will be interesting to observe sources at increasing redshifts at increasing observing frequencies, so that their emissions are probed at similar rest-frame frequencies. The various databases will need to be searched for more compact sources at $z > 3$ to make the sample more complete.

In the meantime, redshift estimates will need to be obtained for the full set of MASIV sources.

On another note, GRB afterglows, while generally less luminous than AGNs, are more compact, have less complicated internal structures, and are also known to exhibit ISS. High-sensitivity survey instruments such as the ASKAP and the SKA will detect a large number of GRB radio afterglows at a range of redshifts. With a sufficiently large sample, it will be interesting to determine if there is a redshift dependence of the ISS of GRB afterglows, or if these sources are scatter broadened by the IGM. In the meantime, available archival GRB ISS data can be examined for preliminary analyses.

On the theoretical front, there is a need to model all the complex effects that go into determining the angular sizes and compact fractions of AGNs, including jet speeds, jet angles, and spectral indices; these can then be used to understand analytically the relationship between AGN morphology and ISS, or by including them into the Monte-carlo simulations for further statistical analysis. The thin screen model for IGM scattering can be easily extended, by integrating the square of the scatter broadening angles over redshift, weighted by intersection probabilities of the various components of the IGM, then summing over all components of the IGM. The main difficulty is in estimating these intersection probabilities, particularly when the various IGM components evolve from one phase to another. This is where the various cosmological hydrodynamical simulations can provide useful input.

Last but not least, it will be of great interest to explore how the limits imposed by temporal smearing in the IGM, as obtained from the observations and the models, affect the optimization of survey strategies for extragalactic radio transients. The detection rates and detection rates per unit cost metrics used by Colegate & Clarke (2011) to compare various observing modes and trade-offs for transient detection on Phase 1 of the SKA should be reexamined with the observational and theoretical limits on IGM scattering obtained in this study. This will provide critical feedback into planned transient surveys.

In pursuing the many lines of investigation proposed here for the near future, the expectation is that more answers will be found, and more questions raised, to drive future surveys on next generation instruments such as the ASKAP and the SKA.

Bibliography

Alfvèn, H., & Herlofsen, N. 1950, *Physical Review*, 73, 616

Armstrong, J. W., Rickett, B. J., & Spangler, S. R. 1995, *The Astrophysical Journal*, 443, 209

Arshakian, T. G., Torrealba, J., Chavushyan, V. H., Ros, E., Lister, M. L., Cruz-González, I., & Zensus, J. A. 2010, *Astronomy & Astrophysics*, 520, A62

Backer, D. C. 1988, in *Radiowave Scattering in the Interstellar Medium*, ed. J.M. Cordes, B.J. Rickett & D.C. Backer (American Institute of Physics Conference Proceedings, Vol. 174; New York: American Institute of Physics), 111

Bahcall, N. A. 1996, in *Allen's Astrophysical Quantities*, ed. A.N. Cox (New York: American Institute of Physics)

Bannister, K. W., & Cornwell, T. J. 2011, *The Astrophysical Journal Supplement*, 196, 16

Bannister, K. W., Murphy, T., Gaensler, B. M., Hunstead, R. W., & Chatterjee, S. 2011, *Monthly Notices of the Royal Astronomical Society*, 412, 634

Bhat, N. D. R., Cordes, J. M., Camilo, F., Nice, D. J., & Lorimer, D. R. 2004, *The Astrophysical Journal*, 605, 759

Bignall, H. E., Jauncey, D. L., Lovell, J. E. J., Tzioumis, A. K., Kedziora-Chudczer, L., Macquart, J.-P., Tingay, S. J., Rayner, D. P., & Clay, R. W. 2003, *The Astrophysical Journal*, 585, 653

Bignall, H. E., Macquart, J.-P., Jauncey, D. L., Lovell, J. E. J., Tzioumis, A. K., & Kedziora-Chudczer, L. 2006, *The Astrophysical Journal*, 652, 1050

Bignall, H. E., Koay, J. Y., Macquart, J.-P, Lovell, J. E. J., Ojha, R., Dutka, M., and Pursimo, T., Rickett, B. J., Jauncey, D. L., & Kedziora-Chudczer, L. 2010, *Proceedings of Science*, PoS(ISKAF2010)004

Bignall, H. E., & Hodgson, J. A. 2012, in *New Horizons in Time Domain Astronomy*, ed. E. Giffin, R. Hanisch, & R. Seaman (Proceedings of the International Astronomical Union Symposium, No. 285; Cambridge: Cambridge University Press), 129

Blandford, R. D. 1990, in *Active Galactic Nuclei*, ed. T.J.-L. Courvoisier & M. Mayor (Saas-Fee Advanced Course 20; Berlin: Springer), 160

Blandford, R. D., Königl, A. 1979, *The Astrophysical Journal*, 232, 34

Blandford, R. D., McKee, C. F., & Rees, M. J. 1977, *Nature*, 267, 211

Blundell, K. M., Rawlings, S., & Willot, C. J. 1999, *The Astronomical Journal*, 117, 677

Born, M., & Wolf, E. 1980, *Principles of Optics* (Oxford: Permagon Press)

Bower, G. C., Whysong, D., Blair, S., Croft, S., Keating, G., Law, C., Williams, P. K. G., & Wright, M. C. H. 2011, *The Astrophysical Journal*, 739, 76

Bregman, J. N. 2007, *Annual Review of Astronomy & Astrophysics*, 45, 221

Brisken, W. F., Macquart, J.-P., Gao, J. J., Rickett, B. J., Coles, W. A., Deller, A. T., Tingay, S. J., & West, C. J. 2010, *The Astrophysical Journal*, 708, 232

Browne, I. W. A., Wilkinson, P. N., Patnaik, A. R., & Wrobel, J. M. 1998, *Monthly Notices of the Royal Astronomical Society*, 293, 257

Browne, I. W. A., Wilkinson, P. N., Jackson, N. J. F., Myers, S. T., Fassnacht, C. D., Koopmans, L. V. E., Marlow, D. R., Norbury, M., Rusin, D., Sykes, C. M., Biggs, A. D., Blandford, R. D., de Bruyn, A. G., Chae, K.-H., Helbig, P., King, L. J., McKean, J. P., Pearson, T. J., Phillips, P. M., Readhead, A. C. S., Xanthopoulos, E., & York, T. 2003, *Monthly Notices of the Royal Astronomical Society*, 341, 13

Burke-Spolaor, S., Bailes, M., Ekers, R., Macquart, J.-P., & Crawford, F. 2011, *The Astrophysical Journal*, 727, 18

Burles, S., & Tytler, D. 1998, *The Astrophysical Journal*, 499, 699

Burles, S., Nollet, K. M., Truran, J. W., & Turner, M. S. 1999, *Physical Review Letters*, 82, 4176

Cen, R., & Ostriker, J. P. 1999, *The Astrophysical Journal*, 514, 1

Cen, R., & Ostriker, J. P. 2006, *The Astrophysical Journal*, 650, 560

Chhetri, R., Ekers, R. D., Mahony, E. K., Jones, P. A., Massardi, M., Ricci, R., & Sadler, E. M. 2012, *Monthly Notices of the Royal Astronomical Society*, 422, 2274

Cimò, G. 2008, *Proceedings of Science*, PoS(IX EVN Symposium)013

Clarke, B. G. 1999, *Synthesis Imaging in Radio Astronomy II*, ed. G.B. Taylor, C.L. Carilli, & R.A. Perley (Astronomical Society of the Pacific Conference Series, Vol. 285; San Francisco: Astronomical Society of the Pacific), 1

Cohen, M. H., & Cronyn, W. M. 1974, *The Astrophysical Journal*, 192, 193

Cohen, M. H., Gundermann, E. J., & Harris, D. E. 1967, *The Astrophysical Journal*, 150, 767

Cohen, M. H., Linfield, R. P., Moffet, A. T., Seielstad, G. A., Kellermann, K. I., Shaffer, D. B., Pauliny-Toth, I. I. K., Preuss, E., Witzel, A., & Romney, J. D. 1977, *Nature*, 268, 405

Colegate, T. M., & Clarke, N. 2011, *Publications of the Astronomical Society of Australia*, 28, 199

Coles, W. A., Rickett, B. J., Codona, J. L., & Frehlich, R. G. 1987, *The Astrophysical Journal*, 315, 666

Condon, J. J., Cotton, W. D., Greisen, E. W., Yin, Q. F., Perley, R. A., Taylor, G. B., & Broderick, J. J. 1998, *The Astronomical Journal*, 115, 1693

Copi, C. J., Schramm, D. N., & Turner, M. S., 1995, *Science*, 267, 192

Cordes, J. M. 2007, *SKA Memo*, 97

Cordes, J. M., & Lazio, T. J. W. 2003, arXiv:astro-ph/0207156v3

Cordes, J. M., & Wolszczan, A. 1986, *The Astrophysical Journal*, 307, L27

Cordes, J. M., Boriakoff, V., & Weisberg, J. M. 1983, *The Astrophysical Journal*, 268, 370

Cordes, J. M., Pidwerbetsky, A., & Lovelace, R. V. E. 1986, *The Astrophysical Journal*, 310, 737

Cordes, J. M., Bhat, N. D. R., Hankins, T. H., McLaughlin, M. A., & Kern, J. 2004, *The Astrophysical Journal*, 612, 375

Cornwell, T., Braun, R., & Briggs, D. S. 1999, *Synthesis Imaging in Radio Astronomy II*, ed. G.B. Taylor, C.L. Carilli, & R.A. Perley (Astronomical Society of the Pacific Conference Series, Vol. 285; San Francisco: Astronomical Society of the Pacific), 151

Cornwell, T., & Fomalont, E. B. 1999, in *Synthesis Imaging in Radio Astronomy II*, ed. G.B. Taylor, C.L. Carilli, & R.A. Perley (Astronomical Society of the Pacific Conference Series, Vol. 285; San Francisco: Astronomical Society of the Pacific), 187

Counselman, C. C., III, Rankin, J. M. 1971, *The Astrophysical Journal*, 166, 513

D'Addario, L. 2010, *SKA Memo*, 123

Danforth, C. W., & Shull, J. M. 2005, *The Astrophysical Journal*, 624, 555

Davé, R., Cen, R., Ostriker, J. P., Bryan, G. L., Hernquist, L., Katz, N., Weinberg, D. H., Norman, M. L., & O'Shea, B. 2001, *The Astrophysical Journal*, 552, 473

DeBoer, D. R., Gough, R. G., Bunton, J. D., Cornwell, T. J., Beresford, R. J., Johnston, S., Feain, I. J., Schinckel, A. E., Jackson, C. A., Kesteven, M. J., Chippendale, A., Hampson, G. A., O'Sullivan, J. D., Hay, S. G., Jacka, C. E., Sweetnam, T. W., Storey, M. C., Ball, L., & Boyle, B. J. 2009, *Proceedings of the IEEE*, 97, 1507

Dennett-Thorpe, J., & de Bruyn, A. G. 2000, *The Astrophysical Journal*, 529, L65

Dennett-Thorpe, J., & de Bruyn, A. G. 2002, *Nature*, 415, 57

Dennett-Thorpe, J., & de Bruyn, A. G. 2003, *Astronomy & Astrophysics*, 404, 113

Dennison, B., Thomas, M., Booth, R. S., Brown, R. L., Broderick, J. J., & Condon, J. J. 1984, *Astronomy & Astrophysics*, 135, 199

de Vos, M., Gunst, A. W., & Nijboer, R. 2009, *Proceedings of the IEEE*, 97, 1431

Dewdney, P. E. F., Hall, P. J., Schilizzi, R. T., & Lazio, T. J. W. 2009, *Proceedings of the IEEE*, 97, 1482

De Zotti, G., Massardi, M., Negrello, M., & Wall, J. 2010 *The Astronomy and Astrophysics Review*, 18, 1

Djorgovski, S. G., Castro, S., Stern, D., & Mahabal, A. A. 2001, *The Astrophysical Journal*, 560, L5

Dunlop, J. S., & Peacock, J. A. 1990, *Monthly Notices of the Royal Astronomical Society*, 247, 19

Evoli, C., & Ferrara, A. 2011, *Monthly Notices of the Royal Astronomical Society*, 413, 2721

Fang, T., Buote, D. A., Humphrey, P. J., Canizares, C. R., Zappacosta, L., Maiolino, R., Tagliaferri, G., & Gastaldello, F. 2010, *The Astrophysical Journal*, 714, 1715

Fender, R. P., & Bell, M. E. 2011, *Bulletin of the Astronomical Society of India*, 39, 315

Fender, R., Braun, R., Stappers, B., Wijers, R., Wise, M., Coenen, T., Falcke, H., Griessmeier, J.-M., van Haarlem, M., Jonker, P., Law, C., Markoff, S., Masters, J., Miller-Jones, J., Osten, R., Scheers, B., Spreeuw, H., Swinbank, J., Vogt, C., Wijnands, R., & Zarka, P. 2006, *Proceedings of Science*, PoS(MQW6)104

Ferrara, A., & Perna, R. 2001, *Monthly Notices of the Royal Astronomical Society*, 325, 1643

Fey, A. L. & Charlot, P. 2000, *The Astrophysical Journal Supplement Series*, 128, 17

Fiedler, R. L., Dennison, B., Johnston, K. J., & Hewish, A. 1987, *Nature*, 326, 675

Fiedler, R., Pauls, T., Johnston, K. J. & Dennison, B. 1994, *The Astrophysical Journal*, 430, 595

Fiedler, R., Dennison, B., Johnston, K. J., Waltman, E. B., & Simon, R. S. 1994, *The Astrophysical Journal*, 430, 581

Fomalont, E. B., & Perley, R. A. 1999, in *Synthesis Imaging in Radio Astronomy II*, ed. G.B. Taylor, C.L. Carilli, & R.A. Perley (Astronomical Society of the Pacific Conference Series, Vol. 285; San Francisco: Astronomical Society of the Pacific), 79

Frail, D. A., Kulkarni, S. R., Nicastro, L., Feroci, M., & Taylor, G. B. 1997, *Nature*, 389, 261

Frey, S., Gurvits, L. I., Paragi, Z., & Gabányi, K. É. 2008, *Astronomy & Astrophysics*, 484, L39

Frey, S., Paragi, Z., Gurvits, L. I., Cseh, D., & Gabányi, K. É. 2010, *Astronomy & Astrophysics*, 524, A83

Frey, S., Paragi, Z., Gurvits, L. I., Gabányi, K. É., & Cseh, D. 2011, *Astronomy & Astrophysics*, 531, L5

Fukugita, M., Hogan, C. J., & Peebles, P. J. E. 1998, *The Astrophysical Journal*, 616, 643

Fukugita, M., & Peebles, P. J. E. 2004, *The Astrophysical Journal*, 503, 518

Fuhrmann, L., Krichbaum, T. P., Witzel, A., Kraus, A., Britzen, S., Bernhart, S., Impellizzeri, C. M. V., Agudo, I., Klare, J., Sohn, B. W., Angelakis, E., Bach, U., Gabányi, K. É., Körding, E., Pagels, A., Zensus, J. A., Wagner, S. J., Ostorero, L., Ungerechts, H., Grewing, M., Tornikoski, M., Apponi, A. J., Vila-Vilaró, B., Ziurys, L. M., & Strom, R. G. 2008, *Astronomy & Astrophysics*, 490, 1019

Garrett, M. A., Cordes, J. M., DeBoer, D. R., Jonas, J. L., Rawlings, S., & Schillizi, R. T. 2010, *SKA Memo*, 125

Gaustad, J. E., McCullough, P. R., Rosing, W., & Van Buren, D. 2001, *Publications of the Astronomical Society of the Pacific*, 113, 1326

Goddard, W. E., & Ferland, G. J. 2003, *Publications of the Astronomical Society of the Pacific*, 115, 647

Godfrey, L., Bignall, H. & Tingay, S. 2011, *SKA Memo*, 135

Goodman, J., & Narayan, R. 1989, *Monthly Notices of the Royal Astronomical Society*, 238, 995

Goodman, J., & Narayan, R. 2006, *The Astrophysical Journal*, 636, 510

Gopal-Krishna 1988, *Astronomy & Astrophysics*, 192, 37

Greisen, E. 2003, *Information Handling in Astronomy–Historical Vistas*, ed. A. Heck (Astrophysics and Space Science Library, Vol. 285; Dordrecht: Kluwer), 109

Griffin, E., Hanisch, R., & Seaman, R., eds. 2012, *New Horizons in Time Domain Astronomy*, (Proceedings of the IAU Symposium, No. 285; Cambridge: Cambridge University Press)

Gunn, J. E., & Peterson, B. A. 1965, *The Astrophysical Journal*, 142, 1633

Gurvits, L. I., Kellermann, K. I., & Frey, S. 1999, *Astronomy & Astrophysics*, 342, 378

Gwinn, C. R., Bartel, N., Cordes, J. M., Wolszczan, A., & Mutel, R. L. 1988, *The Astrophysical Journal*, 334, L13

Gwinn, C. R., Ojeda, M. J., Britton, M. C., Reynolds, J. E., Jauncey, D. L., King, E. A., McCulloch, P. M., Lovell, J. E. J., Flanagan, C. S., Smits, D. P., Preston, R. A., & Jones, D. L. 1997, *The Astrophysical Journal*, 483, L53

Haffner, L. M., Reynolds, R. J., & Tufte, S. L. 1998, *The Astrophysical Journal*, 501, L83

Hall, A. N., & Sciama, D. W. 1979, *The Astrophysical Journal*, 228, L15

Hall, P. J., Schilizzi, R. T., Dewdney, P. E. F., & Lazio, T. J. W. 2008, *Radio Science Bulletin*, 327, 4

Hall, P. J., Colgate, T. M., Macquart, J.-P., Clarke, N., Tingay, S. J., Wayth, R. & Trott, C. 2012, *Proceedings of Science*, in press

Haverkorn, M., Brown, J. C., Gaensler, B. M., & McClure-Griffiths, N. M. 2008, *The Astrophysical Journal*, 680, 362

Haffner, L. M., Reynolds, R. J., Tufter, S. L., Madsen, G. J., Jaehnig, K. P., & Percival, J. W. 2003, *The Astrophysical Journal Supplement Series*, 149, 405

Heeschen, D. S. 1984, *The Astrophysical Journal*, 89, 1111

Heeschen, D. S., Krichbaum, T., Schalinski, C. J., & Witzel, A. 1987, *The Astronomical Journal*, 94, 1493

Heeschen, D. S., & Rickett, B. J. 1987, *The Astronomical Journal*, 93, 589

Hessels, J. W. T., Stappers, B. W., van Leeuwen, J., & the LOFAR collaboration 2008, in *The Low Frequency Radio Universe*, ed. D.J. Saikia, D.A. Green, Y. Gupta, & T. Venturi (Astronomical Society of the Pacific Conference Series, Vol. 407; San Francisco: Astronomical Society of the Pacific), 318

Hewish, A. 1952, *Proceedings of the Royal Society of London*, 214, 494

Hewish, A. 1988, in *Radiowave Scattering in the Interstellar Medium*, ed. J.M. Cordes, B.J. Rickett & D.C. Backer (American Institute of Physics Conference Proceedings, Vol. 174; New York: American Institute of Physics), 88

Hewish, A., Scott, P. F., & Wills, D. 1964, *Nature*, 203, 1214

Hodges, M. W., Mutel, R. L., & Phillips, R. B. 1984, *The Astronomical Journal*, 89, 1327

Hogbom, J. H. 1974, *Astronomy & Astrophysics Supplement Series*, 15, 417

Hovatta, T., Valtaoja, E., Tornikoski, M., & Lähteenmäki, A. 2009, *Astronomy & Astrophysics*, 494, 527

Inoue, S. 2004, *Monthly Notices of the Royal Astronomical Society*, 348, 999

Ioka, K. 2003, *The Astrophysical Journal*, 598, L79

Jarvis, M. J., & Rawlings, S. 2000, *Monthly Notices of the Royal Astronomical Society*, 319, 121

Jauncey, D. L., Kedziora-Chudczer, L., Lovell, J. E. J., Nicolson, G. D., Perley, R. A., Reynolds, J. E., Tzioumis, A. K., & Wieringa, M. H. 2000, in *Astrophysical Phenomena Revealed by Space VLBI*, ed. H. Hirabayashi, P.G. Edwards & D.W. Murphy (Sagimihara: Institute of Space and Astronautical Science), 147

Jauncey, D. L., & Macquart, J. -P. 2001, *Astronomy & Astrophysics*, 370, L9

Jauncey, D. L., Johnston, H. M., Bignall, H. E., Lovell, J. E. J., Kedziora-Chudczer, L., Tzioumis, A. K., & Macquart, J.-P. 2003, *Astrophysics & Space Science*, 288, 63

Jonas, J. L. 2009, *Proceedings of the IEEE*, 97, 1522

Jorstad, S. G., Marscher, A. P., Lister, M. L., Stirling, A. M., Cawthorne, T. V., Gear, W. K., Gómez, J. L., Stevens, J. A., Smith, P. S., Forster, J. R., & Robson, E. I. 2005, *The Astronomical Journal*, 130, 1418

Keane, E. F., Kramer, M., Lyne, A. G., Stappers, B. W., & McLaughlin M. A. 2011, *Monthly Notices of the Royal Astronomical Society*, 415, 3065

Kedziora-Chudczer, L., Jauncey, D. L., Wieringa, M. H., Walker, M. A., Nicolson, G. D., Reynolds, J. E., & Tzioumis, A. K. 1997, *The Astrophysical Journal*, 490, L9

Kedziora-Chudczer, L. 2006, *Monthly Notices of the Royal Astronomical Society*, 369, 449

Kellermann, K. I., & Pauliny-Toth, I. I. K. 1969, *The Astrophysical Journal*, 155, L71

Kellermann, K. I., Sramek, R., Schmidt, M., Shaffer, D. B., & Green, R. 1989, *The Astronomical Journal*, 98, 1195

Klamer, I. J., Ekers, R. D., Bryant, Hunstead, R. W., Sadler, E. M., & De Breuck, C. 2006, *Monthly Notices of the Royal Astronomical Society*, 371, 852

Koay, J. Y., Macquart, J.-P., Rickett, B. J., Bignall, H. E., Lovell, J. E. J., Reynolds, C., Jauncey, D. L., Pursimo, T., Kedziora-Chudczer, L., & Ojha, R. 2011, *The Astronomical Journal*, 142, 108

Koay, J. Y., Bignall, H. E., Macquart, J.-P., Jauncey, D. L., Rickett, B. J., & Lovell, J. E. J. 2011, *Astronomy & Astrophysics*, 534, L1

Koay, J. Y., Macquart, J.-P., Rickett, B. J., Bignall, H. E., Jauncey, D. L., Pursimo, T., Reynolds, C., Lovell, J. E. J., Kedziora-Chudczer, L., & Ojha, R. 2012, *The Astrophysical Journal*, 756, 29

Kovalev, Y. Y., Lobanov, A. P., Pushkarev, A. B., & Zensus, J. A. 2008, *Astronomy & Astrophysics*, 483, 759

Krolik, J. H., & Chen, W. 1991, *The Astronomical Journal*, 102, 1659

Lähteenmäki, A., & Valtaoja E. 1999, *The Astrophysical Journal*, 521, 493

Lähteenmäki, A., Valtaoja, E. & Wiik, K. 1999, *The Astrophysical Journal*, 511, 112

Laing, R. A., & Peacock, J. A. 1980, *Monthly Notices of the Royal Astronomical Society*, 190, 903

Lazio, T. J. W., Cordes, J. M., de Bruyn, A. G. & Macquart, J.-P. 2004, *New Astronomy Reviews*, 48, 1439

Lazio, T. J. W., Ohja, R., Fey, A. L., Kedziora-Chudczer, L., Cordes, J. M., Jauncey, D. L., & Lovell, J. E. J. 2008, *The Astrophysical Journal*, 672, 115

Lee, L. C., & Jokipii, J. R. 1975, *The Astrophysical Journal*, 201, 532

Lee, L. C., & Jokipii, J. R. 1976, *The Astrophysical Journal*, 206, 735

Linsky, J. L., Rickett, B. J. & Redfield, S. 2008, *The Astrophysical Journal*, 675, 413

Lister, M. L., & Marscher, A. P. 1997, *The Astrophysical Journal*, 476, 572

Little, L. T., & Hewish, A., 1966, *Monthly Notices of the Royal Astronomical Society*, 134, 221

Lonsdale, C. J., Cappallo, R. J., Morales, M. F., Briggs, F. H., Benkevitch, L., Bowman, J. D., Bunton, J. D., Burns, S., Corey, B. E., deSouza, L., Doeleman, S. S., Derome, M., Deshpande, A., Gopala, M. R., Greenhill, L. J., Herne, D. E., Hewitt, J. N., Kamini, P. A., Kasper, J. C., Kincaid, B. B., Kocz, J., Kowald, E., Kratzenberg, E., Kumar, D., Lynch, M. J., Madhavi, S., Matejek, M., Mitchell, D. A., Morgan, E., Oberoi, D., Ord, S., Pathikulangara, J., Prabu, T., Rogers, A., Roshi, A., Salah, J. E., Sault, R. J., Shankar, N. U., Srivani, K. S., Stevens, J., Tingay, S., Vaccarella, A., Waterson, M., Wayth, R. B., Webster, R. L., Whitney, A. R., Williams, A., & Williams, C. 2009, *Proceedings of the IEEE*, 97, 1497

Lorimer, D. R., Yates, J. A., Lyne, A. G., & Gould, D. M. 1995, *Monthly Notices of the Royal Astronomical Society*, 273, 411

Lorimer, D. R., Bailes, M., McLaughlin, M. A., Narkevic, D. J., & Crawford, F. 2007, *Science*, 318, 777

Lovell, J. E. J., Jauncey, D. L., Bignall, H. E., Kedziora-Chudczer, L., Macquart, J.-P., Rickett, B. J., & Tzioumis, A. K. 2003, *The Astronomical Journal*, 126, 1699

Lovell, J. E. J., Rickett, B. J., Macquart, J.-P. Jauncey, D. L., Bignall, H. E., Kedziora-Chudczer, L., Ojha, R., Pursimo, T., Dutka, M., Senkbeil, C., & Shabala, S. 2008, *The Astrophysical Journal*, 689, 108

Macklin. J. T. 1982, *Monthly Notices of the Royal Astronomical Society*, 199, 1119

Macquart, J.-P. 2004, *Astronomy & Astrophysics*, 422, 761

Macquart, J.-P. 2011, *The Astrophysical Journal*, 734, 20

Macquart, J.-P., & de Bruyn, A. G. 2007, *Monthly Notices of the Royal Astronomical Society*, 380, L20

Macquart, J.-P., Kedziora-Chudczer, L., Rayner, D. P., & Jauncey, D. L. 2000, *The Astrophysical Journal*, 538, 623

Macquart, J.-P., Bailes, M., Bhat, N. D. R., Bower, G. C., Bunton, J. D., Chatterjee, S., Colegate, T., Cordes, J. M., D'Addario, L., Deller, A., Dodson, R., Fender, R., Haines, K., Hall, P., Harris, C., Hotan, A., Jonston, S., Jones, D. L., Keith, M., Koay, J. Y., Lazio, T. J. W., Majid, W., Murphy, T., Navarro, R., Phillips, C., Quinn, P., Preston, R. A., Stansby, B., Stairs, I., Stappers, B., Staveley-Smith, L., Tingay, S., Thompson, D., van Straten, W., Wagstaff, K., Warren, M., Wayth, R., & Wen, L. 2010, *Publications of the Astronomical Society of Australia*, 27, 272

Maron, O., Kijak, J., Kramer, M., & Wielebinski, R. 2000, *Astronomy & Astrophysics Supplement*, 147, 195

Mathur, S., Weinberg, D. H., & Chen, X. 2003, *The Astrophysical Journal*, 582, 82

Mauch, T., Murphy, T., Buttery, H. J., Curran, J., Hunstead, R. W., Piestrzynski, B., Robertson, J. G., & Sadler, E. M. 2003, *Monthly Notices of the Royal Astronomical Society*, 342, 1117

McLaughlin, M. A., Lyne, A. G., Lorimer, D. R., Kramer, M., Faulkner, A. J., Manchester, R. N., Cordes, J. M., Camilo, F., Possenti, A., Stairs, I. H., Hobbs, G., D'Amico, N., Burgay, M., & O'Brien, J. T. 2006, *Nature*, 439, 817

Moran, J. M., Rodriguez, L. F., Greene, B., & Backer, D. C. 1990, *The Astrophysical Journal*, 348, 147

Murphy, T., & Chatterjee, S. 2009,*VAST Memo*, 1

Mutel, R. L., Hodges, M. W., & Phillips, R. B. 1985, *The Astrophysical Journal*, 290, 86

Myers, S. T., Fassnacht, C. D., Djorgovski, S. G., Blandford, R. D., Matthews, K., Neugebauer, G., Pearson, T. J., Readhead, A. C. S., Smith, J. D., Thompson, D. J., Womble, D. S., Browne, I. W. A., Wilkinson, P. N., Nair, S., Jackson, N., Snellen, I. A. G., Miley, G. K., de Bruyn, A. G., & Schilizzi, R. T. 1995, *The Astrophysical Journal*, 447, L5

Myers. S. T., Jackson, N. J., Browne, I. W. A., de Bruyn, A. G., Pearson, T. J., Readhead, A. C. S., Wilkinson, P. N., Biggs, A. D., Blandford, R. D., Fassnacht, C.

D., Koopmans, L. V. E., Marlow, D. R., McKean, J. P., Norbury, M. A., Phillips, P. M., Rusin, D., Shepherd, M. C., & Sykes, C. M. 2003a, *Monthly Notices of the Royal Astronomical Society*, 341, 1

Narayan, R. 1992, *Philosophical Transactions of the Royal Society of London*, 341, 151

Narayan, R., & Bartelmann, M. 1997, arXiv:astro-ph/9606001v2

Narayan, R. & Goodman, J. 1989, *Monthly Notices of the Royal Astronomical Society*, 238, 963

Nicastro, F., Zezas, A., Drake, J., Elvis, M., Fiore, F., Fruscione, A., Marengo, M., Mathur, S., & Bianchi, S. 2002, *The Astrophysical Journal*, 573, 157

Nicastro, F., Mathur, S., Elvis, M., Drake, J., Fiore, F., Fang, T., Fruscione, A., Krongold, Y., Marshall, H., & Williams, R. 2005, *The Astrophysical Journal*, 629, 700

O'Dea, C. P. 1998, *Publications of the Astronomical Society of the Pacific*, 110, 493

O'Dea, C. P., Baum, S. A., & Stanghellini, C. 1991, *The Astrophysical Journal*, 380, 66

Ofek, E. O. & Frail, D. A. 2011, *The Astrophysical Journal*, 737, 45

Ofek, E. O., Frail, D. A., Breslauer, B., Kulkarni, S. R., Chandra, P., Gal-Yam, A., Kasliwal, M. M., & Gehrels, N. 2011, *The Astrophysical Journal*, 740, 65

Ojha, R., Fey, A. L., Lovell, J. E. J., Jauncey, D. L., & Johnston, K. J. 2004, *The Astronomical Journal*, 128, 1570

Ojha, R., Fey, A. L., Jauncey, D. L., Lovell, J. E. J., & Johnston, K. J. 2004, *The Astrophysical Journal*, 614, 607

Ojha, R., Fey, A. L., Lazio, T. J. W., Jauncey, D. L., Lovell, J. E. J., & Kedziora-Chudczer 2006, *The Astrophysical Journal Supplement Series*, 166, 37

Ojha, R., Pursimo, T., Jauncey, D. L., Lovell, J. E., Macquart, J.-P., & Dutka, M. S. 2008, in *Frontiers of Astrophysics: A Celebration of NRAO's 50th Anniversary*, ed. A.H. Bridle, J.J. Condon, & G.C. Hunt (Astronomical Society of the Pacific Conference Series, Vol. 395; San Francisco: Astronomical Society of the Pacific), 375

Padmanabhan, T. 2002, *Theoretical Astrophysics: Volume 3, Galaxies and Cosmology*, (Cambridge: Cambridge University Press)

Patnaik, A. R., Browne, I. W. A., Wilkinson, P. N., & Wrobel, J. M. 1992, *Monthly Notices of the Royal Astronomical Society*, 254, 655

Peacock, J. A. 1985, *Monthly Notices of the Royal Astronomical Society*, 217, 601

Peebles, P. J. E. 1996, *Principles of Physical Cosmology*, (New Jersey: Princeton University Press)

Phillips, R. B., & Mutel, R. L. 1982, *Astronomy & Astrophysics*, 106, 21

Pursimo, T., Ojha, R., Jauncey, D., Lovell, J., Dutka, M., Bignall, H., Macquart, J.-P., Rickett, B., & Kedziora-Chudczer, L. 2008, in *Extragalactic Jets: Theory and Observation from Radio to Gamma Ray*, ed. T.A. Rector & D.S. De Young (Astronomical Society of the Pacific Conference Series, Vol. 386), 517

Quirrenbach, A., Witzel, A., Wagner, S., Sanchez-Pons, F., Krichbaum, T. P., Wegner, R., Anton, K., Erkens, U., Haehnelt, M., Zensus, J. A., & Johnston, K. J. 1991, *The Astrophysical Journal*, 372, L71

Rankin, J. M., Comella, J. M., Craft, H. D., Jr., Richards, D. W., Campbell, D. B., & Counselman, C. C., III 1971, *The Astrophysical Journal*, 162, 707

Ratcliffe, J. A. 1956, *Reports on Progress in Physics*, 19, 188

Rauch, M. 1998, *Annual Review of Astronomy & Astrophysics*, 36, 267

Readhead, A. C. S. 1994, *The Astrophysical Journal*, 426, 51

Readhead, A. C. S., Kemp, M. C., & Hewish, A. 1978, *Monthly Notices of the Royal Astronomical Society*, 185, 207

Reid, M. J., & Moran, J. M. 1981, *Annual Review of Astronomy & Astrophysics*, 19, 231

Rickett, B. J. 1990, *Annual Review of Astronomy & Astrophysics*, 28, 561

Rickett, B. J., & Coles, W. A. 1988, in *The Impact of VLBI on Astrophysics and Geophysics*, ed. M.J. Reid, & J.M. Moran (Proceedings of the International Astronomical Union Symposium, No. 129: Dordrecht, Kluwer Academic Publishers), 287

Rickett, B. J., Coles, W. A., & Bourgois, G. 1984, *Astronomy & Astrophysics*, 134, 390

Rickett, B. J., Witzel, A., Kraus, A., Krichbaum, T. P., & Qian, S. J. 2001, *The Astrophysical Journal*, 550, L11

Rickett, B. J., Kedziora-Chudczer, L., & Jauncey, D. L. 2001, *The Astrophysical Journal*, 581, 103

Rickett, B., Lovell, J., Macquart, J.-P., Jauncey, D. L., Bignall, H. E., Kedziora-Chudczer, L., Ojha, R., Pursimo, T., Shabala, S., & Senkbeil, C. 2007, *Proceedings of Science*, PoS(MRU)046

Richards, J. L., Max-Moerbeck, W., Pavlidou, V., King, O. G., Pearson, T. J., Readhead, A. C. S., Reeves, R., Shepherd, M. C., Stevenson, M. A., Weintraub, L. C., Fuhrmann, Lars, Angelakis, E., Zensus, J. A., Healey, S. E., Romani, R. W., Shaw, M. S., Grainge, K., Birkinshaw, M., Lancaster, K., Worrall, D. M., Taylor, G. B., Cotter, G., & Bustos, R. 2011, *The Astrophysical Journal Supplement Series*, 194, 29

Romani, R. W., Narayan, R., & Blandford, R. 1986, *Monthly Notices of the Royal Astronomical Society*, 220, 19

Romani, R., Blandford, R. D., & Cordes, J. M. 1987, *Nature*, 328, 324

Rybicki, G. B., & Lightman, A. P. 1979, *Radiative Processes in Astrophysics*, (Weinheim: Wiley-VCH)

Sarazin, C. L. 1986, *Reviews of Modern Physics*, 58, 1

Sault, R. J., Teuben, P. J., & Wright, M. C. H. 1995, in *Astronomical Data Analysis Software and Systems IV*, ed. R.A. Shaw, H.E. Payne, & J.J.E. Hayes (Astronomical Society of the Pacific Conference Series, Vol. 77; San Francisco: Astronomical Society of the Pacific), 433

Savolainen, T., & Kovalev, Y. Y. 2008, *Astronomy & Astrophysics*, 489, L33

Scheuer, P. A. G. 1968, *Nature*, 218, 920

Scheuer, P. A. G., & Williams, P. J. S. 1968, *Annual Review of Astronomy & Astrophysics*, 6, 321

Schillizi, R. T., Alexander, P., Cordes, J. M., Dewdney, P. E., Ekers, R. D., Faulkner, A. J., Gaensler, B. M., Hall, P. J., Jonas, J. L., & Kellerman, K. I. 2007, *SKA Memo*, 100

Schillizi, R. T., Alexander, P., Cordes, J., DeBoer, D., de Vos, M., Diamond, P., Dougherty, S., Hall., P., Jonas, J., Quinn, P., Rawlings, S., Bowler, J., Cloete, K., Crossby, P., Dewdney, P., Greenwood, C., McCool, R., Millenaar, R., & Turner, W. 2011, *Project execution plan: pre-construction phase for the Square Kilometre Array (SKA)*, Technical Report MGT-001.005.005-MP-001, Revision K

Seymour, N., Dwelly, T., Moss, D., McHardy, I., Zoghbi, A., Rieke, G., Page, M., Hopkins, A., & Loaring, N. 2008, *Monthly Notices of the Royal Astronomical Society*, 386, 1695

Shklovsky, I. S. 1953, *Proceedings of the Academy of Sciences U.S.S.R.*, 90, 983 [in Russian; translated with commentary in *A Source Book in Astronomy & Astrophysics*, ed. K.R. Lang, & O. Gingerich, 1979, (Massachusetts: Harvard University Press), 488]

Sieber, W. 1982, *Astronomy & Astrophysics*, 113, 311

Singal, A. K. 2009, *The Astrophysical Journal*, 703, L109

Smith, E. P., Heckman, T. M., Bothun, G. D., Romanishin, W., & Balick, B. 1986, *The Astrophysical Journal*, 306, 64

Smith, F. G. 1986, *Nature*, 165, 422

Sokasian, A., Abel, T., & Hernquist, L. 2002, *Monthly Notices of the Royal Astronomical Society*, 332, 601

Spangler, S. R. 1988, in *Radiowave Scattering in the Interstellar Medium*, ed. J.M. Cordes, B.J. Rickett & D.C. Backer (American Institute of Physics Conference Proceedings, Vol. 174; New York: American Institute of Physics), 32

Spangler, S. R., & Gwinn, C. R. 1990, *The Astrophysical Journal*, 353, L29

Spangler, S. R., Mutel, R. L., Benson, J. M., & Cordes, J. M. 1986, *The Astrophysical Journal*, 301, 312

Sutton, J. M. 1971, *Monthly Notices of the Royal Astronomical Society*, 155, 51

Tatarskii, V. I., & Zavorotnyi, V. U. 1980, *Progress in Optics*, XVIII, 204

Taylor, J. H., & Cordes, J. M. 1993, *The Astrophysical Journal*, 411, 674

Taylor, G. B., Carilli, C. L., & Perley, R. A., eds. 1999, *Synthesis Imaging in Radio Astronomy II*, (Astronomical Society of the Pacific Conference Series, Vol. 180; San Francisco: Astronomical Society of the Pacific)

Thompson, A. R. 1999, in *Synthesis Imaging in Radio Astronomy II*, eds. G.B. Taylor, C.L. Carilli, & R.A. Perley (Astronomical Society of the Pacific Conference Series, Vol. 180), 11

Thompson, A. R., Moran, J. M., & Swenson, G. W. 2001, *Interferometry and Synthesis in Radio Astronomy*, (Weinheim: Wiley-VCH)

Trott, C. M., Wayth, R. B., Macquart, J.-P., & Tingay, S. J. 2011, *The Astrophysical Journal*, 731, 81

Tzioumis, A. K., Tingay, S. J., Stansby, B., Reynolds, J. E., Phillips, C. J., Amy, S. W., Edwards, P. G., Bowen, M. A., Leach, M. R., Kesteven, M. J., Chung, Y., Stevens, J., Forsyth, A. R., Gulyaev, S., Natusch, T., Macquart, J.-P., Reynolds, C., Wayth, R. B., Bignall, H. E., Hotan, A., Hotan, C., Godfrey, L., Ellingsen, S., Dickey, J., Blanchard, J., & Lovell, J. E. J. 2010, *The Astronomical Journal*, 140, 1506

Urry, C. M., & Padovani, P. 1995, *Publications of the Astronomical Society of the Pacific*, 107, 803

van Langevelde, H. J., & Diamond, P. J. 1991, *Monthly Notices of the Royal Astronomical Society*, 249, 7P

Wagner, S. J., & Witzel, A. 1995, *Annual Review of Astronomy & Astrophysics*, 33, 163

Walker, M. A. 1998, *Monthly Notices of the Royal Astronomical Society*, 294, 307

Walker, M. A. 2001, *Monthly Notices of the Royal Astronomical Society*, 321, 176

Walker, M., & Wardle, M. 1998, *The Astrophysical Journal*, 498, L125

Wayth, R. B., Brisken, W. F., Deller, A. T., Majid, W. A., Thompson, D. R., Tingay, S. J., & Wagstaff, K. L. 2011, *The Astrophysical Journal*, 735, 97

Wayth, R. B., Tingay, S. J., Deller, A. T., Brisken, W. F., Thompson, D. R., Wagstaff, K. L., & Majid, W. A. 2012, *The Astrophysical Journal*, 753, L36

Wilkinson, P. N., Browne, I. W. A, Patnaik, A. R., Wrobel, J. M., & Sorathia, B. 1998, *Monthly Notices of the Royal Astronomical Society*, 300, 790

Wilkinson, P. N., Kellermann, K. I., Ekers, R. D., Cordes, J. M., & Lazio, T. J. W. 2004, *New Astronomy Reviews*, 48, 1551

Williamson, I. P. 1972, *Monthly Notices of the Royal Astronomical Society*, 157, 55

Yoshida, N., Sokasian, A., Hernquist, L. & Springel, V. 2003, *The Astrophysical Journal*, 598, 73

You, X. P., Hobbs, G., Coles, W. A., Manchester, R. N., Edwards, R., Bailes, M., Sarkissian, J., Verbiest, J. P. W., van Straten, W., Hotan, A., Ord, S., Jenet, F., Bhat, N. D. R., & Teoh, A. 2007, *Monthly Notices of the Royal Astronomical Society*, 378, 493

Zappacosta, L., Nicastro, F., Maiolino, R., Tagliaferri, G., Buote, D. A., Fang, T., Humphrey, P. J., & Gastaldello, F. 2010, *The Astrophysical Journal*, 717, 74

Note: Every reasonable effort has been made to acknowledge the owners of copyright material. I would be pleased to hear from any copyright owner who has been omitted or incorrectly acknowledged.

Appendix A

Principles of Interferometry and Aperture Synthesis

This section provides a brief introduction to the basic principles of interferometry and aperture synthesis, along with standard terminologies, coordinate systems and data reduction techniques used in the main text. A full treatment of these topics can be found in the classic textbook by Thompson et al. (2001), as well as the collection of lectures from the Sixth NRAO/NMIMT Synthesis Imaging Summer School edited by Taylor et al. (1999).

A.1 Visibilities and Sky Intensity Distributions

The basic quantity measured by an interferometer is the spatial coherence of the electric fields of a radiating source as measured by two antennas (or elements), i.e. the visibility. For antennas at location vectors $\mathbf{r}_1$ and $\mathbf{r}_2$, the visibility is a function only of the separation vector $\mathbf{r}_1 - \mathbf{r}_2$, and is related to the brightness or intensity of the sky in the direction of the unit vector $\mathbf{s}$ (Clarke, 1999):

$$V_\nu(\mathbf{r}_1, \mathbf{r}_2) = \int I_\nu(\mathbf{s}) e^{-2\pi i \nu \mathbf{s}\cdot(\mathbf{r}_1 - \mathbf{r}_2)/c} d\Omega. \tag{A.1}$$

ν is the frequency of the wave and c is the speed of light. Equation A.1 assumes that the sources of radiation on the sky are located at very large distances and distributed on the surface of a so called 'celestial sphere'. The element of solid angle, $d\Omega$, is integrated over the entire celestial sphere. The amplitude of the complex quantity V_ν is measured in units of flux density i.e. $\mathrm{Wm^{-2}Hz^{-1}}$. As the flux densities of radio astronomical sources are very small, radio astronomers often use the unit Jansky (Jy), where $1\,\mathrm{Jy} = 10^{-26}\,\mathrm{Wm^{-2}Hz^{-1}}$. I_ν, on the other hand, has units of $\mathrm{Wm^{-2}Hz^{-1}sr^{-1}}$. Since an image of the sky is just a map of the distribution of intensities on the sky, the spatial distribution of I_ν on the sky can also be referred to as the 'image'.

By introducing appropriate time delays into the various elements of the interferometer, a coordinate system can be chosen so that all the interferometric visibilities are obtained on a single plane. This allows the separation vectors to be expressed, in units of wavelength, as $\mathbf{r}_1 - \mathbf{r}_2 = \lambda(u, v, w = 0)$. The w-axis is usually selected to be parallel to the unit vector $\mathbf{s}_0$, the direction of the source at which the antennas are pointing, also called the phase tracking centre (see Figure A.1). The plane perpendicular to $\mathbf{s}_0$, where all the visibilities are measured, is usually referred to as the uv-plane. The magnitudes of the separation vectors on the plane are then referred to as uv-distances. In this coordinate system, when the phase tracking centre is not at the zenith, the separation vectors on the uv-plane are therefore distinct from the actual separation vectors between antennas on the ground-plane, the latter of which are referred to as baseline vectors, $\mathbf{b}$. An equivalent coordinate system exists at the surface of the celestial sphere, where the source intensities can be assumed to be distributed on an image-plane parallel to that of the uv-plane, so that the unit vector $\mathbf{s}$ can be expressed in coordinates of $(l, m, n = \sqrt{1 - l^2 - m^2})$. Equation A.1 can then be rewritten as (Clarke, 1999):

$$V_\nu(u, v, w = 0) = \int I_\nu(l, m) \frac{e^{-2\pi i(ul+vm)}}{\sqrt{1 - l^2 - m^2}} dldm. \tag{A.2}$$

The assumption of $w = 0$ also requires that the source of radiation is small and is located at the phase tracking centre, which is usually the case for most applications. In this case, l and m are small and $\sqrt{1 - l^2 - m^2}$ is close to unity.

In reality, the antennas will have a finite beamwidth with varying directional sensitivities, so that the true intensity distribution of the sky is modified by the frequency dependent antenna gain pattern (or primary beam), $A_\nu(l, m)$, so that (Clarke, 1999):

$$V_\nu(u, v, w = 0) = \int\int A_\nu(l, m) I_\nu(l, m) \frac{e^{-2\pi i(ul+vm)}}{\sqrt{1 - l^2 - m^2}} dldm. \tag{A.3}$$

Since $A_\nu(l, m)$ is usually well determined for each antenna of an array, it is easily corrected for and will be ignored in the equations that follow.

Equations A.1 to A.3 show that the complex visibility function, $V_\nu(u, v, w = 0)$ and the intensity distribution of the sky (or image), $I_\nu(l, m)$, are related simply by a Fourier transform. From basic Fourier transform theory, it can be inferred that the visibilities at longer uv-distances and baselines probe the fine-scale structure of a source, while that at shorter uv-distances and baselines probe its extended structure.

A.2 Aperture Synthesis

Due to the finite number of antennas in an array, sampling in the uv-plane is always discrete and incomplete. This is described by the sampling function, $S(u, v)$,which has

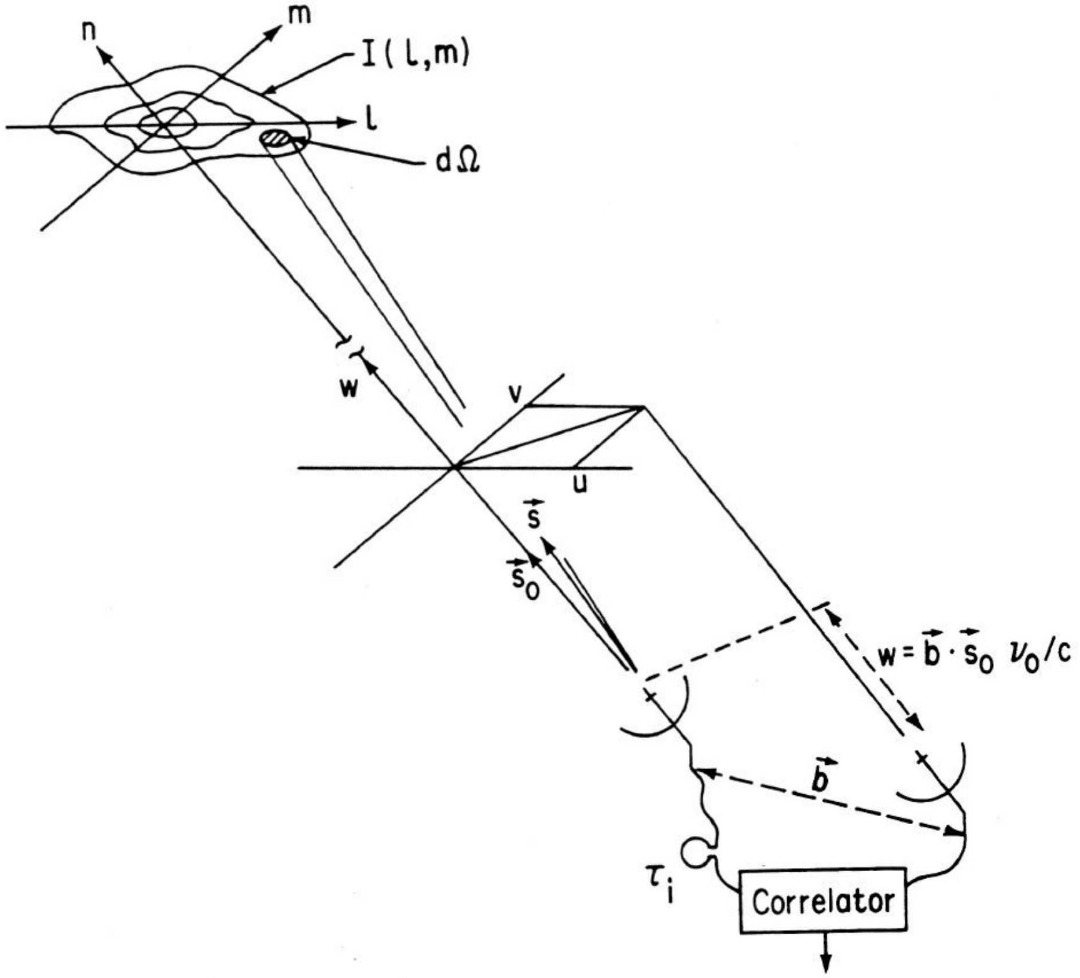

Figure A.1 — *(u,v,w) and (l,m,n) coordinate system used to describe the separation vectors of the visibilities and intensity distributions on the sky; image obtained from Thompson (1999)* a value of 0 where no measurements are obtained. The resultant image is therefore imperfect, commonly referred to as the dirty image, given by (Clarke, 1999):

$$I_\nu^D(l,m) = \int\int V_\nu(u,v)S(u,v)e^{2\pi i(ul+vm)}dudv, \tag{A.4}$$

where $A_\nu(l,m)$ has been ignored and $\sqrt{1-l^2-m^2}$ is assumed to be ~ 1. In the image plane, the dirty image is a convolution of the actual image and the synthesized beam (also called the dirty beam or the point spread function), B, of the array, so that:

$$I_\nu^D(l,m) = I_\nu * B, \tag{A.5}$$

where B is related to the sampling function via a Fourier transform:

$$B(l,m) = \int\int S(u,v)e^{2\pi i(ul+vm)}dudv. \tag{A.6}$$

The aim of aperture synthesis in radio astronomy is to place the antennas in a way that fills in the uv-plane as smoothly and as much as possible. However, since this is not practical, the best way to increase the uv-coverage is to 'move the antennas around', most often achieved by exploiting the natural rotation of the Earth in a technique called Earth-rotation synthesis.

Even then, the sampling will be incomplete, requiring a further processing technique called deconvolution to obtain an estimate of the actual image from a dirty image based on what is known about the synthesized beam of the array. Commonly used algorithms developed for deconvolution, including CLEAN (Hogbom, 1974) and the Maximum Entropy Method (MEM), are described in detail in Cornwell et al. (1999).

A.3 Standard Calibration Techniques

Due to various factors, the observed visibilities, $\tilde{V}_{ij}(t)$, measured at time t by the pair of antenna elements forming the baseline ij, often deviate from the true visibilities, $V_{ij}(t)$. Possible causes of these deviations include:

1. the dependence of antenna gain, $A_\nu(l,m)$, on source elevation, due to gravitational stresses deforming the large dishes.

2. time-varying atmospheric absorption and refraction effects leading to variable visibility amplitudes and phases.

3. differences between actual pointing position and the desired phase tracking centre (pointing errors), which can result from direction-dependent and direction-independent factors e.g. gravitational deformation of the antennas, strong winds, inaccurately determined antenna positions and time delays, as well as atmospheric refraction.

4. random stochastic noise.

The observed visibilities are therefore related to the true visibilities via the following equation (Fomalont & Perley, 1999):

$$\tilde{V}_{ij} = G_{ij}(t)V_{ij}(t) + \eta(t), \tag{A.7}$$

where $G_{ij}(t)$ is the baseline-based complex gain, and $\eta(t)$ represents stochastic noise. $G_{ij}(t)$ is in turn approximated as the product of the complex gains of each antenna, $g_i(t)$ and $g_j(t)$:

$$G_{ij}(t) = g_i(t)g_j^*(t) = a_i(t)a_j(t)e^{i(\phi_i(t)-\phi_j(t))}, \tag{A.8}$$

where $a_i(t)$ and $a_j(t)$ are antenna-based amplitude corrections, while $\phi_i(t)$ and $\phi_j(t)$ are antenna-based phase corrections.

$G_{ij}(t)$ for each of the $N(N-1)/2$ baselines of an interferometer, where N is the number of antennas in the array, can be determined through the observation of calibrator sources interspersed between observations of the target sources. The primary or flux calibrators are sources whose flux densities are well-known and do not vary with time, or at worst vary only slowly with time. Secondary calibrators or phase calibrators are compact sources that have well determined and stable positions on the sky. The complex gains as a function of time determined from these calibrators are recorded in gain tables, where the gains between successive calibrator observations are estimated using various interpolation schemes. Due to the finite interval between calibrator observations, the finite distance between the calibrator source and the target source, as well as imperfect interpolations, there will be residual errors in the determination of $G_{ij}(t)$, leading to errors in the measurement of the flux density.

Self-calibration is another powerful and commonly used method of determining all the $G_{ij}(t)$ values of an interferometric observation. Only relative phases are important in an interferometer, so one antenna is chosen as a reference antenna. Since there are only $2(N-1)$ complex gain error parameters (with $(N-1)$ amplitude errors and $(N-1)$ phase errors) affecting $N(N-1)$ observed visibility quantities (with $N(N-1)/2$ visibility amplitudes and $N(N-1)/2$ phases), the system is overdetermined. As a starting point, a sky intensity model is constructed based on the initial calibrated visibilities; this is usually a ‘CLEANed’ model in which deconvolution has been applied. This intensity model is then used to produce a set of visibilities based on the known separation vectors of all the baselines. These model visibilities are then compared to the observed visibilities, with the goal of minimising their differences iteratively by adjusting the values of $g_i(t)$ and $\phi_i(t)$ of all antennas until convergence is obtained. Algorithms used for self-calibration are described in further detail by Cornwell & Fomalont (1999).

Other application-specific calibration techniques include bandpass calibration (to correct for frequency-dependent instrumental gains and atmospheric effects across all frequency channels) and polarization calibration (to correct for leakages and phase differences between the two polarization channels); these are further explained by Fomalont & Perley (1999).

Appendix B

Variability Characteristics of Observed Sources

Table B.1: Variability Characteristics of Observed Sources

Source	$\tau_{char,4.9}$	$\tau_{char,8.4}$	$m_{4.9}$	$m_{8.4}$	$D_{4.9}$(4d)	$D_{8.4}$(4d)
J0009+1513	-	-	1.2	1.2	1.89e-004 ± 1.55e-004	1.44e-004 ± 1.09e-004
J0017+5312	> 11	-	1.6	1.0	4.68e-004 ± 1.57e-004	1.53e-004 ± 4.86e-005
J0017+8135	-	-	0.6	0.6	1.89e-005 ± 1.52e-005	4.89e-006 ± 5.48e-009
J0056+1625	0.34± 0.10	0.32± 0.04	3.3	3.4	2.40e-003 ± 8.13e-004	1.91e-003 ± 7.00e-004
J0108+0135	> 11	-	1.9	0.9	6.49e-004 ± 1.87e-004	7.94e-005 ± 7.61e-005
J0122+0310	0.30± 0.44	0.55± 0.34	1.7	1.6	3.19e-004 ± 1.47e-004	3.70e-004 ± 1.47e-004
J0122+2502	-	-	0.9	0.5	6.65e-005 ± 4.59e-004	8.03e-007 ± 2.57e-004
J0126+2559	-	-	0.9	0.5	6.85e-005 ± 4.63e-005	3.25e-006 ± 1.02e-004
J0135+2158	0.49± 0.19	-	1.9	1.3	1.02e-003 ± 3.74e-004	2.82e-004 ± 1.78e-004
J0154+4743	0.52± 0.41	0.17± 0.02	2.0	2.4	7.53e-004 ± 1.58e-004	9.47e-004 ± 2.09e-004
J0217+7349	-	-	0.5	0.3	4.50e-007 ± 1.43e-005	4.26e-006 ± 1.42e-005
J0237+2046	0.18± 0.09	0.03± 0.13	2.1	1.5	8.65e-004 ± 2.68e-004	3.10e-004 ± 7.81e-005
J0238+1636	> 11	> 11	2.4	2.6	1.16e-003 ± 3.60e-004	1.59e-003 ± 3.10e-004
J0242+1101	-	-	1.3	1.0	2.62e-004 ± 1.17e-004	1.83e-004 ± 5.06e-005
J0259+1925	> 11	0.56± 0.06	5.5	3.8	4.85e-003 ± 1.45e-003	2.92e-003 ± 9.37e-004
J0308+1208	1.43± 0.68	0.47± 0.20	2.5	2.5	1.29e-003 ± 4.71e-004	1.12e-003 ± 2.80e-004
J0313+0228	> 11	> 11	6.8	4.0	9.36e-003 ± 1.77e-003	2.65e-003 ± 8.44e-004
J0321+1221	-	-	0.9	1.1	4.03e-005 ± 6.29e-006	1.69e-004 ± 1.01e-004
J0323+0446	0.62± 0.16	0.86± 0.01	5.6	3.5	7.27e-003 ± 2.28e-003	2.47e-003 ± 8.19e-004
J0342+3859	> 11	> 11	5.7	7.1	5.77e-003 ± 1.33e-003	9.78e-003 ± 2.21e-003
J0343+3622	2.90± 2.80	1.17± 1.13	2.8	2.5	1.34e-003 ± 2.24e-004	1.18e-003 ± 2.66e-004
J0358+3850	9.86± 1.49	2.50± 1.57	4.1	4.1	4.28e-003 ± 1.01e-003	4.12e-003 ± 4.42e-004
J0403+2600	-	-	0.8	1.0	2.89e-005 ± 1.75e-005	1.37e-004 ± 5.02e-005
J0406+2511	> 11	> 11	8.5	3.9	1.49e-002 ± 2.67e-003	2.65e-003 ± 6.67e-004
J0409+1217	4.52± 3.27	> 11	4.0	5.2	3.52e-003 ± 6.33e-004	6.42e-003 ± 9.76e-004
J0422+0219	0.70± 0.93	0.22± 0.11	1.5	1.5	4.12e-004 ± 2.46e-004	3.73e-004 ± 1.37e-004
J0449+1121	> 11	-	2.3	0.9	6.22e-004 ± 2.31e-004	8.46e-005 ± 3.68e-005
J0459+0229	-	-	1.0	1.0	8.63e-005 ± 5.40e-005	1.23e-004 ± 3.69e-005
J0510+1800	0.50± 0.67	0.95± 0.02	7.7	6.6	7.89e-003 ± 4.64e-003	9.59e-003 ± 3.52e-003
J0530+1331	> 11	2.97± 1.75	5.6	7.1	7.10e-003 ± 1.67e-003	1.16e-002 ± 2.34e-003
J0534+1047	-	-	0.7	0.4	5.70e-006 ± 1.18e-005	4.29e-006 ± 2.81e-005

Continued on Next Page. . .

Table B.1 – Continued

Source	$\tau_{char,4.9}$	$\tau_{char,8.4}$	$m_{4.9}$	$m_{8.4}$	$D_{4.9}$(4d)	$D_{8.4}$(4d)
J0539+1433	0.24± 0.36	0.65± 0.32	3.1	3.6	1.52e-003 ± 7.06e-004	2.73e-003 ± 6.44e-004
J0614+6046	-	-	0.9	1.1	4.87e-005 ± 2.26e-005	1.62e-004 ± 4.84e-005
J0624+3856	> 11	2.90± 1.92	2.2	1.2	1.12e-003 ± 2.38e-004	4.39e-004 ± 8.67e-005
J0646+4451	-	-	0.6	0.3	8.58e-007 ± 1.26e-005	6.51e-007 ± 1.45e-005
J0659+0813	0.86± 0.10	-	1.6	1.1	3.69e-004 ± 1.19e-004	1.80e-004 ± 6.82e-005
J0726+6125	1.36± 1.27	> 11	3.0	2.2	1.85e-003 ± 2.65e-004	8.89e-004 ± 1.37e-004
J0739+0137	7.94± 9.28	> 11	3.7	1.7	3.09e-003 ± 1.32e-003	7.91e-004 ± 1.42e-004
J0739+7527	-	-	1.2	0.9	2.70e-004 ± 4.67e-005	6.27e-005 ± 1.68e-005
J0741+2557	0.09± 0.14	0.53± 0.17	3.4	1.4	1.85e-003 ± 4.89e-004	3.09e-004 ± 9.67e-005
J0745+1011	-	-	0.6	0.7	1.10e-006 ± 2.38e-005	2.94e-005 ± 2.01e-005
J0750+1231	-	-	1.6	1.2	2.91e-004 ± 1.71e-004	2.57e-004 ± 6.50e-005
J0757+0956	0.19± 0.05	0.09± 0.04	3.6	2.5	2.15e-003 ± 4.85e-004	1.18e-003 ± 2.70e-004
J0800+4854	0.07± 0.10	0.02± 0.01	5.0	5.2	4.74e-003 ± 6.22e-004	4.56e-003 ± 5.92e-004
J0805+6144	-	-	0.6	0.4	6.15e-006 ± 2.90e-006	4.82e-007 ± 1.34e-005
J0810+1010	-	-	1.5	1.0	1.43e-004 ± 1.36e-004	1.06e-004 ± 4.74e-005
J0811+0146	2.44± 2.23	7.02± 0.47	4.3	2.4	5.27e-003 ± 9.23e-004	1.43e-003 ± 3.31e-004
J0818+4222	0.08± 0.18	0.06± 0.01	3.8	2.0	2.55e-003 ± 5.71e-004	7.42e-004 ± 1.35e-004
J0821+3107	0.27± 0.06	-	2.3	1.4	8.51e-004 ± 2.14e-004	1.86e-004 ± 4.08e-005
J0825+0309	0.43± 0.25	-	2.3	1.2	8.73e-004 ± 2.17e-004	2.91e-004 ± 1.09e-004
J0850+5159	-	-	1.2	0.9	1.45e-004 ± 3.41e-005	3.43e-005 ± 1.71e-005
J0854+8034	-	-	1.0	0.7	1.25e-004 ± 2.29e-005	1.00e-005 ± 7.34e-006
J0856+7146	0.67± 0.38	> 11	5.4	4.3	4.71e-003 ± 9.65e-004	2.86e-003 ± 4.76e-004
J0914+0245	-	-	1.1	0.7	2.12e-004 ± 7.20e-005	2.61e-005 ± 8.20e-006
J0916+0242	0.34± 0.11	0.17± 0.06	7.7	4.2	9.91e-003 ± 4.26e-003	2.99e-003 ± 9.61e-004
J0920+4441	-	-	0.8	0.6	8.13e-005 ± 3.38e-005	4.92e-006 ± 1.41e-007
J0929+5013	0.30± 0.23	0.04± 0.09	4.1	2.8	3.03e-003 ± 5.08e-004	1.22e-003 ± 1.61e-004
J0953+1720	0.06± 0.07	-	2.0	1.4	6.12e-004 ± 1.48e-004	2.70e-004 ± 8.83e-005
J0958+4725	-	-	0.8	0.7	5.77e-005 ± 2.21e-005	4.08e-005 ± 1.52e-005
J0958+6533	6.64± 2.53	> 11	1.8	1.7	5.30e-004 ± 9.55e-005	4.22e-004 ± 8.06e-005
J1007+1356	-	-	0.9	0.6	6.38e-005 ± 4.41e-005	2.34e-007 ± 1.60e-005
J1016+2037	-	-	0.7	0.5	5.02e-005 ± 4.45e-005	2.13e-006 ± 8.20e-005
J1049+1429	0.20± 0.07	0.02± 0.06	3.0	3.0	1.58e-003 ± 4.16e-004	1.62e-003 ± 1.88e-004
J1056+7011	0.56± 0.51	1.75± 1.51	2.3	1.8	8.90e-004 ± 1.12e-004	6.17e-004 ± 7.58e-005
J1125+2610	-	-	0.9	0.7	9.09e-005 ± 3.01e-005	3.40e-005 ± 1.51e-005
J1159+2914	0.19± 0.02	0.08± 0.13	3.6	1.6	2.63e-003 ± 6.15e-004	4.97e-004 ± 7.11e-005
J1247+7046	0.26± 0.23	0.23± 0.20	2.9	2.0	1.72e-003 ± 2.55e-004	6.96e-004 ± 7.58e-005
J1316+6927	-	-	1.5	0.9	2.83e-004 ± 7.57e-005	7.36e-005 ± 2.36e-005
J1328+6221	0.05± 0.10	0.00± 0.05	5.9	3.0	6.29e-003 ± 7.58e-004	1.62e-003 ± 1.98e-004
J1330+4954	-	-	1.2	0.7	1.53e-004 ± 4.34e-005	1.49e-005 ± 1.08e-005
J1354+6645	0.16± 0.08	0.06± 0.25	2.3	3.1	8.56e-004 ± 1.32e-004	1.16e-003 ± 2.73e-004
J1410+6141	> 11	-	2.0	1.1	6.53e-004 ± 8.67e-005	1.44e-004 ± 4.28e-005
J1417+3818	0.62± 0.59	2.94± 1.84	2.7	1.7	1.32e-003 ± 2.10e-004	4.73e-004 ± 8.80e-005
J1436+6336	-	-	0.9	0.6	5.18e-005 ± 3.88e-005	2.11e-006 ± 1.81e-005
J1437+5112	0.56± 0.33	-	2.1	1.3	6.95e-004 ± 1.44e-004	2.04e-004 ± 3.02e-005
J1442+0625	0.09± 0.05	1.04± 1.03	3.8	3.5	2.41e-003 ± 5.77e-004	1.67e-003 ± 2.89e-004
J1535+4836	-	-	0.9	0.8	2.61e-005 ± 1.88e-005	2.84e-005 ± 2.17e-005
J1549+5038	0.01± 0.09	0.03± 0.13	3.0	2.1	1.62e-003 ± 3.23e-004	7.39e-004 ± 1.54e-004
J1559+0805	-	-	1.1	0.9	1.24e-004 ± 3.92e-005	7.75e-005 ± 3.56e-005
J1610+7809	0.40± 0.35	-	2.6	1.3	1.26e-003 ± 1.78e-004	2.62e-004 ± 4.04e-005
J1616+0459	-	-	0.7	0.9	2.00e-006 ± 1.86e-005	8.35e-005 ± 3.16e-005
J1619+2247	-	-	1.3	1.0	2.12e-004 ± 3.98e-005	1.21e-004 ± 4.43e-005
J1625+4134	-	-	0.9	0.6	5.23e-005 ± 3.00e-005	1.43e-005 ± 1.42e-005

Continued on Next Page…

Table B.1 – Continued

Source	$\tau_{char,4.9}$	$\tau_{char,8.4}$	$m_{4.9}$	$m_{8.4}$	$D_{4.9}$(4d)	$D_{8.4}$(4d)
J1639+4128	> 11	-	3.5	1.7	1.88e-003 ± 3.03e-004	2.91e-004 ± 1.01e-004
J1659+1714	> 11	-	1.9	1.3	5.46e-004 ± 1.55e-004	2.00e-004 ± 6.52e-005
J1701+0338	> 11	0.63± 0.24	3.8	1.7	2.44e-003 ± 8.16e-004	6.11e-004 ± 1.39e-004
J1716+6836	-	-	1.0	0.9	9.73e-005 ± 4.18e-005	7.57e-005 ± 2.17e-005
J1719+0817	-	-	1.3	0.8	2.56e-004 ± 8.74e-005	7.60e-005 ± 2.37e-005
J1719+1745	> 11	0.72± 0.36	2.5	1.6	1.15e-003 ± 2.21e-004	5.11e-004 ± 1.09e-004
J1728+0427	8.68± 0.26	1.44± 0.31	1.6	2.3	5.04e-004 ± 1.16e-004	1.09e-003 ± 3.44e-004
J1733+1635	-	-	1.3	1.1	1.55e-004 ± 5.15e-005	1.05e-004 ± 4.38e-005
J1734+3857	0.39± 0.19	2.46± 2.15	2.0	2.0	4.99e-004 ± 2.14e-004	7.27e-004 ± 1.19e-004
J1740+5211	0.45± 0.29	0.36± 0.20	1.5	1.4	3.48e-004 ± 7.26e-005	3.12e-004 ± 6.72e-005
J1742+5945	1.48± 1.26	-	3.7	1.3	2.78e-003 ± 4.10e-004	2.41e-004 ± 5.09e-005
J1745+4059	4.24± 3.22	0.52± 0.27	6.4	2.7	9.01e-003 ± 1.05e-003	1.52e-003 ± 3.18e-004
J1751+0939	-	> 11	1.1	2.3	2.49e-004 ± 5.61e-005	1.11e-003 ± 3.64e-004
J1757+0531	> 11	> 11	3.1	2.4	1.12e-003 ± 2.36e-004	9.61e-004 ± 2.13e-004
J1800+3848	-	-	1.3	0.8	2.00e-004 ± 7.50e-005	1.12e-004 ± 2.85e-005
J1812+5603	0.77± 0.51	-	1.7	1.0	5.00e-004 ± 1.29e-004	1.83e-004 ± 4.75e-005
J1819+3845	0.23± 0.06	7.55± 6.15	2.0	2.5	4.82e-004 ± 1.21e-004	1.47e-003 ± 2.31e-004
J1832+1357	-	-	1.4	1.1	4.41e-005 ± 4.70e-006	4.73e-005 ± 4.39e-005
J1839+4100	0.16± 0.03	-	1.6	1.2	4.43e-004 ± 1.16e-004	1.57e-004 ± 5.95e-005
J1850+2825	1.53±10.86	-	3.1	1.1	4.34e-004 ± 6.83e-005	8.37e-005 ± 4.73e-005
J1905+1943	0.55± 1.30	0.46± 0.31	2.0	1.5	6.89e-004 ± 3.44e-004	3.67e-004 ± 1.54e-004
J1919+3159	> 11	> 11	5.1	6.7	3.23e-003 ± 1.45e-003	1.20e-002 ± 3.15e-003
J1931+4743	0.10± 0.25	0.06± 0.01	7.2	7.6	9.04e-003 ± 2.59e-003	1.07e-002 ± 2.25e-003
J2002+4725	1.44± 0.73	1.81± 0.72	2.0	1.6	8.22e-004 ± 1.86e-004	5.23e-004 ± 1.66e-004
J2006+6424	> 11	> 11	3.3	2.0	1.70e-003 ± 2.21e-004	9.25e-004 ± 1.75e-004
J2011+7205	2.25± 1.57	0.32± 0.14	6.4	6.4	1.02e-002 ± 1.12e-003	6.47e-003 ± 1.25e-003
J2012+6319	1.31± 0.51	0.43± 0.18	4.9	4.2	5.27e-003 ± 1.66e-003	4.00e-003 ± 9.75e-004
J2016+1632	> 11	> 11	4.8	2.4	5.09e-003 ± 1.81e-003	1.15e-003 ± 3.48e-004
J2113+1121	4.56± 2.94	0.71± 0.04	7.9	5.2	1.76e-002 ± 4.16e-003	4.98e-003 ± 1.54e-003
J2116+0536	6.01± 1.00	1.04± 0.26	4.4	2.5	3.75e-003 ± 9.61e-004	1.13e-003 ± 3.46e-004
J2123+0535	9.96± 6.71	-	1.6	0.9	4.49e-004 ± 1.81e-004	5.72e-005 ± 4.60e-005
J2137+0451	1.23± 0.32	0.20± 0.26	2.1	1.9	7.02e-004 ± 2.14e-004	4.98e-004 ± 1.84e-004
J2203+1725	> 11	0.47± 0.01	3.7	2.1	2.79e-003 ± 9.39e-004	7.00e-004 ± 2.77e-004
J2208+1808	-	-	1.4	1.4	1.66e-004 ± 7.84e-005	1.11e-004 ± 7.10e-005
J2212+2355	> 11	0.63± 0.07	2.3	2.6	1.11e-003 ± 2.04e-004	1.23e-003 ± 4.40e-004
J2221+1117	0.20± 0.36	0.17± 0.43	2.9	2.3	1.05e-003 ± 5.80e-004	6.07e-004 ± 3.94e-004
J2237+4216	1.23± 1.12	0.27± 0.05	5.9	3.2	8.67e-003 ± 1.65e-003	2.14e-003 ± 6.59e-004
J2241+0953	0.54± 0.74	-	1.6	1.0	5.14e-004 ± 2.72e-004	1.31e-004 ± 4.95e-005
J2242+2955	6.25± 3.20	0.11± 0.03	3.9	2.0	3.09e-003 ± 7.11e-004	6.94e-004 ± 1.59e-004
J2253+3236	0.05± 0.24	0.09± 0.03	2.4	2.4	5.90e-004 ± 2.60e-004	8.92e-004 ± 2.46e-004
J2258+0516	-	-	1.1	1.1	3.82e-005 ± 3.04e-005	1.46e-004 ± 7.05e-005
J2304+2710	0.16± 0.01	0.07± 0.04	3.4	2.4	2.17e-003 ± 5.50e-004	9.89e-004 ± 2.21e-004
J2311+4543	1.18± 0.78	1.12± 1.04	3.6	3.1	3.13e-003 ± 7.71e-004	2.35e-003 ± 5.26e-004
J2315+8631	1.78± 1.32	0.43± 0.42	2.8	1.5	1.72e-003 ± 2.11e-004	3.66e-004 ± 5.89e-005
J2339+0244	0.91± 1.21	0.28± 0.16	1.6	1.9	3.49e-004 ± 2.50e-004	6.76e-004 ± 2.18e-004

Note — Column 1: IAU name (J2000.0); Column 2: Estimated characteristic timescale of source variability at 4.9 GHz (days); Column 3: Estimated characteristic timescale of source variability at 8.4 GHz (days); Column 4: Raw modulation index at 4.9 GHz with no error subtraction (%); Column 5: Raw modulation index at 8.4 GHz with no error subtraction (%); Column 6: 4-day structure function at 4.9 GHz with D_{noise} subtracted; Column 7: 4-day structure function at 8.4 GHz with D_{noise} subtracted.

Appendix C

Properties of Observed Sources

Table C.1: Properties of Observed Sources

Source	l	b	I_α	$S_{4.9}$	$S_{8.4}$	$\alpha_{4.9}^{8.4}$	Optical ID	z
J0009+1513	108.25	-46.45	0.7	0.15	0.12	-0.44	fsrq	2.2
J0017+5312	117.85	-9.33	13.3	0.59	0.64	0.14	fsrq	2.6
J0017+8135	121.61	18.80	2.2	1.36	1.26	-0.13	fsrq	3.4
J0056+1625	124.84	-46.43	0.8	0.19	0.23	0.33	bllc	0.2
J0108+0135	131.83	-60.99	0.7	1.53	2.06	0.56	fsrq	2.1
J0122+0310	137.80	-58.82	0.5	0.11	0.11	-0.04	fsrq	4.0
J0122+2502	131.83	-37.29	0.9	0.75	0.66	-0.21	fsrq	2.0
J0126+2559	132.77	-36.21	1.0	0.81	0.66	-0.39	fsrq	2.4
J0135+2158	136.37	-39.74	0.9	0.18	0.14	-0.37	fsrq	3.4
J0154+4743	133.85	-13.80	8.6	0.50	0.60	0.35	fsrq	1.0
J0217+7349	128.93	11.96	2.2	4.31	4.21	-0.05	fsrq	2.4
J0237+2046	153.93	-35.62	1.3	0.13	0.13	-0.03	fsrq	1.9
J0238+1636	156.77	-39.11	1.1	3.66	3.60	-0.03	fsrq	0.9
J0242+1101	161.86	-43.31	1.0	0.92	0.82	-0.22	fsrq	2.7
J0259+1925	160.05	-34.05	1.3	0.14	0.18	0.49	fsrq	0.5
J0308+1208	167.70	-38.52	1.9	0.07	0.06	-0.18	fsrq	1.4
J0313+0228	177.68	-44.80	6.9	0.12	0.11	-0.23	fsrq	1.0
J0321+1221	170.59	-36.24	2.1	1.68	1.52	-0.19	fsrq	2.7
J0323+0446	177.73	-41.41	4.6	0.12	0.13	0.16	fsrq	2.3
J0342+3859	155.66	-12.80	8.1	0.09	0.10	0.24	fsrq	1.1
J0343+3622	157.53	-14.69	7.8	0.32	0.28	-0.22	fsrq	1.5
J0358+3850	158.27	-10.86	12.3	0.18	0.18	-0.01	fsrq	0.6
J0403+2600	168.03	-19.65	4.7	2.13	2.16	0.03	fsrq	2.1
J0406+2511	169.20	-19.69	4.5	0.12	0.11	-0.15	fsrq	0.7
J0409+1217	180.12	-27.90	7.6	0.32	0.29	-0.19	bllc	0.5
J0422+0219	191.59	-31.23	4.6	1.25	1.07	-0.29	fsrq	2.3
J0449+1121	187.43	-20.74	9.8	0.86	0.78	-0.18	bllc	1.2
J0459+0229	197.01	23.34	7.4	1.06	0.72	-0.71	fsrq	2.4
J0510+1800	184.73	-12.79	22.1	0.73	0.96	0.51	fsrq	0.4
J0530+1331	191.37	-11.01	70.5	3.30	3.16	-0.08	fsrq	2.1
J0534+1047	194.24	-11.65	147.0	0.17	0.16	-0.13	fsrq	2.6
J0539+1433	191.60	-8.66	30.3	0.37	0.43	0.30	fsrq	2.7
J0614+6046	153.60	19.15	1.7	0.70	0.49	-0.66	fsrq	2.7
J0624+3856	175.03	11.82	1.7	0.87	0.70	-0.41	fsrq	3.5

Continued on Next Page...

Table C.1 – Continued

Source	l	b	I_α	$S_{4.9}$	$S_{8.4}$	$\alpha_{4.9}^{8.4}$	Optical ID	z
J0646+4451	171.09	17.95	0.9	3.06	3.67	0.33	fsrq	3.4
J0659+0813	206.48	5.48	7.6	0.73	0.67	-0.15	fsrq	2.8
J0726+6125	155.22	27.77	1.0	0.24	0.37	0.79	null	1.5
J0739+0137	216.99	11.38	1.8	1.74	1.94	0.20	fsrq	0.2
J0739+7527	139.27	29.18	1.4	0.22	0.14	-0.80	fsrq	2.8
J0741+2557	194.02	21.90	2.8	0.05	0.08	0.83	fsrq	2.7
J0745+1011	209.80	16.59	1.4	2.95	2.06	-0.67	nlrg	2.6
J0750+1231	208.16	18.76	1.8	3.76	4.15	0.19	fsrq	0.9
J0757+0956	211.31	19.06	1.5	1.02	1.09	0.13	bllc	0.3
J0800+4854	170.11	31.16	0.5	0.10	0.08	-0.39	fsrq	2.1
J0805+6144	155.05	32.35	0.8	0.97	0.72	-0.56	fsrq	3.0
J0810+1010	212.59	22.12	1.3	0.11	0.09	-0.31	fsrq	2.5
J0811+0146	220.71	18.57	1.7	0.65	0.98	0.76	bllc	1.1
J0818+4222	178.23	33.40	1.2	1.35	1.41	0.08	bllc	1.1
J0821+3107	191.46	31.76	2.3	0.08	0.06	-0.66	fsrq	2.6
J0825+0309	221.22	22.39	1.0	1.38	1.53	0.19	bllc	0.5
J0850+5159	166.51	39.18	0.7	0.10	0.08	-0.34	fsrq	1.9
J0854+8034	132.44	31.64	1.6	0.25	0.22	-0.19	fsrq	1.1
J0856+7146	142.03	35.31	0.9	0.07	0.11	0.82	fsrq	0.5
J0914+0245	228.35	32.82	2.1	1.08	0.89	-0.36	syf1	0.4
J0916+0242	228.72	33.23	1.9	0.09	0.11	0.40	fsrq	1.1
J0920+4441	175.70	44.82	0.4	1.09	1.34	0.38	fsrq	2.2
J0929+5013	167.66	45.42	0.6	0.40	0.39	-0.06	bllc	0.4
J0953+1720	216.86	48.01	0.9	0.10	0.07	-0.66	fsrq	0.7
J0958+4725	170.06	50.73	0.7	1.52	1.26	-0.35	fsrq	1.9
J0958+6533	145.75	43.13	1.1	1.07	0.99	-0.16	bllc	0.4
J1007+1356	223.61	49.67	1.1	0.71	0.66	-0.13	fsrq	2.7
J1016+2037	214.85	54.19	0.8	0.61	0.46	-0.53	fsrq	3.1
J1049+1429	230.79	59.00	0.9	0.13	0.15	0.21	fsrq	1.6
J1056+7011	135.96	43.92	-0.2	0.28	0.35	0.40	fsrq	2.5
J1125+2610	210.92	70.89	0.5	1.17	1.02	-0.26	fsrq	2.3
J1159+2914	199.41	78.37	0.5	2.60	3.24	0.41	fsrq	0.7
J1247+7046	123.45	46.34	0.4	0.09	0.11	0.35	fsrq	1.3
J1316+6927	119.70	47.52	0.4	0.12	0.11	-0.20	null	3.7
J1328+6221	115.56	54.23	0.5	0.10	0.08	-0.26	fsrq	1.2
J1330+4954	107.34	66.02	0.5	0.11	0.09	-0.35	fsrq	2.9
J1354+6645	113.50	49.20	0.6	0.08	0.08	-0.00	fsrq	0.6
J1410+6141	107.48	53.00	0.4	0.17	0.18	0.16	fsrq	2.2
J1417+3818	70.13	68.78	0.4	0.12	0.10	-0.31	fsrq	0.4
J1436+6336	105.17	49.73	0.5	1.42	1.65	0.28	fsrq	2.1
J1437+5112	90.42	58.70	0.7	0.11	0.08	-0.53	fsrq	2.1
J1442+0625	359.78	56.52	0.6	0.08	0.08	-0.03	fsrq	0.7
J1535+4836	78.38	51.86	0.2	0.14	0.15	0.10	fsrq	2.6
J1549+5038	80.24	49.06	0.5	0.91	0.93	0.04	fsrq	2.2
J1559+0805	18.84	41.60	0.9	0.12	0.15	0.38	fsrq	2.2
J1610+7809	111.97	34.34	0.8	0.18	0.15	-0.34	fsrq	1.9
J1616+0459	18.05	36.45	1.1	0.93	0.82	-0.24	fsrq	3.2
J1619+2247	39.67	43.03	0.6	0.70	0.68	-0.07	fsrq	2.0
J1625+4134	65.74	44.22	0.4	1.04	0.84	-0.39	fsrq	2.5
J1639+4128	65.63	41.73	0.5	0.13	0.15	0.24	fsrq	0.7
J1659+1714	36.93	32.33	1.1	0.13	0.11	-0.26	fsrq	2.0
J1701+0338	23.08	26.07	2.0	0.11	0.09	-0.37	fsrq	1.3

Continued on Next Page. . .

Table C.1 – Continued

Source	l	b	I_α	$S_{4.9}$	$S_{8.4}$	$\alpha_{4.9}^{8.4}$	Optical ID	z
J1716+6836	99.27	33.75	1.3	0.54	0.61	0.22	fsrq	0.8
J1719+0817	29.96	24.10	2.0	0.59	0.49	-0.34	fsrq	1.2
J1719+1745	39.52	28.10	1.1	0.63	0.60	-0.10	bllc	0.1
J1728+0427	27.29	20.48	2.4	0.47	0.46	-0.04	fsrq	0.3
J1733+1635	39.73	24.61	1.4	0.11	0.07	-0.76	fsrq	2.6
J1734+3857	64.02	31.01	1.4	0.82	0.83	0.01	bllc	1.0
J1740+5211	79.56	31.75	0.9	0.99	1.12	0.24	fsrq	1.4
J1742+5945	88.46	31.78	1.3	0.19	0.19	0.00	bllc	0.4
J1745+4059	66.82	29.33	2.1	0.10	0.11	0.13	fsrq	0.9
J1751+0939	34.92	17.65	3.1	3.88	5.25	0.56	fsrq	0.3
J1757+0531	31.80	14.40	3.4	0.08	0.06	-0.52	nlrg	0.3
J1800+3848	65.17	26.03	2.2	0.82	1.00	0.36	fsrq	2.1
J1812+5603	84.59	27.47	1.8	0.46	0.47	0.04	fsrq	3.0
J1819+3845	66.25	22.46	2.2	0.19	0.23	0.34	syf1	0.5
J1832+1357	43.40	10.40	2.3	0.31	0.33	0.12	fsrq	2.8
J1839+4100	69.83	19.60	2.4	0.10	0.07	-0.66	fsrq	2.3
J1850+2825	58.56	12.73	5.8	1.11	1.45	0.49	fsrq	2.6
J1905+1943	52.11	5.86	3.2	0.26	0.21	-0.40	fsrq	2.3
J1919+3159	64.55	8.65	6.5	0.11	0.11	0.03	fsrq	3.5
J1931+4743	79.98	13.53	5.2	0.11	0.10	-0.12	fsrq	1.8
J2002+4725	82.22	8.79	14.7	0.98	0.87	-0.23	fsrq	2.3
J2006+6424	97.65	16.73	4.3	0.48	0.83	1.01	fsrq	1.6
J2011+7205	105.02	19.92	4.8	0.11	0.10	-0.25	fsrq	2.5
J2012+6319	96.99	15.62	3.9	0.13	0.11	-0.24	fsrq	1.0
J2016+1632	57.65	-10.29	3.6	0.47	0.56	0.33	fsrq	2.2
J2113+1121	61.59	-24.73	1.9	0.07	0.06	-0.10	fsrq	1.3
J2116+0536	56.84	-28.67	1.4	0.21	0.18	-0.21	fsrq	2.2
J2123+0535	58.01	-30.12	1.4	2.06	1.85	-0.19	fsrq	1.9
J2137+0451	59.71	-33.31	1.3	0.13	0.11	-0.29	fsrq	2.4
J2203+1725	75.67	-29.63	1.7	0.98	1.04	0.10	bllc	1.1
J2208+1808	77.23	-29.91	1.4	0.09	0.05	-1.14	fsrq	3.1
J2212+2355	82.24	-26.09	2.3	0.96	1.00	0.07	fsrq	1.1
J2221+1117	74.45	-37.07	1.0	0.08	0.08	0.13	fsrq	2.2
J2237+4216	97.98	-13.99	5.1	0.23	0.21	-0.17	fsrq	1.0
J2241+0953	78.17	-41.44	1.4	0.60	0.53	-0.21	fsrq	1.7
J2242+2955	92.17	-25.12	2.3	0.11	0.10	-0.26	fsrq	1.7
J2253+3236	95.88	-23.99	3.0	0.19	0.19	-0.03	fsrq	0.3
J2258+0516	78.56	-47.62	0.9	0.21	0.19	-0.19	fsrq	2.5
J2304+2710	95.43	-29.92	1.3	0.10	0.12	0.27	fsrq	1.3
J2311+4543	105.32	-13.70	3.2	0.28	0.35	0.40	fsrq	1.4
J2315+8631	121.39	23.95	2.3	0.24	0.24	-0.03	fsrq	0.9
J2339+0244	89.97	-55.46	0.6	0.09	0.08	-0.33	fsrq	2.7

Note — Column 1: IAU name (J2000.0); Column 2: Galactic longitude; Column 3: Galactic latitude; Column 4: line-of-sight Hα intensities (Rayleigh), obtained from (Haffner et al., 2003); Column 5: Mean flux density at 4.9 GHz (Jy); Column 6: Mean flux density at 8.4 GHz (Jy); Column 7: Source spectral index; Column 8: Optical identification, flat spectrum radio-loud quasar (fsrq), BL Lac object (bllc), Seyfert 1 galaxy (syf1), narrow-line radio galaxy (nlrg) or no ID available (null), obtained from the NASA Extragalactic Database (NED), SIMBAD database and Pursimo et al. (submitted); Column 9: Source redshift, obtained from the NASA Extragalactic Database (NED), SIMBAD database and Pursimo et al. (submitted).

Appendix D

Transition Frequencies and Scattering Screen Distances

This section presents the relations used to estimate the transition frequency (v_t) between weak and strong ISS, as well as the scattering screen distance for each source. These values were used for the Monte Carlo simulations in Section 5.4 and to obtain estimates of the apparent angular sizes of the sources in Section 6.3.

The emission measure (EM) is the integral of the square of the electron density along the path from the observer to the source, and for the ISM is related to the line-of-sight Galactic Hα intensity (I_α) in units of Rayleighs as (Haffner et al., 1998):

$$\mathrm{EM} = 2.75\ T_4^{0.9} I_\alpha\ \mathrm{cm}^{-6}\,\mathrm{pc}, \tag{D.1}$$

where T_4 is the temperature of the ionized cloud in units of 10^4 K, typically ~ 8000 K for the warm ionized medium (Haffner et al., 1998). The transition frequency between weak and strong ISS, is then given by Cordes & Lazio (2003) as:

$$v_t = 318\ \mathrm{SM}^{\frac{6}{17}} (D_{\mathrm{ISM}})^{\frac{5}{17}}\ \mathrm{GHz}, \tag{D.2}$$

where D_{ISM} is the effective distance to the ISM scattering screen in units of kpc, while SM is the scattering measure of the ISM, which is defined as the path integral of the strength of turbulence in the ISM along the line-of-sight to the source (see Section 6.2 for more details on the SM), and has units of $\mathrm{kpc}\,\mathrm{m}^{-20/3}$. Cordes & Lazio (2003) also give the relation between the SM and the EM, which for a thin screen can be estimated as:

$$\mathrm{EM} = 544.6\, l_0^{2/3} \epsilon^{-2} (1 + \epsilon^2) \mathrm{SM}\ \mathrm{pc}\,\mathrm{cm}^{-6}, \tag{D.3}$$

where ϵ is the normalized variance of the electron densities within the scattering cloud, which we assume to be ~ 1. l_0 is the outer scale of the turbulence in units of pc, which has been estimated to be $\lesssim 100$ pc (Haverkorn et al., 2008). A value of 100 pc is selected for my calculations. Combining Equations D.1 to D.3, we obtain:

$$v_t = 318\,(D_{\mathrm{ISM}})^{\frac{5}{17}} \left[\frac{I_\alpha}{198\,\mathrm{R}}\left(\frac{T_4^{0.9}\epsilon^2}{l_0^{2/3}(1+\epsilon^2)}\right)\right]^{\frac{6}{17}}\ \mathrm{GHz}. \tag{D.4}$$

The distance to the scattering screen, used in Equation D.3 and for the Goodman & Narayan (2006) fitting functions for ISS, is calculated for each source as $D_{\mathrm{ISM}} = 0.35 \times \csc|b|$ kpc, where b is the Galactic latitude of the source. The value of 0.35 was selected as the constant of proportionality so that $D_{\mathrm{ISM}} \sim 0.5$ kpc at $b = \pm 45^\circ$, increasing to ~ 2.0 kpc at $b = \pm 10^\circ$ and decreasing to ~ 0.35 kpc at $b = \pm 90^\circ$.

It has to be noted that Equation D.3 assumes a particular outer scale of Kolmogorov turbulence, and gives only the upper bounds of EM (see Cordes & Lazio (2003)). Therefore, Equation D.4 in fact gives only the upper limit to ν_t, and initial calculations give $4 \lesssim \nu_t \lesssim 80$ GHz with a median of ~ 12 GHz. It can be inferred from Figure 5.6 that this is not the case, so a factor of 0.25 is multiplied to ν_t to reduce its values to a range of $1 \lesssim \nu_t \lesssim 20$ GHz with a median of ~ 3 GHz.

Appendix E

Extension of Thin Screen Scattering Model to Cosmological Scales

This section describes the formulation of the thin screen scattering model for angular broadening and temporal smearing in the IGM, based on a similar widely-used model for the ISM extended to cosmological scales. This formulation is drawn from an unpublished manuscript by J.-P. Macquart.

E.1 Angular Broadening

Equation 1.1 in Section 1.2 gives the amplitude of the wave received at vector position $\mathbf{X}$ at the plane of the observer, for the case where the source is at infinite distance. In the case of the IGM where the distance between the scattering screen and the source is comparable to the distance between the scattering screen and the observer, the equation is given by Goodman & Narayan (1989) as:

$$\psi(\mathbf{X}) = \frac{e^{-i\pi/2}}{2\pi r_F^2} \int \exp\left[i\phi(\mathbf{x}) + \frac{i}{2r_F^2}\left(\mathbf{x} - \frac{D_{LS}}{D_S}\mathbf{X}\right)^2 \right] d^2\mathbf{x}, \tag{E.1}$$

where $\mathbf{x}$ is a positional vector on the scattering screen, $\phi(\mathbf{x})$ represents the phase fluctuations imprinted on the scattered wave by the density inhomogeneities of the scattering screen. At cosmological scales, D_{LS} and D_S are the angular diameter distance to the source and the angular diameter distance from the source to the scattering screen respectively. The modified Fresnel scale is now given by:

$$r_F = \sqrt{\frac{cD_L D_{LS}}{2\pi\nu D_S(1+z_L)}} \tag{E.2}$$

where c is the speed of light, ν is the observing frequency, z_L is the sourceredshift, and D_L is the angular diameter distance to the scattering screen. These equations are similar in form to that used in the gravitational lensing literature (see for example, Macquart (2004)).

The quantity of interest in the formulation of scatter broadening is the second order moment of the the wavefield, or mutual coherence of the wavefield at two locations separated by a distance $\mathbf{r}$ at the plane of the observer. This is equivalent to the visibility function in radio interferometry, where the average visibility of the scattered wave is given by:

$$V(\mathbf{r}) = \langle \psi(\mathbf{r}' + \mathbf{r}) \psi^*(\mathbf{r}') \rangle. \tag{E.3}$$

Substituting Equation E.3 into Equation E.1, and averaging the visibilities over all phase fluctuations, one obtains a simple solution given by Tatarskii & Zavorotnyi (1980):

$$V(\mathbf{r}) = \exp\left[-\frac{1}{2} D_\phi \left(\frac{D_{LS}}{D_S} \mathbf{r} \right) \right], \tag{E.4}$$

where $D_\phi(\mathbf{r})$ is the structure function of the phase fluctuations, defined in Equation 1.2. In the case of anisotropic scattering, $\mathbf{r}$ becomes direction independent, and the phase structure function can be written as:

$$D_\phi(r) = \left\langle \left[\phi(r + r') - \phi(r') \right]^2 \right\rangle = \left(\frac{r}{r_{\rm diff}} \right)^{\beta - 2}, \tag{E.5}$$

where r is the magnitude of $\mathbf{r}$. β is the exponent for a power law spectrum of density inhomogeneities, and is often assumed to be 11/3 following Kolmogorov turbulence for the ISM. Assuming that $r_{\rm diff} > l_0$, the value of $r_{\rm diff}$ is given as:

$$r_{\rm diff} = \left[2^{2-\beta} \frac{\pi c^2 r_e^2 \beta}{\nu^2 (1 + z_L)^2} {\rm SM} \frac{\Gamma(-\beta/2)}{\Gamma(\beta/2)} \right]^{1/(2-\beta)} \tag{E.6}$$

where r_e is the classical electron radius, and $\Gamma(x)$ is the gamma function.

Substituting Equations E.5 and E.6 into Equation E.4, and performing a Fourier transform of the visibilities, gives the brightness distribution on the sky (see Appendix A), $B(\theta)$. Solving for the case where $B(\theta)$ is half the maximum value, the scatter broadened image can be calculated to have an angular size (at full width half maximum) equivalent to:

$$\theta_{scat} = f \frac{D_{LS}}{D_S k r_{\rm diff}} = f \, \frac{{\rm SM}^{\frac{3}{5}}}{\nu^{2.2} (1 + z_L)^{1.2}} \left(\frac{D_{LS}}{D_S} \right) \tag{E.7}$$

where the f term gathers all the constants, and $k = 2\pi/\lambda$ is the wavenumber. Note that in performing the Fourier transform, k is in the rest frame of the observer.

E.2 Temporal Smearing

The temporal smearing of a pulse in the context of the scattering of gravitational waves is given by Macquart (2004) as:

$$\tau = \frac{1}{ck}\left(\frac{r_F}{r_{\mathrm{diff}}}\right)^2. \tag{E.8}$$

Combining Equations E.7 and E.8, one obtains:

$$\tau = \frac{D_L D_S \theta_{scat}^2}{2cD_{LS}(1+z_L)}. \tag{E.9}$$

The additional factor of 2 in the denominator arises from the fact that Macquart (2004) defines θ_{scat} as the half width at half maximum, while I define θ_{scat} to be the full width at half maximum scatter broadened image.

When I heard the learned astronomer;
When the proofs, the figures, were ranged in columns before me;
When I was shown the charts and the diagrams,
to add, divide, and measure them;
When I, sitting, heard the astronomer,
where he lectured with much applause in the lecture-room,
How soon, unaccountable, I became tired and sick;
Till rising and gliding out, I wandered off by myself,
In the mystical moist night-air, and from time to time,
Looked up in perfect silence at the stars.
— ***Walt Whitman***